Investigations into the molecular mechanisms of α2β1 integrin activation.

A thesis submitted to The University of Manchester for the degree of Doctor of Philosophy in the Faculty of Life Sciences

2005

Dimitra Valdramidou

ProQuest LLC.
789 East Eisenhower Parkway
P.O. Box 1346
Ann Arbor, MI 48106 – 1346

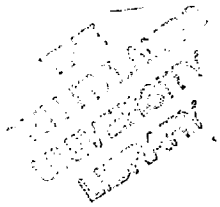

Th26502

Table of contents

List of Figures

List of Tables

Abstract

Integrin α2β1 belongs to the sub-family of integrins that include an A domain in the α subunit (αA). Ligand binding to α2β1 takes place at the MIDAS cation-binding site within αA. In non-αA-domain-containing integrins, the primary ligand-binding site is a MIDAS site in a homologous A-domain in the β subunit (βA). Two additional metal ion binding sites in the βA domain, the ADMIDAS (adjacent to the MIDAS) and LIMBS (ligand-induced metal-binding site), clustered around the MIDAS, suggest that ligand binding is regulated in a complex manner by cations. However, in α2β1, the βA domain is not directly involved in ligand binding. To study the functional relationship of the αA with the βA domain, the entire ectodomains of human α2 and β1 integrin subunits were expressed as Fc-fusion proteins in mammalian cells to generate a soluble integrin. Full-length and truncated variants of the soluble α2β1-Fc integrin, that retained the structural and functional characteristics of the parent integrin, were used as substrates in collagen-binding solid phase assays to study the role of cations in integrin activation. Using a mutagenesis-based approach, it was shown that the loss of metal occupancy at any one of the three β1 cation-binding sites perturbed the ligand-binding activity of α2β1. An activating mutation at the C-terminus of the α2 A domain rescued collagen-binding activity, but with impaired affinity. These data demonstrated that β1 A domain affinity state contributes to α2β1 affinity modulation primarily by altering the apparent affinity of the MIDAS for its ligand. The regulatory effect of divalent ions was examined further and it was found that the inhibitory profile of cation binding for the MIDAS and ADMIDAS mutants was similar to that for α5β1, a non-αA domain-containing integrin. It was also found that the LIMBS mutations prevented the augmentation of Mg^{2+}-induced collagen binding by Ca^{2+}, suggesting that the LIMBS is a stimulatory Ca^{2+} regulatory site. Taken together these data indicate that regulation of ligand binding through the cation binding sites in the βA domain plays an important role in both αA domain-containing and non-αA domain-containing integrins.

Declaration

No portion of the work referred to in the thesis has been submitted in support of an application for another degree or qualification of this or any other institute of learning.

Copyright and the ownership of intellectual property rights

Acknowledgments

This Ph.D. has been a challenging and an extremely rewarding experience. It would not have been made possible without the help and support of many academics, friends and family.

First, I would like to thank my supervisor Prof. Martin Humphries for his enthusiasm, invaluable advice and guidance. A long time ago he impressed upon me the notion that integrin signalling and activation was an exciting and vital science, and encouraged me to pursue it, even when I wasn't quite sure what contribution I could make through it. Next, I would like to extend my appreciation to Dr. Linda Green who has been instrumental in the development of my technical skills and Dr. Paul Mould who has been a great source of information and scientific advice. I would also like to thank my project advisor Dr. Andrew Gilmore for his helpful insightful comments concerning some of my arguments. My thanks also go to Dr Horst Blum who was the originator of the idea to investigate into integrin-platelet biology and supported the funding of this project from Sanofi-Aventis.

Attributions and a special 'thank you' to all my colleagues / friends in the Humphries' lab. Anthea, Kirsty, Jon, Sue and Mr Bass have seen me through a lot of dilemmas, whether they have been science related and not. But most of all, my 'lab twin' Tanja encouraged me to envision optimism at times when all I could see in front of me was a blank binding-assay plate.

Thank you,
to all my mates, and especially to Michelle, for providing all sorts of entertainment, plus dancing trips or in-the-house gatherings that made me a more pleasant person, i.e. kept me from going loco, throughout these three years. To Tania, Villy and the Greek 'tsoliades' who have provided a lot of insight information and gossip into Hellenic matters (inc. fashion tips, celebrity news) over coffee and dinner parties. This also goes out to my gym buddies for motivating me to let off steam and recharge my energy to carry on my work. And to my partner, Nick, who has been supportive and extremely understanding throughout this entire process.

I dedicate this thesis to my family.

Abbreviations

α2[x]β1[x]-Fc	Recombinant soluble human α2β1-Fc integrin, where 'x' is the mutated amino acid residue
a.a.	Amino acid
Ab	Antibody
ABTS	2, 2'-azino-bis (3-ethylbenzthiazoline 6-sulphonic acid)
ADMIDAS	Adjacent to MIDAS
ATP	Adenosine triphosphate
BCA	Bicinchoninic acid
BSA	Bovine serum albumin
β-TD	β-Tail domain
CA	Constitutive active GST α2 A domain a.a.140-339 [I332G]
C-linker	C-terminal linker sequence connecting the α7-helix in αA domain to the β-propeller
C-terminal	Carboxy-terminal
DMEM	Dulbecco's modified Eagle medium
dNTP	Deoxynucleotide triphosphate
DTT	Dithiothrietol
ECM	Extracellular matrix
EDTA	Ethylenediaminetetra-acetic acid
EGF	Epidermal growth factor
ELISA	Enzyme-linked immunosorbant assay
FACS	Fluorescence-activated cell sorter
FAK	Focal adhesion kinase
FCS	Foetal calf serum
Fn	Fibronectin
FRET	Fluorescence resonance energy transfer
Fl	Full-length recombinant GST α2 A domain (a.a. 124-339)
FL	Full-length recombinant soluble human α2β1-Fc integrin
GST	Glutathione S-transferase
HBS	HEPES buffered saline
HBSS	Hanks' balanced salt solution
HEPES	2-hydroxyethylpiperazine-N'-2-ethanesulphonic acid

HRP	Horse-radish peroxidase
ICAM	Intercellular adhesion molecule
Ig	Immunoglobulin
IgG	Immunoglobulin G
IPTG	Isopropyl-1-thio-β-D-galactopyranoside
LB	Luria Bertani medium
LABS	Ligand attenuated binding site
LIBS	Ligand induced binding site
LIMBS	Ligand induced metal binding site
mAb	Monoclonal antibody
MAdCAM	Mucosal addressin cell adhesion molecule
MEM	Minimum essential medium
MIDAS	Metal ion-dependent adhesion site
MOPS	3-(N-morpholino)propane sulphonic acid
NMR	Nuclear magnetic resonance
N-terminal	Amino-terminal
PBS	Phosphate buffered saline
PCR	Polymerase chain reaction
PKC	Protein kinase C
PMSF	Phenylmethylsulphonyl fluoride
PSI	Plexin/Semaphorin/Integrin-like
SDS-PAGE	Sodium dodecyl sulphate-polyacrylamide gel electrophoresis
SH2/ SH3	Src homology domain 2/ Src homology domain 3
TBS	Tris-buffered saline
TRIS	Tris (hydroxymethyl) methylamine
TR	Truncated recombinant soluble human $\alpha 2\beta 1$-Fc integrin
VCAM-1	Vascular cell adhesion molecule-1
vWF	von Willebrand factor
wt	Wild-type recombinant $\alpha 2\beta 1$-Fc integrin
Wt	Wild-type GST $\alpha 2$ A domain a.a.140-339

Chapter
1.0 Introduction

1.1 Cell adhesion

Cell adhesion regulates a wide variety of dynamic processes, such as cell migration, growth and differentiation. All of these functions are crucial for cell survival and development of multicellular organisms. In addition, cellular adhesion also controls components of a sophisticated signalling machinery that enables cells to communicate and, subsequently, coordinate their behaviour for the benefit of the organism as a whole. Over the past decade, extensive research has been undertaken to try and understand the mechanisms of adhesion at the cellular level. These studies have involved identifying both adhesion factors in extracellular matrices and the cell-surface receptors recognising them. Molecular and biophysical characterisation of the components of cell adhesion complexes is vital to the understanding of how particular complexes activate cytoskeletal and signal transduction pathways that ultimately control cell behaviour and normal development. Moreover, exploring the structure and molecular mechanisms of how these molecules are regulated present new targets for rational drug development and therapeutic intervention in selected adhesion pathways that may treat many human disorders.

1.2 Integrins as cellular adhesion receptors

Integrins comprise a large family of cell surface receptors found in almost all cell types that participate in the control of cell adhesion. These molecules are now recognised as central components of fundamental biological processes including embryonic development, apoptosis, haemostasis, immune recognition and wound healing [Hynes R.O., 2002; Calderwood D.A., 2004]. Moreover, the importance of integrin activation is not limited to normal development. Abnormal integrin functions have been implicated in a variety of pathological disorders, including thrombosis, tumour cell growth and metastasis, inflammation, osteoporosis, ulceration, rheumatoid arthritis and microbial and parasitic infection [Liddington & Ginsberg, 2002]. Elucidation of the mechanisms involved in integrin activation to regulate adhesion with the ECM and signalling would therefore be of a great advantage in understanding the molecular basis of such diseases.

Integrins exist as transmembrane heterodimers, composed of α and β subunits (Figure 1.1a). The two subunits are produced by different genes, the products of which are independently processed and expressed as type-I transmembrane glycoproteins (Figure 1.1b). A number of different isoforms have been described for each subunit; at least 18 α subunits (α1-α11, αIIb, αD, αE, αM, αL, αV, αX) and 8 β subunits (β1-β8) have been identified in mammals. Non-covalent association of a pair of subunits results in 24 known different dimers (Figure 1.1c) [Arnaout *et al.*, 2004]. In the past, integrins were grouped on the basis of a common β subunit, but it is now clear that α subunits can combine with more than one β subunit. The structural and functional diversity of integrins reflects the lack of well-defined integrin classes; subfamilies can be based on shared β subunits, ligand-binding properties or shared structural features of the α subunits. Using the latter criterion, two subfamilies can be formed depending on the presence or absence of a 200 amino acid conserved domain, the 'αA domain' in the α integrin subunit.

Each integrin subunit comprises a large extracellular domain, approximately 1200 amino acids long in the α and 800 amino acids in the β subunit, a single transmembrane helix and a short cytoplasmic domain (usually 30-50 amino acids long or less) with the exception of β4 in which the cytoplasmic domain is over 1000 residues. Early electron microscopy (EM) of rotary shadowed and negatively stained preparations of integrins showed these heterodimeric receptors to be comprised of a 10 nm diameter globular head and two long stalks that anchor the protein on the membrane [Carrell *et al.*, 1985; Nermut *et al.*, 1988]. This picture changed considerably with the advances in EM and atomic resolution of two different integrin heterodimers in recent years, which have allowed the definitive domain structure of both extracellular subunits to be determined (Section 1.5).

a)

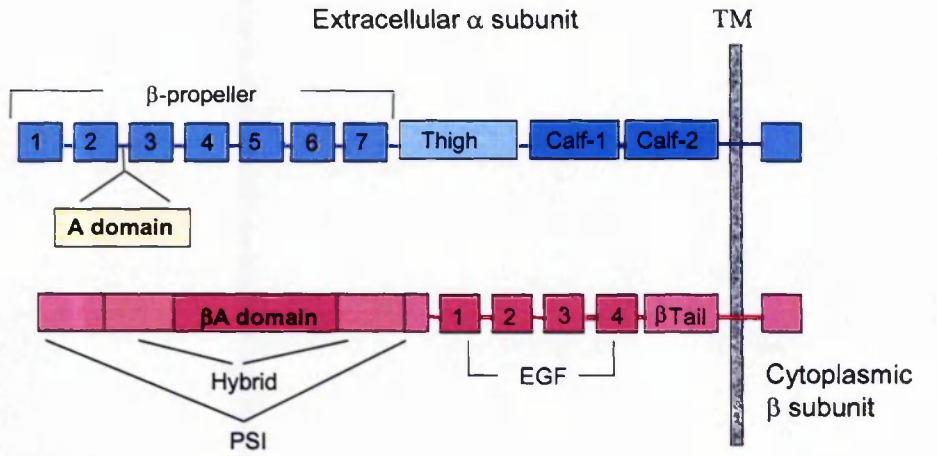

b)

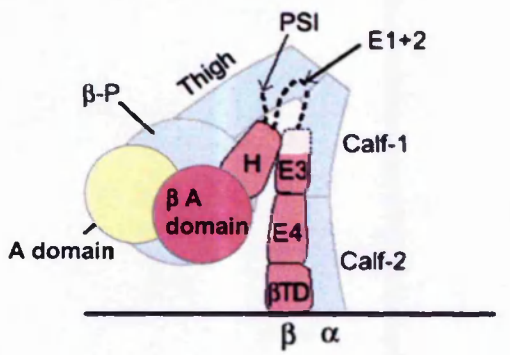

c)

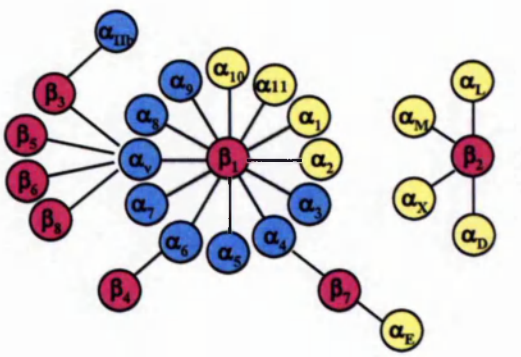

Figure 1.1. Integrin architecture. a) The domain structure of a generic integrin. An integrin α subunit associates with a β subunit in a non-covalent fashion. **b) Proposed quaternary structure of the extracellular integrin domains.** Based on the crystallographic data of αVβ3 integrin extracellular domain but with a putative αA domain added where it would be located in integrins that contain an αA domain; an αA domain absent in αVβ3 (reproduced from Beglova *et al.*, 2002). c) **Vertebrate αβ integrin subunit associations.** 18 α and 8 β subunits form 24 heterodimers, indicated by connecting lines. α subunits are in blue and β subunits are in pink. Half of the α subunits contain A-domains, shown in yellow.

1.3 Integrin bi-directional signalling

Integrins are diverse cell adhesion molecules that mediate the attachment of cells to the extracellular matrix, as well as linking cells to each other. Integrin extracellular head domains bind to an array of ligands in the extracellular matrix (ECM) including collagens, fibronectin and laminins, or to ligands on the surface of other cells, i.e. to intercellular adhesion molecules (ICAM) and vascular cell adhesion molecules (VCAM) [Hynes R.O., 1992]. Extracellular ligand binding elicits a cascade of conformational changes within the integrin that results in recruitment of cytoplasmic proteins to the integrin cytoplasmic tail and formation of adhesion plaques. The propagation of these changes from the extracellular domain through the plasma membrane to the inside of the cells, where the downstream effects take place is called 'outside-in' signalling. In addition, integrin-ligand binding is modulated (stimulated / inhibited) by cytoplasmic signals. Interactions of the cytoplasmic tails of integrins with intracellular proteins initiates the propagation of conformational changes from the cytoplasmic environment to the extracellular face. Thus, the binding of integrins to ligands as regulated by intracellular stimuli is called 'inside-out' signalling. Moreover, integrins possess the ability to modulate their activity on a timescale of <1 s in response to intracellular signals [Takagi & Springer, 2002]. On the whole, rapid and reversible integrin function mediates the connection of the cell with the ECM and controls normal cell behaviour that in turns directs the ECM re-assembly, cell adhesion and subsequently cell survival and tissue formation.

1.3.1 Outside-in signalling

One important mechanism by which cells can modulate integrin-mediated adhesion is by changing integrin affinity for ECM ligands [Calderwood D.A., 2004]. For some years it has been known that after cellular activation, conformational changes take place in many of the integrin extracellular domains. However, it has been questioned whether conformational change in integrins is a result from ligand binding rather than a cause of ligand binding (affinity regulation) [Bazzoni & Hemler, 1998]. It is now evident that conformational changes upon activation, are physiologically relevant for regulating integrin affinity for ligand. Recently, the term 'integrin priming' was introduced to indicate the acquisition of ligand-binding ability. This term can be used to distinguish integrin affinity regulation from integrin activation, which would be used to define the process of ligand-induced conformational changes leading to intracellular signalling events

[Humphries *et al.*, 2003]. Here, the term integrin activation denotes ligand-induced changes to describe the increase in monomeric affinity that is coupled to alterations in integrin conformation [Calderwood D.A., 2004]. Thus, integrin activation followed by integrin cross-linking with ECM ligands results in the formation of integrin clusters. Integrin aggregation ultimately leads to the formation of focal adhesions, where cytoskeletal proteins link integrins to the actin cytoskeleton (Figure 1.2). Some of the cytoplasmic proteins found in focal adhesions as a result of integrin clustering are talin, α-actinin, vinculin, tensin, paxillin and filamin, many of which interact with filamentous actin [Critchley D.R., 2000]. These only represent a small repertoire of the 50 proteins found to date in focal adhesions [Zamir & Geiger, 2001] and the list of newly discovered components is rapidly expanding.

Based on results from *in vitro* peptide-binding studies α-actinin [Otey *et al.*, 1990; Sampath *et al.*, 1998], filamin [Pfaff *et al.*, 1998] and talin [Knezevic *et al.*, 1996; Sampath *et al.*, 1998] have been shown to bind to the cytoplasmic domains of specific β subunits. In particular, the talin head domain has been shown to directly activate αIIbβ3 integrin [Calderwood *et al.*, 2002; 1999], and bind to several other β subunits including β1, β5,β7 [Calderwood *et al.*, 2003] and β2 cytoplasmic tails [Kim *et al.*, 2003]. Because talin is a cytoskeletal protein known to interact with actin filaments [Hemmings *et al.*, 1996], the above findings demonstrated that actin filaments can be directly linked to integrins through at least one cytoskeletal protein, and indirectly through talin-associated cytoskeletal proteins. Other β tail-binding proteins that might directly affect integrin activation are cytohesin [Kolanus *et al.*, 1996], β3-endonexin [Kashiwagi *et al.*, 1997] and CD98hc [Fenczik *et al.*, 1997; Zent *et al.*, 2000]. The calcium- and integrin-binding (CIB) protein is an α tail-binding protein has also been reported to directly regulate integrin activation [Tsuboi S., 2002]. The functional relevance of these integrin-associated proteins awaits further definition.

In addition to forming a mechanical link between the extracellular matrix and the acto-myosin contractile apparatus, the recruitment of structural proteins to integrins is believed to serve as a framework for the association of signalling proteins involved in signal transduction pathways that regulate cell behaviour [Clark & Brugge, 1995]. In particular, GTP-binding proteins of the Rho family of low molecular weight GTPases, are involved in

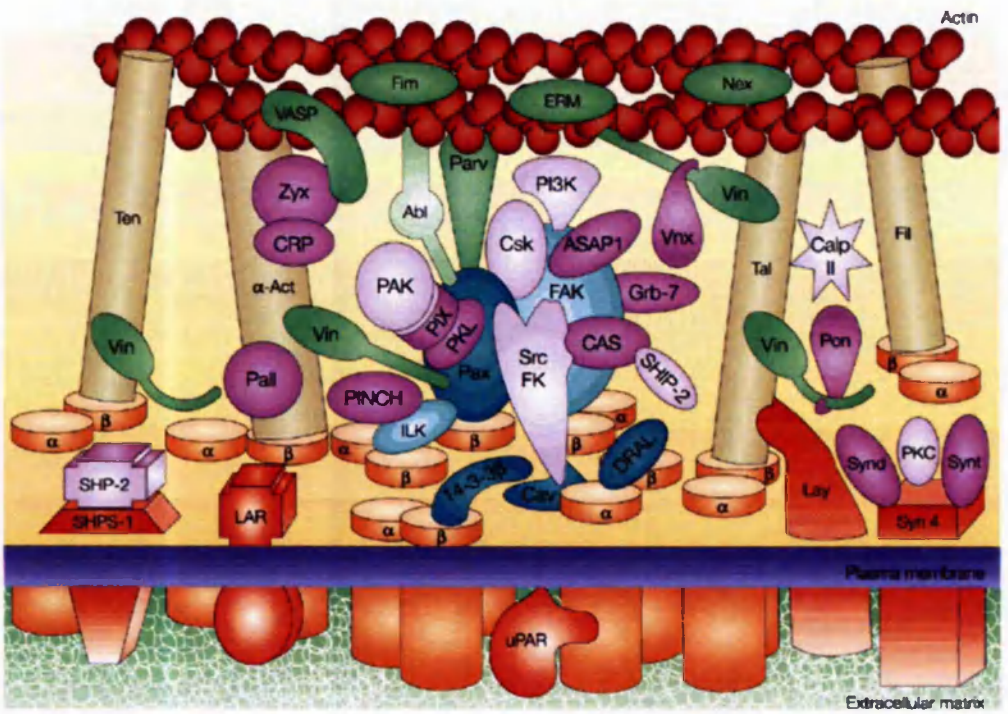

Figure 1.2. Schematic depicting the complexity of the main molecular domains of cell–matrix adhesions. The primary adhesion receptors are heterodimeric (α and β) integrins, represented by orange cylinders. Additional membrane-associated molecules enriched in these adhesions (red) include syndecan-4 (Syn4), layilin (Lay), the phosphatase leukocyte common antigen-related receptor (LAR), SHP-2 substrate-1 (SHPS-1) and the urokinase plasminogen activator receptor (uPAR). Proteins that interact with both integrin and actin, and which function as structural scaffolds of focal adhesions, include α-actinin (α-Act), talin (Tal), tensin (Ten) and filamin (Fil), shown as golden rods. Integrin-associated molecules in blue include: focal adhesion kinase (FAK), paxillin (Pax), integrin-linked kinase (ILK), down-regulated in rhabdomyosarcoma LIM-protein (DRAL), 14-3-3 and caveolin (Cav). Actin-associated proteins (green) include vasodilator-stimulated phosphoprotein (VASP), fimbrin (Fim), ezrin–radixin–moesin proteins (ERM), Abl kinase, nexillin (Nex), parvin/actopaxin (Parv) and vinculin (Vin). Other proteins, many of which might serve as adaptor proteins, are coloured purple and include zyxin (Zyx), cysteine-rich protein (CRP), palladin (Pall), PINCH, paxillin kinase linker (PKL), PAK-interacting exchange factor (PIX), vinexin (Vnx), ponsin (Pon), Grb-7, ASAP1, syntenin. As taken from Geiger *et al.*, 2001.

the reorganisation of specialised actin structures; principal examples include: Rho in stress fibre formation, Rac in lamellipodia and Cdc42 in filopodia formation [Brakebush & Fassler, 2003]. Other signalling molecules implicated in outside-in signalling are adaptor proteins, such as ILK, Cas, Shc [Miao *et al.*, 2002]. Intracellular protein kinases recruited to the adhesion complex include tyrosine kinases like focal adhesion kinase (FAK), Src, Yes, Fyn [Geiger *et al.*, 2001], and serine-threonine kinases including the mitogen-activated protein kinases (MAPK) [Geiger *et al.*, 2001], PAK [Sells *et al.*, 2000] or PKC [Parsons *et al.*, 2002]. Different integrin-stimulated signalling events have been reported to involve phospholipid metabolism and changes in cytoplasmic calcium levels [Kanner *et al.*, 1993].

1.3.2 Inside-out signalling

Cell adhesion can be regulated both by controlling the cellular repertoire of integrins as well as by limiting their affinity for extracellular ligands. The remarkable ability of integrins to modulate their activity in response to intracellular signalling events adds to the multiplicity of integrin functions. 'Affinity modulation', the process by which integrins can regulate the binding of ligands in the extracellular environment according to the information they receive from the intracellular face of the cell, is well documented. Platelet aggregation is an example of a physiological process reliant on integrin affinity modulation. Under normal conditions, platelets exist in a resting state as single cells as platelet αIIbβ3 integrin receptors are in a largely inactive conformation that bind fibrinogen with a very low affinity. Following platelet activation by agonists such as ADP, collagen or thrombin, αIIbβ3 integrins become activated gaining the ability to bind soluble fibrinogen with high affinity, resulting in platelet aggregation [Bennet & Vilaire, 1979; Shattil *et al.*, 1998].

In response to cellular events, inside-out signalling is proposed to involve the propagation of conformational changes from the integrin cytoplasmic domains to the membrane-distal ligand-binding site through the transmembrane domains. Williams *et al.* (1994) proposed four different movements for the orientation of the α / β integrin transmembrane domains to each other depending on the position of the membrane-proximal segments that could mediate spatial rearrangements and subsequently the transmission of conformational changes participating in integrin activation. In the 'piston' model the conserved

membrane-proximal segments are inserted into the plasma membrane, with the more polar KR and hDRRE sequences (in α and β cytoplasmic domains respectively) preventing further insertion of the fragments. In the 'twist' and 'hinge' models the conserved membrane-proximal regions acted as a fulcrum to allow the propagation of conformational changes, while the 'zipper' model predicted direct association / dissociation of the two subunits. In support of the pistoning hypothesis, Armulik *et al.* (1999) developed the model to include the existence of different α and β transmembrane domain arrangement (tilted or coiled) relative to their length across the plasma membrane depending on the affinity state of the integrin receptor. A subsequent glycosylation mapping study by Stefansson *et al.* (2004) supported that activating mutations in the membrane-proximal region resulted in shortening of the membrane-embedded transmembrane segments.

More recently, protein engineering studies of integrin transmembrane domains have been published demonstrating a regulatory role for integrin α / β transmembrane interface in inside-out activation. Li *et al.* (2005) supported the hypothesis that mutations of residues in the αIIb/β3 helical interface can activate integrin ligand binding by disrupting heterodimeric interactions *in vivo*, expanding on previous *in vitro* data reporting a constitutive active αIIbβ3 phenotype by enhancing homomeric transmembrane associations with asparaginine mutations [Li *et al.*, 2003]. Moreover, constraining the integrin α and β transmembrane domains with intersubunit, intramembranous disulphide bonds blocked the effect of αIIb cytoplasmic mutations known to universally activate integrins from the inside of the cell [Luo *et al.*, 2004]. In addition, perturbing transmembrane interactions by leucine scanning mutagenesis of residues located at the αIIbβ3 helical interface defined in the previous study activated ligand binding [Luo *et al.*, 2005]. A different transmembrane packing interface was suggested by Partridge *et al.*, (2005), albeit consistent with the hypothesis that heterodimeric α/β transmembrane interactions stabilise the integrin in a low affinity state. Random and site-specific mutagenesis of the β3 transmembrane domain identified 13 novel mutations that led to integrin activation. Computational modelling suggested that several of the β3 membrane-embedded activating mutations hindered intersubunit interactions either directly or indirectly by altering helical length/tilt angle [Partridge *et al.*, 2005]. Thus, a number of *in vivo* studies suggested that disruption of the heteromeric helical interface between the α/ β transmembrane domain is necessary for integrin activation. At present, the experimental

data to support the separation model or the pistoning model [Armulik *et al.*, 1999] are incomplete, and the mechanisms by which integrins transduce signals through the plasma membrane remain elusive.

Several conserved regions involved in integrin activation have been identified in the short cytoplasmic tails of integrins. Truncations / and or mutations in either of the conserved GFFKR sequences in α [O'Toole *et al.*, 1991; 1994] or NxxY in β subunit [Hughes *et al.*, 1995; O'Toole *et al.*, 1995] have been shown to result into constitutively active integrins, independent of the cytoplasmic signalling pathways. Based on mutational analysis data, Hughes *et al.*, (1996) proposed that a salt bridge is formed between Arg-Asp residues found on the membrane-proximal regions of the α and β cytoplasmic domains respectively, constraining integrin αIIbβ3 into a non-signalling state. More recent evidence from NMR analyses supported the interaction between membrane-proximal regions of the α and β subunit cytoplasmic domains [Vinogradova *et al.*, 2002; Weljie *et al.*, 2002]. Overall, the data suggest that the positioning of the cytoplasmic tails close together restrains the integrin receptor in an inactive signalling state [Lu *et al.* 2001b; Takagi *et al.*, 2001b] whereas enhancing separation promotes activation [Takagi *et al.*, 2002a; Xiong *et al.*, 2003c]. Conformational movements that separate the two cytoplasmic domains may therefore allow the propagation of conformational changes through the transmembrane domain to the distant ligand-binding sites, hence determining the signalling status of the receptor.

The binding of integrin-associated proteins such as talin may represent a way of disrupting integrin α / β subunit association; directly by affecting the membrane-proximal regions or indirectly by inducing conformational changes. Determination of the X-ray structure of the talin F3 domain-β3 tail complex revealed that the talin phosphotyrosine-binding (PTB) domain recognised the integrin NPLY motif [Garcia-Alvarez *et al.*, 2003]. Most integrin β tails contain one or two NPXY/F motifs. The above observations suggest that other PTB domain-containing proteins may also activate integrins. Moreover, the presence of conserved serine, threonine and tyrosine residues suggests that phosphorylation could contribute (promote or inhibit) in the regulation of integrin activation, however the molecular basis of such mechanism remains unclear. A detailed description of inside-out integrin regulation is beyond the aims of this thesis; however excellent reviews have been

published recently by Brakebusch & Fassler (2003), Brunton *et al.*, (2004), Calderwood D.A. (2004).

There is a great deal of information available about the structure of integrins and their ligand-binding capabilities, but much is still to be discovered concerning the biochemical pathways that integrins activate. The limited knowledge gained from such investigations can only emphasise the complexity and diversity of integrin-mediated signalling events. *In vitro* cell culture studies have implicated integrins in modulation of a variety of cellular processes such as adhesion, spreading and migration and revealed that integrin-mediated signalling is involved in cell proliferation and differentiation, cell survival and prevention of apoptosis. Excellent reviews of the current knowledge of integrin-stimulated events and downstream signalling pathways include ffrench-Constant & Colognato, 2004; Gibbins J.M., 2004; Guo & Giancotti, 2004; Steeber *et al.*, 2005; Stupack & Cheresh, 2004; Stupack *et al.*, 2005.

Integrins are dynamic adhesion molecules that exist in different conformations reflecting the ligand-binding capabilities of these receptors. The remarkable ability of integrins to modulate their activity in response to intracellular signals not only adds to the multiplicity of integrin functions but also signifies the complexity of tight regulated integrin activation. The importance of cellular control of integrin activation is underscored in health and disease, which is briefly discussed below.

1.4 Biological function

Integrin gene-disruption studies, at both the whole animal and tissue-specific levels, enabled the study of the physiological relevance of integrin-mediated cell adhesion and signal transduction and provided valuable information of integrin functions in disease. Despite the great differences in development and tissue organisation, loss-of-function effects in intact invertebrate model organisms, *Caenorhabditis elegans* and *Drosophila melanogaster*, revealed that integrins are required in embryonic developmental processes. Inhibiting the function of the sole integrin β subunit in *C. elegans* or βPS, one of two integrin β subunits, in *D. melanogaster* resulted in embryonic lethality [Williams & Waterston, 1994; Brown N.H., 1993]. In nematode worms and fruit flies adhesion of integrins to the extracellular matrix is required for muscle connection to the body wall that

translates to movement of the exoskeleton [Brown N.H., 2000]. The defects in the absence of integrins are envisaged in muscle paralysis or detachment, but also in delayed or failing cell migration and abnormal morphogenesis between epithelia [Bokel & Brown, 2002]. Moreover, the effects of integrin knockout genetic studies in mice (summarised in Table 1.1, adapted from Bouvard *et al.*, 2001) have contributed greatly to our understanding of integrin function. Integrin disruption influences all aspects of tissue development and maintenance including hemostasis (αIIb, β3, α2), vasculogenesis and angiogenesis (α1, β3), and leucocyte trafficking and inflammation (αL, αM, αE, β2, β7, β6). The phenotypes range from severe anatomical and histological defects (α4, α5, αV, β8) to perinatal lethality (α3, α6, α8, αv, β4, β8) or even embryonic lethality (β1). Yet, where normal development takes place, this emphasises the fact that these receptors function within a network of signalling processes and in collaboration with other integrins or other receptor families [Schwartz & Ginsberg, 2002], the compensatory ability of which is likely to reduce the effect of integrin loss [ffrench-Constant & Colognato, 2004]. Overall, the loss-of-function studies in genetic model organisms highlighted that integrins are used for conserved biological processes with fundamental physiological roles.

The functional consequences of integrins mutations in humans are highlighted by the severe symptoms of human genetic integrin defects. Leukocyte adhesion deficiency (LAD) type I syndrome, caused by a defect in the β2 gene resulting in failure to express β2 integrins, is typified by recurrent bacterial infections [Etzioni et al., 1999; Hogg & Bates, 2000]. A second example is the bleeding disorder Glanzmann's thrombasthenia, which arises from mutations in either subunit of the αIIbβ3 platelet integrin [Kato A., 1997; Clemetson & Clemetson, 1998]. Mutations in α6 or β4 genes result in the lethal skin blistering disorder epidermolysis bullosa with pyrolic atresia [Vidal *et al.*, 1995]. Also, a type of congenital myopathy has been associated to defects in the α7 integrin gene [Hayashi *et al.*, 1998].

Gene		Phenotype
α_1	V, F	Increased collagen synthesis, reduced tumor vascularization
α_2	V, F	Defects in hemostasis, abnormalities in branching morphogenesis
α_3	L, birth	Defects in kidneys, lungs, and cerebral cortex; skin blistering
α_4	L, E11–E14	Defects in chorioallantois fusion and cardiac development
α_5	L, E10	Defects in extraembryonic and embryonic vascular development
α_6	L, birth	Defects in cerebral cortex and retina; skin blistering
α_7	V, F	Muscular dystrophy
α_8	L+V/F	Small or absent kidneys; inner ear defects
α_9	L, perinatal	Bilateral chylothorax
α_{10}	V, F	No apparent phenotype
α_{11}	...	...
α_V	L, E12–birth	Defects in placenta and in CNS and GI blood vessels; cleft palate
α_D	...	...
α_L	V, F	Impaired leukocyte recruitment and tumor rejection
α_M	V, F	Impaired phagocytosis and PMN apoptosis; obesity; mast cell development
α_X	...	...
α_E	V, F	Inflammatory skin lesions
α_{IIb}	V, F	Defective platelet aggregation
β_1	L, E5.5	Inner cell mass deterioration
β_2	V, F	Impaired leukocyte recruitment; skin infections
β_3	V, F	Defective platelet aggregation; osteosclerosis
β_4	L, perinatal	Skin blistering
β_5	V, F	No apparent phenotype
β_6	V, F	Skin and lung inflammation and impaired lung fibrosis
β_7	V, F	Abnormal Peyer's patches; decreased No. of intraepithelial lymphocytes
β_8	L, E12–birth	Defects in placenta and in CNS and GI blood vessels; cleft palate

Table 1.1. Ablation of integrin genes in mice and their resulting phenotypes *in vivo*. V indicates viable; F, fertile; L, lethal; L+V/F, mutations that disrupt development but also allow survival in a fraction of mice; CNS, central nervous system; GI, gastrointestinal; and PMN, polymorphonuclear neutrophil. Adapted from Bouvard *et al.*, 2001.

1.5 Integrin structure

In 2001, Xiong *et al.* solved the structure of αVβ3 at the atomic level. This three-dimensional (3-D) structure was soon to be followed by the structure of αVβ3 in the presence of an RGD peptidomimetic ligand [Xiong *et al.*, 2002]. The second integrin heterodimer to be crystallised was αIIbβ3, a closely related integrin to αVβ3. Four αIIbβ3 structures were crystallised with an antibody fragment alone / and with one of three ligand-mimetic antagonists, in the presence of cacodylate ion(s) [Xiao *et al.*, 2004]. Moreover, independently folded A domains in the α subunits that retain the functional characteristics of the parent integrin have facilitated the determination of several other crystals, described here first.

Crystallography is undoubtedly a powerful tool but provides only a snapshot of a single conformation that an integrin can adopt. Crystallographic structural information combined with the data from antibody analyses, NMR and EM studies are more instructive in favour of the dynamic integrin structure and to the understanding of how conformational changes lead to integrin activation and ultimately to signal transmission.

1.5.1 The extracellular domain

1.5.1a The αA domain

The αA domain is approximately 200 amino acids long and shows high sequence homology to the A domain of von Willebrand factor (vWF), cartilage matrix protein, type VI collagen and complement factor B [Colombalti & Bonaldo, 1991]. Because this domain is found 'inserted' in only half of the integrin α subunits, it has also been named 'I-domain'. The successful expression of recombinant isolated αA domains [Randi & Hogg, 1994; Ueda *et al.*, 1994; Calderwood *et al.*, 1997] facilitated structural studies that have solved the crystal structures of A domains from αM [Lee *et al.*, 1995a; 1995b], αL [Qu & Leahy, 1995; 1996; Shimaoka *et al.*, 2003a], α2 [Emsley *et al.*, 1997; 2000] and α1 [Nolte *et al.*, 1999; Karpusas *et al.*, 2003] integrin subunits.

The crystal structure of the αM A domain revealed a classical dinucleotide-binding fold (or αβ Rossmann fold), that is conserved in all integrin A domains (Figure 1.3) and included a

Figure 1.3. Rossmann fold of integrin αA domains. A central hydrophobic six-stranded β-sheet is surrounded by six amphipathic α-helices; in the αM and αL A domains the β-sheet contains five parallel and one anti-parallel β-strand alternating between the six helices. The additional 'helix C' found in the α2 and α1 A domains is shown in orange. α-helices are in red, β-strands are in cyan and loops are in grey. Mg^{2+} ions are shown as green spheres, the magenta sphere represents a Mn^{2+} ion. All A-domains are shown in the same conformation. All ribbon diagrams were prepared with WebLab ViewerLite. Brookhaven data base references for the A domains of α1–1QCS, α2–1AOX, αM–1BHO and αL–1ZOP.

unique divalent cation-binding site designated the 'metal ion dependent adhesion site' or 'MIDAS' at the top of the domain [Lee *et al.*, 1995a]. A 'DxSxS' motif formed by residues found in the loop connecting the β1-strand and α1-helix, is a critical site for ligand binding (described in detail in section 1.5.1). Comparisons among the X-ray diffraction data revealed differences between the αA domains. The most striking of these was an additional turn–and-a-half of an α-helix, between β5-strand and helix-α6, in the α2 A and α1 A domains that has been named 'helix-C' [Emsley *et al.*, 1997].

Resolution of the α2 A domain co-crystal with a ligand established that αA domains can exist in two distinct conformations, the 'closed' and 'open' forms (Figure 1.4). Moreover, it was concluded that the αA domain conformation is independent of the nature of the metal ion but dependent on the presence of an acidic residue, donated either by a ligand or a ligand-mimetic lattice contact bound at the MIDAS. In all αA domain crystal structures, the MIDAS cation is coordinated by a total of six bonds in an octahedral arrangement. However, the open and closed conformation differ in the residues completing the coordination sphere as well as in the structure of the surrounding loops and the position of the C-terminal α7-helix of the αA domain [Shimaoka *et al.*, 2002b], discussed in greater detail in a later section. In addition, numerous studies have shown that the closed and open forms are functionally relevant and correspond to the low affinity (inactive) and high affinity (active) states of the corresponding integrins [Li *et al.*, 1998; Oxvig *et al.*, 1999; Emsley *et al.*, 2000; Shimaoka *et al.*, 2003a].

a)

b)

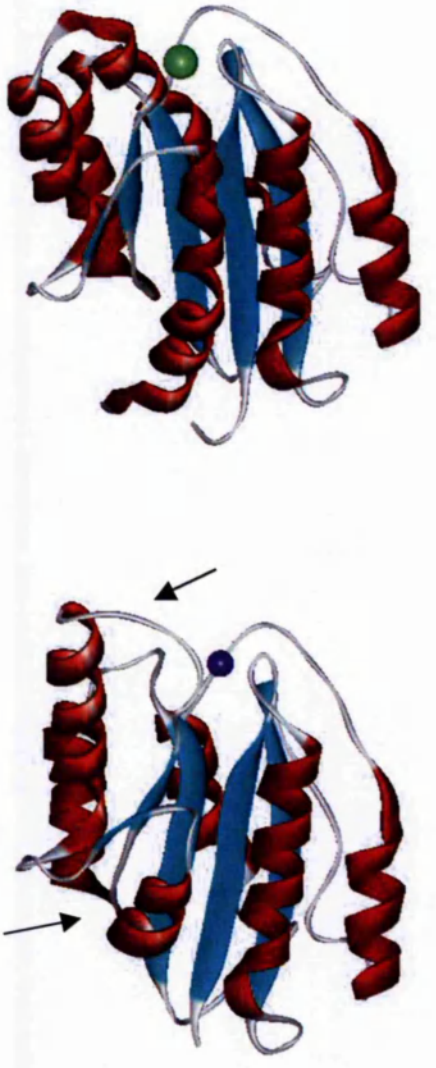

Figure 1.4. The two conformations of the α2 A domain crystal structures. Ribbon diagram of the α2 A domain in the a) closed and b) open conformation. The closed conformation was crystallised with a Mg^{2+} ion (green sphere) at MIDAS. The open conformation was captured with a Mn^{2+} ion (magenta sphere) at MIDAS. α-helices are in red, β-strands are in cyan, and loops are in grey. Arrows point at α-helices that undergo major conformational rearrangements from the transition of the closed to the open form. Note that in b) there is a large downward shift of the α7-helix (a truncated form of the protein was used for crystallisation, and therefore helix-α7 appears shorter). WebLabViewer Lite was used to design the two structures.

1.5.1b The extracellular domain of the αV subunit

The first crystal structure of a complete integrin extracellular domain was the integrin αVβ3 that lacks an αA domain, and was solved at 3.1Å resolution by Xiong *et al.* (2001) (Figure 1.5). Seven N-terminal homologous repeats in the primary sequence are seen in the crystal structure of αV to be arranged radially into a 'seven-bladed β-propeller' (Figure 1.6a). Each blade is formed by a four-stranded (A-D) anti-parallel sheet, with strand D found in the outer edge of each blade and strand A positioned at the core channel of the propeller. The loops of the β-propeller domains are solvent exposed, whereas highly conserved secondary structural elements are located in the core of the propeller. For example, a conserved 'cage' motif is outlined by 'cup'-like structures formed by a mostly aromatic tetrapeptide preceding strand A, and from residues in strands B and C. Sequential cups build up the cage motif and hold in place a positively charged β-subunit residue, Arg261, which is the main contact with the β3 subunit [Xiong *et al.*, 2001]. In the lower face of the β-propeller, the β-hairpin loops connecting strands A-B in blades 4-7 make up four cation-binding sites. These EF-hand-like motifs previously predicted from the primary αV structure to bind Ca^{2+}, coordinate cations regardless of bound ligand [Xiong *et al.*, 2002].

The C-terminus of the β-propeller is linked to a β-sandwich immunoglobulin (Ig)-like domain, designated the 'thigh' domain [Xiong *et al.*, 2001]. Two more, very similar β-sandwich domains, the 'calf-1'and 'calf-2' domains, complete the remainder of the αV extracellular segment. At the junction between the thigh and calf-1 domain, which has been termed the 'genu', there is the fifth cation-binding site formed in the αV subunit. Based on a calculated 700$Å^2$ interface between the thigh domain and the lower face of the β-propeller Xiong *et al.*, (2001) proposed that an interdomain movement can take place, and is possibly regulated by the Ca^{2+} ions present in the β-propeller. In addition, the transformation of the compact integrin conformer [Xiong *et al.*, 2001; 2000] to the extended form [Xiao *et al.*, 2004] that occurred at the genu revealed that the interface between the thigh and calf-1 is very flexible (discussed in more detail in section 1.5.3).

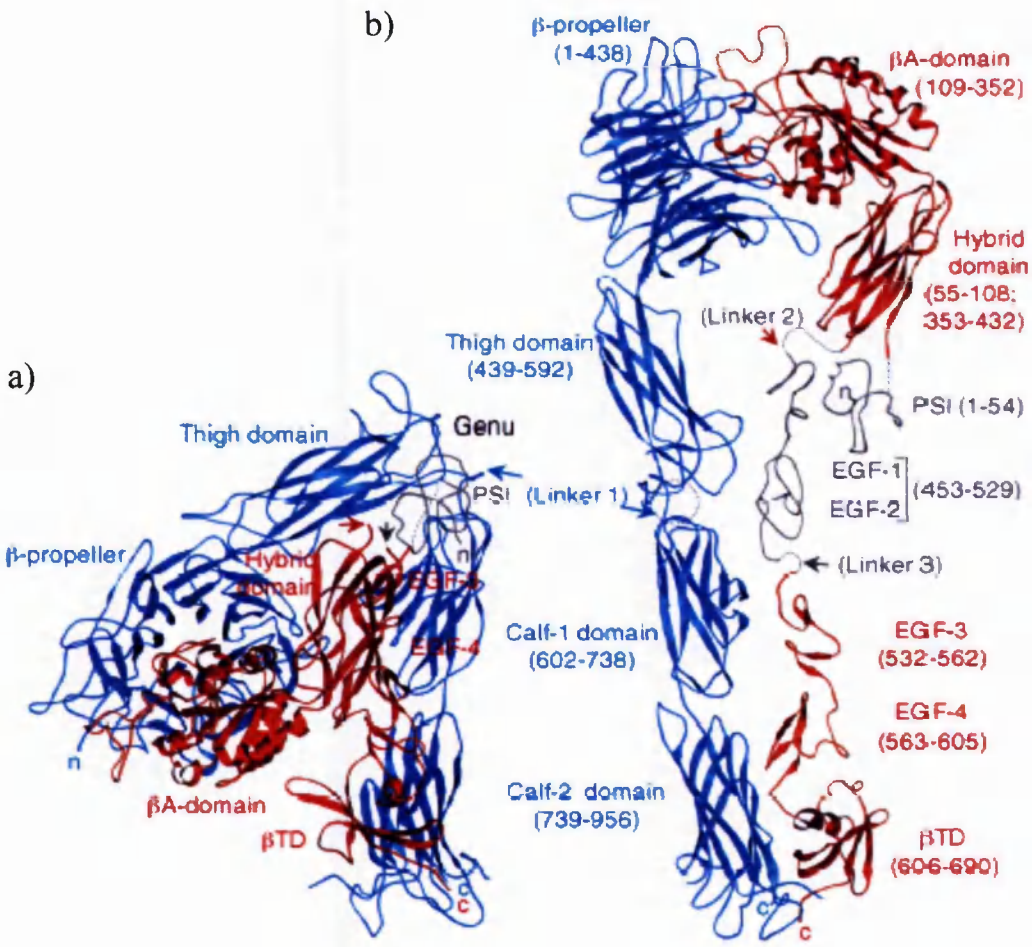

Figure 1.5. The crystal structure of the extracellular segment of αVβ3. a) Ribbon diagram of the crystallised αVβ3 in the bent conformation. The αV subunit is shown in blue and the β3 subunit is in red. b) Model of the straightened extracellular segment of αVβ3. The PSI-domain and EGF-1 and EGF-2 domains in the β subunit, in grey, have not been included in the crystal structure. From Xiong *et al.*, 2001.

a)

b)

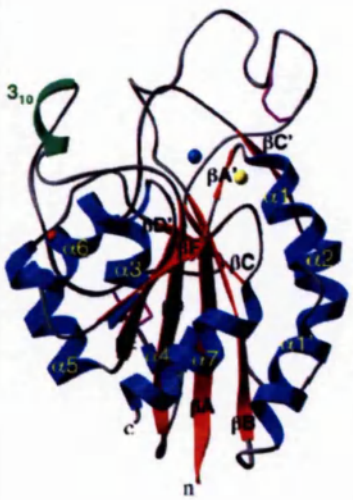

Figure 1.6. Secondary structure elements of αVβ3. a) Structure of the αV subunit β-propeller. The figure depicts the bottom view of the seven-bladed (numbered 1-7) β-propeller, as determined from the crystal structure. Each blade, indicated by a different colour, is formed from a four-stranded anti parallel sheet, labelled A-D. Disulphides (sticks) and glycans (spheres) are in red. Ca^{2+} ions are in green spheres, were detected in each of the blades 4-7. b) Structure of the βA domain. α-helices and β-sheets are labelled and are shown in blue and red respectively. A Ca^{2+} ion locates to the ADMIDAS motif, shown as a yellow sphere. The predicted location of the MIDAS divalent cation is shown in purple. Highlighted in green is the 3_{10}-helix from the $\beta 3$ subunit that is positioned in the centre core of the β-propeller/ βA domain interface. Of note, the βB-βC loop protruding from the top of β3 A domain is the 'specificity' loop. Both pictures were as taken from Xiong *et al.*, 2001.

1.5.1c The extracellular domain of the β3 subunit

The quaternary structure of the N-terminal β3 subunit was not visible in the original crystal structure of αVβ3 due to flexibility of this cysteine-rich domain. This domain was named 'PSI' domain due to sequence homology with domains in plexins, sematophorins and integrins [Bork *et al.*, 1999]. In the most recently published crystal structure of αIIbβ3 [Xiao *et al.*, 2004], the electron density of the PSI domain (β3 residues 1-54 and residues 433-435) allowed for four disulphide bonds to be traced, with the fourth disulphide link formed between Cys13 and Cys435. The latter disulphide link stabilised the backward fold of the PSI domain, which has been proposed for the β3 [Calvete *et al.*, 1991] and β2 integrin subunits [Tan *et al.*, 2001] but remained undefined until now.

The β3 subunit showed more unexpected quaternary arrangements. The β3 crystals exposed a β-sandwich module named the 'hybrid' domain that is folded from amino acid sequence segments on either side of a A-like domain [Xiong *et al.*, 2001, 2002], while itself is inserted in the PSI domain [Xiao *et al.*, 2004]. The 240 amino acid long 'βA' domain is projected from one of the loops at the upper face of the hybrid domain at the opposite end to the location of the PSI domain. The βA domain is highly conserved among all integrin β subunits and adopts a Rossmann fold that resembles the αA domain fold (Figure 1.6b). A central six-stranded β-sheet is surrounded by eight helices with the MIDAS metal ion-binding sequence motif (DxSxS) at the top of the central β-strand, although the MIDAS motif did not have a cation engaged. The metal-ion binding site termed 'ADMIDAS' (adjacent to the MIDAS) coordinated a Ca^{2+} ion [Xiong *et al.*, 2001], a Mn^{2+} ion [Xiong *et al.*, 2002] or a Mg^{2+} ion [Xiao *et al.*, 2004] (depending which cation was present in the crystallisation buffer), regardless the presence of bound ligand. However, the MIDAS site was occupied only in the liganded αVβ3 structure [Xiong *et al.*, 2002]. In addition, another cation-binding site only 6Å from the MIDAS, termed the 'LIMBS' (ligand-induced metal-binding site) formed also exclusively when ligand was bound to the integrin [Xiong *et al.*, 2002].

The "leg" of the β3 extracellular domain comprised four 'epidermal growth factor (EGF)-like repeats' and a 'β-tail domain'. The structures of the main body of EGF-1 and EGF-2 are predicted based on sequence homology to EGF-3 and EGF-4 domains that were the two EGF domains with complete electron density maps. Each EGF domain contained a

cysteine-rich repeat that formed both intra domain disulphide bonds within each EGF domain and an intermolecular disulphide bridge between succeeding domains. These regions of the β subunit are functionally important as evidenced by the large number of activation-associated epitopes and mutations that map to these regions [Humphries M.J., 2000; Lu *et al.*, 2001a]. The final domain to be revealed in the crystallographic frame of αVβ3 is the β-tail motif of the β3 extracellular domain, which consists of a four-stranded β-sheet and an N-terminal α-helix, with a very weak but detectable homology to cystatin C [Xiong *et al.*, 2001].

1.5.2 Transmembrane and cytoplasmic domains

The transmembrane domains of α and β integrin subunits cross the plasma membrane by a single α-helix of 20-25 amino acids, connecting the extracellular domains to the cytoplasmic domains. Several studies including mutagenesis of specific residues, deletions and truncations as well as epitope mapping, have highlighted the importance of characteristic membrane-proximal motifs in integrin heterodimer configuration and activation [Hughes *et al.*, 1996; Ginsberg *et al.*, 2001; Lu *et al.*, 2001b; Takagi *et al.*, 2001b]. Direct interaction between the two tails has also been proposed based on surface plasmon resonance and circular dichroism studies [Haas & Plow, 1996; Vallar *et al.*, 1999]. A study by Weljie *et al.* (2002) reported detailed NMR data of synthetic peptides corresponding to αIIb and β3 cytoplasmic regions. Remarkably, in this study two different conformations were detected for β3 tail residues 719-725, one of which showed remarkable bend in the principal α-helical structure. A different NMR study on the αIIb and β3 cytoplasmic tails reported changes in the spectra only when the two helical tails were mixed together [Vinogradova *et al.*, 2002], indicative of interactions taking place. Hydrophobic and electrostatic interactions between the cytoplasmic tails were predominantly detected in the N-terminal membrane-proximal regions of both tails.

1.5.3 Overall morphology of the integrin heterodimer

In summary, the αVβ3 integrin crystals characterised in detail 8 of the 12 extracellular domains in integrins that lack an αA domain. The remaining missing domains were characterised by NMR on the structure of the β2 subunit. New information received from the αIIbβ3 crystal complemented the domain structure of the extracellular segment. However, some regions of the EGF domains are still awaiting crystallisation. The

globular integrin head in N-terminal α subunit is folded into what has been correctly predicted, a seven-bladed β-propeller; whereas in the β subunit, the ligand-binding βA domain showed remarkable similarities to the structurally independent αA domain fold. Each integrin 'tailpiece' is composed of β-sandwich domains that give both subunits the rod-like appearance, as visualised in electron micrographs.

The X-ray crystal structures of αVβ3 and αIIbβ3 enriched the knowledge of the heterodimeric integrin configuration and revealed an intimate association between the α subunit β-propeller and the βA domain. The βA domain is positioned against the upper face of the β-propeller and the β-propeller / βA domain interface, which is principally hydrophobic, is the main contact site between the αV / αIIb and β3 subunits. An arginine (Arg261) in the helical region on the top of the βA domain 3_{10} helix is inserted into the core of the α subunit β-propeller. Several other contacts are formed between the two subunits in a buried surface area of approximately 1600Å^2 , in both αVβ3 and αIIbβ3 crystals.

The crystal structure of αVβ3 revealed a surprising quaternary structure; the αVβ3 crystal featured a high degree of flexibility at the genu between the integrin headpiece and tailpiece [Xiong *et al.*, 2001]. In this 'bent' conformation the N-terminal extracellular integrin regions are folded over the tailpiece (Figure 1.1b, 1.5a). More specifically, the bent occurred between the thigh and calf-1 in the α-genu and between the EGF-1 and EGF-2 in the β-genu. The liganded-αVβ3 crystal that was solved next also showed a V-shaped, bent integrin [Xiong *et al.*, 2002]. The authors proposed that the bent conformation represents the active integrin. However, for the generation of the liganded αVβ3 crystallographic data, the ligand–mimetic peptide was soaked into the crystal containing the bent integrin, and therefore due to crystal lattice packing constraints changes would be limited in the ligand-binding pocket. In addition, both αVβ3 crystals were obtained in Ca^{2+}, a cation that stabilises integrins in the inactive or low affinity conformation. On the other hand, an extended integrin was observed in the αIIbβ3 crystal [Xiao *et al.*, 2004] that was crystallised with a ligand-mimetic antagonist that had induced in advance the ligand-bound, high affinity conformation. The αIIbβ3 integrin also lacked the integrin tailpiece and thus, the possible restraints of these regions that keep the legs

together and the integrin inactive. The fine structural changes (at atomic resolution) of the bent relative to the extended extracellular β3 domain are described in a later section.

In support of the extended morphology of ligand-bound integrins are the data from studies combining EM observations of soluble β3 and β1 integrins. High-resolution EM images revealed integrins that can adopt both the bent and the extended form in solution [Takagi *et al.*, 2002a; 2003]. Although the high-resolution EM observations confirmed the presence of both conformers, the above studies were done with recombinant integrins suggesting the transition from one conformer to another might take place under physiological conditions. The body of evidence to support the gross conformational changes as they relate to integrin affinity regulation are described in section 1.8. The crystal structures of the soluble truncated integrins also suggested a potential location for the αA domain. In αA domain containing integrins, the A domain is inserted between blades 2 and 3 of the β-propeller. The αA domain is therefore accommodated on the top of the β-propeller and adjacent to the βA domain [Alonso *et al.*, 2002]. The crystallisation of the extracellular segments of an αA domain-containing integrin will be needed to confirm this prediction.

1.6 Integrin-ligand interactions

Integrins bind to a large repertoire of cell surface and extracellular matrix ligands (Table 1.2). Using experimental approaches based on inhibition of adhesion to defined receptors with specific monoclonal antibodies (mAbs) or affinity chromatographic isolation, a number of ligands have now been identified for most integrin receptors. Most integrins bind proteins on the extracellular face of the cell membrane (i.e. fibronectin, collagen), with specific integrins being able to bind soluble ligands (i.e. fibrinogen) or receptors on adjacent cells (i.e. ICAM). In general, β1 and β3 integrins are involved in cell-matrix adhesion and are expressed in most cell types. For example, collagen is the main ligand for α10β1, α11β1 in muscle and for α2β1 receptors in platelets and fibroblasts, whereas collagen and laminin will bind to α2β1 and α1β1 in endothelial and epithelial cells [Elices & Hemler, 1989]. Likewise broadly distributed β3 integrins (αIIb, αV), interact with 'vascular' ligands such as fibrinogen, von Willebrand factor, thrombospondin and vitronectin [Byzova *et al.*, 1998]. In contrast, β2 integrins, that are restricted to cells of the

Integrin		Ligand			
		ECM	**Soluble**	**Cell-cell**	**Pathogens/toxins**
α1	β1	Co; Ln			Echovirus 1,8; Rotavirus
α2	β1	Co; Ln; Chad	MMP-1	E-cadherin	*Yersinia* spp. (invasin); Echovirus 1; snake venoms
α3	β1	Ln; Rn; Tsp-1;Co; Fn		(α2β1; α3β1)	*Yersinia* spp. (invasin); rotavirus
α4	β1	Fn; Op	pp-vWF; tTG; FXIII; angiostatin	VCAM-1; (α4)	
	β7	Fn		VCAM-1; MAdCAM; (α4)	
α5	β1	Fn	TTG; endostatin	ADAM-15, 17;	*Yersinia* spp. (invasin); *B. burgdorferi*; *Shigella* spp.; *B. pertussis*; foot-and-mouth disease virus
α6	β1	Ln	Fisp12/mCTGF; Cyr61	ADAM-2, 9	Papilloma virus; *Yersinia* spp. (invasin)
	β4	Ln			
α7	β1	Ln			
α8	β1	Fn; Tn; Nn	TGFβ1-LAP		
α9	β1	Tn; Op; Co; Ln	pp-vWF; tTG; FXIII; angiostatin	VCAM-1, ADAM-12, 15	
αD	β2			ICAM-3; VCAM-1	
αE	β7			E-cadherin	
αIIb	β3	Vn; Fn; vWF	Cyr61;Fisp12/mCTGF; Fg; prothrombin		*B. burgdorferi*; snake venoms (disintegrins); ticks (variabilin, disagregin); leech (decorsin, ornatin)
αL	β2			ICAM-1-5	
αM	β2		Fg; iC3b; Factor X	ICAM-1; VCAM-1	*B. burgdorferi*; *B. pertussis*; *C. albicans*
αV	β1	Fn; Vn	TGFβ1-LAP		Parechovirus 1
	β3	Vn; Fn; vWF; Op; Tn; Bsp; Tsp-1	Fg; MMP2; endostatin; angiostatin; tumstatin	ADAM-15, 23; CD31	Snake venoms; adenovirus; rotavirus; foot-and-mouth disease virus; coxsackievirus A9; parenchovirus 1; hantaviruses; HIV (tat protein)
	β5	Vn; Bsp	TGFβ1-LAP; Cyr61; endostatin		HIV (tat protein)
	β6	Fn; Tn	TGFβ1-LAP		Foot-and-mouth disease virus
	β8	Co; Ln; Fn	TGFβ1-LAP		
αX	β2		Fg; iC3b		Rotavirus

Table 1.2. Integrins and their ligands. Abbreviations: ADAM-A disintegrin and metalloprotease; Bsp- bone sialoprotein; Chad-chondroadherin; Co-collagen; Fg-fibronogen; FX-factor X; iC3b-inactivated complement component; Lm-laminin; MAdCAM-mucosal addressin cell adhesion molecule; Nn-nephronecti; Op-osteopontin; Rn-reelin; Tn-tenascin; Tsp-thrombospondin; Vn-vitronectin. Adapted from Van der Flier & Sonnenberg, 2001.

leukocyte lineage, recognise one or more members of the ICAM family, mediating homotypic leukocyte and leukocyte-endothelial cell adhesion [Harris *et al.*, 2000].

Two important features of the ligand binding specificities of integrins are apparent. Firstly, certain integrins are able to bind to several ligands with diverse structural morphology. Secondly, the same ligand may interact with more than one integrin receptor. For example, fibronectin has been reported to bind to as many as eight different integrin receptors [Geiger *et al.*, 2001]. This biological redundancy suggests that different receptors mediate different functions or different aspects of the same functions. Although it is well established that the ligand binding properties of an integrin receptor depend on its particular α-β subunit combination, the determinants of the integrin-specific adhesive activity of a particular heterodimer are not fully understood and may be dependent on the contributions of associated receptors including syndecans, tetraspanins and growth factor receptors.

An adverse consequence of integrin function is represented by the cellular uptake of infectious agents, including viral, bacterial and protozoan pathogens [Kerr J.R., 1999]. These include enteropathogenic *Eschericia coli* and *Bordetella pertussis* species, *Candida albicans*, mycoplasmas and several types of adenovirus, coxsackie virus A9, foot and mouth disease virus, hantaviruses and HIV virus [Kerr J.R., 1999]. Microorganisms that bind to integrins have evolved specific protein sequences to resemble the binding motifs present in integrin ligands and hence facilitate the interactions with the integrin receptors that are required for entry into the cell and completion of the pathogen's life cycle.

1.6.1 Active sites in integrin ligands

The commonality of integrin-ligand interactions can be partly explained by the presence of shared structural features within the ligands. Initially, proteolytic and chemical cleavage of integrin ligands were used to identify major cell adhesive domains. Further reductionist approaches were employed to pinpoint distinct integrin recognition motifs within these domains. In this way, the prototype adhesion motif RGD was originally found in the central cell-binding domain of fibronectin [Pierschbacher & Ruoslahti, 1984]. Since then it has been demonstrated that this tripeptide is responsible for the adhesive activity of a large number of adhesive extracellular molecules [Humphries M.J., 1990] and snake venom disintegrins [Calvete J.J., 1999]. A second major recognition motif identified in

multiple ligands of several integrins is the short LDV peptide [Komoriya *et al.*, 1991; Plow *et al.*, 2000; van de Flier & Sonnenberg, 2001]. This is present in the alternatively spliced CS-1 region of fibronectin, but is more commonly found in immunoglobulin ligands for integrins as a variable L/I-D/E-S/T/V sequence.

Subsequent studies demonstrated that multiple adhesion sites exist within any one ligand and specific sets of adhesion sequences are recognised by any given integrin for optimised ligand-integrin interactions. For example fibronectin binding to α5β1 integrin depends on the prototype adhesion motif RGD (in the 10^{th} type III repeat) and is synergistically enhanced by an additional PHSRN sequence (in the 9^{th} type III repeat) [Aota *et al.*, 1994]. Such findings highlighted the importance of synergy sites in integrin-ligand binding and explained to some extent how integrin receptors discriminate for ligand binding. Data from small angle X-ray scattering combined with mutagenesis data supported the direct interaction of the synergy site to the α5 β-propeller [Mould *et al.*, 2003c]. However, direct observations of α5β1 with fibronectin repeats 7-9 by EM, failed to demonstrate the integrin head contacting the synergy site on fibronectin [Takagi *et al.*, 2003]. The authors proposed that the synergy site increased the ligand-binding affinity in an indirect manner: either by positioning the RGD sequence in a more favourable orientation for integrin engagement, or by electrostatically steering the ligand onto the integrin via transient interactions.

In the first crystal structure of a liganded extracellular integrin, the cyclic pentapeptide containing the prototypical Arg-Gly-Asp (RGD) ligand was soaked into αVβ3 crystals in the presence of Mn^{2+} ions [Xiong *et al.*, 2002]. The cyclic peptide is inserted into the crevice formed between the αV β-propeller and the β3 A domain (Figure 1.7a). The ligand Arg exclusively contacts the αV subunit, with the side chains of Arg stabilised by salt bridges from residues D218 and D150 at the top of the β-propeller. The ligand Gly is positioned deeper in the groove and makes several hydrophobic interactions with the β-propeller of αV. Yet, it is the ligand Asp that is completely buried in the βA domain interface. The Asp carboxyl group of the RGD peptide forms a direct bond to the Mn^{2+} metal ion in the MIDAS of the β3 A domain. No bonds are formed between the remaining two residues of the pentapeptide and the integrin molecule.

a)

b)

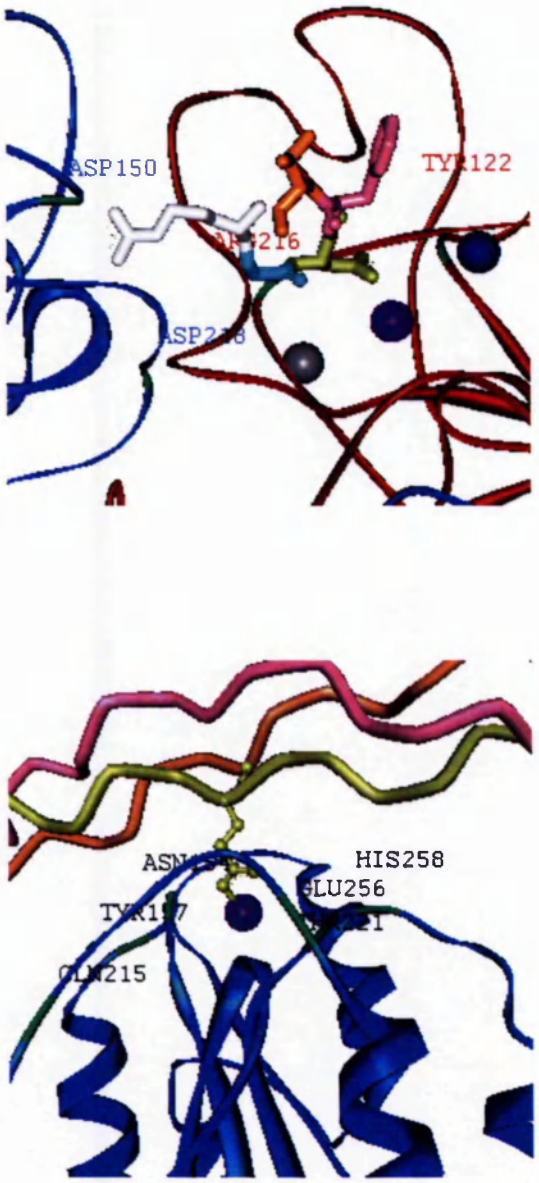

Figure 1.7. Ligand-integrin interactions. a) Diagram of the αVβ3 in complex with the RGD peptide. The αV β-propeller is in blue and the β3 A domain in red. The ligand Arg residue is shown in yellow. The three Mn^{2+} ions in β3 are shown as grey, purple and blue spheres. b) Diagram of the α2 A domain bound to the collagen GFOGER peptide. The collagen triple helix is a homotrimer of the 'leading' (orange), 'middle' (yellow) and 'trailing' (pink) strand. The collagen Glu residue that coordinates the Mn^{2+} ion in MIDAS (purple sphere) is shown in yellow. The α2 A domain ribbon is in blue. Labelled amino acids interact with ligand residues and are coloured in green.

The crystallographic data allowed the dissection of the RGD peptidomimetic ligand – integrin atomic interactions; the structural basis of the RGD consensus was defined, elucidating why conserved substitutions of Arg to Lys, Gly to Ala or Asp to Glu are not tolerated [Metha *et al.*, 1998; Dechantsreiter *et al.*, 1999].

A different ligand structure is a prerequisite for high affinity collagen binding integrins. Knight *et al.*, (2000) identified the collagen type-I sequence GFOGER (Gly-Phe-hydroxyPro-Gly-Glu-Arg) as the major collagen-binding site for α1 A and α2 A domains as well as for the intact integrins. In this study, the synthetic hexapeptide that adopts a triple-helical helix was also utilised for mutational analyses; swapping the Glu for Asp completely abolished recognition by α1 A and α2 A domains, revealing an absolute requirement for the collagen glutamate within the recognition motif [Knight *et al.*, 2000]. Co-crystallisation of α2 A domain with the collagen triple-helical peptide containing the GFOGER motif revealed that the glutamate carboxyl group from the middle strand is the only charged group in contact with the Mg^{2+} ion of the αA domain [Emsley *et al.*, 2000] (Figure 1.7b). Several other contacts are established between the collagen middle and trailing strands with residues in the upper loops of the α2 A domain.

More recently, the structure of an integrin αA domain was determined in complex with a member of the Ig superfamily [Shimaoka *et al.*, 2003a]. In this crystal, residue Glu-34 that is found within an extended flexible loop in ICAM-1 is directly coordinating a Mg^{2+} ion in the MIDAS of the αL A domain. The above findings explain how ligands that are structurally diverse i.e. in a linear or in the triple-helical configuration, can bind integrins. The essential feature of integrin-binding motifs is an acidic residue from the ligand that donates a negatively charged oxygen to the coordination of the metal ion in the MIDAS. Thus, the ligand carboxylate, usually an aspartate or glutamate, within the defined recognition sequences is critical for the direct coordination of the metal ion in the MIDAS site of the integrin ligand-binding pocket. Co-crystallisation of additional ligand-occupied integrins will help to examine different ligand-binding interfaces so as to define in fine detail the binding pocket. More significantly, co-crystallisation with physiological, macromolecular ligands will reveal any additional contact sites to elucidate how specificity to different ligands takes place.

1.7 Ligand-binding sites in integrin extracellular domains

Advances in X-ray crystallography have solved the crystal structures of the complete extracellular portion of integrins as well as isolated αA domains, and characterised their ligand-binding contacts at the βA domain / α subunit β–propeller interface or at the αA domain. However, at present the 3-D structure of an αA domain-containing integrin heterodimer and / or the co-crystal of integrin(s) with macromolecular physiological ligands are awaited. Therefore, further particulars of integrin structure and molecular determinants of ligand binding remain to be discovered. Chemical cross-linking of ligand peptides, synthesis of recombinant integrin fragments and peptides, anti-functional mAb epitope mapping, domain-swapping and mutational analyses are some of the additional approaches in use to identify and characterise ligand-binding sites within the integrin αβ heterodimers. Results from such studies have implicated the N-terminal regions of both subunits in forming the integrin-ligand pocket. Key sites include the αA domain, the βA domain and other integrin α subunit sites.

1.7.1 The αA domain MIDAS

In 2000, the resolution of the tertiary structure of a liganded αA domain defined the MIDAS-ligand interface at the atomic level to complement and congregate information from numerous studies investigating the ligand-binding properties of integrin αA domains. The α2 A domain-collagen co-crystallisation identified the loop residues that coordinated the MIDAS directly (Figure 1.8a) but also residues that affected it allosterically [Emsley *et al.*, 2000]. In the co-crystal structure a Mg^{2+} ion is coordinated by residues located in loop 1 (βA-α1), loop 2 (α3-α4) and loop 3 (βD-α5) on the top of the α2 A domain. The highly conserved D151xSxS MIDAS motif in loop 1 coordinated the metal ion indirectly via a water-mediated bond by D151 and directly via two hydrogen bonds by the critical residues S153 and S155. The hydroxy oxygen of residue T221 in loop 2 formed the third direct bond to the metal ion. Two water molecules completed the coordination sphere around the metal ion; D254 and E256 in loop 3 formed the water-mediated bonds. The collagen glutamate coordinated the metal ion directly and the octahedral coordination sphere is completed by two water molecules.

a)

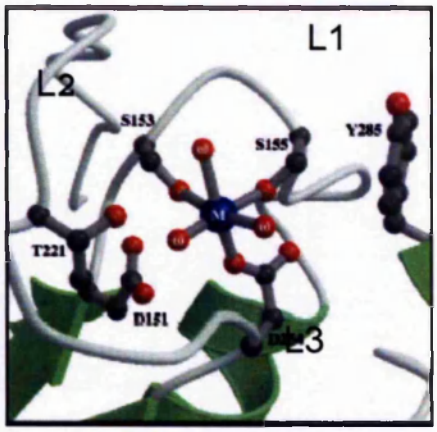

b)

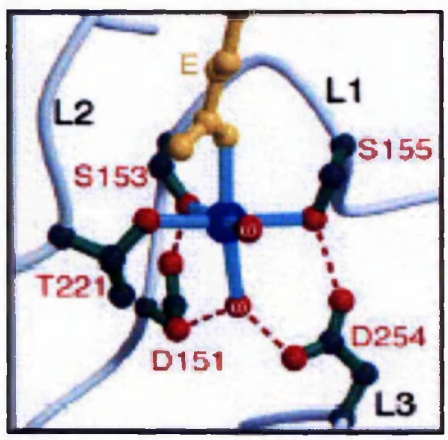

Figure 1.8. Coordination of the MIDAS cation of the α2 A domain crystal structures. In a) the closed and b) open conformation of the α2 A domain. The MIDAS ion is shown in blue. Residues interacting with the divalent cation are shown in ball-and-stick representation. The collagen E coordinating the MIDAS ion in the open form is in yellow. Water molecules are labelled 'ω'. In the closed α2 A domain conformation the metal is directly coordinated by residues S153 and S155 (Loop 1) and D254 (Loop 3), and by three water molecules. In the open α2 A domain conformation, a glutamate donated by the collagen, plays the critical role of stabilising the structure by a direct bond to the metal ion. In this structure, T221 coordinates the metal ion directly, whereas D254 is displaced into the secondary coordination sphere and coordinates via a water-molecule. Two water molecules complete the primary coordination sphere. Pictures a) and b) were taken from Emsley *et al.*, 1997; 2000 respectively.

In the closed α2 A domain conformation, a metal ion is directly coordinated by residues S153, S155 and D254, and by three water molecules (Figure 1.8b) [Emsley *et al.*, 1999]. The transition from the closed to the open structure is accompanied by a 2.3Å sideways movement of the metal ion towards loop 2, that allowed T221 to replace a water molecule and coordinate the metal ion directly. In order for the H-bonds of the conserved S153 and S155 to be maintained, helix-α1 and loop 1 moved in concert with the metal ion towards loop 2. Changes in loop 3 are driven from D254 that is switched from the primary to the secondary coordination sphere and E256, which formed a new water-mediated bond to the metal ion. The loss of the ionic interaction within the MIDAS is replaced from the ligand glutamic acid, which provided the sixth metal coordination to the MIDAS. Structural changes propagated to the C-terminal part of the molecule resulted in a radical rearrangement of the C-helix and α6-helix; the C-helix lost a turn-of-a-helix and this is added to the proceeding N-terminal of α6. The 'slinking' motion of the C-helix has been proposed to 'open up' the collagen-binding site. More strikingly, the closed and open conformations differed in the position of the C-terminal α7-helix. In the closed, unliganded αA domain conformation, loop 1 is packed against α7-helix. In the open conformation, the shift of α1-helix and loop 1 pushed the C-terminal α7-helix down the body of the αA domain, resulting in the displacement of the hydrophobic contacts of α7 to the central β-sheet. This downward 10Å movement of α7-helix was almost identical as in the open αM A domain crystal, which was also coupled to major reconstructions of the preceding loop [Lee *et al.*, 1995b].

Thus, comparison of the ligand-bound α2 A domain crystal structure to the unoccupied α2 A domain structure revealed changes in the residues that coordinated the metal ion in MIDAS as well as rearrangements in the organisation of the α-helices, and in particular in the position of the C-terminal α7-helix. In contrast, the central β-sheet did not change its conformation.

1.7.1a The Lovastatin-binding site

More recently a second ligand-binding site within the αL A domain and distinct from the MIDAS site was identified. The discovery of lovastatin by high throughput screening for small molecule antagonists of LFA-1 (αLβ2) triggered a series of detailed investigations into the inhibitory mechanisms of αLβ2 – ICAM-1 binding by the statin family of

compounds. Kallen *et al.* (1999) studied the interaction of isolated LFA-1 A domain with lovastatin by NMR. The spectra of αL A domain with lovastatin did not detect chemical shift displacements of residues in the MIDAS site. However, a site in and around the C-terminal α7-helix was affected upon lovastatin binding to αL A domain. The X-ray crystallographic data of lovastatin bound to the αL A domain resolved at 2.6Å supported the above results (Figure 1.9). The lovastatin-binding site was shown to be distal to the MIDAS site, in the hydrophobic crevice formed between α7 and α1-helices and the central β-sheet. Binding of lovastatin established several contact sites with the C-terminal pole of the αL A domain and large changes of up to 1.4Å were identified for α7-helix residues 302 and 304.

The site termed 'L-site' for lovastatin-binding site [Kallen *et al.*, 1999; Weitz-Schmidt *et al.*, 2001] has also been named 'I-domain allosteric site' or 'IDAS' by others [Huth *et al.*, 2000]. Quantitative analysis, in both ELISA-type αL A domain – ICAM-1 binding assays and cell adhesion assays, measured the affinity of the L-site for lovastatin and lovastatin-like compounds in the lower micromolar range [Weitz-Schmidt *et al.*, 2001]. Since then, compounds of diverse chemical classes including hydantoins [Last-Barney *et al.*, 2001] and cinnamide derivatives [Liu *et al.*, 2001] have also been identified to interact with LFA-1 in the L-site. These compounds are believed to inhibit adhesion of LFA-1 to ICAM-1 by lowering the affinity of LFA-1 for ICAM-1 through an increase in the K_D of the receptor or through stabilising the low affinity state of LFA-1 [Liu G., 2001].

The presence of a ligand-binding site, which is located at the lower face of the αA domain, thus opposite site from the MIDAS, suggested that there are different ligand-binding pockets on specific integrin domains rather than an extended ligand-binding interface. Moreover, the presence of such regulatory sites suggested that it is possible to identify small molecules which bind with high affinity to the integrin to inhibit activation and subsequently hinder cell adhesion. Thus, allosterically blocking integrin activation in selected adhesion pathways presented new targets for the development of integrin antagonists with therapeutic applications.

a)

b)

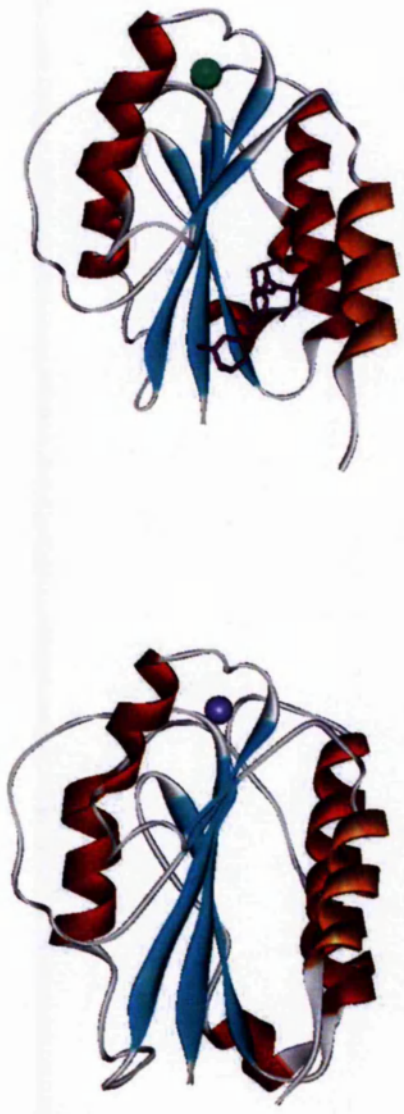

Figure 1.9. The Lovastatin binding site. Structures of a) αL A domain–lovastatin complex and of b) αL A domain in the closed conformation. The Mg^{2+} and Mn^{2+} ions in the MIDAS motif are shown as green and magenta spheres respectively. Lovastatin (in purple) binds in a crevice formed between αL A domain β4, β5-sheets and the α7-helix, which is highlighted in orange.

1.7.2 The βA domain MIDAS

Until recently the domain structure of integrin β subunits was less well defined than the α subunits. The resolution of αVβ3 crystal established the presence of a domain resembling an αA domain in the β subunit that is the major site for ligand binding. Chemical cross-linking of RGD-containing peptides to integrin extracellular domains has identified broad segments of the extracellular β subunit that are important in ligand binding including residues 61-203 of αVβ3 and 107-171 of αIIbβ3 that fall within the βA domain [D'Souza *et al.*, 1988; Smith & Cheresh, 1988].

The first 3-D structure of a liganded integrin [Xiong *et al.*, 2002] confirmed models based on structure predictions and detailed biochemical analyses relating to β integrin structure [reviewed by Humphries M.J. 2000; 2002]. In the crystal structure of αVβ3-RGD, a Mn^{2+} metal ion in the MIDAS is coordinated by the acidic Asp from the ligand peptide (Figure 1.10a, b). The MIDAS is formed from the hydroxyl oxygens of the DxSxS motif (in β3 D119, S121, S123), the carboxyl oxygens from E220 and D251, and the carboxylate group from the ligand Asp. The LIMBS site is formed by the side chains of D158, N213 and D217 and the carbonyl oxygens of D217 and P219. The sixth coordination is provided by the other carboxylate oxygen of E220, which is also coupled to the MIDAS site. In the absence of the ligand E220, which is hydrogen bonded with D119, side chain occupied the space where the MIDAS cation would bind, thus blocking metal ion binding by steric hindrance [Xiong *et al.*, 2002]. This explained why there was not a metal ion present in the MIDAS in the unliganded structure. Although, the Mn^{2+} ion at the LIMBS site did not contact the ligand but the coordination parameters for this site were dependent on the presence of the ligand. Likewise, the third Mn^{2+} ion at ADMIDAS did not have a direct role in ligand binding. However, in the liganded αVβ3 structure, the ADMIDAS is more intimately linked to the MIDAS as the M335 coordinate is replaced by the MIDAS residue D251 and α1-helix is drawn closer to the complex. It would appear that in the unliganded βA, the ADMIDAS ion maintained the integrin inactive by maintaining the link of the α1-helix to the βF-α7 loop [Xiong *et al.*, 2002].

Structural comparisons of αVβ3 in the presence or absence of ligand mainly involved rearrangements in the three metal-binding sites and the surrounding loops. In the open structure, the ADMIDAS cation is positioned closer to the MIDAS. This movement

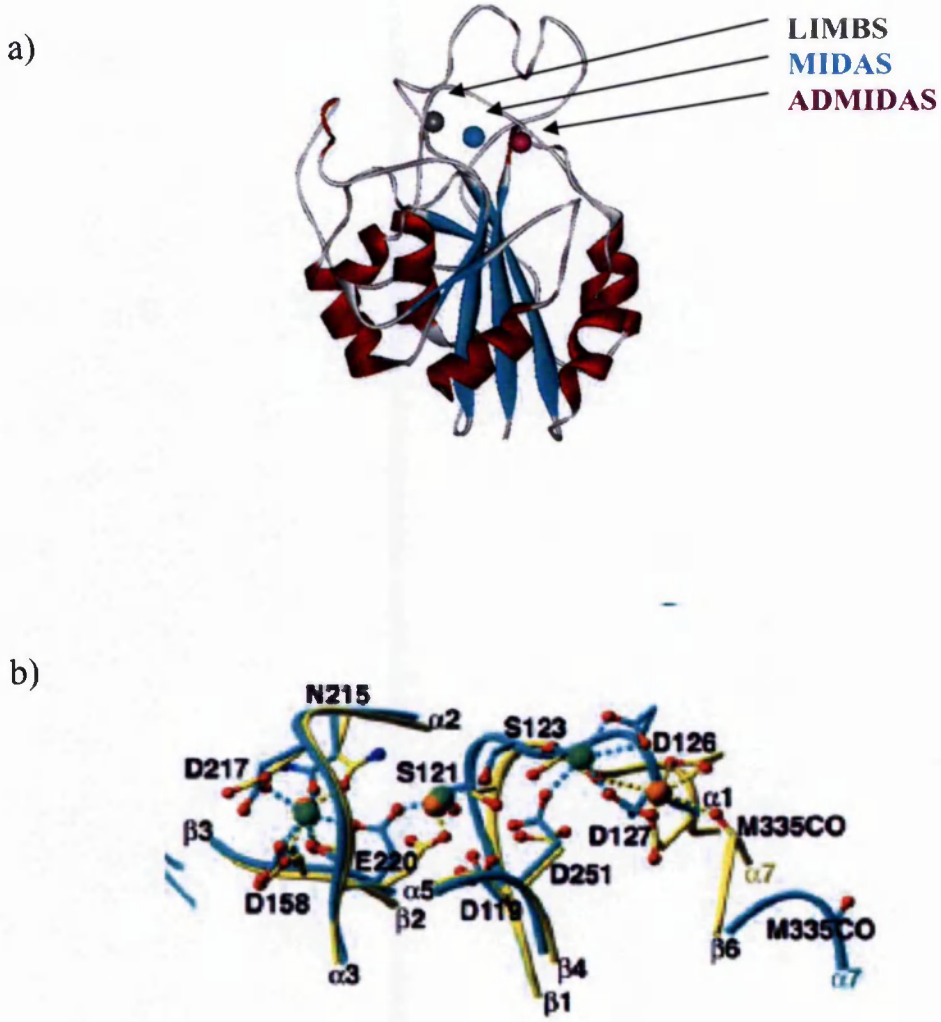

Figure 1.10. Coordination of the divalent cation sites in and around MIDAS in the liganded β3 crystals. The three Mn^{2+} divalent cations in the β3 A domain are present at MIDAS (cyan), LIMBS (grey) and ADMIDAS (magenta). a) Ribbon diagram of the β3 A domain b) Metal ion coordination sites in the open and closed β3 A domain. The open conformation is illustrated in cyan, based on the liganded αIIbβ3 crystal. The closed β3 A domain conformation is shown in yellow, based on the αVβ3 crystals; ADMIDAS coordinating parameters as seen in the unliganded-closed αVβ3 [Xiong *et al.*, 2002], LIMBS and MIDAS parameters taken from the liganded-closed structure [Xiong *et al.*, 2003]. As published by Xiao *et al.*, 2004.

required the α1-helix to shift inwards. In addition, the formation of the LIMBS site repositioned E220 in loop 2 for optimal metal ion coordination in MIDAS. Consequently, the major structural changes were observed in the regions of the α1-helix (S121, S123), in the bottom of helix-α2 (E220) and the surrounding loops α1-α2 and α2-βC', including the specificity loop βB-βC. A small movement in loop βF-α7, adjacent to helix-α7, is also observed when the link with helix-α1 is severed. However, as discussed above, the liganded αVβ3 integrin is bent in the crystal and the full extent of conformational rearrangements upon activation have been restrained.

Independent investigations into the molecular mechanisms of β1 A domain activation highlighted significant structural changes into the configuration of helix-α1 and helix-α7 in the β1 A domain and a large rearrangement of the preceding hybrid domain [Mould *et al.*, 2003a]. Comparisons of the αVβ3 and the liganded αIIbβ3 structures verified findings by Mould *et al.*, whereby there was a large upward movement in the α1-helix, while a downward movement of α7-helix pushed the hybrid domain to swing away from the α subunit (Figure 1.11), which has been proposed to act as a lever for the transition from bent to extended integrin. The crystallographic frame of αIIbβ3 revealed that there was a more pronounced α1-helix movement than the one seen in αVβ3. The α1-helix is actually remodelled in the liganded open αIIbβ3 structure [Xiao *et al.*, 2004]; the unwinding of 3_{10}-helix (preceding the α1-helix) by one-turn, added five residues at the N-terminal of the α1-helix that at the same time was displaced laterally. This was in concert with an upward movement of the α1-helix which accompanied reorientation of the βA'-α1 loop that includes the metal-coordinating residues. Small shifts observed in the positions of the MIDAS and LIMBS ions reflected the reorientation of the metal coordinating residues at similar positions. In contrast, in a large move the βF'-α7 loop was displaced downwards to allow realignment of the ADMIDAS coordination parameters. Most of the remaining structural changes materialised as a consequence of this downward movement that pushed the following α7-helix to move downwards. In addition, the α7-helix pivoted laterally resulting in a large 5.3Å displacement for residues 333-352. The latter two residues unwrapped from the helix and relocated to the exterior of the new smaller interface. Therefore, this downward movement of α7 relayed to the βC strand of the neighbouring hybrid domain and forced the hybrid domain to 'swing-out' and away from the β-propeller.

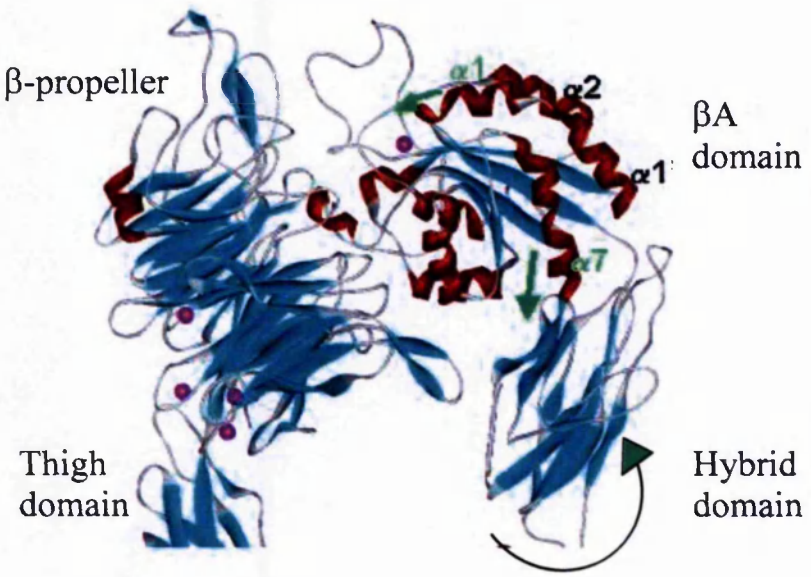

Figure 1.11. Conformational changes in the βA domain that regulate ligand binding in non-αA domain-containing integrins. The model was built with the α5β1 sequence according to the αVβ3 crystal structure. The α subunit is on the left, β subunit on the right. The critical conformational changes upon ligand binding as seen in the αIIbβ3-ligand crystal are highlighted with green arrows. The transition to the open, high affinity integrin involved downward displacement of the C-terminal α7-helix of the βA domain which forced the hybrid domain to swing-out and away from the α subunit β-propeller. The α1-helix moved upwards and pivoted laterally to allow for ligand occupancy at the MIDAS. A single divalent cation at the βA MIDAS and the four cations at the bottom of the β-propeller are shown as magenta spheres. The ADMIDAS and LIMBS metal ions are omitted for the sake of clarity. No change is observed in the orientation of the β-propeller relative to the βA domain.

The reorientation of the hybrid domain relative to the βA domain has been shown recently to be essential to the transition to high activity βA domain [Luo *et al.*, 2003; 2004; Mould *et al.*, 2003a]. Taken together, the above findings suggested an important functional role for α7-helix in the βA domain activation. Consequently, the transition from closed to open β3 A domain involved changes in the loops at the top of the βA domain and at the C-terminal helix of βA domain. These changes were similar to those seen in the αA domain, in particular the downward displacement of α7-helix that is characteristic of ligand-bound αA domains.

Mutagenesis and domain swapping studies utilising interspecies or interdomain chimeras identified another βA domain region involved in ligand binding. For example, replacement of β1 residues 187-193 with the corresponding ^{177}CYDMKTTC^{184} loop region of αVβ3, resulted in a αVβ1 chimeric receptor with increased binding to fibronectin, vWF and vitronectin, thus displaying binding specificities more similar to αVβ3 [Takagi *et al.*, 1997]. Moreover, it was shown that this 'specificity' determining region is required for ligand binding to α5β1 [Takagi *et al.*, 2002b]. In the β3 A domain the specificity segment corresponds to residues in loop βB-βC. In fact, the crystal structures of β3 showed that the specificity loop is positioned at the top of β3 A domain, framing the ligand-binding sites. In the αIIββ3 crystal the β3 specificity loop is closely associated with the cap subdomain [Xiao *et al.*, 2004]. As a consequence of these data, it is thought that the orientation of this loop relative to the α subunit β-propeller contact sites may determine ligand specificity among integrins.

The αV and αIIb subunits lack an αA domain, so the ligand-binding head is comprised of the β subunit A domain (with a MIDAS motif very similar to the αA MIDAS motif). By contrast, the major ligand-binding site within αA domain-containing integrins is located mainly within the α subunit A domain. However, several lines of evidence have shown the βA domain to be functionally important. Mutagenesis studies investigating the role of the individual residues forming the conserved DxSxS motif found in the β subunits, revealed a strict requirement for the three adjacent oxygenated residues for ligand binding in all cases including β1 [Takada *et al.*, 1993], β2 [Bajt *et al.*, 1995] and β3 integrins [Bajt & Loftus, 1994]. Moreover, antibody-mapping studies indicated that the βA domain has

an indirect regulatory role. For example, in a study by Huang *et al.* (2000), 12 antibodies with at least five distinct classes of epitopes within the β2 A domain, were all shown to inhibit binding of αLβ2 to ICAM-1 and ICAM-3. Thus, the βA domain regulates activation via the αA domain rather than directly participating in ligand binding.

Overall, the crystal structures of the open β3 A domain signify a similar mechanism of ligand-induced activation to the αA domains. The critical structural rearrangements that take place in α1-helix, α7-helix and the surrounding loops are comparable in both A domains of α and β subunits. Although the magnitude of the α1- or α7-helix movements between the two A domain are not the same, the conservation in the direction of the movements is noticeable. The shift of the C-terminal helix towards the lower face of the A domains can be considered as a marker of integrin activation. Especially, in the βA domain the downward displacement of α7-helix is vital to the propagation of conformational changes to the hybrid domain. In the current model of αA domain-containing integrin activation, the downward pull of the α7-helix is also thought to communicate the conformational changes to interacting domains. However, the large shift of α7-helix in isolated αA domains may be exaggerated because the domain is not constrained by intramolecular contacts with the propeller and therefore the α7 movement may be less in the whole integrin.

1.7.3 The α subunit β-propeller

Evidence for additional sites of the α subunit taking part in ligand binding come from ligand-receptor cross-linking experiments on integrin heterodimers that lack the αA domain. Originally, regions implicated in ligand binding on e.g. αVβ3 and αIIbβ3 were mapped close to or overlapped with the N-terminal repeats of the α subunit [D'Souza *et al.*, 1990; Smith & Cheresh, 1990]. Inter-integrin chimera experiments have been valuable in defining the regions involved further. Loftus *et al.*, (1996) showed that αIIb / αV chimeras containing the N-terminal repeats 1-5 of αIIb retained αIIb ligand-binding specificity, whereas the chimera containing repeats 4-7 did not. This suggested that ligand binding specificity is contained within blades 1-3 of the β-propeller.

Comparisons of the αV and αIIb propeller domains based on the two integrin crystals verify data from almost 10 years ago. Four insertions in blades 1, 2, and 3 of the β-propeller make up a 'cap' subdomain that is positioned on the protein surface opposite to the β3 specificity loop. Corresponding to inserts 1, 2 and 3 are two β-hairpins and an α-helix which emanate from loops in the upper face of the propeller. Insert 4 is an α-helix plus a long loop which protrude from a loop on the lower face of the β-propeller. The differences in the cap subdomain of αV and αIIb and their orientation relative to the neighbouring βB-βC specificity loop in β3 appear to be responsible for the ligand-binding specificity of these two highly homologous RGD-binding β3 integrins [Xiao *et al.*, 2004].

The same upper face β-propeller regions have been implicated in ligand recognition specificity in other non αA domain integrins. In a study by Mould *et al.* (2000), integrin α5 residues 154-159 of blade 2, 4-1 loop (with current structural knowledge are assigned to cap insert 3) were identified to hold ligand-recognition properties. In this study, α5 loops from blades 2 and 3 inserted into αV, conferred α5 ligand-binding specificity to the chimera as well as the epitopes for all function-blocking α5 monoclonal antibodies. Likewise loss-of-function chimera studies have implicated blades 2 and 3 in ligand binding of α4 [Irie *et al.*, 1997] and α3 integrins [Zhang *et al.*, 1999]. Finally, antibody epitope mapping studies supported the above findings; inhibitory monoclonal antibody epitopes mapped within the first three blades on the upper face of the β-propeller in α3 [Zhang *et al.*, 1999], α4 [Munoz *et al.*, 1996; 1997] and α5 [Burrows *et al.*, 1999].

The structural data gathered from recent studies on αIIbβ3 and αVβ3 contribute significantly to our understanding of the structural and molecular basis of integrin-ligand interaction. Accumulated data from numerous studies show that multiple sites in the N-terminal region of both the α and the β subunits collaborate in ligand recognition. In general, the cap loops locate to the β-propeller / βA domain interface that comprise the ligand binding face of the integrin molecule. A similar mechanism of ligand recognition and specificity determination is likely to be conferred by structural arrangements between α subunit cap subdomain and β subunit specificity loop in all integrins. Differences in the sequence and length of the inserts comprising the cap subdomain are postulated to sculpture the ligand-binding surface and confer specificity [Xiao *et al.*, 2004]. Of note, in

integrins that contain an A domain in the α subunit, the αA domain is positioned by the α-helix of cap insert 3.

There are still several questions that remain unanswered. How is a local conformational change in the αA domain linked elsewhere in the integrin? How does the βA domain communicate to the αA domain to regulate ligand binding? It is yet to be determined how long-range conformational rearrangements result in signal transduction from the cytoplasmic end of the molecule to extracellular head domain. And are the mechanisms of signal transduction the same for outside-in and inside-out signalling the same? These questions are addressed below.

1.8 Models of integrin activation

Atomic resolution studies advanced the knowledge of integrin structure but cannot report alone on how the observed conformational changes regulate activity and function. The next major challenge is to understand how a local change in the extracellular ligand-binding pocket is transmitted across the whole integrin to regulate binding inside the cell, and vice versa. Several models have been proposed to explain the structural mechanisms of integrin activation including the 'switchblade / flick-knife' model [Beglova *et al.*, 2002; Takagi *et al.*, 2002a], the 'bell-rope' model [Takagi & Springer, 2002], the 'deadbolt' model [Xiong *et al.*, 2003a], and the 'pull-spring' model [Yang *et al.*, 2004]. The above models, despite their differences, have two main features the same: a) the active integrin is in the extended conformation and b) where present, the αA domain acts as an intrinsic ligand for the βA domain. Experimental confirmation of any one of these models is awaiting crystallisation of additional ligand-bound integrin heterodimers. At present, combining structural data together with biochemical, mutational and modelling data provides a useful framework for interpreting experimental evidence on the structure-affinity correlation of integrin molecules. Below is some of the evidence contributing to the general model of integrin affinity regulation as it stands at present.

1.8.1 Integrin 'unbending' and activation

Beglova *et al.* (2002) first proposed that the bent integrin, seen in the unliganded-αVβ3 crystal, represents the inactive integrin. Structural data collected by NMR studies on recombinant β2 modules were modelled on the 3-D structure of αVβ3. The predicted

model was used to localise the epitopes of αLβ2 antibodies that bind to the active- or ligand-occupied integrin [Beglova *et al.*, 2002]. In the bent conformation the activation epitopes were buried and thus inaccessible. Moreover, β2 residues that interact with the α subunit to restrain activation were localised in an interface with the α subunit. The above led the authors to propose that upon activation gross conformational changes lead to a 'switchblade-like' opening motion and result in an extended integrin conformation. The latter straightened form reveals the binding sites for integrin ligands and permits binding of activating antibodies to the previously masked epitopes. The transition to the active state involved separation of the α and β subunits at their transmembrane and cytoplasmic domains [Vinogradova *et al.*, 2002, Kim *et al.*, 2003, Luo *et al.*, 2004]. Therefore, in conjunction with previous models of integrin activation, in the model proposed by Beglova *et al.* (2002) the juxtamembrane regions of α and β were spatially distant.

In support of the extended morphology of integrins in the high affinity, ligand-bound conformation were the data from a study combining EM, mutagenesis of soluble β3 integrins and ligand-binding measurements. High resolution EM images revealed integrins that can adopt both the bent and the extended form in solution (Figure 1.12) [Takagi *et al.*, 2002a]. In the presence of Ca^{2+} / Mg^{2+} and / or a C-terminal disulphide clasp, predicted to restrain the integrin inactive, the recombinant soluble αVβ3 molecules appeared in the V-shaped morphology, characteristic of the bent αVβ3 crystal. Addition of a ligand-mimetic peptide did not change the overall morphology of the C-terminally constrained integrins, whereas addition of Mn^{2+} alone and / or ligand converted the unclasped integrin molecules in a fully extended form, as visualised by EM. Surface plasmon resonance measurements of fibronectin and vitronectin binding to the same integrin preparations used for EM showed that the extended but not the bent conformation has high affinity for biological ligands. Moreover, the researchers examined the effect of an engineered intersubunit disulphide bond between the α headpiece and β tailpiece, predicted to lock the integrin in the bent conformation, on cell surface integrins. The binding of biological ligands to wild-type and mutated αVb3 and αIIbβ3 integrins expressed on cells was measured by fluorescence-activated flow cytometry. Results showed that the removal of the introduced disulphide bridge by dithiothreitol (DTT) reduction, and thus release from the bent conformation, was required for activation of ligand binding to the mutated β3 integrins. These studies showed that binding to a small ligand-mimetic peptide converted the β3

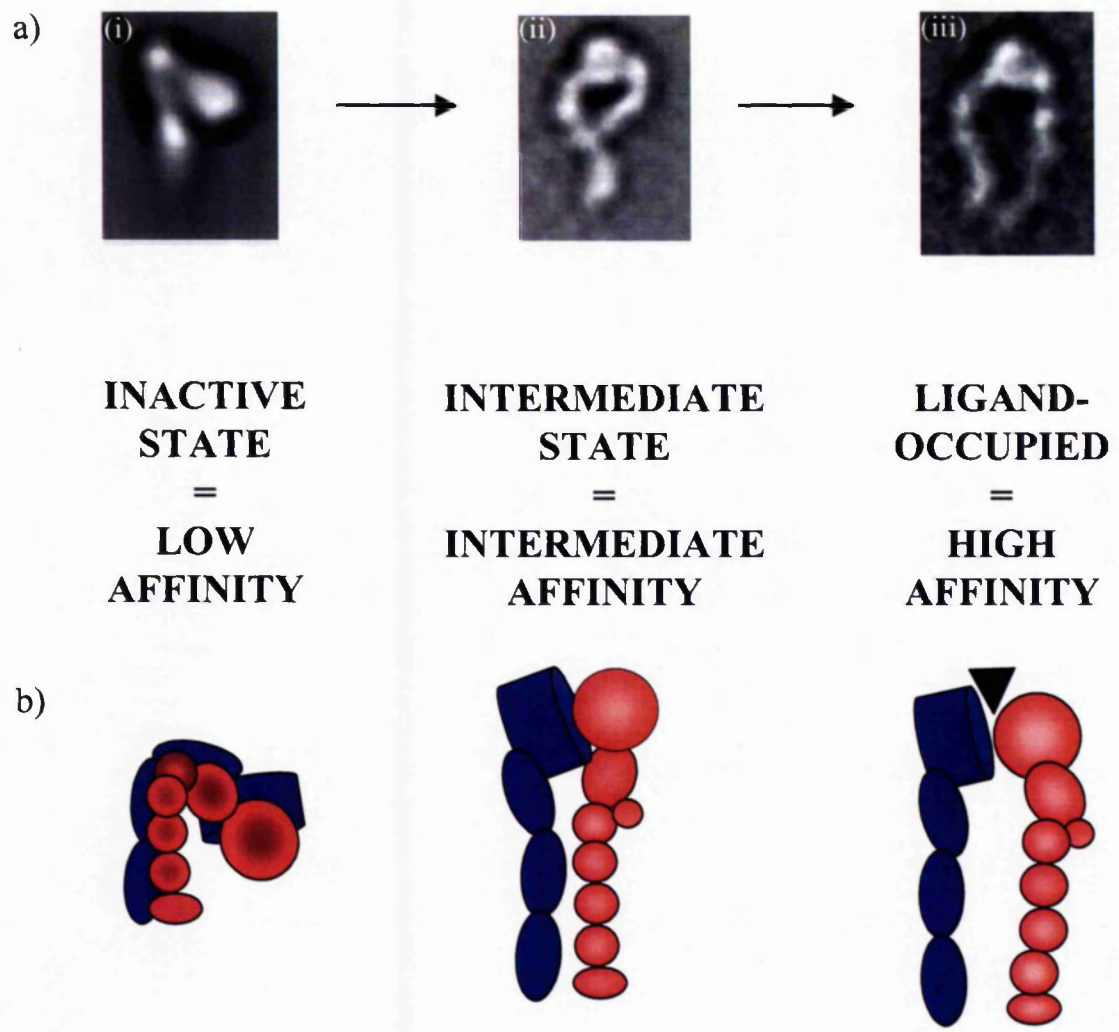

Figure 1.12. Physiological integrin conformations. Truncated soluble aVb3 micrographs obtained by negative stain EM [Takagi *et al.*, 2002]. Integrins as visualised in a) the bent (i), extended (ii) and ligand-occupied (iii) conformations and in b) Schematic representation of the three conformers. The a subunit is depicted in blue, with the b subunit in red.

integrin extracellular domain from the compact bent conformation into an extended conformation, and that this conversion was essential for integrin activation.

The same group also utilised high EM images to visualise a clasped α5β1, truncated integrin bound to a macromolecular ligand [Takagi *et al.*, 2003]. In this study, a fibronectin fragment (containing the type three repeats modules 7–10) was seen bound to the top of the α5β1 headpiece which assumed an 'open' conformation. This α5β1 conformer showed great differences to the 'closed' headpiece, in the absence of bound ligand, in the position of the β-subunit tailpiece that moved away from the α subunit β-propeller. The opening of the angle between the βA domain and the hybrid was estimated at 80° and substantiated that the swing-out movement of the hybrid domain is directly linked with ligand binding. Based on the EM micrographs and biophysical data, Takagi *et al.*, (2002a, 2003) supported the switchblade-like model of integrin activation. The authors added that upon integrin activation an extensive interdomain movement between the βA domain and hybrid domain induced the bent, low affinity integrin conformer to rise to an extended integrin with a 'closed' headpiece. Upon ligand binding, the latter intermediate affinity integrin converted to 'open' headpiece integrin that bound ligand with higher affinity. Although the high-resolution EM observations confirmed the presence of both conformers, the above studies were done with recombinant integrins suggesting the transition from one conformer to another might take place under physiological conditions.

The evidence for a global shape change upon integrin activation on live cells, for both non-αA domain and αA domain-containing integrins, were recently obtained with the fluorescent resonance energy transfer (FRET) technique. Unbending of integrins upon activation would be expected to lead to changes in the vertical distance of the integrin subunits relative to the plasma membrane. Indeed, these structural changes were detected as changes in the magnitude of fluorescent signal exchanged between fluorescein (FITC)-labelled integrin ligands and rhodamine-labelled cell-surface probes. Using FITC-labelled peptide bound to α4β1 and rhodamine lipid incorporated into cell membranes, it was shown that 1 mM Mn^{2+} triggered extension of the integrin, whereas 1 mM Mn^{2+} + 1 mM Ca^{2+} did not cause full extension of the α4β1 i.e. increased the quenching efficiency of FRET [Chigaev *et al.*, 2004]. The same process was applied to αLβ2 except for using FITC-labelled antibody fragments directed against αLβ2. When cells were activated with

DTT or Mn^{2+}, αLβ2 changed its height relative to the cell surface as detected by the increase in fluorescence [Larson *et al.*, 2005]. The above data suggested that although the conversion from bent to extended form is also true for the αA domain-containing integrins, there may be differences between the different integrin heterodimers. In addition, the data implied that depending on the activation condition, there are multiple overall shapes between the bend and the extended state an integrin can adopt. FRET measurements between integrin and ligand/antagonist or the plasma membrane allow for direct characterisation of the spatio-temporal activation of integrins *in situ*. Undoubtedly, imaging of molecular interactions using FRET or other high-resolution spectroscopy methods will be needed to visualise complex molecular interactions or even uncover activation-dependent conformational changes in integrins in a physiological context.

Taken together the current data suggest that the bent integrin conformation is physiological, as is the extended conformation. The combined structure-function studies suggest that resting integrins on cell surface are in the bent conformation, inactive or with low affinity for ligands. This compact conformation where the headpiece is facing the cell surface is unfavourable for macromolecular ligand binding. In response to activation stimuli the low affinity conformers convert to extended integrins. At the tertiary level, the extended integrin headpiece will bind ligands in the 'open' conformation but not in the 'closed' conformation. For cell surface integrins, acquisition of high affinity by local conformational changes and better ligand accessibility by full-length integrin extension may both be important to ensure efficient cell adhesion [Takagi *et al.*, 2003]. Ligand binding increases the affinity for ligand, which reinforces the extended form as at the same time the swing-out of the hybrid domain structurally changes the overall conformation of the receptor (Figure 1.13). This movement acts as a lever to separate the membrane-proximal segments and the binding signal is transmitted across the plasma membrane. Movement apart of the cytoplasmic tails triggers binding to intracellular signalling molecules initiating a cascade of events.

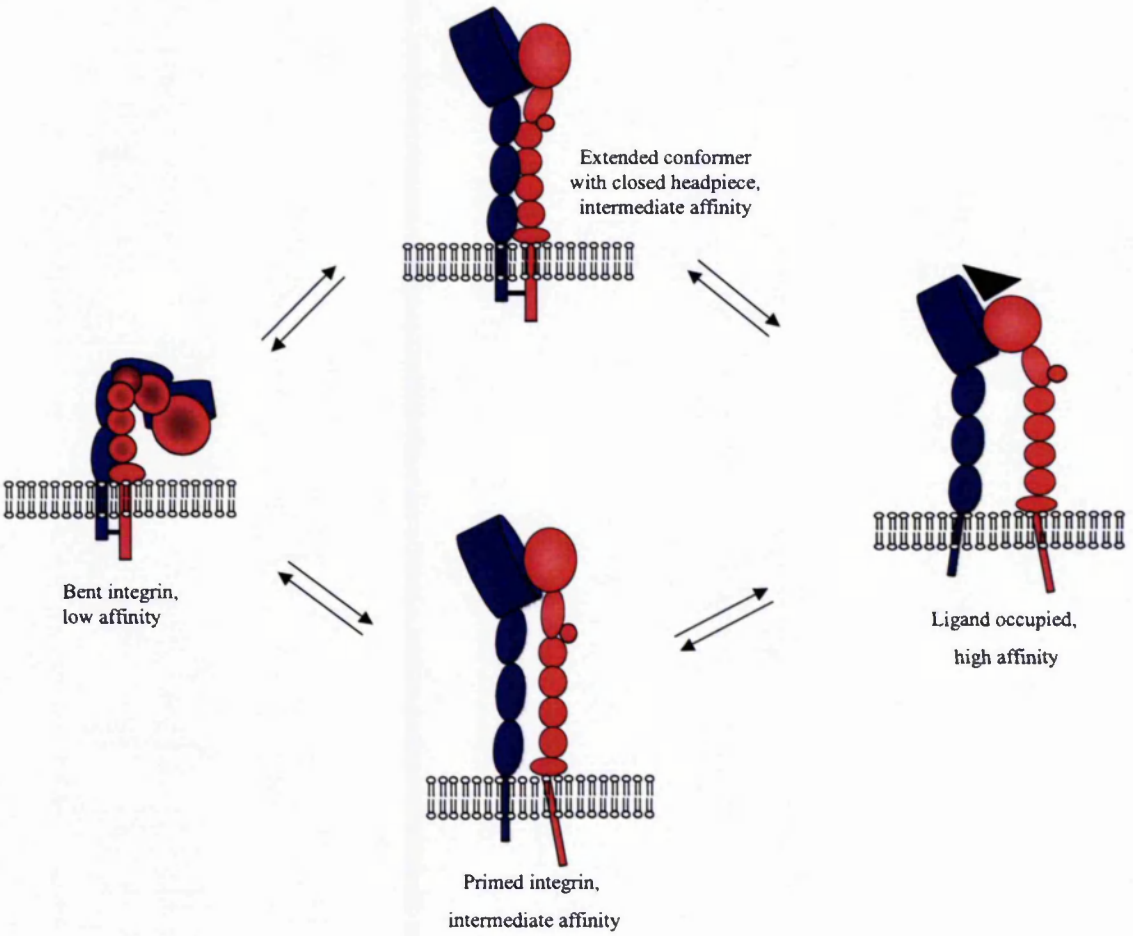

Figure 1.13. Structural rearrangements in integrin activation. In the bent form the ligand-binding integrin head is facing the cell membrane and has low affinity for other molecules. Integrin priming may induce variable intermediate conformations with intermediate affinities for ligand. Ligand binding stabilises the outward swing of the hybrid domain and the equilibrium switches to the high affinity for ligand. Integrin activation also requires separation of α / β cytoplasmic tails and legs. The α subunit is depicted in blue, with the β subunit in red. Note that this model is for integrins not containing an αA domain.

1.8.2 Activation of integrins containing an αA domain

Structure-function correlations of αA domain-containing integrins have been the subject of detailed studies investigating how conformational changes in αA domains are linked to specific structural alterations elsewhere in the integrin. As already mentioned, the open and closed conformation of the isolated αA domain seen in the crystals corresponded to the liganded and unliganded protein, respectively. Mutagenesis approaches have been taken to stabilise one conformation over another and study the functional significance of the alternative conformations of the αA domains. For example, disulphide-locked forms of αL [Lu *et al.*, 2001c] and αM A domain [Shimaoka *et al.*, 2002a] which assumed active, ligand-binding or closed, inactive conformations have been produced confirming that αA domain conformational changes took place in the context of the whole integrin and underlie affinity regulation. More recently, multiple conformations were demonstrated structurally for the αL A domain [Shimaoka *et al.*, 2003a]. The disulphide-bonded αL A domain mutants were crystallised in an open and a second, novel conformation which showed an open state in the absence of bound ICAM-1. Affinity and kinetics analyses using surface plasmon resonance demonstrated that these structures belonged to high and intermediate affinity states of the αL A domains, whereas a locked-closed conformation [Qu & Leahy, 1995] corresponded to a low affinity A domain.

The crystal structure of αVβ3 suggested that the large interface between the β-propeller and the βA domain can accommodate the α subunit A domain [Xiong *et al.*, 2001]. The αA domain protrudes from loop D3-A3 of the propeller, which in αV and αIIb integrins forms part of the ligand-binding pocket with the β3 subunit. The N- and C-termini of αA domain are expected to be in close proximity to the top of βA domain and the MIDAS site [Alonso *et al.*, 2002]. In the current model of αA domain-containing integrin activation, the αA domain acts as an intrinsic ligand for the βA MIDAS (Figure 1.14) [Alonso *et al.*, 2002; Shimaoka *et al.*, 2002b]. An invariant acidic glutamate (E) residue at the flexible C-terminal linker that connects the α7-helix of the αA domain to the propeller, fulfils the requirement for an acidic ligand-residue to bind to βA MIDAS. Engagement of this internal ligand leads to downward displacement of the α7-helix which switches the αA domain in the open conformation. Mutations of the conserved glutamate in αMβ2 [Alonso

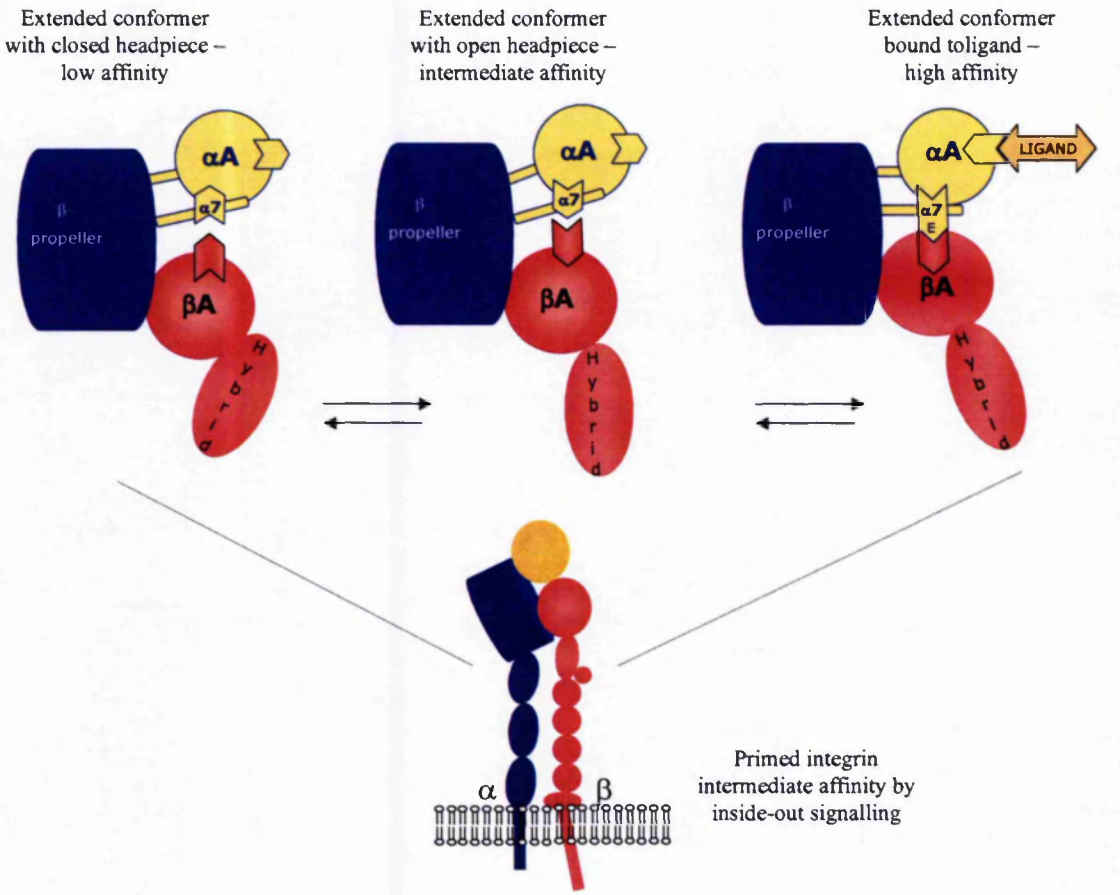

Figure 1.14. Schematic representation of the activation model of integrins that contain an αA domain. Outward movement of the hybrid domain activates the βA MIDAS which in turn ligates and pulls the C-terminal α7-helix of the αA domain. Downward displacement of the α7-helix converts the extended headpiece from low to intermediate affinity and binding of the ligand to the αA domain MIDAS switches the integrin in the high affinity.

et al., 2002] and αLβ2 [Shimaoka *et al.*, 2004; Huth *et al.*, 2000] abolished binding of the receptors to activation-dependent ligands.

Functional mutations, both activating and inactivating, are located at the top and at the base of helix-α7 and the following linker sequence demonstrating the structural importance of this region for activation of αA domain-containing integrins [Alonso *et al.*, 2002; Lupher *et al.*, 2001; Huth *et al.*, 2000]. Strong evidence for the interaction of the αA domain to βA MIDAS provided a recent study by Yang *et al.* (2004) describing second-site suppressor cysteine mutations. The effect of the individual cysteine mutations in either subunit, which included substitution of the conserved αL E310 to Cys, was inhibitory in respect to ICAM-1 binding. By creating an interdomain disulphide crosslink, between αL and β2 A domains, it was shown that the receptor was constitutive active. However, the effect of the double mutation could be reversed by allosteric αA domain inhibitors. The data overall suggested that the interdomain link is required for ligand binding and supported the hypothesis that the βA domain regulates the activity of the αA domain by pulling down the α7-helix. Thus the connection resembles more a 'pull spring' [Yang *et al.*, 2004] than a rigid rod or bell rope.

This link would explain how mutations on the βA MIDAS can regulate ligand binding in the primary binding pocket of the αA domain [Goodman & Bajt, 1996; Bajt *et al.*, 1995]. Moreover, it would explain the negative regulatory effect of antibodies [Welzenbach *et al.*, 2002; Lu *et al.*, 2001c; Huang *et al.*, 2000] and small-molecule compounds that are directed against the β subunit [Shimaoka *et al.*, 2003b; Gadek *et al.*, 2002]. Of note, allosteric αLβ2 antagonists belong to two distinct classes: a) inhibitors that bind at the bottom of α7-helix and stabilise the A domain in the closed, inactive conformation [Liu *et al.*, 2001; Lu *et al.*, 2001a; Weitz-Schmidt *et al.*, 2001] and b) inhibitors that do not require the αA domain but bind to the β2 A domain MIDAS instead. The latter promote induction of integrin extension, as shown by exposure of activation epitopes on the α subunit and β subunit including in the β2 A domain [Shimaoka *et al.*, 2003b]. These 'α / βA domain allosteric antagonists' are thought to inhibit ligand binding by the αA domain by acting as intrinsic ligand mimetics for the βA domain. Compound binding to the βA MIDAS prevents its interaction with the αA domain rendering it inactive. Yet, βA

MIDAS occupancy activates the open βA domain conformation, induce hybrid domain swing out and stabilise the extended integrin form.

In *in vivo* studies, the α / βA domain allosteric antagonists of αLβ2 - ICAM-1 enhanced rolling adhesion of murine lymphocytes in lymph node microvessels and also reduced firm adhesion [Salas *et al.*, 2004]. In the same study, cells transfected with the αL-E310A mutation demonstrated complete inhibition of rolling and firm adhesion. Rolling but not firm adhesion was rescued by treatment with an α/β A domain allosteric antagonist. Overall, the data suggested that distinct conformations of αLβ2 regulate rolling and firm adhesion and that an extended conformation favours rolling. The authors proposed that rolling might be mediated by an intermediate conformation of αLβ2 with an extended conformation but with the A domain in a low or intermediate affinity state. These findings emphasize further the structural complexity of the regulation of αA domain-containing integrins.

1.8.3 Summary

The atomic resolution studies have helped to unravel the physiological relevance of different domains in integrin function. In addition, numerous studies highlighted the direct link between gross conformational rearrangements and affinity regulation in ligand binding. Taken together, the latest solved crystal of αIIbβ3 in complex with ligand signified that this structure represents the active integrin conformation and that the mechanisms of activation of αA and βA domains are analogous. For both the αA and βA domains, the positions of the α1- and α7-helix affected the metal-ion coordination spheres controlling ligand binding at the MIDAS site. Coordination of the cation at the MIDAS site by the carboxyl group of the acidic-ligand residue, guided strikingly similar movements in both A domains. In particular, the downward displacement of the α7-helix could be considered a determinant of integrin activation.

The current model of integrin activation proposes that when the α and β cytoplasmic domains are bound together the integrin adopts the bent conformation with the closed headpiece adjacent to the membrane in a low affinity state. Upon activation, local conformational changes in the extracellular ligand-binding domain result in the open integrin conformation with intermediate affinity for extracellular ligands. The binding of

which stabilises the extended conformation and shifts the equilibrium towards the high affinity for ligand. At the same time the transmembrane and cytoplasmic domains separate. This movement is sensed by intracellular signalling molecules that bind to the integrin tails and activate downstream pathways. Similarly, inside-out signalling can induce separation of the cytoplasmic tails causing gross conformational rearrangements to be transmitted across the plasma membrane. The primed integrin can engage with ligands in the extracellular matrix to enhance activation. At present there is little evidence to suggest that the changes in integrin shape are different in outside-in and inside-out signalling.

As discussed above, αA domain-containing integrins adopt a similar overall extended morphology to the non-αA domain-containing integrins. In this situation, bi-directional signal transduction is mediated via the αA-βA interdomain link. The βA mediates ligand binding in αA-containing integrins by regulating the 'opening' of the αA domain. Essentially, ligand binding to αA domain-containing and non-αA domain-containing integrins is regulated by the activation status of the βA domain. Experimental confirmation of this hypothesis needs resolution of the structures of different integrins in distinct affinity states. Evidently, crystallisation of an entire integrin bound to ligand is awaiting in anticipation. Therefore, despite the advances in integrin structure, the precise mechanisms of how conformational changes are propagated between integrin domains by both outside-in and inside-out signalling remain unclear, but in recent years some key features have been elucidated.

1.9 Modulation of integrin activation

Following receptor occupancy and subsequent increase in ligand-binding affinity, the binding signal is transduced across the plasma membrane in a process that triggers integrin clustering (avidity modulation) and enhancement of cellular adhesion interactions. The relative contribution of affinity and avidity modulation to ligand binding varies according to integrin type and cellular context [Calvete J.J., 2004]. In this section, the modulation of conformational changes within the individual receptors' domains is explored. In general, integrin priming can be induced artificially by the use of cations, specific monoclonal antibodies or small-molecule antagonists. Of course, internal structural changes of integrin architecture also provided evidence for direct modulation of integrin conformational states.

These alterations included truncation studies exploring the ligand-binding activity of the recombinant integrins by breaking extracellular constraints or by deleting the transmembrane / cytoplasmic segments. More elaborate structure-based studies produced recombinant soluble receptors that assumed active, ligand-binding conformations by engineering disulphide bridges [Lu *et al.*, 2001b, c; McCleverty & Liddington, 2003] or glycosylation wedges [Luo *et al.*, 2003a]. Yet, allosteric up- or down-regulation has been described by less disruptive mutational approaches such as substitution of single amino acid conformational switches. Some of these tools for studying integrin structure and affinity modulation used in the author's research are described below.

1.9.1 Cations

The integrin crystal structures demonstrated that these molecules contain several regions that are competent to bind divalent cations in each of the integrin subunits. The α2 A domain bound to the collagen peptide was crystallised with a Mg^{2+} ion ligated to the MIDAS site, whereas unligated αA domain crystals have been crystallised with either a Mn^{2+} or a Mg^{2+} ions occupying the MIDAS. The first crystal snapshot of the extracellular segment of αVβ3 was determined in the presence of Ca^{2+} or Mn^{2+} ions. There were four solvent exposed cation sites in blades 4-7 of the β-propeller, a fifth metal ion at the thigh / calf-1 interface and a sixth metal ion in the ADMIDAS site. In the RGD-bound β3 crystals, in addition to ADMIDAS two more Mn^{2+} ions were present in the MIDAS site and in the LIMBS site. The cation-binding sites in the αV or αIIb subunits were not involved in regulation of ligand binding. Of course, where present in the α subunit, the αA domain MIDAS site is essential in ligand-binding and integrin activation.

Biochemical evidence to support regulation of integrins by cations comes from numerous studies. Mould *et al.* (1995a) have shown that α5β1 has several cation-binding sites that fall into three functionally distinct classes. In this study the effects of Ca^{2+}, Mn^{2+} and Mg^{2+} ions were examined in the modulation of α5β1-fibronectin binding; Mn^{2+} and Mg^{2+} supported high and low levels of ligand binding. Moreover, Ca^{2+} was found to be a non-competitive inhibitor of Mn^{2+}-supported ligand binding, suggesting that the two cations recognise separate binding sites. In contrast, the effects of Ca^{2+} on Mg^{2+}-supported ligand binding were dependent on the relative concentrations of the cations. At low micromolar concentrations Ca^{2+} was proposed to bind to an alternative, high affinity effector site,

increasing the affinity of Mg^{2+} for its binding site. However, at millimolar concentrations, Ca^{2+} inhibited Mg^{2+}-supported binding by directly competing with the Mg^{2+} for the binding site.

The presence of two separate cation sites with distinct cation affinities has also been proposed for the A domain-containing integrin αLβ2 [Labadia *et al.*, 1998]. Mn^{2+} or Mg^{2+} were shown to preferentially bind to a ligand-competent site, whereas Ca^{2+} bound to an effector site inhibiting ligand binding. The mixed combination of both Mg^{2+} and Ca^{2+} increased the affinity of either site by approximately 10-fold; low Ca^{2+} concentration increased the affinity of Mg^{2+} for αLβ2 but high concentrations inhibited Mg^{2+}-induced ICAM-1 binding. Similar studies of the effects of these cations on α2β1-collagen binding also demonstrated a mixed type of inhibition; 2 mM Mg^{2+} supported collagen binding to α2β1 and Ca^{2+} at the same concentration inhibited the integrin-ligand interaction, while 10 μM Ca^{2+} synergistically enhanced Mg^{2+}-induced collagen binding [Dickeson *et al.*, 1997; Onley *et al.*, 2000].

Given the fact that several cation-binding sites exist per integrin molecule, the exact role of each binding site has yet to be defined. The importance of the ADMIDAS and LIMBS cation-binding sites in ligand binding to the α5β1 is demonstrated by loss-of-function mutations of residues that make up the β1 cation-binding sites [Mould *et al.*, 2003b]. Another significant finding of the above study is that the ADMIDAS was shown to be the negative regulatory Ca^{2+} site [Mould *et al.*, 2003b]. Preliminary evidence exists to suggest that LIMBS is the stimulatory Ca^{2+} site [Dr. P.A. Mould, personal communication], but are discussed extensively in chapter 6.

Integrin binding is universally divalent cation dependent. The affinity of different ligands for a particular integrin heterodimer can be differentially regulated depending on the cation. It is of particular interest that the same general trend of cation regulation applies to αA domain-containing integrins and non-αA domain-containing integrins. In general, Mn^{2+} and Mg^{2+} promote ligand binding, whereas Ca^{2+} fails to support ligand binding. In addition, Ca^{2+} binding sites fall into two classes – one high affinity and stimulatory and the second low affinity and inhibitory. Integrin αIIbβ3 is unusual in that ligand binding can take place in the presence of Ca^{2+} [Rivas & Gonzalez-Rondrigues, 1991; Cierniewski *et*

al., 1994]. *In vivo* the concentrations of these cations are in the millimolar range and hence could alter integrin activity. However, the physiological relevance of cations in ligand binding by integrins remains unclear at present.

1.9.2 Monoclonal antibodies

The functional states of integrins correspond to different integrin conformations which with a minimalist view can be portrayed as closed / inactive, open active, ligand bound. These different integrin conformations are recognised by monoclonal antibodies (mAbs). For many years, mAbs have been used *in vitro* to monitor binding to specific domains and to report conformational alterations upon integrin activation. Some examples of the large repertoire of mAbs being utilised in biochemical analyses include non-blocking, activating or inhibitory mAbs, are described below (for excellent reviews see Humphries M.J., 2000; 2004).

Interestingly, most activating mAbs recognise the β integrin subunits. The activating anti-α5β1 mAbs N29 and 8E3 were reported to bind to the β1 PSI domain and favour the extended/ active integrin conformation [Mould *et al.*, 2005]. Using recombinant integrin-domain fragments it was shown that the stimulatory action of these mAbs was dependent on the α5 calf-1 domain. This suggested that the epitopes on the β1 subunit are likely to lie on the side of this domain that faces the α5 subunit knee [Mould *et al.*, 2005]. Both these regions are predicted to undergo structural rearrangements during straightening of the integrin tailpiece. Therefore, N29 and 8E3 mAbs binding induced structural changes in regions that are functionally important in the open integrin and provided direct evidence that the conformational changes are linked to activation of the α5β1 holoreceptor. Several other activating mAbs have been to mapped to the regions of the cysteine-rich EGF-like repeats. TASC and 9EG7 are anti-β1 mAbs [Bazzoni *et al.*, 1995; Shih *et al.*, 1993], CBR LFA-1/2 KIM185, KIM 127 recognise the β2 subunit [Huang *et al.*, 2000; Takagi *et al.*, 2001a], and LIBS2, 3 and 6 are mapped to the β3 EGF-like repeats [Du *et al.*, 1993]. The high number of activating mAbs that recognise the cysteine-rich repeats, pointing to the importance of this region in signal transduction. In particular, the broad area recognised by regulatory mAbs is in agreement with the concept that large-scale shape alterations, not limited to the binding regions, take place during integrin activation.

Binding of the ligand to the integrin brings about conformational changes that result in the exposure of 'ligand-induced binding sites' or LIBS. A subset of antibodies that react preferentially with the ligand-occupied conformation of the integrin have been termed anti-LIBS mAbs (Mould *et al.*, 1996a). 12G10 is an example of an anti-β1 anti-LIBS mAb that has been extensively utilised to study α5β1 modulation. Mould *et al.* (1995c) showed that availability of 12G10 binding is promoted by Mn^{2+} and inhibited by Ca^{2+}, reflecting the cation dependency of the ligand. Examples of activation- and cation-sensitive mAbs that bind to the integrin α subunit are more sparse. The mAb JA208, which is in fact the first anti-α2 A domain anti-LIBS mAb reported; showed increased binding by addition of the collagen GFOGER peptide [Tuckwell *et al.*, 2000]. Anti-LIBS mAbs are thought to recognise a natural occurring ligand- and cation-bound conformation of integrins hence stabilising the ligand–occupied conformation and enhancing ligand binding.

Other mAbs have been found to act as ligand-mimetics and therefore decrease the affinity of the integrin for the ligand in a competitive fashion. Examples include PAC1 anti-αIIbβ3 [Abrams *et al.*, 1994] and WOW1 anti-αVβ3 mAbs [Pampori *et al.*, 1999]. The αA domains have been shown to contain the epitopes for several anti-functional anti-α subunit mAbs. A thorough study of anti-α2β1 mAbs that blocked collagen binding to α2β1 mapped mAbs, namely JA202, JA215 and JA218, to the α2 A domain [Tuckwell *et al.*, 2000]. JA202 epitope was mapped to residues 199-216 of helix-α3, in close proximity to the MIDAS site and therefore was proposed to inhibit collagen binding by steric hindrance. However, most integrin inhibitory mAbs have been shown to modulate integrin activation in an allosteric manner. For instance, Mould *et al.* (1996a) studied the reduced recognition of the anti-β1 mAb13 by α5β1 upon binding of a fibronectin fragment and a GRDGS peptide. Using competitive ELISA it was demonstrated that this inhibitory mAb did not compete directly with the ligand for binding to α5β1, but that the epitope was perturbed in an allosteric manner. The subset of mAbs that recognise epitopes expressed on the inactive integrin, known as 'ligand attenuated binding sites' or LABS, hence these are known as anti-LABS mAbs (Mould *et al.*, 1996b). These mAbs are though to stabilise the inactive conformers of integrins or prevent the conformational changes required for activation.

The importance of mAbs in integrin studies can be simply demonstrated by the broad use of mAbs in research. In a vast majority of studies the utilisation of antibodies to check for correct receptor folding and cell surface expression are the first necessary steps in subsequent analyses. The identification of activation / conformation-sensitive mAbs provides useful probes to study structural reorganisation of the integrin receptors as a result of ligand binding and pinpoint functionally important regions within the active domains.

1.9.3 Small molecules

The identification of compounds that bind to the regulatory L-site in the αL A domains represents another way by which integrin activation can be studied. The inhibitory properties of lovastatin on αLβ2 adhesion to ICAM-1 has been investigated extensively by several pharmaceutical companies. Moreover, high throughput library screens have identified several novel non-peptide compounds that prevent LFA-1 binding to ICAM-1. Structure optimisation has successfully yielded potent LFA-1 antagonists including statin-derived compounds [Novartis AG], and derivatives of p-arylthio cinnamides [Abbot Labs/ ICOS Corp] and of 5-substituted-3- phenylhydantoins [Boehringer Ingelheim] – all referenced in a review by Liu G., 2001.

In a study by Welzenbach *et al.* (2002) the molecular mechanisms of the αLβ2 integrin activation were explored by the use of small molecular compounds. In this novel approach no mutagenesis strategies were employed to modulate integrin activation. Monoclonal antibodies were used as reporters of the conformational changes on the LFA-1 A domain, the β-propeller and the β2 A domain upon binding of small molecule inhibitors to LFA-1. The binding of the statin-derived compounds to the L-site ligands induced epitope changes in both the αL A domain and in the βA domain and inhibited LFA-1 activation. The propagation of conformational changes to the βA domain depended on the chemical structure of the statin-derived molecules. Moreover, binding of XVA143, a dual αLβ2 / αMβ2 inhibitor, to the βA domain of the active LFA-1 receptor abolished ICAM-1 binding by structural alterations of the βA domain alone; no conformational changes were detected in the αA domain of LFA-1. On the basis of these data and data published by Lu *et al.* (2001a) the authors hypothesised that the binding of this small molecule to the β2 A domain induced conformational changes, which disturbed the interaction between αL A domain and the β2 A domain necessary for ICAM-1 binding.

More recently, Shimaoka *et al.* (2003b) provided elaborate data to support the mechanism of inhibition of the α / β I-like allosteric inhibitors, by which this class of antagonists inhibited αA domain activation while stabilising the rest of the integrin in the active conformation. The above studies demonstrated that there is a great degree of manipulation of the integrin structure by small molecules that bind to sites other than the MIDAS site. The above findings also implied that it is possible to synthesise small molecule inhibitors against the other β-subunits that function in an allosteric way to impair αA domain-containing integrins binding to physiological ligands. This is an attractive aspect of integrin antagonism for the pharmaceutical industry.

At present, a number of antagonists of integrins that function as modulators of integrin activation are being developed. These small molecule antagonists appear to mimic / inhibit physiological ligand interactions and therefore their analysis provides new insights into the molecular mechanisms of integrin activation.

1.9.4 Conformational switches

The 3-D data of integrin domains have facilitated the design of mutagenesis studies of considerable value in exploring integrin activation. To understand how conformational changes regulate affinity for ligands, mutations are introduced to promote the open or closed conformation and tested at both the molecular and the cellular level. A small number of studies where a single amino acid outside the ligand-binding pocket can allosterically modulate the αA domain function have emerged over the past years. In the closed αM A domain conformation, Ile316 is part of a hydrophobic socket, named 'SILEN' (socket for isoleucine), which links the α7-helix to the central β-sheet and is replaced by Leu312 in the open conformation [Xiong *et al.*, 2000]. Deletion or substitution of Ile316 displaced this residue from SILEN and resulted in the crystallisation of the mutated αM A domain in the open conformation. In addition the holoreceptor was found to be in the high affinity state [Xiong *et al.*, 2000]. The equivalent Ile306 to Ala substitution in αL A domain was also shown to increase αLβ2 binding to ICAM-1 [Huth *et al.*, 2000; Lupher *et al.*, 2001]. Moreover, a Ile314 to Gly substitution in αX increased the affinity of the mutated αX A domain by 200-fold relative to the wild type A domain [Vorup-Jensen *et al.*, 2003]. It is significant that the residues forming SILEN in αM are

either identical or conserved in all the other A domains. This suggests a similar mechanism of activation is shared by all integrin αA domains [Xiong *et al.*, 2000].

A second allosteric, single amino acid switch has been reported for α2 and αM. Residue Glu318, at the N-terminal end of helix-α7, is buried in the closed α2 A domain but is solvent exposed in the open conformation. Substitution of Glu318 to Trp / Tyr / Ile in α2 A domain resulted in an increase in ligand binding: in collagen I, collagen VI, collagen I C-propeptide, laminin and E-cadherin [Aquilina *et al.*, 2002]. The glutamic acid substitutions promoted the open A domain state by disruption of a single H-bond and possibly by alterations of the hydrophobic interactions. A gain-of-function P302W mutation was first reported for αM A domain residue Phe302, corresponds to Glu318 in α2, by Li *et al.* (1998). Glu318 is conserved in α1, α10 and α11 and has been hypothesised that the same activation strategy may be extended in these integrin domains.

Allosteric up-regulation and mutant integrin receptors stabilised in a locked state that override the blocking effect of mAbs / inhibitory compounds, are helping to characterise the structural requirements underlying integrin affinity modulation. The crystal structure of an αA domain-containing integrin heterodimer would undoubtedly be of a great advantage in studying the substantiation of cation-binding sites but nevertheless, further biochemical investigations are required to understand integrin-cation interactions. The solution of more integrin 3-D crystallographic data will help to distinguish the more subtle conformational changes that may occur in different integrin heterodimers to confer the ability to recognize various ligands with appropriate specificities. Undoubtedly, how the αA domain contacts the β-propeller and how the α subunit interacts with the β integrin subunit will be the focus of intense structural and biochemical investigations.

1.10 The αA domain-containing integrin α2β1

Integrin α2β1, also known as very late antigen (VLA)-2, CD49b/CD29 and glycoprotein (GP) Ia/IIa, is expressed on several different cell types. It is a collagen and laminin receptor on endothelial and epithelial cells [Elices & Hemler, 1989], but it binds exclusively to collagen when it is expressed on megakaryocytes and blood platelets [Zutter & Santoro, 1990]. The biological and physiological importance of integrin α2β1 mediated collagen binding in thrombosis and hemostasis is well documented [Santoro & Zutter, 1995]. The importance of α2β1 integrin in normal hemostasis is demonstrated by severe bleeding disorder in patients who lack α2β1 on their platelets [Nieuwenhuis *et al.*, 1985] or have developed autoimmune antibodies against α2β1 [Deckmyn *et al.*, 1990]. Recent studies have implicated α2β1 density on platelets to hemostasis, arteriothrombosis and several cardiovascular disorders. Integrin α2β1 density on platelets is an inherited trait determined by three α2 alleles; allele 1 is associated with increased α2β1 levels, whereas allele 2 and 3 are associated with lower levels of α2β1 [Kritzik *et al.*, 1998]. The inheritance of allele 2 or 3 in patients with Willebrand disease type I is associated with increased risk of bleeding [Di Paola *et al.*, 1999] and inheritance of allele 1 may predispose patients to acute coronary disease [Moshfegh *et al.*, 1999], stroke [Carlsson *et al.*, 1999] or diabetic retinopathy [Matsubara *et al.*, 2000]. In addition, the α2-knockout animal model showed abnormalities of mammary gland branching morphogenesis and revealed important roles for α2β1 in platelet biology. Platelets from α2β1-deficient mice failed to adhere to type I collagen under static or flow conditions and showed impaired collagen-induced aggregation [Chen *et al.*, 2002]. Further examinations in an *in vivo* model of thrombosis revealed that α2β1-deficient mice showed defects in thrombus formation after acute vascular injury [He *et al.*, 2003]. Therefore, integrin α2β1 is particularly interesting because of its role in thrombosis and hemostasis.

Integrin α2β1 is composed of a 150 kDa α2 subunit and a 130 kDa β1 subunit. Within the α2 subunit, the 200 amino acid A domain is the main collagen-binding site for collagen [Emsley *et al.*, 1997; 2000]. Crystallisation of open (liganded) and closed forms of the α2 A domain has demonstrated the existence of at least two conformers. The two crystal forms have allowed definition of the structural basis of the α2 A domain MIDAS-collagen interactions. Yet, the molecular mechanisms of α2β1 activation are not fully understood.

The α2 A domain is predicted to be tethered to one face of the β-propeller domain. In response to agonists, changes in the position of the C-terminal helix of α2 A domain relative to the rest of the α2β1 heterodimer are thought to result in gross conformational alterations that are propagated along the integrin heterodimer and through to the cytoplasmic domains to initiate signalling cascades.

The ability of αA domains to fold independently from β subunits [Hangan *et al.*, 1996] and the successful expression of recombinant α2 A domains that retain the ligand affinity and specificity of the intact integrins in the same cation-dependent manner [Calderwood *et al.*, 1997] facilitated a number of different studies. However, the biochemical and structural characterisation of the α2β1 holoreceptor has been limited. Moreover, the finding of the allosteric IDAS / L-site in αLβ2 integrin or of the SILEN pocket in αMβ2 suggested that it is possible to identify regulatory sites in other αA domain integrins. Consequently, exploring the contributions of the activation-regulatory C-terminal α7-helix of α2 A domain with the prospect of identifying gain-of-function or loss-of-function mutations that modulate functional activity of the whole integrin is attractive. In addition, other studies showed that some point mutations in the βA domain significantly reduced binding of the intact αA domain-containing integrin to their ligands [Bajt *et al.*, 1995; Kamata *et al.*, 1995b]. These observations made the β1 A domain an exciting target. Alternatively, the presence of regulatory site(s) within the α2β1 integrin distinct from the α subunit that leads to conformational changes and to allosteric inactivation of the whole integrin is also to be considered.

1.11 Aims

At the outset of this project, the aim was to generate soluble human α2β1 integrin at readily sufficient levels to conduct functional analyses to study the mechanisms that regulate α2β1 activation. A mammalian cell line was utilised to express truncated α2β1 lacking the transmembrane and cytoplasmic integrin segments; albeit targeting the production of recombinant integrin that retained the folding and functionality of the native molecule. The individual extracellular subunits of the α2β1 integrin were co-expressed each fused to the Fc region of IgG1 to aim heterodimerisation of the integrin subunits. The soluble α2β1-Fc integrin was characterised using anti-α2 and anti-β1 conformation sensitive monoclonal antibodies and collagen type I so as to confirm the parent integrin structure and function.

This work was undertaken to produce a system where the functional relative to the structural relationships of α2 and β1 integrin subunits could be studied using mutagenesis. A series of mutations were introduced into the critical A domains, mainly in and around the integrin-ligand active sites, to study their effect into α2β1-collagen interactions. Gain-of-function mutations, as previously described for other αA domains, were engineered to investigate allosteric up-regulation of the α2 A domain in the context of the holoreceptor. Other αA domain activation-sensitive and / or βA cation-dependent mutations, as modelled on the β3 structure, aimed to examine whether the αA domain ligand-binding affinity was regulated by the β1 A domain.

The collagen-binding properties of the recombinant integrins were examined in detailed biochemical investigations to study α2β1-collagen interactions at the molecular level. In particular, analysis of the divalent ion requirements for ligand recognition of the mutated receptors compared to the unmodified recombinant or native, whole α2β1 integrin helped to a better understanding of cation-mediated integrin activation. The data generated in this study in combination with data from similar studies in non-αA domain-containing integrins aimed to elucidate the mechanisms that regulate integrin activation.

Integrin α2β1 is abundantly expressed in various tissues suggesting an important biological role. Understanding the molecular mechanisms of α2β1-collagen binding is

important in devising ways to control receptor activation and function. Ultimately, dissecting the structural basis of ligand binding will allow rational drug design against $\alpha 2\beta 1$-mediated diseases such as thrombosis.

Chapter

2.0 Materials and Methods

2.1 Materials

All solutions were made using de-ionised or Milli-Q water (Millipore, Billerica, MA, USA). Oligonucleotides were purchased from MWG Biotech UK Ltd. (Milton Keynes, UK). Restriction and modification enzymes were purchased from Boehringer Mannheim Ltd (East Sussex, UK), Promega (Southampton, UK) or Roche Molecular Biochemicals (Lewes, East Sussex, UK). All enzymes were used according to the supplier's instructions with the supplied buffers unless otherwise stated. Cell culture reagents were purchased from Biowhittaker (Cambrex Bioscience Wokingham Ltd, Wokingham, UK), tissue culture vessels were obtained from Corning (Costar UK Ltd, High Wycombe, UK). All other reagents were purchased from Sigma (Poole, Dorset, UK) or BDH (Lutterworth, Leicestershire, UK) unless otherwise stated. Where necessary, solutions and equipment were sterilised by autoclaving (20 minutes at 121 °C, 15 psi). All kits were used according to the manufacturers' instructions unless otherwise stated.

2.1.1 Antibodies, purified proteins and integrin ligands

A number of monoclonal antibodies (mAb) raised against human integrin α2, α5 and β1 subunits were used in this study. Mouse anti-human integrin α2 mAb included: Gi9 (Beckman Coulter, High Wycombe, UK), 12F1 (BD Pharmingen, Oxford, UK), P1H5 (Serotec, Oxford, UK), JBS2 and 10A4 (lab stocks). Mouse anti-human integrin α2 A domain mAb JA202, JA212, JA215 and JA218 (Tuckwell *et al.*, 2000). Mouse anti-human integrin β1 mAb TS2/16 was a gift from Dr. A. Sonnenberg (Netherlands Cancer Institute, Amsterdam, The Netherlands). Mouse anti-human integrin β1 mAb 12G10 (Mould *et al.*, 1995c) 8E3 (Mould *et al.*, 1997), 4B4 was purchased from Coulter Immunology. Rat anti-human integrin α5 JBS5 (Serotec), mAb16 was a gift from K. Yamada (NIH, Bethesda, MD, USA). Goat anti-human γ1 Fc and peroxidase-conjugated anti-human Fc were purchased from Jackson Immunochemicals (Stratech Scientific Ltd., Bedfordshire, UK). Immunoglobulin G (IgG) monoclonal anti-mouse and peroxidase-conjugated secondary antibodies were purchased from Jackson Immunochemicals. ExtrAvidin-horse-radish peroxidase (HRP) was purchased from Sigma.

Human integrin α2β1 was purified from the human fibrosarcoma cell line HT1080 [Mould P.A., 2002, Current Protocols in Cell Biology], human integrin α5β1 was purified from human placenta [Mould P.A., 2002, Current Protocols in Cell Biology]. Acid soluble rat tail type I collagen was obtained from Sigma. The recombinant 50 kDa fragment of fibronectin containing of fibronectin type III repeats 6-10 – $FnIII_{6-10}$, was provided by Dr. P.A. Mould (University of Manchester).

2.1.2 Bacterial strains and plasmids

Human integrin α2 full-length cDNA in the pcDM8 vector and human α2 A domain cDNA in the pGEX-2T vector were generated as described in Tuckwell *et al.*, 1995. The full-length integrin α5 (residues 1-613) construct in pEE12.2hFc was generated as described in Coe *et al.*, 2001. The pEE12.2hFc is a derivative of pEE12, in which the vector *Sal*I site has been replaced by a *Not*I site, and had a *Sal*I-*Eco*RI genomic fragment of human IgG1 γ chain inserted [Takahashi *et al.*, 1982]. The extracellular domain of β1 (residues 1-708) in pV.16hFc was generated as described in Coe *et al.*, 2001. pV.16hFc is a derivative of pEE6 HCMV [Stephens & Cockett, 1989] in which the vector *Sal*I site has been removed and replaced by a *Not*I site. A second *Not*I site has been introduced at the 5' end of the HCMV promoter fragment. This vector also contains the human γ1 Fc as a *Sal*I - *Eco*RI genomic fragment. The C-terminally truncated β1 constructs in pV.16hFc were provided by S. Barton (University of Manchester). These consisted of a fragment of the human β1 cDNA, encoding amino acids 1-455, containing a series of single amino acid substitutions.

Competent *Escherichia coli* DH5a' strain: F^-ϕ80d*lac*ZΔMΔ(*lac*ZYA-*arg*F) U169 *deo*R *rec*A *end*A1 *hsd*R17 (rk^-, mk^+) *pho*A *sup*E44 λ^- *thi*-1 *gyr*A96 *rel*A1 was purchased from Invitrogen Ltd (Paisley, UK). Competent *E.coli* XL-1 Blue strain (*rec*A1 *end*A1 *gyr*A96 *thi*-1 *hsd*R17 *sup*E44 *rel*A1 *lac* F'[*pro*AB^+ $lacI^q$ *lac*ZΔM15 Tn1-(tet^r)]) was purchased from Stratagene Ltd (Cambridge, UK).

2.1.3 Mammalian cell lines

The Chinese Hamster Ovary L761h (CHO) cell line was a kind gift from P. Stephens (Celltech Group plc, Slough, UK). This is a CHO cell line variant with enhanced production of secreted protein [Cockett *et al.*, 1991].

2.1.4 Oligonucleotides

Synthetic oligonucleotides were purchased from MWG Biotech (Milton Keynes, UK). All sequences are quoted 5' to 3'.

2.1.4a Construction primers for cloning the α2 cDNA into pEE12.2hFc

- DT24 5' - CGC AAG CTT ATG GGG CCA GAA CGG ACA GG - 3'

sense primer to introduce a *Hind*III restriction site at 5' end of α2 cDNA

- DT23 5' - CGC GTC GAC TTC GGC TTT CTC ATC AGG TT - 3'

antisense primer to introduce a *Sal*I restriction site at 3' end of α2 cDNA

- DT 32 5' - CGC GTC GAC TAT TTG TCG GAC ATC TAG GAC

antisense primer to truncate the α2 cDNA sequence and introduce a *Sal*I restriction site

- DT03 5' - GCT GAT GTA GCT ATA GAA GCC TCA TTC ACA CCA GAA AAA - 3' sense primer to remove the internal *Hind*III restriction site
- DT02 5' - TTT TTC TGG TGT GAA TGA GGC TTC TAT AGC TAC ATC AGC - 3' antisense primer to remove the internal *Hind*III restriction site

2.1.4b Construction primers for engineering mutations into the α2 cDNA

- DT26 5' - ACA TTA GGA CAA GGT TTC AGC ATT GAA GGT - 3'

sense primer to introduce I332G

- DT27 5' - ACC TTC AAT GCT ACC TTG TTC TCC TAA TGT - 3'

antisense primer to introduce I332G

- DT28 5' - CAA ATT TTC AGC ATT GCA GGT ACT GTT CAA GGA - 3'

sense primer to introduce G336A

- DT29 5' - TCC TTG AAC AGT ACC TGC AAT GCT GAA AAT TTG - 3

antisense primer to introduce G336A

- DT30 5' - GGA GAA CAA GGT TTC AGC ATT GCA GGT ACT GTT - 3'

sense primer to introduce I332G and G336A

- DT31 5' - AAC AGT ACC TGC AAT GCT GAA ACC TTG TTC TCC - 3'

antisense primer to introduce I332G and G336A

- DT35 5' - ATA GAT GTT GTG GTT TGT GCT GAA TCA AAT AGT ATT TAT CCT - 3' sense primer to introduce D151A
- DT36 5' - ACA CAC AAC CAC AAC ATC TAT GAG GGA AGG GCA - 3' antisense primer to introduce D151A
- DT38 5' - CAA GGA GGA GAC AAC GCT CAG ATG GAA ATG TCA - 3' sense primer to introduce F345A
- DT39 5' - TGA CAT TTC CAT CTG AGC GTT GTC TCC TCC TTG - 3' antisense primer to introduce F345A

2.1.4c Construction primers for cloning the α2 A domain cDNA into pGEX-2T (Stop codons are shown underlined)

- DT08 5' - CGC GGA TCC TGC CCT TCC CTC ATA GAT GTT - 3' sense primer to introduce a *Bam*HI restriction site
- DT06 5' - GGG AAT TCT CAA ACA GTA CCT TCA ATG CTG - 3'
- DT22 5' - GGG AAT TCT CAA ACA GTA CCT TCA ATG CTG AAA CCT TGT TCT CCT AAT GTC –3' antisense primer to engineer I332G

2.1.4d Sequencing primers

- DT25-pEE12 5' - GCT GAC AGA CTA ACA GAC TGT TCC - 3'
- pGEX forward 5' - GGG CTG GCA AGC CAC GTT TGG TG - 3'
- pGEX reverse 5' - CG GGA GCT GCA TGT GTC AGA GG - 3'
- DT13, +133 5' - AGT GAA CGA TTT GGG TAT GCA GTG - 3'
- DT14, +643 5' - CAG TAT GCC AAT AAT CCA AGA GTT - 3'
- DT15, +1093 5' - GAA GGT ACT GTT CAA GGA GGA GAC - 3'
- DT16, +1513 5' - ATT ACA GAC GTG CTC TTG GTA GGT - 3'
- DT17, +1873 5' - TAT GGA GAT TTA AAT GGG GAT TCC - 3'
- DT18, +2293 5' - CCT GGC ACT AGC CCT GCC CTT GAA - 3'
- DT19, + 2713 5' - CAG GCG TCT CTC AGT TTC CAA GCC - 3'
- DT20, +3073 5' - CCA CTG AAA ATA GGA CAA ACA TCT - 3'

2.2 Methods

2.2.1 Bacterial cultures

2.2.1a Growth of bacterial cultures

Bacteria were grown as broth cultures in Luria -Bertani [LB; 1% (w/v) bacto-tryptone, 0.5% (w/v) yeast extract, 1% (w/v) NaCl pH 7.4] medium or on LB-agar [as LB but including 1.5% (w/v) bacto-agar] plates under aerobic conditions for 14-16 hours at 37 °C. Antibiotics were used in selective media. To select for vector transformed DH5α' and XL1-Blue *E.coli* strains were cultured in the presence of 50 μg/ml ampicillin. Isolated bacterial colonies were picked with a toothpick under aseptic techniques and patched out onto LB-agar plates, containing the appropriate antibiotics for storage at 4 °C.

2.2.1b Transformation of *E.coli*

Frozen competent *E.coli* cells were thawed on ice for approximately 5 minutes. 50-100 μl of the thawed *E.coli* competent cells were transferred into pre-chilled, sterile 17x 100 mm polypropylene culture tubes with immediate addition of the sample DNA and incubation for a minimum of 30 minutes on ice. Next, the cells were heat shocked at 42 °C for 45-50 seconds, followed by further incubation in ice for 2 minutes. 300 μl of LB medium at room temperature was added to each transformation reaction and the cells were incubated at 37 °C for 60 minutes in the absence of antibiotics in order to allow the antibiotic resistance genes to be expressed. Finally the transformation mix was spread into LB-agar plates containing appropriate antibiotics, left to dry and incubated overnight at 37 °C.

2.2.2 DNA manipulations

2.2.2a Plasmid DNA purification

10-20 μg plasmid DNA was isolated using a QIAprep Spin Miniprep kit (Qiagen, Surrey, UK) according to the manufacturer's instructions. After overnight growth in 5 ml LB broth, the bacteria were harvested by twice centrifuging 1.5 ml aliquots, in a single Eppendorf tube, for 2 minutes at 24,100 g at room temperature (RT). Briefly, the pellets were resuspended in RNase A containing buffer and lysed under alkaline conditions. Neutralisation of the lysis reaction was followed by the absorption of the plasmid DNA onto a silica-gel membrane in the presence of high salt concentration, allowing the DNA to bind. Elution and concentration of the plasmid DNA was achieved in low salt buffer – 50 μl TE (10 mM Tris-HCl, 1 mM EDTA). The DNA was stored at 4 °C for further use.

2.2.2b Polymerase chain reaction (PCR)

PCR reactions were carried out using one of two thermostable DNA polymerase enzymes. 2 µl cDNA or 5 µl template DNA was mixed with 15 pmol of each of the PCR primers, 1.5 µl 10 nM dNTPs, 1 unit Advantage cDNA polymerase (Clontech, Hampshire, UK)) or Expand High Fidelity DNA polymerase (Roche), 5 µl of the appropriate 10x PCR reaction buffer, in a total volume of 50 µl. PCR was performed in a automated DNA thermal cycler (GeneAmp PCR System 24000, Perkin Elmer, Chesire, UK) according the regime of: 40 cycles of 94 °C (1 minute) and 55 °C (1 minute) followed by 72 °C (1 minute per 1 kb of DNA to be amplified). PCR products were analysed by 1% agarose gel electrophoresis and the DNA was purified as described in section 2.2.2g.

2.2.2c Restriction digestions

Restriction endonucleases were routinely used in the analysis and construction of recombinant DNA. The amount of DNA used varied according to the nature of the experiment (analytical, preparative). The restriction endonucleases, supplied with the appropriate buffers, were obtained from Boehringer Mannheim or Roche and were used according to the instructions of the supplier. In general, digestion reactions were performed at 37 °C for 2 ½ hours.

2.2.2d Ligation reactions

Ligation reactions were carried out with 50 ng restriction digested vector DNA and approximately equimolar amount of DNA to be subcloned. The reactions were accomplished in a total volume of 10 µl also containing 2 µl T4 DNA Ligase (Promega, Southampton, UK) and the appropriate buffers (supplied with the enzyme) according to the manufacturer's instructions. The reactions were left to complete over 16 hours at 15°C.

2.2.2e DNA concentration determination

DNA concentration was estimated by measuring absorbance at 260 nm, assuming that 50 µg/ml of double stranded DNA has an absorbance value at 260 nm of 1.0. Purity of the plasmid DNA preparation was assessed by 1% agarose gel electrophoresis.

2.2.2f Agarose gel electrophoresis

The DNA samples were mixed with 10x loading buffer [50% (w/v) glycerol, 5 mM EDTA pH 7.5, 0.02% (w/v) bromophenol blue] before loading. DNA samples were separated in 1% (w/v) agarose gels prepared in 1x TAE buffer [2 M Tris-acetate, 0.05 M EDTA]. Electrophoresis was performed in a horizontal gel apparatus (Amersham Pharmacia Biotech, Sweden) using 60 ml gel and were run for approximately 1 ½ hours at 70 Volts or until the visible bromophenol blue dye had migrated to a desired position. HyperLadder I (BIOLINE, London, UK) was used as DNA molecular weight marker standard. Gels were stained with 10 μg/ml ethidium bromide for 10 minutes and then destained in several changes of water. Bands were visualised under short ultraviolet (u.v.) transilluminator (UVP white/ u.v. transilluminator). Gel photographs were captured with an image analysis system (Grab-IT 2.0, Win 32 Application).

2.2.2g DNA gel extraction

DNA bands that were destined to be excised from the gels were visualised under longer wavelength u.v. light to minimise DNA damage. Removal and isolation of DNA from agarose gels and enzymatic manipulation reactions was performed by the QIAquick Gel Extraction kit (Qiagen). Briefly, DNA was bound to silica matrix in the presence of high salt concentration. Impurities were removed by washing in a NaCl/Tris/EDTA/ethanol mixture, and then the DNA was recovered by eluting in TE or sterile deionized water.

2.2.3 DNA sequencing

2.2.3a Preparation of the sequencing reactions

DNA preparation was performed using the ABI PRISM® BigDye™ Terminator Cycle Sequencing Ready Reaction kit (PE Applied Biosystems, Chesire, UK) was used. For optimised results the protocols provided were modified as follows. For each reaction the following reagents were added to a separate 0.2 μL tube, in the above order: 200-500 ng double-stranded DNA, 4 μl 450 mM Tris-HCl pH 9.0 / 10 mM $MgCl_2$, 3.2 pmol of the provided primer, 4 μl Terminator Ready Reaction mix. Finally sterile deionised water was added to bring the reaction volume to 20 μl. The tubes were placed into a DNA thermal cycler (Perkin Elmer) according the regime of: 25 cycles of 96 °C (30 seconds) and 50 °C (15 seconds) followed by 60 °C (4 minutes). For removal of the unbound dye the DyeEx™ 2.0 Spin kit was used (Qiagen). DNA sequencing was carried out as a

service by the Faculty of Medicine and Human Sciences core facility, The University of Manchester.

2.2.4 Tissue culture and soluble integrin expression

2.2.4a Mammalian cell lines

CHO cells were maintained in Dulbecco's Modified Eagle's Medium (DMEM) without sodium pyruvate, with 4500 mg/l glucose, with pyridoxine supplemented with 10% (v/v) FCS and 2 mM L-glutamine and 1% (v/v) non-essential amino acids (NEAA). CHO cells were passaged at 1:20 every three/four days, according to their rate of growth. All cell lines were cultured in a defined medium at 37 °C in 5% (v/v) CO_2 in a humidified atmosphere. Penicillin and streptomycin were used in mammalian cell cultures at 100 μg/ml where required.

2.2.4b Transfection of CHO cells by Lipofectamine 2000 reagent

CHO L671h cells were transfected transiently using the Lipofectamine 2000 reagent (Invitrogen Ltd, Paisley, UK). Cells were passaged three days before transfection and transferred into 75 cm^2 so that they were 90-95% confluent on the day of transfection.

5 μg pEE12.2hα2-Fc DNA and 5 μg pV.16hβ1-Fc DNA was diluted into 1.9 ml OPTI-MEM dilution medium. 60 μl Lipofectamine 2000 was added to 1.9 ml OPTI-MEM medium in another tube and let to stand at room temperature for 5 minutes. Next, the DNA was mixed with the Lipofectamine 2000 reagent for 20 minutes at room temperature. While DNA-Lipofectamine reagent complexes were forming, the growth medium on the cells was replaced with 10 ml fresh growth medium without antibiotics. At the end of the incubation period the medium containing the complexes was added to each well containing cells, mixed gently and incubated at 37 °C at 5% CO_2 overnight. The next day the medium was replaced with 25 ml of fresh pre-warmed growth medium. Transfected CHO cells were assayed for expression of α2β1-Fc integrins 72 hours post transfection. The supernatant was harvested by centrifugation at 258 g for 5 mins and stored at 4 °C.

2.2.4c Purification of integrin-Fc proteins by Protein A affinity chromatography

200 μl Protein A-Sepharose Fast Flow beads (Amersham Pharmacia) was added to transfection medium and rotated for one hour at room temperature. Beads were placed in a

2 ml disposable column (Bio-Rad, Hemel Hemstead, Herts, UK) to form an affinity matrix, and were washed with at least five column volumes of PBS(-) ((Phosphate buffered saline without Mg^{2+} and Ca^{2+}, Biowhittaker). Bound protein was eluted using 10 mM NaOAc, pH 3.0 (into 1 M Tris-HCl pH 9.0 to neutralise).

2.2.5 Production of recombinant α2 A domain proteins

2.2.5a Bacterial expression of GST fusion proteins

Large scale preparations of E.coli strain DH5aF'carrying the pGEX-2T expression vectors were cultured as follows. Overnight cultures (100 ml) of stationary phase bacteria were used to inoculate 1 l of LB broth containing 50 μg/ml ampicillin. The cells were allowed to grow for approximately 2.5 hours at 37 °C or until optical density at 600 nm reach 0.6. GST-fusion protein expression was induced by addition of isopropyl-β-D-thiogalactopyranoside (IPTG) to a final concentration of 0.1 mM and the cultures were incubated for an additional 4 hours at 37 °C. Bacteria were then collected by centrifugation and resuspended in a minimal volume of 150 mM NaCl 25 mM Tris-HCl, pH 7.4 (TBS), before being frozen at –80 °C until further usage.

2.2.5b Purification of GST-fusion proteins by glutathione-agarose affinity chromatography

The bacterial pellets from induced *E.coli* cultures were thawed on ice and lysed by sonication in an ultrasonic processor (Sonics and Materials Incorporation, Dansbury, USA). Cell debris was removed by centrifugation at 35,000 g for 20 minutes. The bacterial lysate was applied to a 5 ml glutathione-agarose column (Sigma; prepared according to the manufacturer's instruction and equilibrated in TBS) and allowed to flow by gravity. The column was washed with 20 ml TBS buffer and the bound protein was eluted with 5 mM glutathione reduced form in TBS pH 8.0. In total, nine 1.5 ml eluate fractions were collected and each fraction was assayed for protein content by SDS-PAGE electrophoresis.

2.2.6 Protein analysis

2.2.6a Collagen I solid-phase binding assay

Purified integrins or recombinant α2 A domains were tested for ligand-binding activity using a solid-phase protein-protein assay. 50 μl transfectant culture supernatant (~1 μg/ml) or 50 μl of purified α2 A domain proteins diluted to 5-20 μg/ml in TBS / 5 mM Mn^{2+},

were immobilised into a high-binding half-area 96-well microtiter plate (Costar) overnight at 4 °C. Unbound protein was removed and 200 µl blocking buffer [5% (w/v) BSA in 1 mM $MnCl_2$ TBS, pH 7.4] was added per well to block non-specific binding sites. The plate was incubated for 2-3 hours at room temperature. The blocking solution was removed and the plate was washed three times with 200 µl/well binding buffer [0.1% (w/v) BSA, 2 mM $MnCl_2$, TBS pH 7.4]. 50 µl of biotinylated collagen I (0.5-1 µg/ml) in binding buffer was added per well, and incubated for 3 hours at room temperature to prevent collagen precipitation. The plate was washed three times with 200 µl binding buffer before the addition of 50 µl /well ExtrAvidin-peroxidase diluted 1:500 in binding buffer, and incubated for 30 minutes at room temperature. After washing the plate four times with binding buffer (200 µl /well), bound ligand was visualised with 50 µl ABTS developing solution [0.01% (v/v) H_2O_2, 2% (w/v) 2,2'-azino-bis (3-ethylbenzthiazoline 6-sulphonic acid) in 0.1 M NaOAc, 0.05 M NaH_2PO_4, pH 5.0]. The colour was allowed to develop until a mid-green coloration was attained. The absorbance was measured at 405 nm using a multiscan OPSYS MR Dunex plate reader (Dynatech). The results were the average of three replicates for each sample.

2.2.6a.i Biotinylation of protein ligands

Collagen I and 50K were covalently labelled with biotin to facilitate detection in ligand-binding assays. Proteins were diluted in TBS to 1 mg/ml and dry EZ-Link™ Sulfo-NHS-LC-biotin (Pierce, Chester, UK) was added to give a ratio of 1:1 (w/w) protein: biotin. The mixture was incubated for 1 hour at 4 °C for collagen I and at room temperature for 50K. Next, the mixture of biotin-labelled protein and biotin was dialysed extensively against TBS to remove the unincorporated biotin.

2.2.6b Fc-capture ELISA assay

In these assays the Fc partner was used to recover the recombinant proteins from cell culture supernatants and test for correct folding and function of the soluble α2β1-Fc integrins. Wells of 96-well plates (half-volume area, Costar) were coated with 50 µl goat anti-human γ1 Fc antibody diluted to 2.6 µg/ml in PBS+, overnight at 4 °C. Next, the wells were incubated with 200 µl blocking buffer for 1 hour at room temperature. The blocking buffer was removed and the wells were washed three times with 200 µl wash

buffer [0.1% (w/v) BSA, 1 mM $MnCl_2$, 150 mM NaCl, 25 mM Tris-HCl, pH 7.4]. 50 µl of culture supernatant was added to each well and incubated for 1 hour at room temperature. The wells were washed three times with 200 µl wash buffer before addition of 50 µl 10 µg/ml anti- human integrin mAb or 1 µg/ml biotinylated collagen I and incubation for 3 hours at room temperature. Detection was performed by the addition of 50 µl of the appropriate peroxidase-conjugated secondary antibody (5-10 µg/ml) or ExtrAvidin-peroxidase diluted 1:500 in blocking buffer. The plate was washed four times with wash buffer (200 µl /well), before developing with 50 µl /well ABTS developing solution. The absorbance was then measured at 405 nm using the OPSYS MR Dunex plate reader. The results were the average of at least three replicates for each sample, per experiment.

2.2.6c Divalent cation titrations in binding assays

In the solid-phase binding assays examining the effect of divalent cations on collagen I binding the buffers used following the blocking step were treated with Chelex beads (Bio-Rad) to remove any small contaminating amounts of endogenous Ca^{2+} and Mg^{2+} ions.

2.2.6d ELISA assay

The recombinant α2 A domain proteins were assayed for correct folding by detection of human anti-integrin α2 A domain mAbs epitopes. 50 µl of purified α2 A domain fusion protein at 10 µg/ml in PBS(+) [as PBS(-) plus 0.5 mM Mg^{2+} and 1mM Ca^{2+}, Biowhittaker], was coated into a 96-well microtiter plate (half-volume area, Costar) for 2 hours at room temperature or overnight at 4 °C. The coating solution was removed and replaced with 200 µl blocking buffer, and the plate was incubated for 2 hours at room temperature. The blocking solution was removed and the wells were washed three times with 200 µl wash buffer. 50 µl pre-diluted antibody at 10 µg/ml in binding buffer were then added to the wells and incubated for a further 2 hours at room temperature. The wells were washed three times with 200 µl wash buffer, before the addition of 50 µl the appropriate secondary antibody diluted 1:1000 in binding buffer. The plate was incubated for 30 minutes at room temperature. After washing four times with binding buffer (200 µl /well), bound ligand was visualised with 50 µl ABTS developing solution. The absorbance was measured at 405 nm using the OPSYS MR Dunex plate reader.

2.2.6e SDS-Polyacrylamide gel electrophoresis (PAGE)

Protein samples were prepared by addition of 1/5 volume of SDS-PAGE loading buffer [200 mM Tris-HCl, pH 6.8, 7% (w/v) SDS, 30% (v/v) glycerol, 0.02% (w/v) bromophenol blue] before heating the sample up to 90°C for 4 min. For reduced samples 10% (v/v) β-mercaptoethanol was included in the loading buffer. Samples were then run on a NuPAGE™ 4-12% Bis-Tris pre-prepared gel (Novex, San Diego, U.S.A.) in 1x MES [50 mM 2-N-morpholino ethane sulphonic acid, 50 mM Tris Base, 3.46 mM SDS, 1.025 mM EDTA] at 150 V (PowerPac 300; Bio-Rad) for approximately 40 minutes. Molecular weights were determined by running samples against the Pre-stained, Broad Range Precision Protein™ Standard (Bio-Rad). Gels were removed from the plastic plates and stained for 30 mins in Coomassie Blue stain [0.025% (w/v) Coomassie Brilliant Blue, 25% (v/v) propan-2-ol, 10% (v/v) acetic acid]. Next, the gels were de-stained in 10% acetic acid for approximately 1 hour, transferred to 3 mm paper and dried under vacuum at 80 °C for 1 hour.

2.2.6f Western blotting

After resolution by SDS-PAGE, proteins were transferred to nitrocellulose membrane (Schleicher and Schuell Inc., Keene, NH, USA) at a constant voltage of 30V for 90 minutes using the NuPAGE western blotting system (Invitrogen Ltd). Non-specific binding sites on the membranes were blocked with 3% milk in TBS-Tween, for ~60 minutes at room temperature. Anti-α2 A domain JA212 mAb diluted in blocking solution was utilised at 10 μg/ml. The primary antibody was added for 2 hour at room temperature or 16 hours at 4 °C, and the membrane washed 6x 5minutes with TBS-Tween. Secondary antibody conjugated to HRP (0.5 μg/ml) was added for 45 minutes at room temperature (in blocking solution), and the membrane washed as above. Proteins were visualised using enhanced chemiluminescence (Western lightning Reagent, Perbio Sciences, Cheshire, UK), exposure to photographic film, and processing by an automatic film processor (Kodak, Rochester, NY, USA).

2.2.6g Protein concentration assay

The BCA protein assay kit (Pierce) was used to determine α2 A domain protein concentration, according to the manufacturer's instructions.

Chapter

3.0 Expression and purification of recombinant soluble α2β1-Fc integrins for functional studies

To study the biochemical and structural mechanisms of intramolecular signal propagation between the α2 A domain and the β1 A domain in regulating the collagen I binding, a soluble recombinant α2β1 integrin was produced. In general, the expression of soluble integrins has generated sufficient amounts of the desired protein to allow *in vitro* studies. In this way, the problems of purifying these complex membrane receptors have been avoided. The expression systems that have been described in the literature have adopted a similar cloning strategy in which the integrin transmembrane and cytoplasmic domains have been excised from the recombinant integrin constructs. In addition, the successful production of functional integrins has required the addition of a tag to drive dimer formation. The incorporation of complementary C-terminal tags in the α, β subunits has almost invariably facilitated the dimerisation of the two integrin subunits, and this has been shown to be required for correct integrin folding and function [Stephens *et al.*, 2000]. In particular, the Fos and Jun dimerisation domains have been utilised to produce functional soluble α3β1 [Eble *et al.*, 1998] and αVβ5 [Mathias *et al.*, 1998]. In a similar approach, the Fc portion of the human immunoglobulin (Ig) G γ1 chain has been utilised to keep the α and β subunits together, resulting in the production of functional soluble integrins including α4β1 [Stephens *et al.*, 2000], α5β1 [Coe *et al.*, 2001], and α4β7 [M. Travis, Ph.D. 2004].

In this chapter I describe the construction, expression and characterisation of a soluble α2β1 integrin heterodimer in which the extracellular domains of the α and β subunits were linked covalently to separate Fc domains of the human γ1 IgG. Firstly, DNA coding for the entire ectodomain of integrin α2 was amplified by PCR and fused in-frame to the hinge and Fc regions of the human IgG γ1 chain. A similar construct expressing the entire extracellular domain of integrin β1 cloned upstream of the human γ1 Fc domain has been previously described [Coe *et al.*, 2001]. Both expression plasmids were co-transfected into a mammalian cell line, and the culture supernatants were examined for soluble wild-type (wt) full-length (FL) α2β1-Fc expression using an Fc-capture ELISA assay.

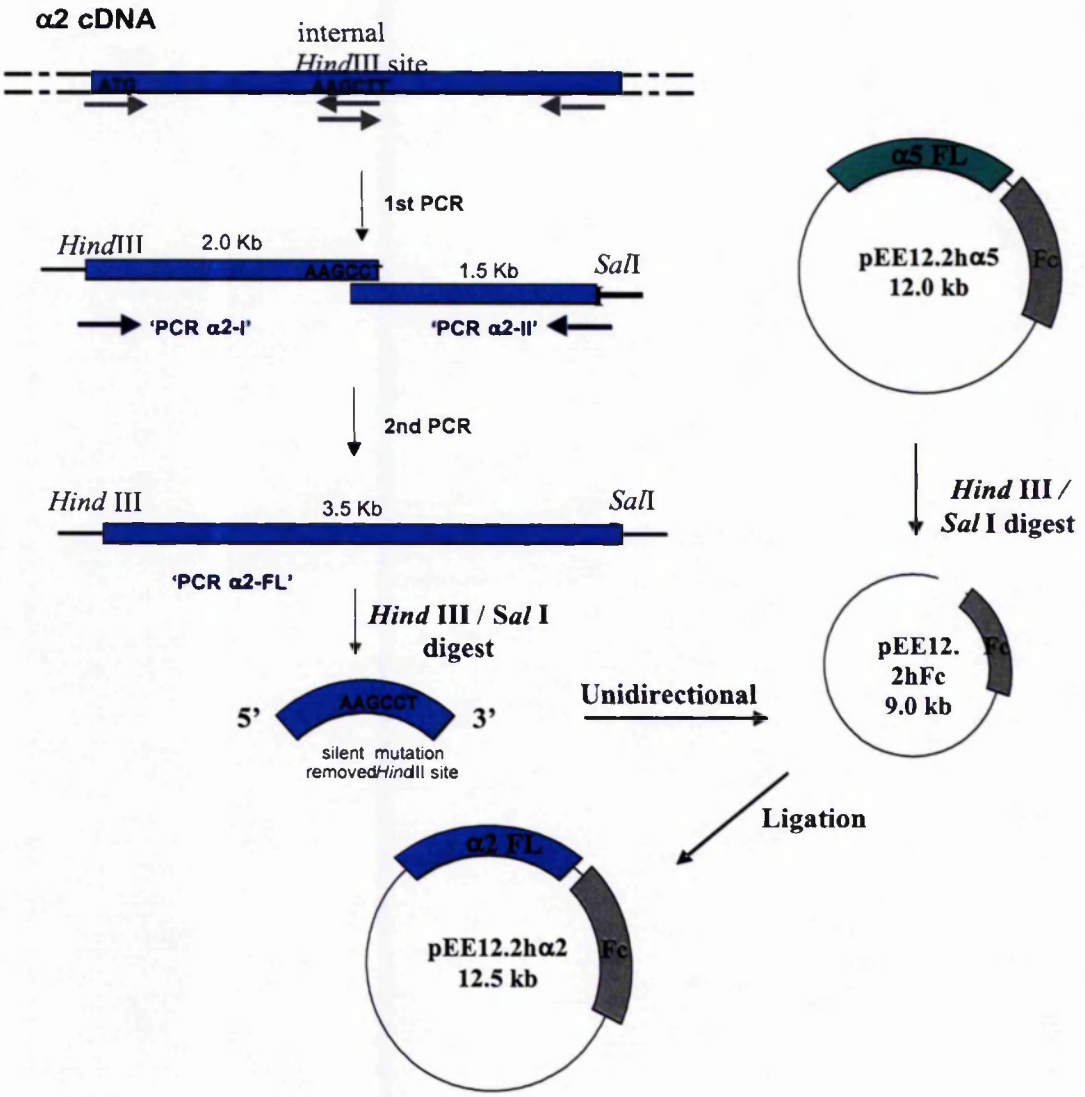

Figure 3.1. Diagrammatic illustration of the construction of the pEE12.2hα2 integrin mammalian expression vector. The DNA coding for the α2 integrin extracellular subunit from residue 1 to residue 1129 was amplified in a two-step PCR reaction. The PCR-generated fragments were designed to introduce a *Hind*III and a *Sal*I restriction site at the 5' and the 3' ends of the final full-length (FL) α2 PCR fragment respectively. This allowed for ligation of the *Hind*II / *Sal*I digested α2-FL fragment into enzyme pre-treated pEE12.2hFc vector, upstream and in-frame with the cDNA of IgG1 Fc domain.

To test if the recombinant integrin retained the native α2β1 fold, anti-human α2β1 integrin monoclonal antibodies were examined for their ability to bind to the recombinant protein in Fc-capture sandwich ELISA assays. Finally, the functional properties of the soluble Fc-captured α2β1 were examined in collagen I binding solid-phase assays.

The N-terminal head domains of integrins have been shown to form the ligand-binding pocket [Xiong *et al.*, 2000; 2001, Xiao *et al.*, 2004], whereas the C-terminal extracellular segments contain activation-regulatory domains important for bi-directional signal transduction in cellular context [Kamata *et al.*, 2005]. Removal of the C-terminal extracellular integrin domains should produce a minimised integrin without affecting the ligand-binding specificity, in a cell-free system. If successful, an engineered C-terminal truncated α2 subunit co-expressed with a truncated β1 subunit, described by Coe *et al.* (2001), would yield the first preparation of a truncated variant of a recombinant α2β1 integrin. A truncated soluble α5β1-Fc integrin has been previously described and studied in integrin-ligand binding studies [Coe *et al.*, 2001]. The truncated α5β1 integrin had a low constitutive ligand-binding activity compared to that of full-length α5β1 integrin when captured onto Fc-coated ELISA plates. Moreover, mutations in the β1 A domain that favoured the active conformation of α5β1 were exposed [Mould *et al.*, 2003a]. In this scenario, the effects of activating mutations on the ligand-binding activity of α2β1 could be explored. In addition, the truncated β1 subunit has been engineered to incorporate a number of inactivating mutations in the cation-binding sites [Mould *et al.*, 2002, 2003b]. Therefore, truncated wild-type and mutated integrin variants would facilitate the studies of putative control regions of the α2 subunit - β1 subunit interaction(s). The results of the analyses of soluble integrin-Fc variants in solid-phase assays are presented in this chapter.

3.1 Production of soluble full-length α2β1-Fc integrin

3.1.1 Cloning of pEE12.2hα2^{E1129} mammalian expression vector

A 3.5 kb DNA fragment encoding the entire extracellular domain of human integrin α2 was amplified by two-step PCR using human integrin α2 cDNA as a template [Tuckwell *et al.*, 1995]. A two-step procedure was employed to remove an internal *Hind*III site in the integrin α2 subunit by introducing a silent mutation at position 1987 bp with internal primers in the first round of PCR. Two separate PCR fragments of approximately 2 kb and

1.5 kb were generated as shown in Figure 3.1. Primers were designed to include a *Hind*III restriction site at the 5'end of the 2 kb DNA fragment and a *Sal*I restriction site at the 3'end of the 1.5kb DNA fragment. The two products were used in a second round of PCR to amplify the full-length extracellular subunit of integrin α2 to amino acid (a.a.) Glu1129. Agarose gel electrophoresis demonstrated the successful generation of the final PCR product of 3.5 kb. DNA was excised from the agarose gel and purified. The purified DNA was digested with *Hind*III and *Sal*I, and as a single band of 3.5 kb was produced, this confirmed the removal of the internal *Hind*III restriction site (Figure 3.2). The *Hind*III - *Sal*I fragment permitted the directional in-frame cloning into the pre-treated expression vector pEE12.2hFc.

The pEE12.2hFc vector backbone was isolated from the pEE12.2hα5 construct (a gift from Dr. A. Coe, University of Manchester). Briefly, the α5 subunit was cut out with *Hind*III and *Sal*I restriction endonucleases and the *Hind*III – *Sal*I digested pEE12.2hFc vector was gel-purified to ensure separation of the vector. The purified product was run on an analytical agarose gel to check that the bands were of the correct sizes and for estimation of the amount of DNA present (Figure 3.2). Then, the *Hind*III – *Sal*I α2 fragment was ligated to the digested pEE12.2hFc vector. The product of the ligation mixture was transformed into *E. coli* XL1-Blue competent cells. Transformed *E. coli* cells were selected on LB agar plates containing ampicillin. More than 100 colonies grew on the experimental plates, whereas no colonies grew on the negative control plates, indicating that a high proportion of the transformants contained the insert. DNA was prepared from overnight cultures of eight colonies and restriction digestion with *Hind*III and *Sal*I confirmed clones contained the 3.5 kb insert. Two positive integrin clones were fully sequenced using the Big Dye™ dideoxy terminator kit and an ABI Prism DNA sequencer to verify that no mutations had been inserted during the PCR process (data not shown).

Comparisons with the published sequence [Takada & Hemler, 1989] revealed that the two clones differed from the published sequence at several positions. The two clones contained the same mutations and it was concluded that the mutations were introduced in the sequence at the initial stages of PCR amplification. As none of the sequenced clones matched the published sequence, the two-step PCR was repeated using High Fidelity polymerase. High Fidelity polymerase is a Taq polymerase that has a proof reading

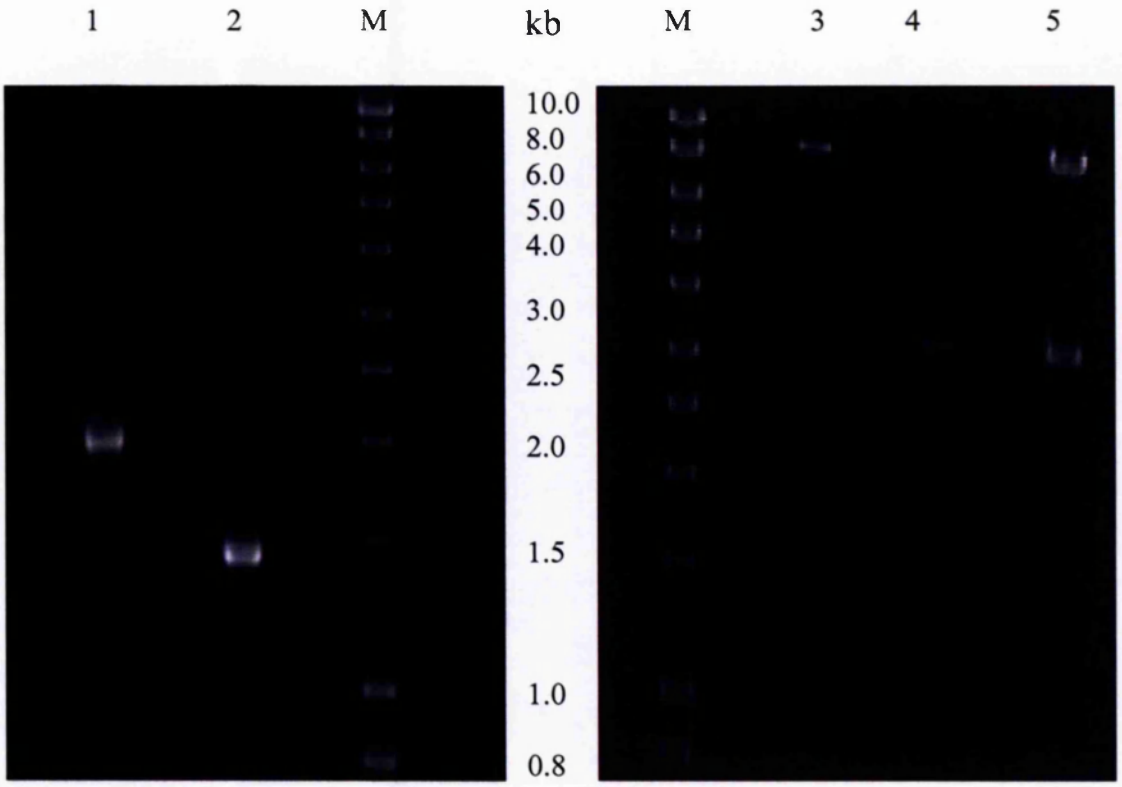

Lane	Contents – *Hind*III / *Sal*I digested	Expected Sizes (kb)
1	PCR α2-I – none	2.0
2	PCR α2-II – none	1.5
3	pEE12.2hFc	9.0
4	PCR α2-FL	3.5
5	pEE12.2hα2	9.0, 3.5
M	HyperLadder I	0.2 - 10.0

Figure 3.2. Cloning of the integrin α2 extracellular domain into pEE12.2hFc expression vector. PCR-generated DNA, α2-I (lane 1) and α2-II (lane 2) fragments, were used to amplify a single DNA fragment encoding the extracellular α2 domain (a.a. 1-1129) (PCR α2-FL). Following *Hind*III / *Sal*I restriction digest of the pEE12.2hFc expression vector (lane3) and the PCR α2-FL fragment (lane 4), the two pieces were ligated to produce pEE12.2α2. *Hind*III / *Sal*I restriction digest of a pEE12.2α2 clone #5 is shown in lane 5. See table above for description of fragments' sizes.

activity. The final PCR product was purified, *Hind*III – *Sal*I digested and ligated into pre-treated pEE12.2hFc as described above. Following transformation of E. *coli* XL1-Blue competent cells, plasmid DNA purification and control restriction digests of 10 transformants, it was confirmed that all clones carried the correct size insert. Due to limitations on the number of sequencing primers required to fully sequence the clones, only three clones, picked at random, were sequenced. Sequencing of all clones showed single nucleotide substitutions in the codons encoding Gly49 and Leu202 that resulted in silent mutations. Thus, there were no amino acid changes in the α2 protein sequence. The construct was designated pEE12.2hα2 and upon expression would be expected to produce the extracellular domain of the human integrin α2 coding region up to amino acid E1129 fused to the hinge and Fc domain of IgG γ1 chain.

3.1.2 Expression and analysis of soluble full-length α2β1-Fc integrin

In this study, the DNA encoding the extracellular domain of integrin α2 was fused upstream of the Fc region of human IgG γ1 in the pEE12.2hFc plasmid. Variants of the β1 extracellular domain have previously been cloned as similar Fc-fusion proteins in the pV.16hFc vector [Coe *et al.*, 2001]. The pEE12.2hFc and pV.16hFc vectors have been used in this laboratory to successfully produce soluble α5β1 integrin [Coe *et al.*, 2001; Mould *et al.*, 2002] as well as recombinant α4β7 integrin [M. Travis, Ph.D. thesis 2004, University of Manchester]. The above vectors have been designed to produce a fusion protein consisting of the integrin subunit followed by the human IgG γ1 Fc domain. To increase the likelihood of heterodimerisation of the Fc-chimeras, the CH3 domain of the Fc coding regions of pEE12.2hFc and pV.16hFc have been engineered [Ridgway *et al.*, 1996]. Briefly, residue 407 in the Fc of pEE12.2hFc has been changed from a tyrosine to a smaller threonine residue creating a 'hole'. Similarly, in the Fc of pV.16hFc, a threonine at position 366 has been replaced by a bigger amino acid, a tyrosine, creating a 'knob'. The above amino acid substitutions aimed to favour the formation of heterodimers.

To generate soluble wt FL α2β1-Fc integrin, the $\alpha2^{E1129}$ subunit expression vector was transiently co-transfected with the $\beta1^{D708}$ subunit expression vector into mammalian cells. The recombinant fusion protein $\alpha2^{E1129}\beta1^{D708}$ -Fc will be referred to as FL α2β1-Fc. A schematic representation of the domain structure of the wt FL α2β1-Fc is shown in Figure 3.3.

a)

```
      1          11         21         31         41         51         61
    1 MGPERTGAAP LPLLLVLALS QGILNCCLAY NVGLPEAKIF SGPSSEQFGY AVQQFINPKG  NWLLVGSPWS   70
   71 GFPENRMGDV YKCPVDLSTA TCEKLNLQTS TSIPNVTEMK TNMSLGLILT RNMGTGGFLT  CGPLWAQQCG  140
  141 NQYYTTGVCS QISPDFQLSA SFSPATQPCP SLIDVVVVCD ESNSIYPWDA VKNFLEKFVQ  GLDIGPTKTQ  210
  211 VGLIQYANNP RVVFNLNTYK TKEEMIVATS QTSQYGGDLT NTFGAIQYAR KYAYSAASGG  RRSATKVMVV  280
  281 VTDGESHDGS MLKAVIDQCN HDNILRFGIA VLGYLNRNAL DTKNLIKEIK ASIPTDRY   FFNVSDEAAL  350
  351 LEKAGTLGEQ IFSIEGTVQG GDNFQMEMSQ VGFSADYSSQ NDILMLGAVG AFGWSGTIVQ  KTSHGHLIFP  420
  421 KQAFDQILQD RNHSSYLGYS VAAISTGEST HFVAGAPRAN YTGQIVLYSV NENGNITVIQ  AHRGDQIGSY  490
  491 FGSVLCSVDV DKDTITDVLL VGAPMYMSDL KKEEGRVYLF TIKKGILGQH QFLEGPEGIE  NTRFGSAIAA  560
  561 LSDINMDGFN DVIVGSPLEN QNSGAVYIYN GHQGTIRTKY SQKILGSDGA FRSHLQYFGR  SLDGYGDLNG  630
  631 DSITDVSIGA FGQVVQLWSQ SIADVAIEAS FTPEKITLVN KNAQIILKLC FSAKFRPTKQ  NNQVAIVYNI  700
  701 TLDADGFSSR VTSRGLFKEN NERCLQKNMV VNQAQSCPEH IIYIQEPSDV VNSLDLRVDI  SLENPGTSPA  770
  771 LEAYSETAKV FSIPFHKDCG EDGLCISDLV LDVRQIPAAQ EQPFIVSNQN KRLTFSVTLK  NKRESAYNTG  840
  841 IVVDFSENLF FASFSLPVDG TEVTCQVAAS QKSVACDVGY PALKREQQVT FTINFDFNLQ  NLQNQASLSF  910
  911 QALSESQEEN KADNLVNLKI PLLYDAEIHL TRSTNINFYE ISSDGNVPSI VHSFEDVGPK  FIFSLKVTTG  980
  981 SVPVSMATVI IHIPQYTKEK NPLMYLTGVQ TDKAGDISCN ADINPLKIGQ TSSSVSFKSE  NFRHTKELNC 1050
 1051 RTASCSNVTC WLKDVHMKGE YFVNVTTRIW NGTFASSTFQ TVQLTAAAEI NTYNPEIYVI  EDNTVTIPLM 1120
 1121 IMKPDEKAEV PTGVIIGSII AGILLLLALV AILWKLGFFK RKYEKMTKNP DEIDETTELS  S        1181
```

b)

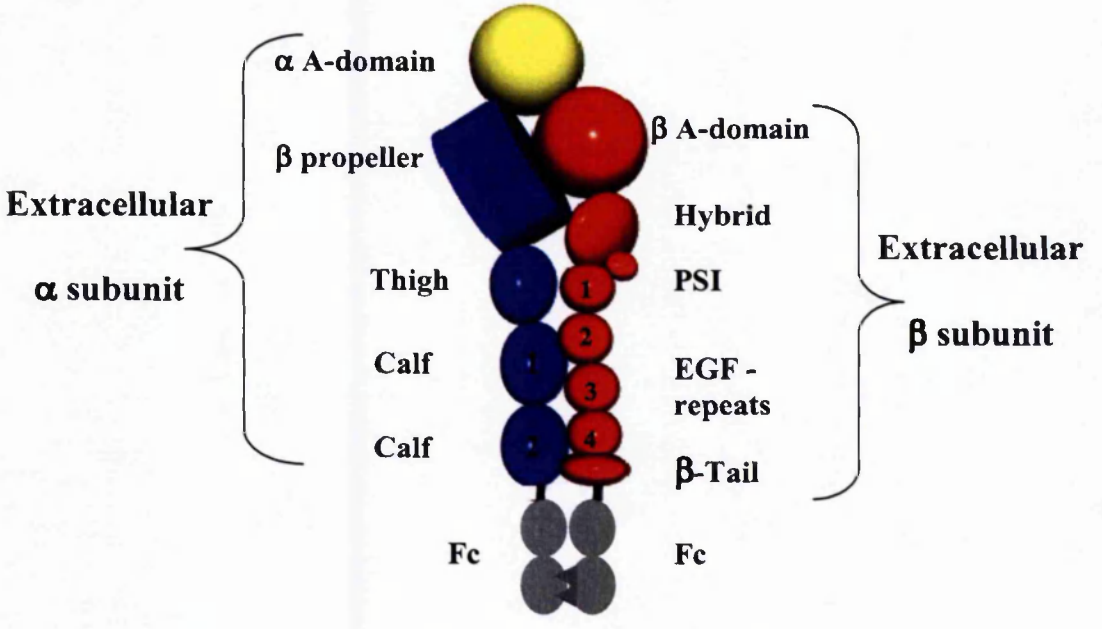

c)

	α2 whole	α2 Extracellular	FL α2-Fc soluble	β1 whole	β1 Extracellular	FL β1-Fc soluble	Fc
kDa	165	121	147	130	114	140	26

Figure 3.3. The amino acid sequence of the human α2 integrin extracellular subunit. a)DNA encoding the ectodomain of α2 subunit (residues 1-1129) was cloned in the pEE12.2hFc vector. The initiation methionine is assigned number 1 in the protein sequence, followed by a 29 a.a. long signal polypeptide, shown in grey. The α2 A domain is highlighted in yellow. Residues shown in green, Gly49 and Leu202, contained silent nucleotide base substitutions. Highlighted amino acids in cyan have been mutagenised to alanines. Amino acid E1129 is highlighted in blue. b) Schematic representation of the structure of the full-length α2β1-Fc integrin. Co-transfection of the $\alpha2^{E1129}$ subunit in pEE12.2hFc and the $\beta1^{D708}$ subunit in pV.16hFc into CHO cells should produce a soluble full-length α2β1-Fc integrin. The extracellular α2 subunit is fused to the Fc 'hole domain' (grey ovals), whereas the extracellular β1 subunit is fused to the Fc 'knob domain' (grey ovals with triangles) to aid α2β1 heterodimerisation. c) Expected sizes of integrin α2β1 subunits- calculated in Prosite.

To examine the expression of wt FL α2β1-Fc, small-scale transfections were carried out in a 6-well plate format. To examine variability between clones, three clones of pEE12.2hα2^{E1129} were used in the initial investigations. Briefly, 2μg DNA of each of the three plasmids expressing the α2 subunit were transfected simultaneously with 2μg DNA of the β1-expressing construct pV.16hβ1^{D708} into Chinese Hamster Ovary L761h (CHO) cells using the Lipofectamine 2000 method, similarly to the method described in section 2.2.4b. CHO L761h cells have been optimised for high protein secretion [Cockett *et al.*, 1991]. This mammalian cell line has been successfully utilised in the lab for the expression of soluble α5β1-Fc integrin. Therefore, CHO cells co-transfected with pEE12.2hα5 and pV.16hβ1^{D708}, known to express wt FL α5β1-Fc, were included in initial experiments as positive controls. Mock transfections with no DNA were carried out as negative controls.

The culture supernatants were harvested 72 hours post-transfection. In general, culture medium was removed from each transfectant well, centrifuged to remove cell debris and the supernatant was stored at 4 °C until further testing. Analysis of integrin-Fc expression secreted in the media was undertaken in Fc-capture assays. Briefly, an anti-human γ1 Fc antibody is immobilised onto a 96-well ELISA microtiter plate. The wells are incubated with a BSA blocking solution to reduce non-specific ligand binding. Next, Fc-containing proteins are captured on the plate by the addition of neat transfection culture supernatant. Detection of the Fc tag is accomplished with a peroxidase-conjugated anti-Fc antibody and ABTS colorimetric development. Alternatively, the ability of the captured proteins to bind to human anti-integrin monoclonal antibodies (mAbs) or integrin ligands can be tested.

Sequenced clones pEE12.2hα2#3, pEE12.2hα2#5 and pEE12.2hα2#7 were examined for wt FL α2β1-Fc integrin production in Fc-capture ELISA assays. Figure 3.4 illustrates the results of the Fc-capture analyses of the different clones of pEE12.2hα2^{E1129} co-expressed with the pV.16hβ1^{D708} construct in CHO cells. A polyclonal anti-Fc antibody detected the presence of integrin-Fc proteins in all but the negative control (Figure 3.4a). Absorbance readings for all clones were comparable to data obtained with the control α5β1-Fc integrin, demonstrating good expression levels for all recombinant Fc-fusion proteins. Clone #7 gave the highest Fc expression levels of all transfectants.

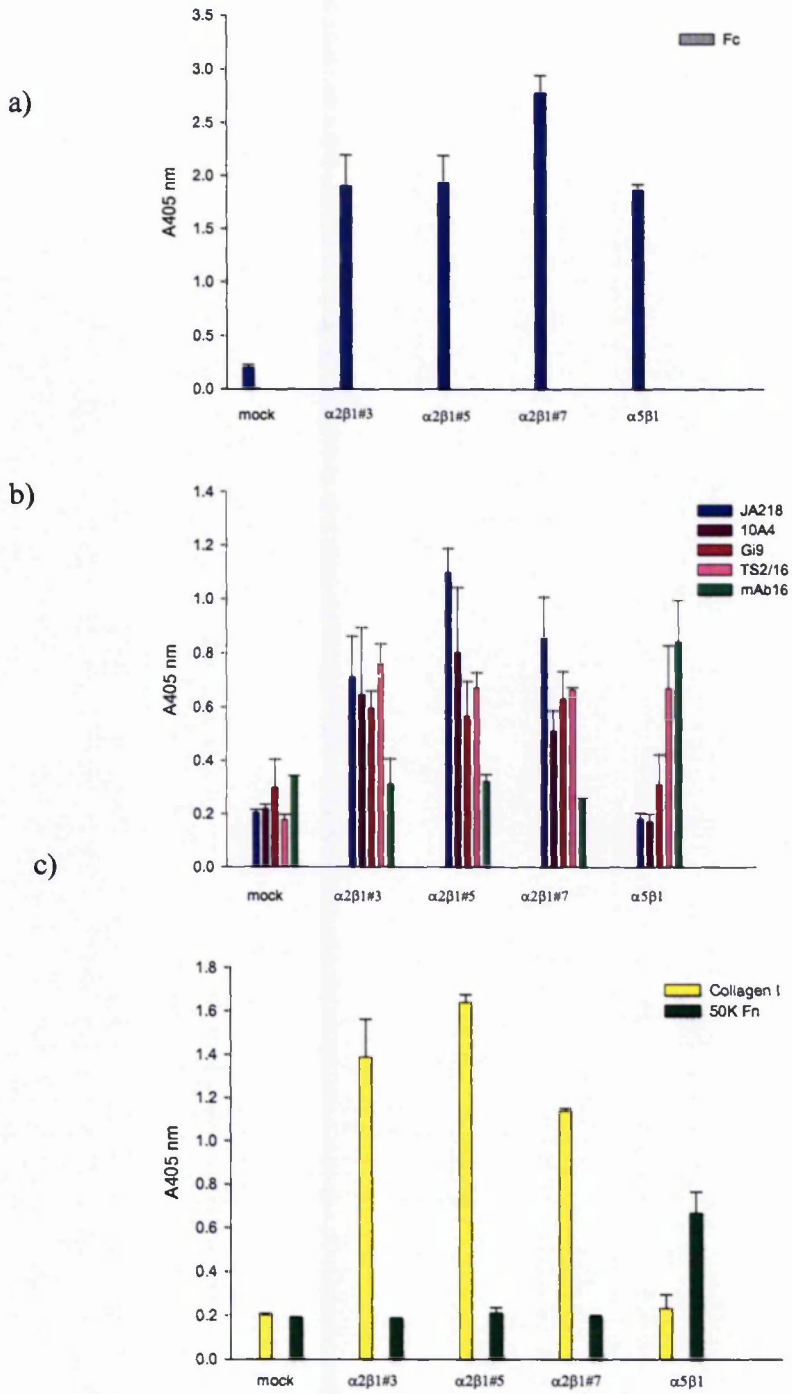

Figure 3.4. Antibody and ligand binding to soluble FL Fc-tagged integrins. Culture supernatants from CHO cells transfected with clones of α2[E1129]β1[D708] integrin-Fc DNA, α5[E951]β1[D708]-Fc and without DNA (mock) were analysed in Fc-capture assays, performed in the presence of 1 mM Mn^{2+}. Binding was detected with a) 1μg/ml anti-Fc antibody, b) 10 μg/ml integrin mAbs: anti-α2 (JA218, 10A4, Gi9), anti-α5 (mAb16) or anti-β1 (TS2/16) mAbs and c) with biotinylated ligand: collagen I (1 μg/ml) or 50K fragment of fibronectin (Fn) (0.1 μg/ml). Bound mAbs were detected with the appropriate HRP-conjugated secondary antibodies (1 μg/ml), whereas bound biotinylated ligands were detected using ExtrAvidin-peroxidase. Absorbance (405 nm) values and error bars represent the average and standard deviation of three readings.

Using a number of human anti-α2 and anti-β1 specific mAbs the correct folding of the recombinant α2β1-Fc integrin was also examined (Figure 3.4b). The α2β1-Fc integrins produced by clones #3, #5 and #7 were detected with a panel of anti-α2 mAbs directed against the α2 A domain, namely JA218, Gi9 and 10A4. The mAb TS2/16 was utilised as a specific probe for the β1 integrin subunit. Although the anti-α2 human integrin mAb Gi9 showed high background binding to the mock control, all anti-α2 antibodies bound to all three α2β1-Fc proteins at levels higher than the mock. The anti-β1 mAb antibody also recognised all three α2β1-Fc recombinant proteins. In addition, none of the anti-α2 mAbs recognised the control α5β1-Fc integrin, whereas the anti-β1 TS2/16 mAb bound to the α5β1-Fc integrin, as expected. The anti-α5 monoclonal antibody, mAb16, bound to α5β1-Fc but did not bind to any of the α2β1-Fc proteins.

The ligand-binding activity of the soluble wt FL α2β1-Fc integrin to biotinylated collagen I was also investigated in Fc-capture solid-phase assays (Figure 3.4c). All three wt FL α2β1-Fc recombinant integrins retained the ligand-binding ability and were able to bind collagen I. Clone #5 expressing α2β1-Fc bound collagen I at high levels. No collagen I binding was detected in the mock control. Recombinant α5β1-Fc integrin also did not bind biotinylated collagen I, but was able to bind to biotinylated 50K fragment of fibronectin, an α5β1 integrin ligand.

In summary, all three of the recombinant α2β1-Fc protein products of pEE12.2hα2#3, pEE12.2hα2#5 and pEE12.2hα2#7 when co-expressed with pV.16hβ1^{D708}, formed soluble α2β1-Fc proteins that were recognised by the anti-α2 and anti-β1 integrin antibodies to a similar extent. Moreover, all three of the α2β1-Fc proteins bound collagen I and were therefore functional. Although pEE12.2hα2 clone #7 expressed high levels α2β1-Fc, this Fc-fusion protein had low collagen I binding activity. Therefore, based on the ligand binding data, pEE12.2hα2 clone #5 was selected as the best expressing construct for subsequent experiments.

To characterise the recombinant protein further, the binding of a larger panel of anti-α2 and anti-β1 integrin antibodies to soluble wt FL α2β1-Fc integrin was examined. In the experiment described in Figure 3.5, all of the anti-α2 and anti-β1 mAbs recognised the

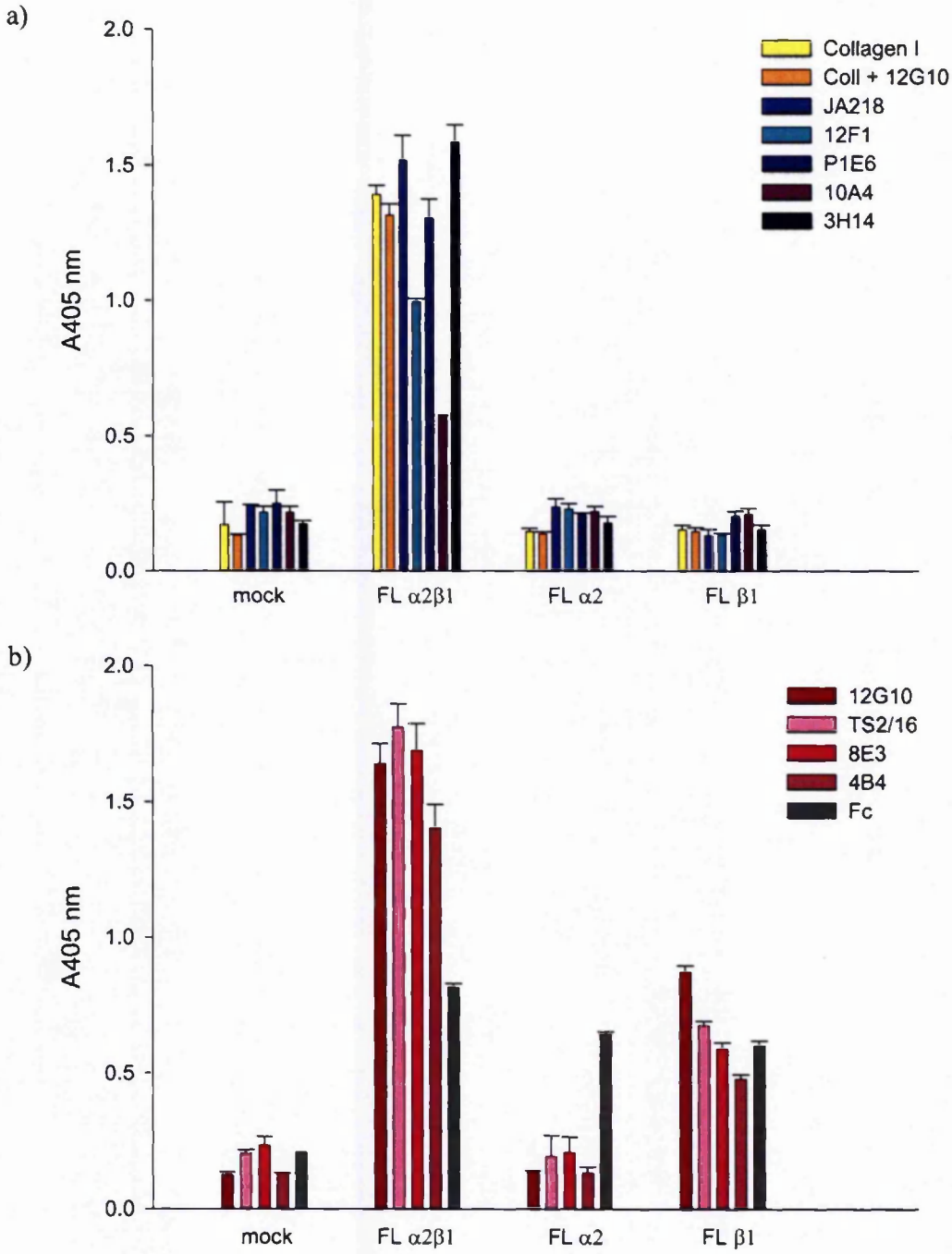

Figure 3.5. Antibody and ligand binding to soluble FL α2β1-Fc integrin. Culture supernatants from transfected CHO cells with the α2[E1129] subunit and/or the β1[D708] subunit, and without DNA (mock) were analysed in Fc-capture assays, performed in the presence of 1 mM Mn^{2+}. Recombinant proteins were detected with 5 μg/ml anti-α2 (JA218, 12F1,P1E6, 10A4, 3H14) antibodies, 5 μg/ml anti-β1 (12G10, TS2/16, 8E3, 4B4) antibodies, 1 μg/ml anti-Fc antibody or 1 μg/ml biotinylated collagen I. Bound mAbs were detected with anti-mouse HRP-conjugated secondary antibodies (1 μg/ml), whereas bound biotinylated collagen was detected using ExtrAvidin-peroxidase. Absorbance (405 nm) values and error bars represent the average and standard deviation of three readings.

recombinant heterodimeric protein well with comparable absorbance levels. The individual integrin subunits were also able to be expressed in isolation, as taken from the Fc binding data. Monomeric α integrin protein products failed to express the epitopes for the anti-α2 mAbs. Subsequently, no ligand binding was observed to the α2-Fc integrin subunit expressed in isolation, or to the β1 alone, as expected. In agreement to the data presented in Figure 3.4c, the heterodimeric wt FL α2β1 integrin supported collagen I binding in the presence of 1mM Mn^{2+}. Moreover, when the functional recombinant protein was examined for its collagen I binding ability in the presence of the β1-activating mAb 12G10, the collagen I binding levels of the recombinant wt FL α2β1-Fc integrin remained unaltered (Figure 3.5a). Thus, the soluble wt FL α2β1-Fc integrin appeared to be expressed in a high affinity activation state.

In conclusion, $\alpha2^{E1129}$ sub-cloned in pEE12.hFc was co-transfected with $pV.16h\beta1^{D708}$ into CHO L671h cells. Integrin α2β1-Fc expression, correct protein folding and ligand binding were examined in Fc-capture solid-phase assays. Three different clones of $pEE12.2h\alpha2^{E1129}$ were examined and $pEE12.2h\alpha2^{E1129}$ clone #5 was favoured as it showed high levels collagen I binding activity.

3.2 Production of soluble truncated α2β1-Fc integrin

The successful production of functional recombinant FL α2β1-Fc prompted the construction of variants of α2β1 in an attempt to generate a truncated (TR) soluble α2β1-Fc integrin that retained the folding and functionality of the native molecule.

3.2.1 Cloning of $pEE12.2h\alpha2^{I806}$ mammalian expression vector

Truncation points in the α2 subunit were chosen based on the previously described C-terminal truncations of the minimal α5 subunit that has been shown to be functional. The sequences of α2 and α5 were aligned using CLUSTALW (www.expasy.ch) and three truncation sites were selected based on sequence comparisons. The truncation sites were at K821, E811 and I806 (Figure 3.6), yielding a soluble α2 subunit comprising the α2 β-propeller, with the inserted α2 A domain, and the adjacent thigh domain but excluding the calf-1, calf-2 domains, and as expected the transmembrane and cytoplasmic domains. The truncated β1 subunit, kindly supplied by Dr. A. Coe, contains the β1 A domain, the hybrid

a)

```
αV      LIVGAFGVDRAILYRARPVITVNAGLEVYPSILNQDNKTCSLPGTALKVSCFNVRFCLKA 511
α5      LIVGSFGVDKAVVYRGRPIVSASASLTIFPAMFNPEERSCSLEGNP--VACINLSFCLNA 531
αiib    LIVGAYGANQVAVYRAQPVVKASVQLLVQDS-LNPAVKSCVLPQTKTPVSCFNIQMCVGA 524
α2      VSIGAFG--QVVQLWSQSIADVAIEASFTPEKITLVNKNAQIILKL----CFSAKFRPTK 689

αV      DGKGVLPRKLNFQVELLLDKLKQKGAIRRALFLYSRSPSHSKNMTISRGGLMQCEELIAY 571
α5      SGKHVAD-SIGFTVELQLDWQKQKGGVRRALFLASRQATLTQTLLIQNGAREDCREMKIY 590
αiib    TG-HNIPQKLSLNAELQLDRQKPRQG-RRVLLLGSQQAGTTLNLDLGGKHSPICHTTMAF 582
α2      QN---NQVAIVYNITLDADGFSSRVT-SRGLFKENNERCLQKNMVVN--QAQSCPEHIIY 743

αV      LRDESEFRDKLTPITIFMEYRLDYRTAADTTGLQPILNQFTPANISRQAHILLDCGEDNV 631
α5      LRNESEFRDKLSPIHIALNFSLDPQAPVDSHGLRPALHYQSKSRIEDKAQILLDCGEDNI 650
αiib    LRDEADFRDKLSPIVLSLNVSLPP----TEAGMAPAVVLHGDTHVQEQTRIVLDCGEDDV 638
α2      IQEPS---DVVNSLDLRVDISLEN------PGTSPALEAYSETAKVFSIPFHKDCGEDGL 794

αV      CKPKLEVSVD-----SDQKKIYIGDDNPLTLIVKAQNQGEG-AYEAELIVSIPLQADFIG 685
α5      CVPDLQLEVF-----GEQNHVYLGDKNALNLTFHAQNVGEGGAYEAELRVTAPPEAEYSG 705
αiib    CVPQLQLTAS-----VTGSPLLVGADNVLELQMDAANEGEG-AYEAELAVHLPQGAHYMR 692
α2      CISDLVLDVRQ[■]PAAQ[■]QPFIVSNQN[■]RLTFSVTLKNKRES-AYNTGIVVDFSENLFFAS 853

αV      VVRNNEALARLSCAFKTENQTRQVVCDLGNPMKAGTQLLAGLRFSVHQQSEMDTSVKFDL 745
α5      LVRHPGNFSSLSCDYFAVNQSRLLVCDLGNPMKAGASLWGGLRFTVPHLRDTKKTIQFDF 765
αiib    ALSNVEGFERLICNQKKENETRVVLCELGNPMKKNAQIGIAMLVSVGNLEEAGESVSFQL 752
α2      FSLPVDG-TEVTCQVAASQKS--VACDVGYPALKREQQVTFTINFDFNLQNLQNQASLSF 910

αV      QIQSSNLF-DKVSPVVSHKVDLAVLAAVEIRGVSSPDHIFLPIPNWEHKENPETEEDVGP 804
α5      QILSKNLN-NSQSDVVSFRLSVEAQAQVTLNGVSKPEAVLFPVSDWHPRDQPQKEEDLGP 824
αiib    QIRSKNSQ-NPNSKIVLLDVPVRAEAQVELRGNSFPASLVVAAEEGEREQN--SLDSWGP 809
α2      QALSESQEENKADNLVNLKIPLLYDAEIHLTRSTN-INFYEISSDGNVPSIVHSFEDVGP 969
```

b)

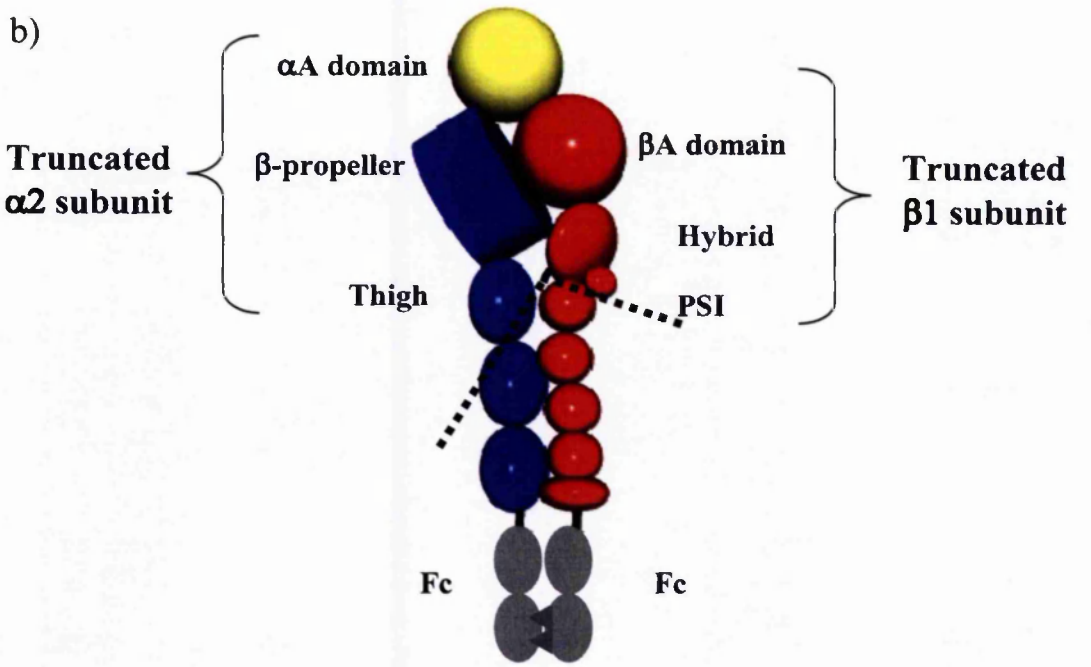

c)

	α2 extracellular	β1 extracellular	soluble FL α2-Fc	soluble FL β1-Fc	soluble TR α2-Fc	soluble TR β1-Fc
kDa	121	114	147	140	110	110

Figure 3.6. Truncation positions in human α2 integrin to produce the truncated extracellular domain construct. a) The amino acid sequence of integrin α2 was aligned with those of αV, αIIb, and α5 using CLUSTALW (accessed through www.expasy.ch/). Amino acids shown in the αV subunit sequence: in blue - the thigh domain, in sky blue the calf1 domain, boxed in cyan is the αV genu. Truncation positions are highlighted in blue and were chosen based on the published structure of αVβ3 to exclude the calf 1-2 domains of the α subunit. Integrin α2 DNA sequences were cloned in the pEE12.2hFc expression vector, transiently expressed in CHO cells and tested for functionality. The sorter applied sequence was represented by the DNA encoding the ectodomain of α2 subunit a.a. 1 to a.a. 806. b) Schematic representation of the structure of the truncated wt extracellular $\alpha2^{I806}\beta1^{P445}$-Fc integrin. Co-transfection of the $\alpha2^{I806}$ subunit in pEE12.2hFc and the $\beta1^{P445}$ subunit in pV.16hFc into CHO cells produced soluble 'truncated' wt α2β1-Fc integrin. c) Expected sizes of the integrin α2β1 subunits.

and the PSI domain. Thus, the soluble truncated β1 subunit lacked the four EGF-repeats and the β-tail domain. The cloning strategy to generate the truncated α2 integrin subunit was essentially the same as described in section 3.2.1 except that the 3' primers were designed to anneal further upstream in the human integrin α2 cDNA sequence. The same restriction sites were incorporated into the PCR-generated fragments to permit cloning into the pEE12.2hFc expression vector. Briefly, after removal of the internal *Hind*III site, the two sequences were joined in one piece and ligated into the cut pEE12.2hFc as a single *Hind*III-*Sal*I sequence. Transient co-transfection of a vector coding for the truncated α2 (generated in this study) with an existing vector coding for the truncated β1 subunit [Coe *et al.*, 2001] generated a soluble truncated α2β1-Fc integrin variant. Moreover, in order to gain a better understanding of the interaction of the α and β subunits in regulating collagen binding, a number of truncated α2β1-Fc single mutants were generated in the truncated α2β1-Fc integrin. Each mutant contained an amino acid substitution of a single residue forming one of the β1 A domain cation-binding sites. Following the expression of the single β1 mutations as part of the α2β1 recombinant integrin, the effects of the mutations on the collagen-binding properties of α2β1-Fc were investigated in Fc-capture ELISA assays, which are described in the sections below.

3.2.2 Expression and analysis of soluble truncated α2β1-Fc integrin

The CHO L761h cells were utilised for the expression of soluble truncated α2β1-Fc integrin, in the same manner as for the production of FL α2β1-Fc. The Lipofectamine 2000 reagent was used to co-transfect the truncated α2-Fc [K821, E811, I806] constructs with the pV.16hFc vector carrying a truncated version of the β1 subunit ($\beta1^{P455}$) [Coe *et al.*, 2001] in transient transfection experiments. All three recombinant α2β1 heterodimers were expressed as functional proteins, as taken from the positive collagen I binding activity in Fc-capture ELISA assays (data not shown). Therefore, the shortest C-terminal truncated version of the soluble α2 subunit, $\alpha2^{I806}$, was chosen for further analysis. For simplicity $\alpha2^{I806}$ is referred to as TR α2.

Anti-α2 and anti-β1 mAbs, used as probes of correct integrin folding, were found to bind to the soluble TR α2β1-Fc in a similar manner compared to the wt FL α2β1-Fc integrin (Figure 3.7). Moreover, the levels of binding to the different mAbs for both Fc-fusion

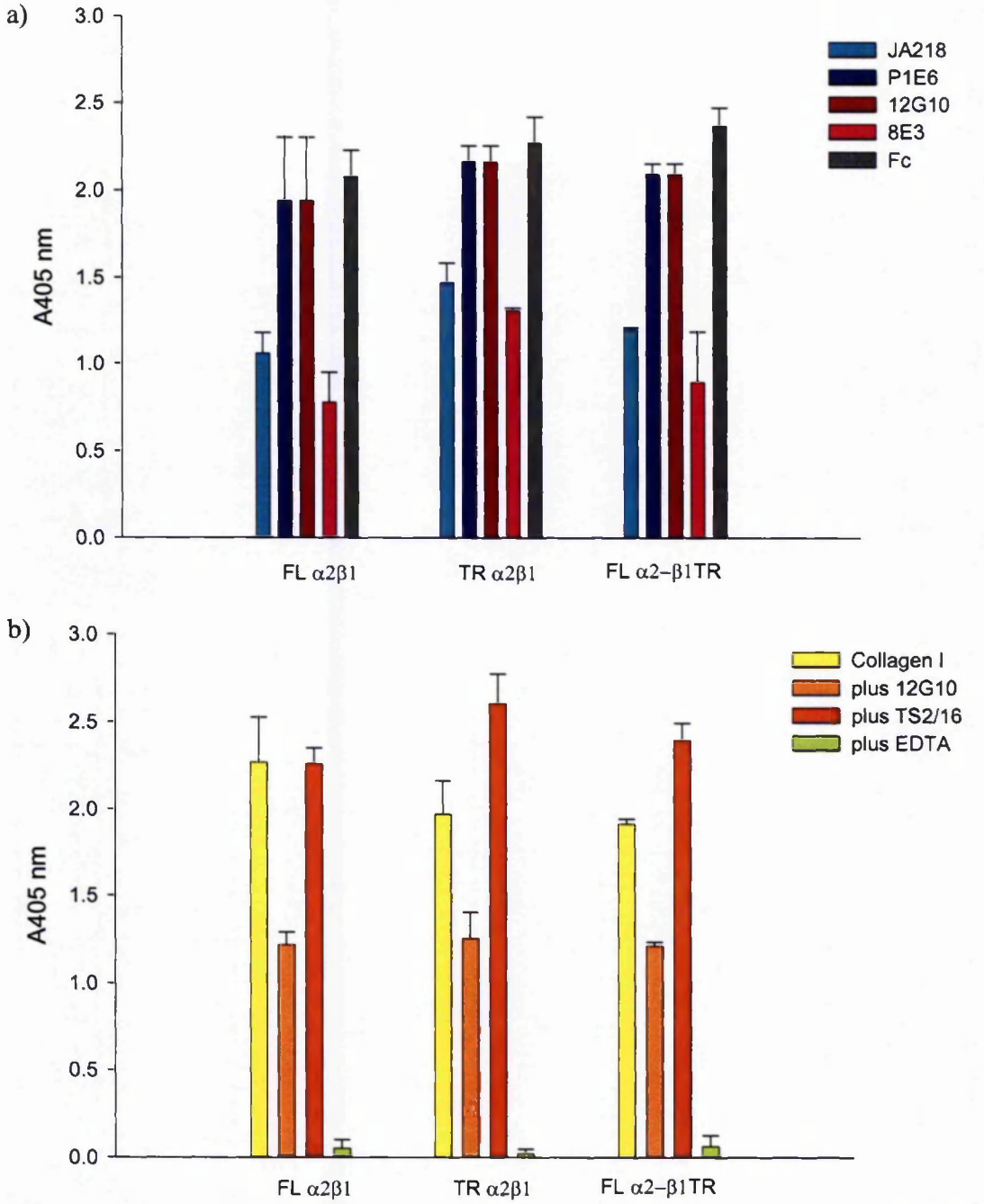

Figure 3.7. Antibody and ligand binding to soluble α2β1-Fc integrin variants. Culture supernatants from transfected CHO cells $\alpha2^{E1129}\beta1^{D708}$, $\alpha2^{I806}\beta1^{P455}$, and $\alpha2^{E1129}\beta1^{P455}$ were analysed in Fc-capture assays, performed in the presence of 1 mM Mn^{2+}. Recombinant Fc-fusion integrins were detected in a) with 5 μg/ml anti-α2 (JA218, P1E6) antibodies, 5 μg/ml anti-β1 (12G10, 8E3) antibodies and 1 μg/ml anti-Fc antibody. In b) detection was accomplished with 1 μg/ml biotinylated collagen I, either alone or with 10 μg/ml activating anti-β1 (12G10, TS2/16) antibodies. Bound mAbs were detected with anti-mouse HRP-conjugated secondary antibodies (1 μg/ml), whereas bound biotinylated collagen was detected using ExtrAvidin-peroxidase. Absorbance (405 nm) values and error bars represent the average and standard deviation of three readings. Non-specific binding as estimated from the mock transfection has been incorporated in the calculations.

integrins were almost identical. This was also true for a third integrin-Fc variant, which was composed of the full-length α2-Fc integrin subunit dimerised to the truncated β1-Fc integrin subunit [α2[FL] β1[TR] –Fc] that was also produced in transfected CHO cells. The similar level of anti-human Fc binding (Figure 3.7a) suggested that the hybrid α2[FL] β1[TR] –Fc integrin was expressed at similar protein levels to the FL and TR α2β1-Fc integrins, whereas the identical profile of mAb binding of all three recombinant proteins (Figure 3.7a) indicated that the α2[FL] β1[TR] –Fc integrin was also correctly folded.

The ligand binding data for the recombinant wt α2β1-Fc variants are shown in Figure 3.7a. Fc-captured TR α2β1 and α2[FL] β1[TR] integrins were able to bind biotinylated collagen I in the presence of 1 mM Mn^{2+}. In the presence of TS2/16, which is an anti-human β1 stimulatory mAb that binds to the βA domain, collagen I binding increased by ~25% for both of the two integrin variants that contained the truncated β1 subunit. The FL wt α2β1-Fc appeared to have a fully activated form as the presence of the activating agent had no effect on integrin activity. Surprisingly, upon addition of 5 μg/ml of the β1 activating mAb 12G10, the levels of collagen binding to the Fc-tagged integrins decreased.

3.3 Effect of mutations in the β1 A domain cation-binding sites on soluble truncated α2β1-Fc integrins

A number of β1 mutants have been generated in the pV.16hβ1^{P455} vector, expressed in CHO cells and examined in a series of detailed investigations into α5β1-ligand binding [Barton *et al.*, 2004, Mould *et al.*, 2003b]. The β1 mutations were designed based on the structural homology between β3 and β1 A domains and were constructed in the truncated β1 extracellular domain ending at residue Pro455. To study the role of the β1 A domain in regulating the collagen I binding capacity of the α2 A domain, mutations that targeted residues that form the β1 A domain cation-binding sites (Table 3.1) were selected to be studied in the soluble α2β1 integrin expression system.

Cation-binding site		**Residues**				
MIDAS	β3	Asp119	Ser121	Ser123	Glu220	Asp251
	β1	Asp130	Ser132	Ser134	Glu229	Asp259
	mutation	**D130A**				
ADMIDAS	β3	Ser123	Asp126	Asp127	Met335	Asp251
	β1	Ser134	Asp137	Asp138	Ala341*	Asp259 **
	mutation		**D137A**	**D138A**		
LIMBS	β3	Asp158	Asn215	Asp217	Pro219	Glu220
	β1	Glu169	Asn224	Asp226	Pro228	Glu229
	mutation	**E169A** **E169D**		**D226A** D226N		

Table 3.1. Cation-binding sites in the β1 and β3 A domains and their coordinating residues. Cation-binding site mutants made in β1 are shown in bold. Mutations were based on β3 structure (as identified in the αVβ3 crystal structures), -the cation-coordinating residues in β3 are shown alongside the corresponding residues in β1. Residues found only in the unliganded structure are marked with '*' [Xiong *et al.*, 2001] or residues found only in the liganded structure are marked with '**' [Xiong *et al.*, 2002]. The table was taken from Mould *et al.*, 2003b with the authors' permission.

Single amino acid mutations in the β subunit MIDAS have previously revealed a strict requirement for the conserved DxSxS motif in integrin function [Bajt *et al.*, 1995; Hogg *et al.*, 1999; Kamata *et al.*, 1995a; Mathew *et al.*, 2000; Mould *et al.*, 2002; Puzon-McLaughlin & Takada, 1996]. In the present study, alanine substitution of the MIDAS residue D130 was included in the investigations. The β1 ADMIDAS site contains residues Ser134, Asp137, Asp138 and Ala341 (or Asp259) (Table 3.1). The carboxylate oxygens from the side chains of Asp137 and Asp138 coordinate the ADMIDAS metal ion and mutation of either residue would be expected to abrogate cation binding to the ADMIDAS site [Mould *et al.*, 2003b]. The third metal ion-binding site in the β1 subunit, the β1 LIMBS site contains residues Glu169, Asn224, Asp226, Glu229, and Pro228 (Table 3.1). Of these residues Asn224 and Glu229 are integral residues of other β1 A domain sites in addition to forming the LIMBS site, and Pro228 contributes only a backbone carbonyl. The side chains of E169 and D226 are specific for the LIMBS. Hence, mutation of E169 or D226 to alanine would be expected to abrogate cation binding to the LIMBS site. The E169D mutation is a conservative mutation. This mutation is unlikely to block cation binding since an aspartate residue is present in place of glutamate in the other β subunits (with the exception of β6). To summarise, the β1 MIDAS (D130A) and ADMIDAS (D137A, D138A) mutations, also previously described in the recombinant α5β1 integrin, and the LIMBS mutations (D226A, E169A, E169D) were chosen to be examined in this study.

First, the truncated single $\beta1^{P455}$ mutants were co-transfected with the wt TR $\alpha2^{I806}$ in CHO cells, as described for the wt FL and TR α2β1-Fc integrins to generate six different α2β1 variants. Transfection with the wt FL or wt TR α2β1-Fc served as a positive control in subsequent analyses, whereas a mock transfection with no DNA added was used as a negative control. After the culture supernatants were harvested from each transfectant, supernatants were assayed for α2β1-Fc protein expression and correct protein folding in Fc-capture ELISA assays.

All combinations of α2 and mutated β1 were successfully expressed as integrin-Fc fusion proteins as assessed by polyclonal anti-human Fc antibody binding in solid-phase assays (Figure 3.8, Figure 3.9). As seen in Figure 3.8a and Figure 3.9a, a series of anti-α2 mAbs recognised all α2β1-Fc transfectants to a similar extent as the positive control, wt TR

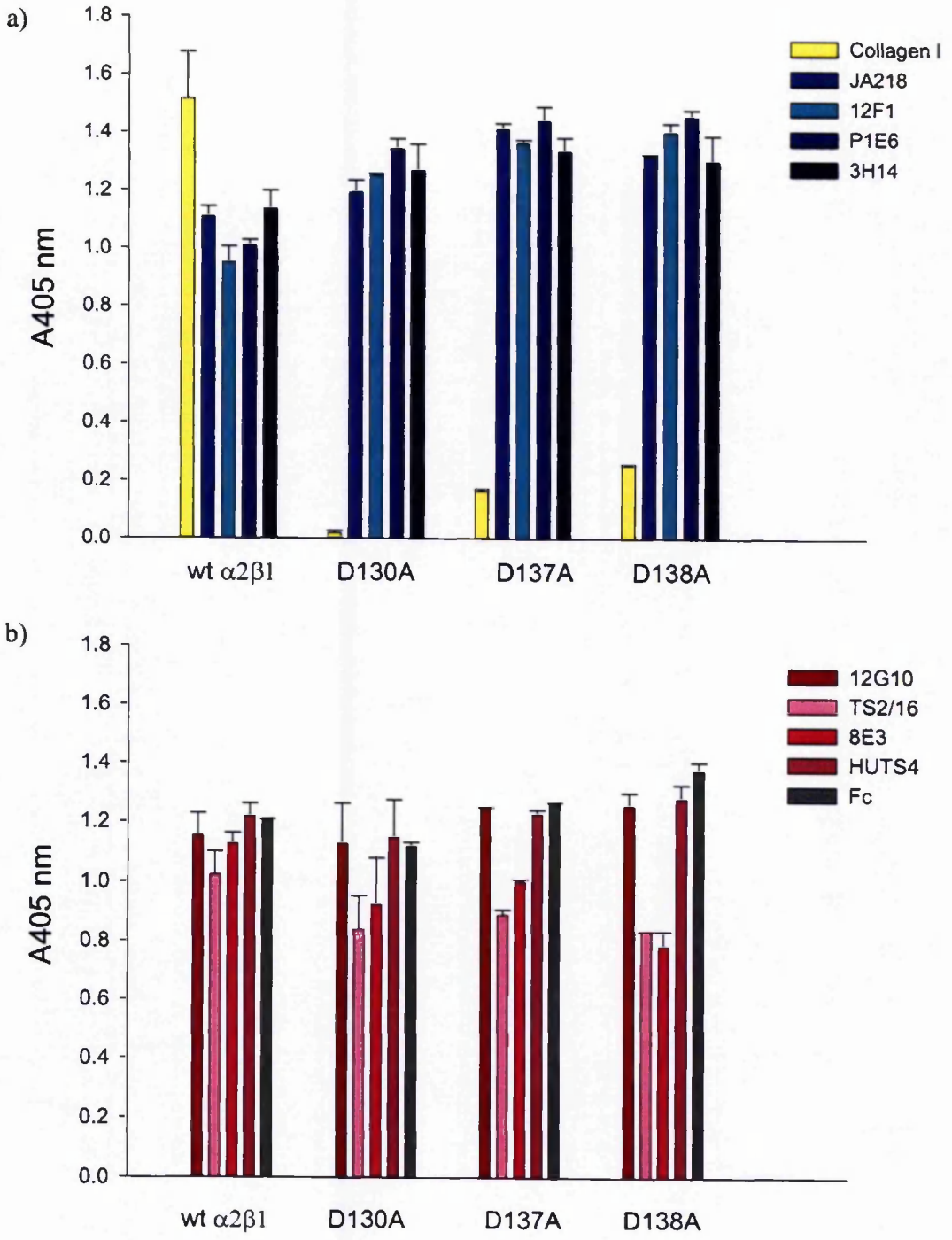

Figure 3.8. Antibody and ligand binding to soluble α2β1-Fc integrin MIDAS, ADMIDAS mutants. Culture supernatants from transfected CHO cells $\alpha 2^{I806}\beta 1^{P455}$ with the $\beta 1^{P455}$ MIDAS (D130A) and ADMIDAS (D137A, D138A) mutations were analysed in Fc-capture assays, performed in the presence of 1 mM Mn^{2+}. Recombinant Fc-fusion integrins were detected in a) with 5 μg/ml anti-α2 and with 1 μg/ml biotinylated collagen I, in b) with 5 μg/ml anti-β1 antibodies and 1 μg/ml anti-Fc antibody. Bound mAbs were detected with anti-mouse HRP-conjugated secondary antibodies (1 μg/ml), whereas bound biotinylated collagen was detected using ExtrAvidin-peroxidase. Absorbance (405 nm) values and error bars represent the average and standard deviation of three readings. Non-specific binding as estimated from the mock transfection has been incorporated in the calculations.

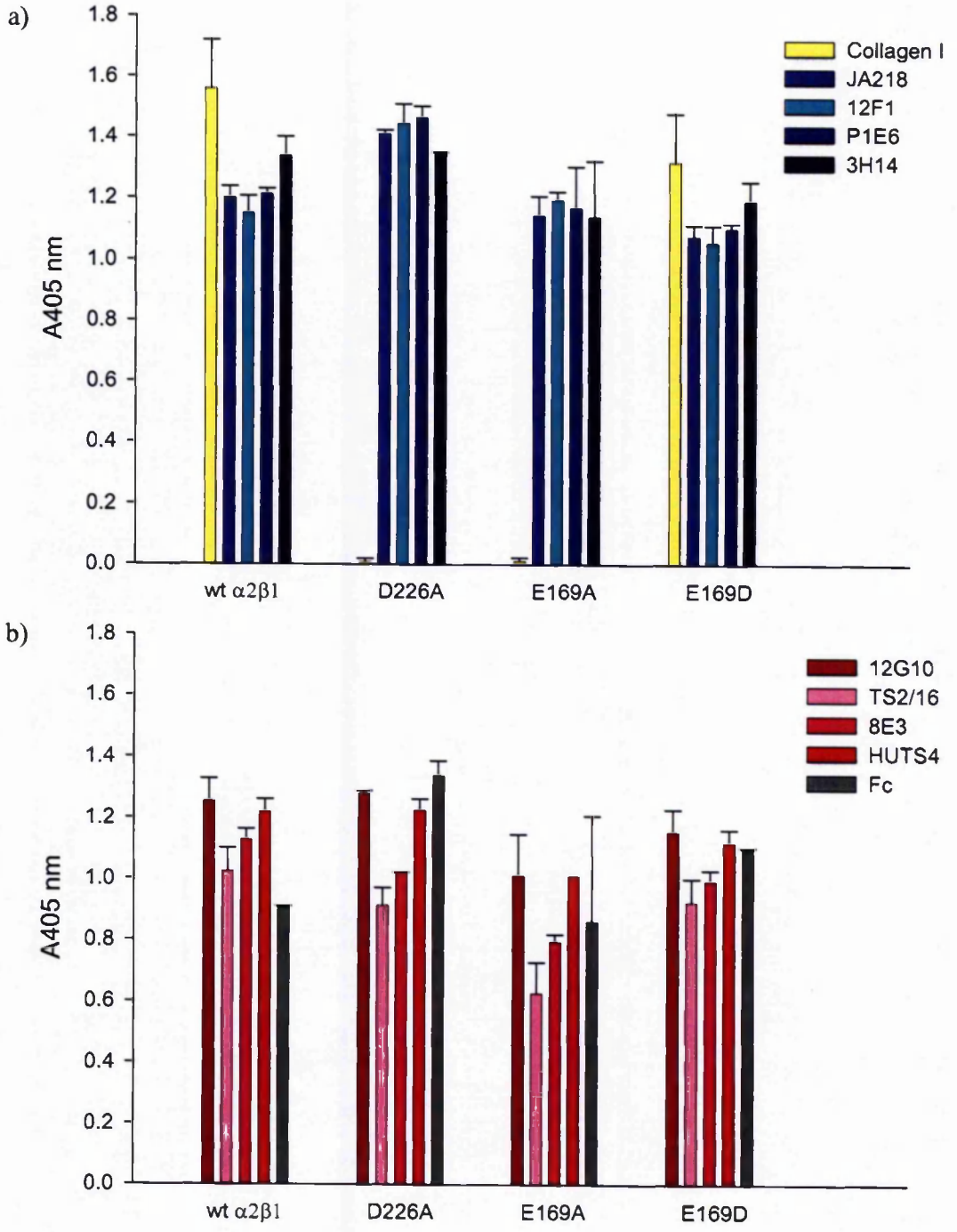

Figure 3.9. Antibody and ligand binding to soluble α2β1-Fc integrin LIMBS mutants. Culture supernatants from transfected CHO cells $\alpha 2^{I806}\beta 1^{P455}$ with the $\beta 1^{P455}$ LIMBS mutations were analysed in Fc-capture assays, performed in the presence of 1 mM Mn^{2+}. Recombinant Fc-fusion integrins were detected in a) with 5 μg/ml anti-α2 and with 1 μg/ml biotinylated collagen I, in b) with 5 μg/ml anti-β1 antibodies and 1 μg/ml anti-Fc antibody. Bound mAbs were detected with anti-mouse HRP-conjugated secondary antibodies (1 μg/ml), whereas bound biotinylated collagen was detected using ExtrAvidin-peroxidase. Absorbance (405 nm) values and error bars represent the average and standard deviation of three readings. Non-specific binding as estimated from the mock transfection has been incorporated in the calculations.

α2β1-Fc. Likewise, for all integrin-Fc heterodimers, the anti-β1 mAbs (Figure 3.8b, 3.9b), gave similar binding profiles to the positive control. Therefore it was concluded that each of the integrin-Fc fusion proteins was folded correctly.

The collagen-binding activity of the recombinant soluble TR α2β1 integrins relative to that of the wt TR α2β1 was also examined in an Fc-capture solid-phase assay. Of the six mutated integrins, the α2β1 LIMBS E169D mutant bound biotinylated collagen I to the same extent as the wt TR α2β1 (Figure 3.8a). In contrast, the β1 LIMBS E169A and D226A mutants did not support collagen I binding. The β1 MIDAS D130A mutation also abolished ligand binding, while both ADMIDAS mutants, D137A and D138A, bound collagen I weakly, but above basal levels (Figure 3.9a).

This initial result was investigated further to test the effects of the stimulatory anti-human monoclonal antibodies TS2/16 and 12G10 that bind to the β1 A domain. As shown in Figure 3.10, the D130A, D226A and E169A mutants did not bind collagen under any experimental condition, with or without antibody addition. The E169D LIMBS mutant bound collagen in identical manner as the control wt TR α2β1-Fc. Thus, both the wild type and E169D mutant bound collagen to the same extent in the absence of the activating antibodies, while addition of 12G10 decreased collagen binding slightly from 2 to 1.75 (A_{405} nm). The ADMIDAS mutants D137A and D138A, supported low collagen binding levels in the absence of the stimulatory antibodies, as observed previously. Upon addition of 12G10 and TS2/16, the collagen I binding signal increased dramatically, with TS2/16 having a more potent effect. Similar findings were observed for all integrin mutants that bound collagen, i.e. the highest collagen binding levels were obtained in the presence of TS2/16. No signal was developed in the presence of EDTA, as expected.

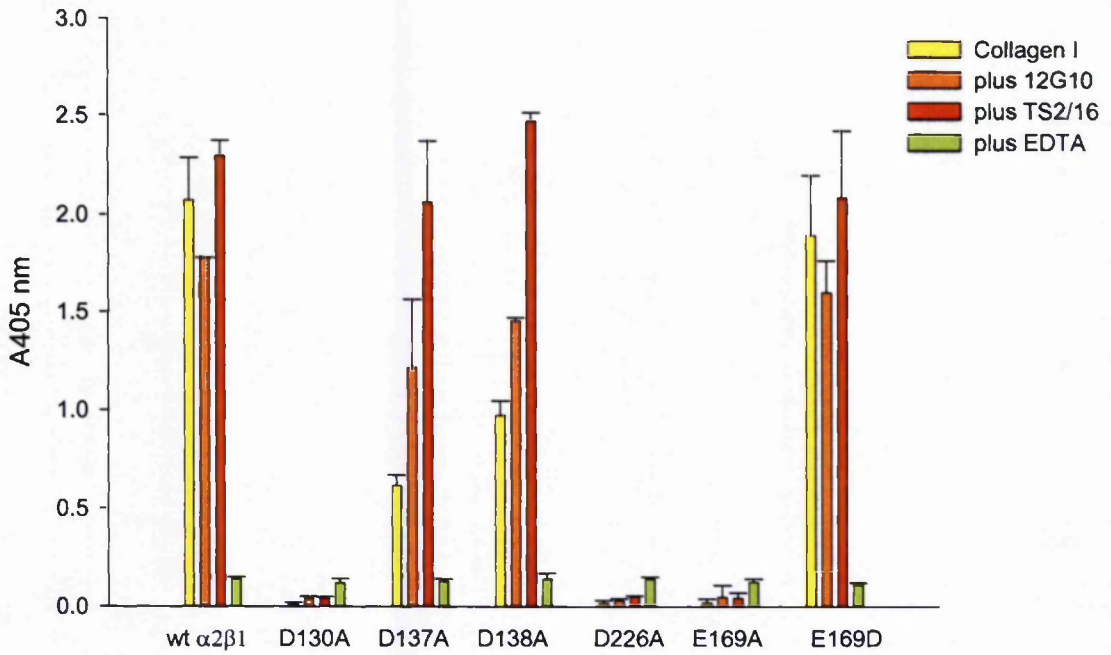

Figure 3.10. Collagen I to soluble TR α2β1-Fc integrin mutants. Culture supernatants from transfected CHO cells with $\alpha 2^{I806}\beta 1^{P455}$ were analysed in Fc-capture assays, performed in the presence of 1 mM Mn^{2+}. The ligand-binding activity of the recombinant Fc-fusion integrin mutants was detected with 1 μg/ml biotinylated collagen I, either alone or with 10 μg/ml activating anti-β1 (12G10, TS2/16) antibodies. 5 mM EDTA was also included in the investigations. Bound biotinylated collagen was detected using ExtrAvidin-peroxidase. Absorbance (405 nm) values and error bars represent the average and standard deviation of three readings. Non-specific binding as estimated from the mock transfection has been incorporated in the calculations.

3.4 Quantification of expression levels for α2β1-Fc variants

To estimate the amount of soluble α2β1-Fc integrins produced in each transient transfection, the protein contents of transfection supernatants were compared against known concentrations of recombinant α5β1-Fc integrin (a gift from Dr. P.A. Mould). Purified α5β1-Fc was diluted 10-200 ng/ml and captured on the anti-human Fc pre-coated ELISA plates. Recombinant α2β1-Fc integrins from neat culture supernatants were diluted one-in-eight in the assay buffer and captured on the ELISA plate. To detect the amount of integrin-Fc captured on each well a peroxidase-conjugated anti-human Fc antibody was used. A standard curve was plotted for the purified α5β1-Fc and the relative amounts of wt FL, wt TR and mutated α2β1-Fc were estimated by interpolation (Figure 3.11).

The estimated amounts of recombinant integrin expression varied from 0.8 – 1.2 μg/ml. These results indicated that the α2β1-Fc integrins are produced in the transient transfection system in good levels.

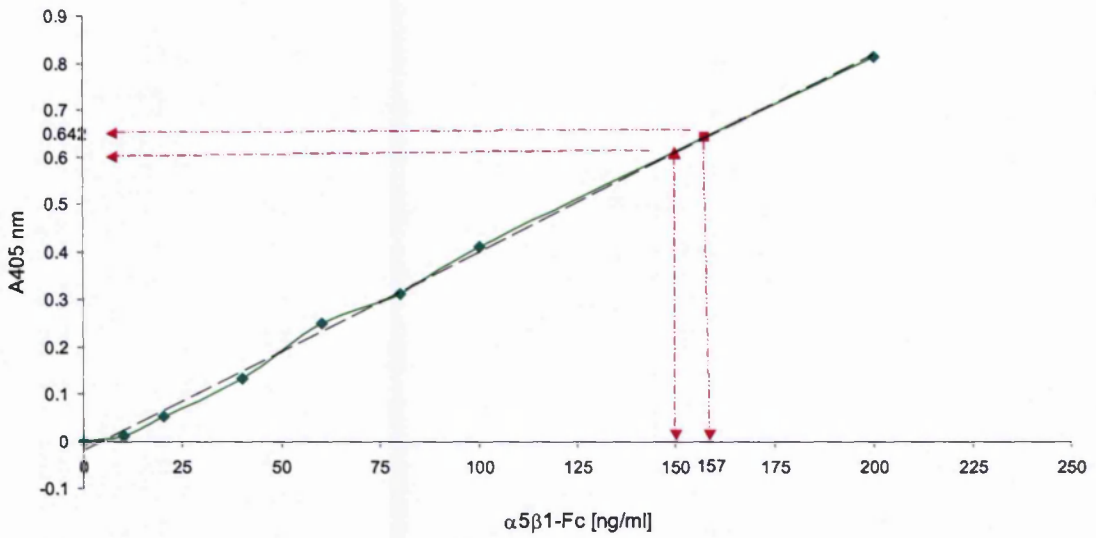

α2β1-Fc	OD_{405} nm	1:8 dilution [ng/ml]	Total [ng/ml]
FL	0.642	157	1256
TR	0.607	150	1200
TR D130A	0.410	103	824
TR D137A	0.439	109	872
TR D138A	0.437	108	864
TR D226A	0.572	141	1128
TR E169A	0.606	149	1192
TR E169D	0.466	116	928

Figure 3.11. Quantification of soluble α2β1-Fc protein yields from transient transfections. a) Known concentrations of α5β1-Fc integrin were detected with an anti-human Fc-HRP antibody to draw a standard curve. b) Transfection culture supernatants were diluted 1:8 and the approximate amount of α2β1-Fc in the supernatant was interpolated from the α5β1-Fc standard curve, likewise to the examples shown for wt FL and TR α2β1-Fc in the magenta lines.

3.5 Purification of soluble α2β1-Fc integrins

The soluble FL and TR α2β1-Fc integrins were purified from transfection culture supernatants by Protein A – Sepharose chromatography as described in section 2.2.4c. Fractions were collected and analysed by SDS-PAGE electrophoresis, followed by Coomassie blue staining. In Figure 3.11a, purification of FL α2β1-Fc was carried out from 2 x T75 cm^2 flasks of transfected CHO cells, while twice as many cells as utilised for the purification of TR α2β1-Fc described in Figure 3.11b. The recombinant integrin subunits, α2-Fc and β1-Fc, dimerised by disulphide bonds at the human Fc domains forming stable structures.

Under reducing conditions, a FL α2-Fc protein of approximately 190 kDa (Figure 3.12a) and a TR α2-Fc protein of 150 kDa were observed (Figure 3.12b). The molecular masses of the bands differed from the calculated molecular weights of ~150 kDa for the FL α2-Fc and 110 kDa for the TR α2-Fc (Figure 3.6c). Therefore, the α2-Fc subunits resolved on SDS-PAGE gels at higher points than expected. Recombinant soluble α2β1-Fc has been previously reported to migrate at an apparent molecular mass of a 185 kDa fragment corresponding to the α2 subunit [Kainoh & Tanaka, 2002]. The higher molecular weight of the α2 integrin subunit suggested that this is due to glycosylation. The band corresponding to the FL β1-Fc was 140 kDa (Figure 3.12a) and to the TR β1-Fc was 110 kDa (Figure 3.12b) as expected.

Because of the relative large volume of purified protein needed to be used in SDS-PAGE analysis, it was decided that protein containing fractions were to be identified in Fc-capture solid-phase assays by anti-α2β1 sandwich ELISA assays.

For further characterisation of the α2β1-Fc integrins, Protein A purified samples were utilised in Western blotting experiments utilising an anti-human α2 A domain antibody, JA212 (Figure 3.13). It also became apparent that the low pH used in the Protein A purification method affected the stability of the soluble α2β1-Fc heterodimeric integrins. Alternatively, storage of protein samples at 4 °C over a prolonged time may have led the heterodimer to fall apart.

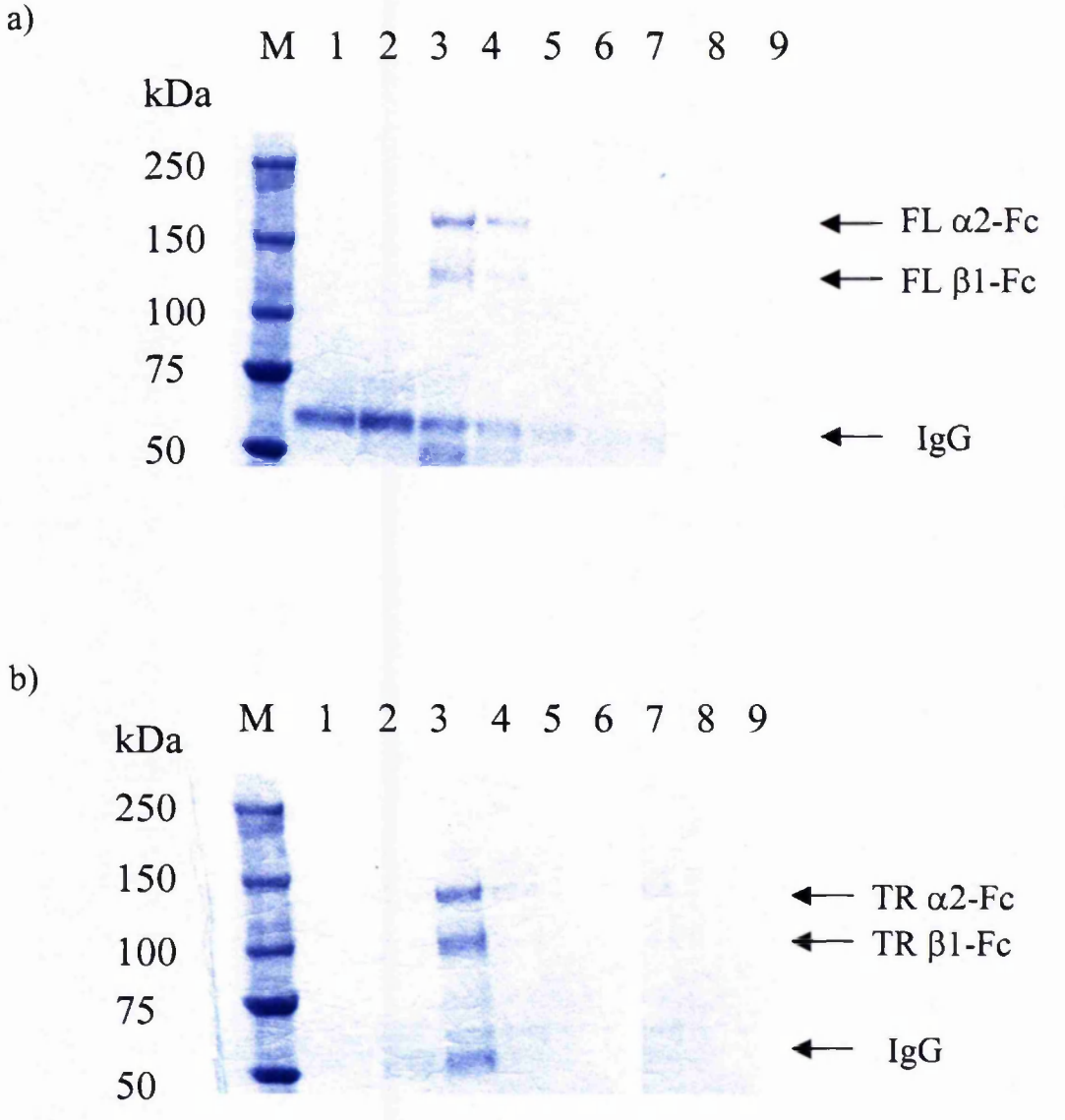

Figure 3.12. Analysis of Protein A purified a) FL wt α2β1-Fc and b) TR wt α2β1-Fc integrins by SDS-PAGE electrophoresis. Purified protein samples were dissolved in reducing SDS sample buffer, subjected to SDS-PAGE on 3-8% Tris – Acetate Novex gels, and subsequently stained with Coomassie blue. Lane M: precision prestain protein standards, lane1-9: Protein A chromatography fractions.

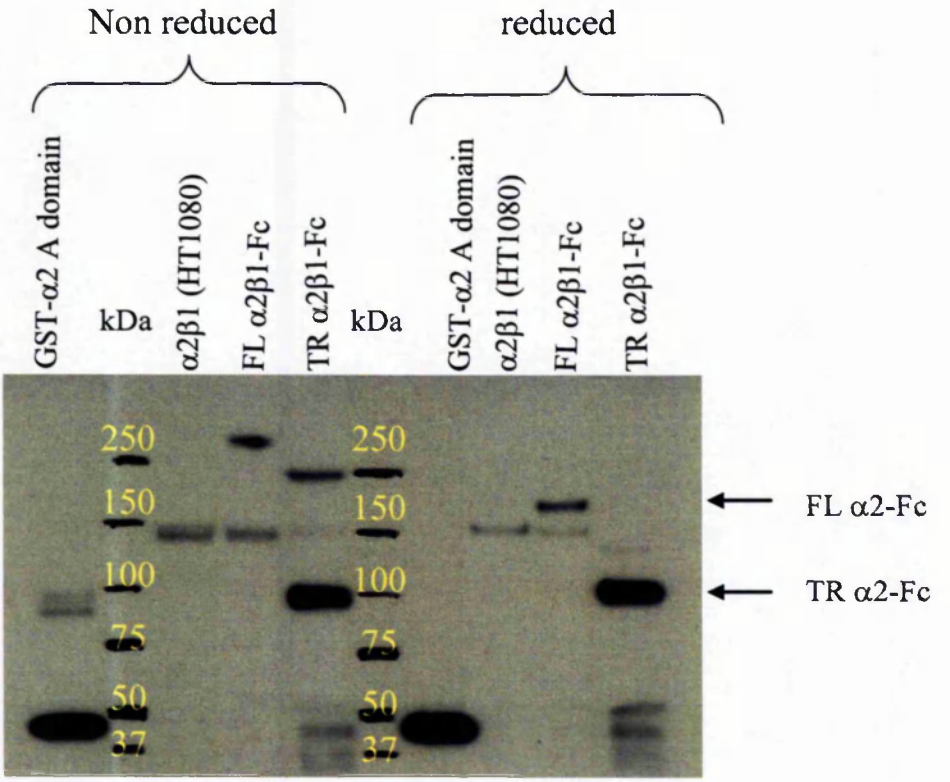

Fig 3.13. Western blotting of α2 A domain-containing integrins. Purified GST-α2 A domain, α2β1 integrin, soluble FL α2β1-Fc and TR α2β1-Fc integrins were resolved by non-reducing and reducing SDS-PAGE. Following protein transfer to nitrocellulose membrane, the proteins were detected with JA212 anti-human α2 A domain mAb (10 μg/ml) and a peroxidase-conjugated secondary antibody (0.5 μg/ml). Molecular weight markers are labelled on the membrane in kDa. Identity of protein bands is labelled on the right.

3.6 Summary

In this study the extracellular domains of human α2 integrin subunit and β1 subunit were co-expressed as Fc-fusion proteins, in mammalian CHO cells, to produce a soluble α2β1 integrin heterodimer. Antibody binding to the recombinant α2β1 integrin using a panel of monoclonal antibodies that recognise the native α2β1 integrin, suggested that the soluble α2β1-Fc was folded correctly. Furthermore, the full-length extracellular soluble integrin, FL α2β1-Fc, possessed the ability to bind to collagen I, and was therefore biologically functional.

The successful production of the FL α2β1-Fc prompted the production of a novel soluble α2 subunit that has been truncated in the C-terminal extracellular domain to amino acid I806 to remove long-range regulatory elements involved in integrin activation and to identify a minimised α2β1 integrin that retained the structure and function of the native integrin. The truncation of the α2 subunit was designed to exclude the calf-1 and calf-2 domains of the α2 subunit from the soluble integrin-Fc. Following co-expression with the previously described truncated $\beta1^{P455}$ subunit, the structure of the truncated α2β1, was analysed in solid-phase assays. The truncated $\alpha2^{I806}$ –Fc subunit was successfully dimerised with the truncated $\beta1^{P455}$–Fc subunit in mammalian cells to generate TR α2β1-Fc, a truncated soluble integrin. The data suggested that the recombinant truncated integrin maintained the default high affinity state of the full-length α2β1 integrin.

To study the role of the β1 A domain in α2β1-collagen binding, a site-directed mutagenesis strategy was adopted. Six β1 A domain mutants were expressed as truncated α2β1-Fc integrins and analysed for their ability to support ligand binding in Fc-capture ELISA type assays. The β1 A domain mutants contained single amino acid mutations in the cation-binding sites of the β1 subunit (i.e. LIMBS, MIDAS and ADMIDAS). Only the control β1 E169D mutant was shown to be able to bind collagen I and to the same extent as the wt TR α2β1 Fc-fusion protein. The ADMIDAS D137A and D138A mutants appeared to exhibit low affinity for collagen I, whereas the LIMBS D226A and E169A mutants as well as the MIDAS mutant lost the collagen I binding ability. The significance of each mutation is discussed in chapter 6.

Chapter

4.0 Characterisation of the regulatory properties of mutations in the functional domains of soluble α2β1-Fc integrin

In the previous chapter the production of soluble α2β1 integrins was described. Briefly, recombinant α2β1 integrins were expressed transiently in a mammalian Fc-expression system. The soluble integrins included αβ heterodimers containing the entire ectodomain of α2β1, referred to as full-length (FL), or C-terminal truncated variants (TR) that lack the calf 1-2 domains in the α2 subunit and the EGF repeats in the β1 subunit. Recombinant proteins composed of the unmodified sequence of human integrin α2β1 (excluding silent mutations introduced for cloning purposes) are referred to as wild-type (wt) proteins. Analysis of the recombinant wt proteins in ELISA and ligand-binding solid-phase assays suggested that the recombinant proteins retained structural and functional characteristics of the parent α2β1 integrin. In addition, truncated integrins with single amino acid mutations of the β1 A domain cation-binding sites: MIDAS, ADMIDAS and LIMBS, were also expressed. Mutations of the key residues that form part of the β1 cation-binding sites did not perturb the overall structure of the mutated α2β1-Fc, as assessed by mAb binding directed against the integrin subunits. However, in ligand-binding assays the single β1 mutants either did not bind collagen I or bound collagen very weakly. Thus, detailed examination of the collagen I binding properties of the single β1 mutants in the TR α2β1-Fc was not feasible.

To enable further study of α2β1-collagen interactions, an activating mutation was generated in the isolated α2 A domain and subsequently introduced in the α2-Fc construct. This approach resulted in the generation of a series of double mutants, carrying a mutation in the TR α2-Fc and a second mutation in the TR β1-Fc integrin subunit. The construction of bacterial and mammalian expression vectors containing mutations in the integrin α2 A domain is described in this chapter. The structural and functional analysis of soluble TR α2β1-Fc double mutants are also presented below.

4.1 Production of recombinant α2 A domain proteins

The aim of this part of the project was to identify an 'activating' mutation that favoured the primed conformation of the α2β1-Fc receptor. This would allow further studies of the subunit interactions in the activated α2β1 integrin by measuring collagen binding in solid-phase assays. Since the α2 A domain is the principal collagen-binding domain of integrin α2β1, it is the logical region to target for an activating mutation. In fact, studies of the isolated αA domains of other integrins have previously identified activating mutations that induce a high affinity integrin state in an allosteric manner. Such activating mutations, located around the interface between the C-terminal α7-helix and the opposing β-sheet, have been shown to increase ligand-binding affinity by stabilising the open αA domain conformation relative to the closed conformation. In particular, the substitution of a conserved isoleucine to a glycine has also been shown to produce constitutive activation in all αA domains. [Vorup-Jensen *et al.*, 2002; Huth *et al.*, 2000; Xiong *et al.*, 2000]. The above data suggested that the same allosteric regulation would apply to other A domains too. This provided the structural rationale for mutating this invariant isoleucine residue to a glycine in the α2 integrin; that is residue Ile332 in the α2 A domain (Figure 4.1).

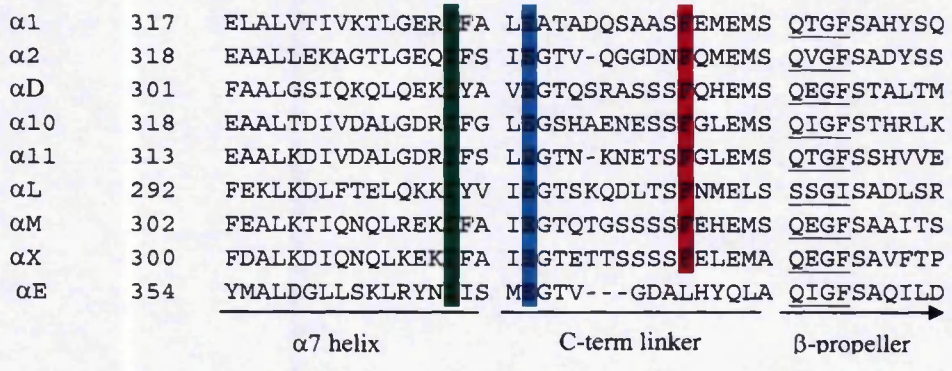

Figure 4.1. Alignment of human αA domains C-terminal α7-helices and C-terminal linker sequences. Conserved residues are highlighted in green, grey and pink. In the α2 A domain they correspond to Ile332, Glu336, Phe345 and were selected for mutagenesis studies.

The successful production of recombinant wild-type α2 A domain protein with similar properties to the parent integrin has previously been achieved in this laboratory [Tuckwell *et al.*, 1995]. Therefore, the α2 A domain was used as a prototype in collagen I solid-phase binding assays to examine the effect of the Ile332 to Gly substitution.

In this section I describe the production of recombinant α2 A domain proteins in a bacterial expression system. The coding region of human α2 A domain was amplified from human α2 A domain cDNA, cloned into the pGEX-2T vector and two α2 A domain variants, one unmodified and one mutated, were expressed as glutathione S-transferase fusion proteins. Purified fusion proteins were initially characterised structurally in ELISA assays with a panel of anti-α2 A domain antibodies. Next, the functional state of the recombinant proteins was investigated in solid-phase assays by testing for collagen I binding. The divalent cation dependency of each recombinant protein was also examined.

4.1.1 Cloning of α2 A domains into the pGEX-2T expression vector

As mentioned above, a functional α2 A domain protein has been cloned and expressed in isolation in this laboratory by Tuckwell *et al.* (1995). The above protein contained the entire unmodified α2 A domain sequence and is referred here as 'Fl'. However, more recently a truncated α2 A domain protein has been utilised successfully in crystallisation trials by Emsley *et al.* (2000). For the purposes of the present study I have produced the truncated α2 A domain protein that comprises the unmodified, wild-type α2 A domain sequence but differs in the amino acid chain length from the Fl α2 A domain originally produced by Tuckwell *et al.* (1995).

For cloning of the wt α2 A domain, a DNA sequence encoding residues Cys140 to Val339 was amplified by PCR from a human cDNA clone contained in pGEX-2T vector, kindly provided by Dr. D. Tuckwell (University of Manchester). A mutated α2 A domain$^{140\text{-}339}$ was also generated in parallel by including a substitution of isoleucine at position 332 to glycine, in the 3'end amplification primer. Primers were designed so that all of the amplification products would contain a *Bam*HI restriction site at their 5'ends and a *Eco*RI restriction site at their 3'ends. The reverse primers were also designed to introduce an in-frame stop codon. The PCR products were digested with *Bam*HI and *Eco*RI restriction endonucleases and purified by excision of 0.6 kb bands from agarose gels. The purified DNA was next ligated to *Bam*HI / *Eco*RI digested pGEX-2T glutathione S-transferase (GST) expression vector. The ligation mixtures were used to transform *E. coli* DH5αF' cells, and transformants were grown in LB-agar plates containing ampicillin. Ten colonies were chosen at random and plasmid DNA was purified from overnight cultures. *Bam*HI / *Eco*RI restriction digests of purified DNA (Figure 4.2) confirmed that all the clones

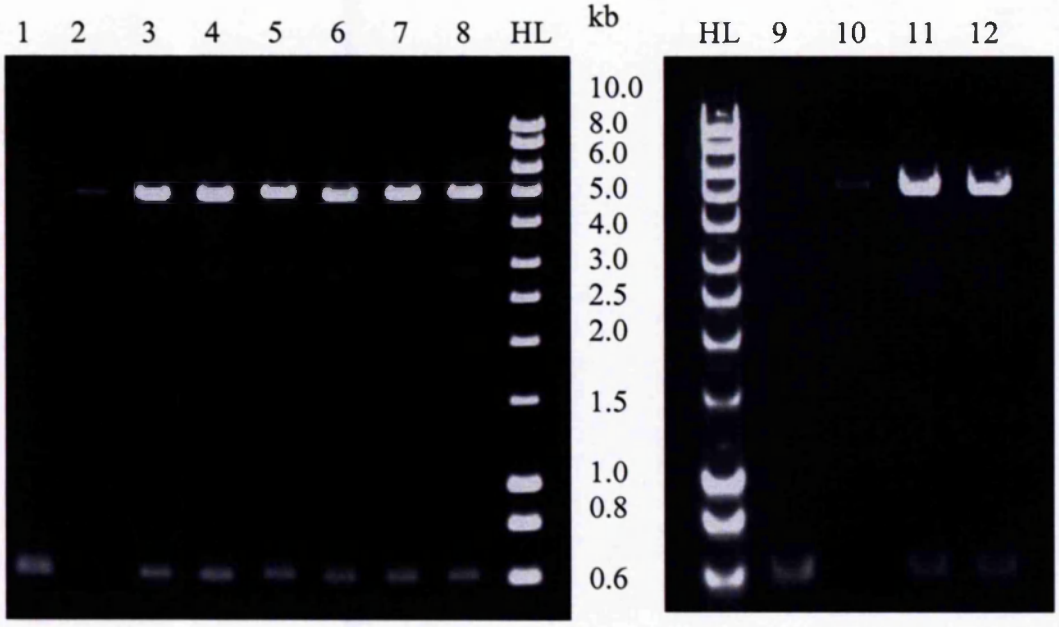

Lane	*Bam*HI / *Eco*RI digests	Expected size (kb)
1	PCR α2A dom$^{140-339}$	0.6
2,10	pGEX-2T	4.9
3 - 8	pGEX α2A$^{140-339}$ clones # 1-6	4.9, 0.6
9	PCR α2A dom$^{140-339}$ [I332G]	0.6
11	pGEX α2A$^{140-339}$ [I332G] clone #1	4.9, 0.6
12	pGEX α2A$^{140-339}$ [I332G] clone #2	4.9, 0.6

HL	HyperLadder I	0.2 - 10.0

Figure 4.2. Agarose gel analysis of PCR-generated fragments used in the construction of the pGEXα2A$^{140-339}$ vectors. PCR fragments of the wild-type and mutated [I332G] α2 A domain encoding a.a. C140-V339 were amplified from human α2 A domain cDNA in a single step PCR reaction. All PCR-generated fragments were designed to include a *Bam*HI and an *Eco*RI restriction site at their 5' and 3' ends respectively. This allowed for in-frame insertion to the GST expression vector pGEX-2T. All DNA fragments shown above were *Bam*HI / *Eco*RI digested. Restriction digests of pGEXα2A$^{140-339}$ clones generated correct size fragments. For content and size description of each lane see the table above.

contained the 0.6 kb insert. *Bam*HI and *Eco*RI restriction digests of the PCR fragments, the vector and of the clones containing the correct size inserts, are shown in Figure 4.2. The DNA sequences of two clones per construct were checked by dideoxy DNA sequencing and compared to the published α2 DNA sequence, confirming the absence of mutations except for the engineered I332G substitution in the mutated construct. In conclusion, two variants of the α2 A domain encoding for amino acids C140-V339, a wt and a mutant [I332G], were cloned in the pGEX-2T bacterial expression vector. These expression vectors allowed the production of N-terminal GST-fusion α2 A domain proteins (Figure 4.3). The constructs were designated pGEXα2A$^{140\text{-}339}$, pGEXα2A$^{140\text{-}339}$[I332G].

4.1.2 Purification of GST-fusion α2 A domain proteins

Following transformation of the pGEXα2A plasmids into *E. coli* strain DH5αF' cells, bacterial cells were grown in one litre cultures as described in section 2.2.1a. Briefly, *E. coli* bacterial cultures were induced with IPTG and allowed to express recombinant GST fusion proteins for four hours. The cells were lysed by sonication and the GST-tagged α2 A domain proteins were purified from bacterial lysates by affinity chromatography on glutathione-agarose columns. The collected fractions were analysed by SDS-PAGE electrophoresis for GST-protein content and purity (Figure 4.4a). The purified proteins ran as single bands of approximately 50 kDa under reducing conditions, and no major contaminants were present. The purified GST-α2 A domains produced in this study are illustrated in Figure 4.4b.

Based on the results of the SDS-PAGE analysis, fractions containing the GST-fusion protein were collected, pooled together and dialysed against TBS. This step was necessary for removal of the glutathione present in the elution buffer. Next, the GST-fusion protein concentration was estimated using the BCA method. The yields of both recombinant α2 A domains were similar. Typical yields from 1 litre bacterial cultures for the α2 A domain$^{140\text{-}339}$ were calculated in the order of 20 mg protein. The α2 A domain$^{140\text{-}339}$ [I332G] was expressed at slightly lower levels of 15 mg/l.

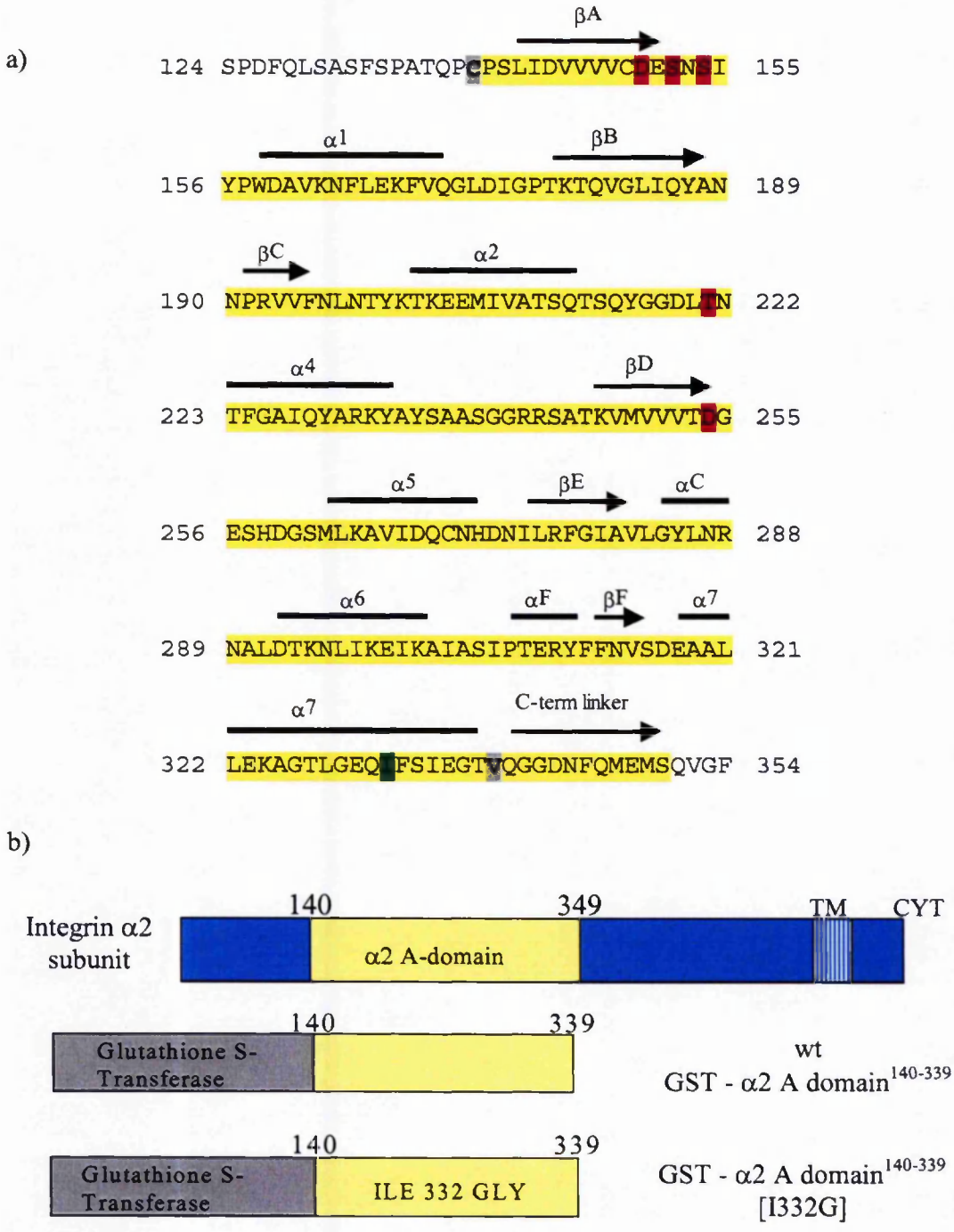

Figure 4.3. Cloning the A domain of α2 integrin subunit in isolation. (a) Protein sequence of the α2 integrin A domain. α-helices and β-strands secondary structures are represented by bars and arrows respectively. The residues that comprise the MIDAS motif are highlighted in magenta. Highlighted in green is the Ile332, which has been mutated to a glycine for the generation of the mutated α2 A domain in the present study. Residues Cys140 and Val339, representing the starting and ending residues of the recombinant α2 A domain, are highlighted in grey. (b) Schematic representation of the GST-fusion α2 A domain proteins expressed in isolation in this study. Numbers represent the amino acid residues at the boundaries of the cloned α2 A domain protein sequences.

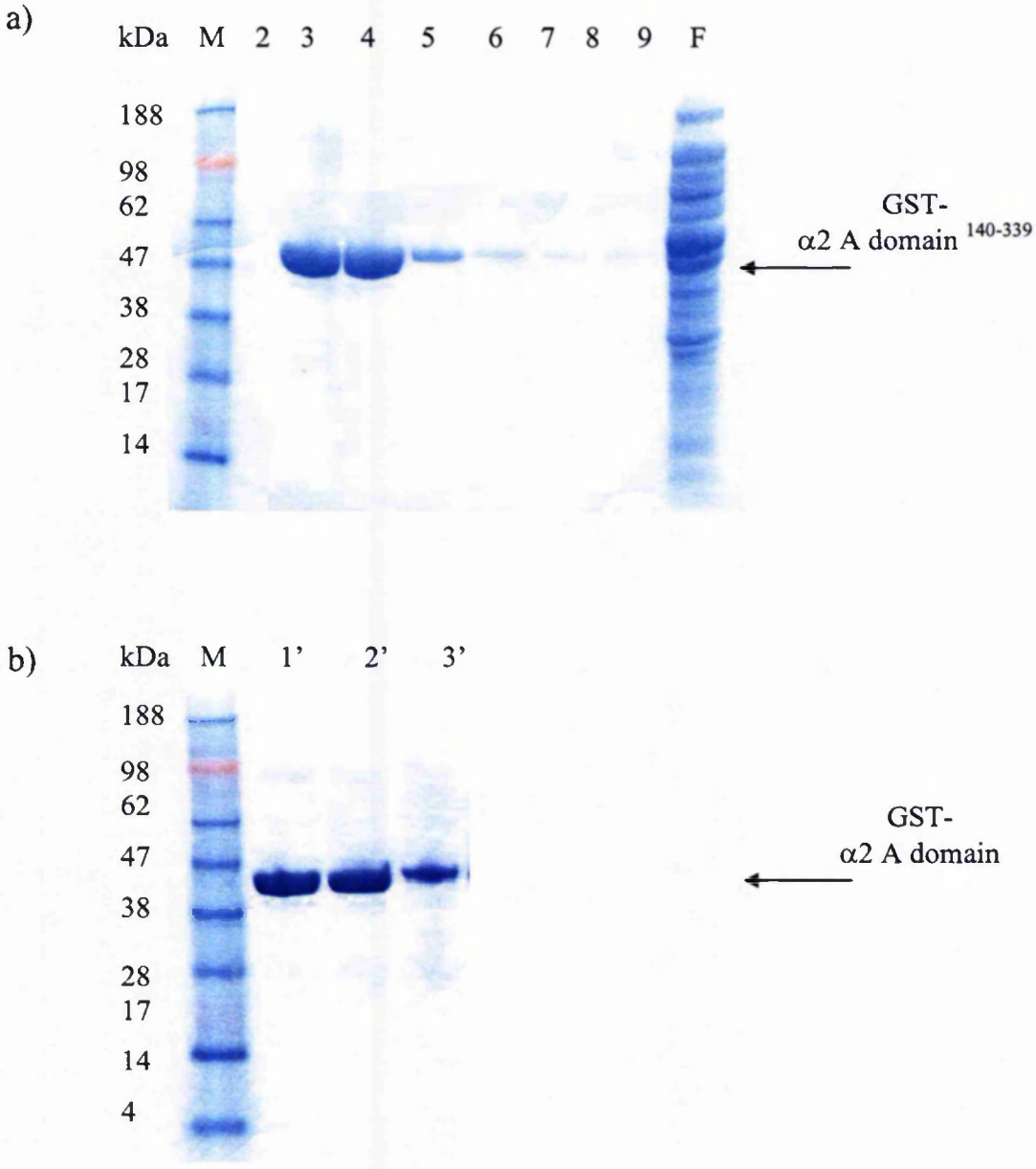

Figure 4.4. SDS-PAGE analysis of recombinant GST- α2 A domain proteins. (a) GST - α2 A domain$^{140-339}$ protein purification by affinity chromatography. Lysate from 1 l bacterial culture was passed over a 5 ml glutathione-agarose column. Following the wash step, the bound proteins were eluted in 5 mM glutathione / 50 mM Tris pH 8.0. Typically, 1.5 ml fractions were collected and 5 µL of each elution fraction was analysed on 4 - 12% Bis-Tris Novex gels under reducing conditions. Lane M: SeeBlue protein standards; F: 20 µl flow through; 2-9: 5 µl of elution fractions 2 to 9. (b) Reducing SDS PAGE of purified α2 A-domain - GST proteins. Lane M: SeeBlue protein standards; GST- α2 A domain proteins in lane-1': a.a. 140-339, wt; 2': a.a. 140-339 [I332G]; 3': Fl. SDS PAGE gels were developed with Coomasie blue stain.

4.1.3 Functional analysis of the isolated α2 A domain

For the experiments testing protein folding and ligand binding activity of the recombinant proteins, described in this section, the GST tag was not removed. To assess the structural integrity of the recombinant α2 A domains, each protein was tested in ELISA with a panel of five mAbs directed against the integrin α2 A domain (P1E6, Gi9, JA202, 12F1 and JA218). All proteins were immobilised at 10 μg/ml. The antibody binding data for each of the recombinant α2 A domain proteins are summarised in Figure 4.5. The α2 A domain labelled 'Fl' (encoding integrin amino acids 124-339), has been previously described and fully characterised by Dr. D. Tuckwell in this laboratory. This functional recombinant α2 A domain was used as a positive control. The P1E6 and Gi9 mAbs recognised the recombinant proteins to the same degree as the positive control. This was also true for the JA202, 12F1 and JA218 mAbs that bound to all α2 A domains to the same extent. The anti-α2 subunit mAb, 10A4, which binds outside the α2 A domain, was utilised as a negative control and as expected did not bind to the α2 A domains. The anti-GST polyclonal antibody was also included in the assay to normalise the amount of α2 A domain immobilised in the plates. In conclusion, the above results suggested that the isolated α2 A domains produced in this study as GST-fusion proteins were folded correctly.

Next, the ligand binding ability of the recombinant α2 A domains was examined using biotinylated collagen I in solid-phase assays. For the immobilisation of the purified recombinant integrin domain in the initial experiments the α2 A domain variants were pre-diluted in PBS(+) buffer [as supplied by Biowhittaker]. The above experiments were performed with 1 μg/ml biotinylated collagen I, in the presence of 1 mM Mn^{2+}. Under these conditions, 5 μg/ml of the mutated α2 A domain$^{140\text{-}339}$ [I332G] demonstrated high levels of collagen I binding (Figure 4.6). However, under the same conditions, 20 μg/ml of Fl and α2 A domain$^{140\text{-}339}$ supported collagen I binding at very low levels (Figure 4.6). In fact, Tuckwell *et al.* (1995) used a preparation of 40 μg/ml Fl α2 A domain to demonstrate collagen recognition in the binding assays. Taken together, the ability of the Fl and α2 A domains$^{140\text{-}339}$ to bind ligand in conjunction with the functional data for the Fl α2 A domain by Tuckwell *et al.* suggested that the two wild-type, unmodified A domains proteins were not defective in ligand binding, but were expressed in a low activation state.

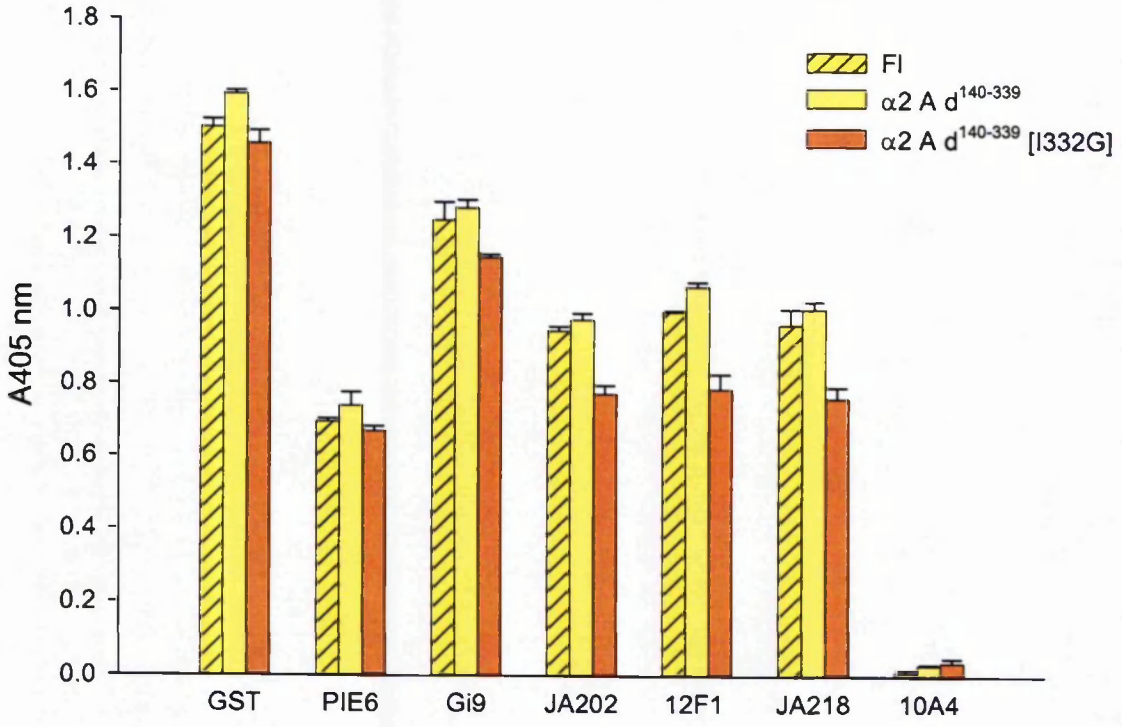

Figure 4.5. Antibody binding to recombinant α2 A domain proteins. The binding of α2 A domain mAbs (PIE6, Gi9, JA202, 12F1, JA218) to recombinant α2 A domain$^{140-139}$ proteins was examined in ELISA assays. Recombinant Fl α2 A domain, previously characterised by Tuckwell *et al.* (1995), was used as a positive control. The anti-α2 integrin mAb 10A4 epitope is located outside the A domain and was used as a negative control. All α2 mAbs were used at 10 μg/ml. Detection with an anti-GST antibody was used to normalise the data. Results are means ± standard deviations (n=4) from two experiments.

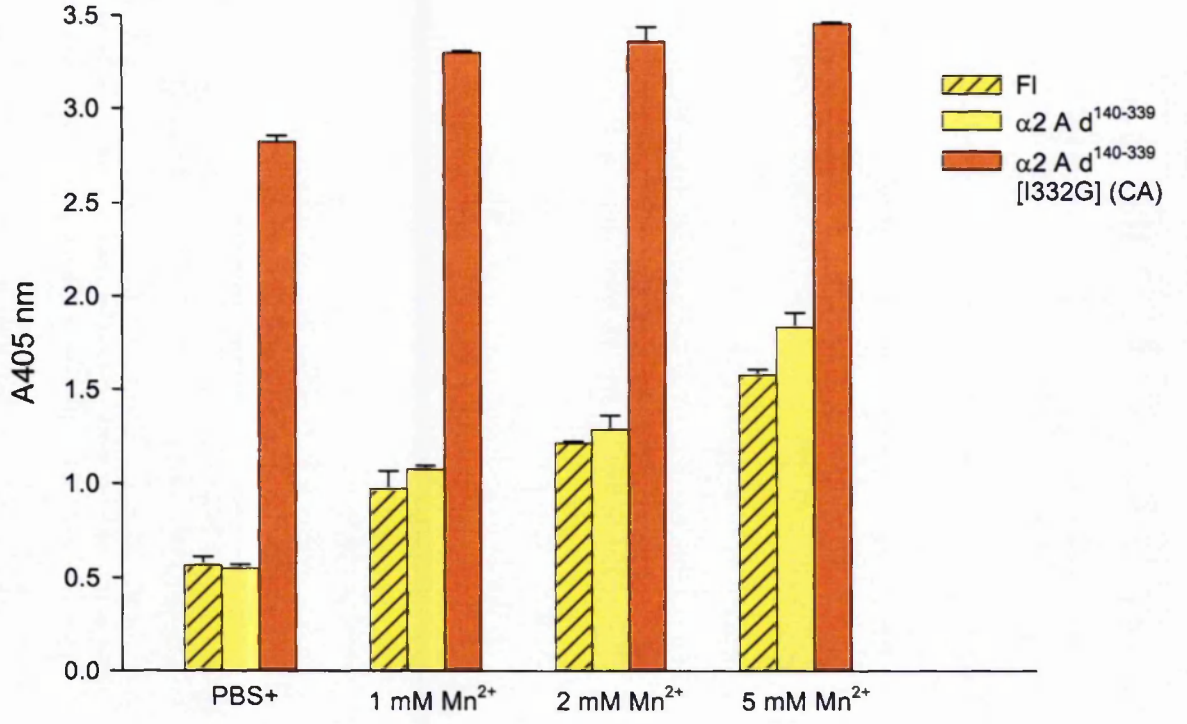

Figure 4.6. Effect of increasing Mn^{2+} concentration on the activation state of recombinant α2 A domain proteins. Recombinant α2 A domains were immobilised onto microtiter plates in the presence of PBS(+) or TBS buffer with increasing concentrations of Mn^{2+}. The unmodified Fl and α2 A domain$^{140-339}$ proteins were immobilised at 20 μg/ml, the mutated α2 A domain$^{140-339}$ [I332G], also referred to as CA, was used at 5 μg/ml. The plates were blocked with 5% BSA and biotinylated collagen was added at 1 μg/ml in the presence of 1 mM Mn^{2+}. Unbound collagen was washed off, ExtrAvidin-peroxidase was added and detection was carried out with ABTS. Absorbance (405 nm) values and error bars represent the average and standard deviation from two experiments (n=8).

In an effort to stimulate the binding of collagen I to the unmodified α2 A domains, the effect of Mn^{2+} cations on the activation state of the recombinant α2 A domains was investigated further. Collagen I binding to the recombinant GST-fusion Fl α2 A domain has been reported to be cation-dependent and similar to that of the parent integrin [Tuckwell *et al.*, 1995]. Therefore, Mn^{2+} was chosen as it is known to activate integrin α2β1. The addition of manganese immediately prior to coating the microtiter wells with the α2 A domain proteins was assessed (Figure 4.6.).

Addition of increasing concentrations of Mn^{2+} to the Fl α2 A domain and α2 A domain$^{140-339}$ preparations prior to immobilisation on the 96-well plates was found to increase levels of collagen I binding in a dose-dependent manner. Conversely, addition of up to 5 mM Mn^{2+} only marginally increased the collagen I binding to the α2 A domain$^{140-339}$ [I332G]. This suggested that the mutated α2 A domain$^{140-339}$ [I332G] was expressed in a constitutively active state with respect to collagen binding, whereas the unmodified α2 A domains$^{140-339}$ and Fl proteins were expressed in a low affinity state and required stimulation of activation by external agents. To discriminate between the two α2 A domain encoding residues Cys140 to Val339, the mutated α2 A domain is also referred to as CA (constitutive active). Unless otherwise stated, subsequent experiments were performed with 5 μg/ml immobilised CA α2 A domain in PBS(+) without the addition of external divalent cations, or 20 μg/ml α2 A domain$^{140-339}$ immobilised on solid-phase in TBS and in the presence of 2 mM Mn^{2+} ions.

It has been previously reported that type I collagen binding to α2 A domain is supported by Mn^{2+} and Mg^{2+} ions [Tuckwell *et al.*, 1995]. This is consistent with the data displayed in Figure 4.7. Mn^{2+} ions supported greater levels of collagen I binding than Mg^{2+} ions. In contrast, Ca^{2+} ions did not support collagen I binding to α2 A domain$^{140-339}$ in the mM concentration range. Consistent with the cation dependency of collagen binding to the recombinant GST-tagged α2 A domains, addition of 10 mM EDTA greatly reduced collagen I binding levels to BSA levels (Figure 4.7). The divalent cation dependency of the collagen binding to the α2 A domain is examined in detailed investigations in Chapter 5.

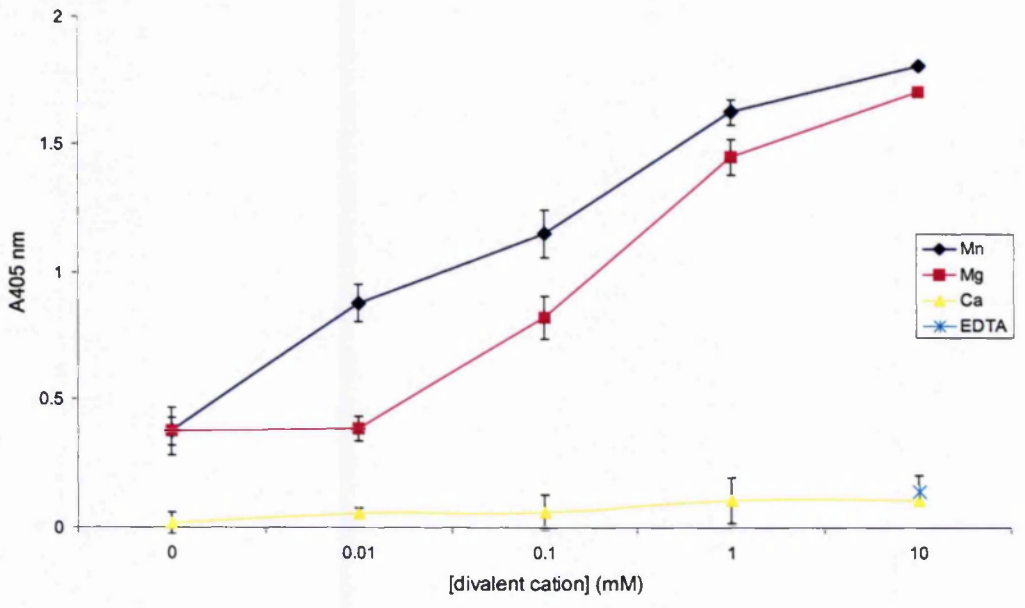

Figure 4.7. Divalent cation dependency of α2 A domain a.a. 140-339 binding to type I collagen. Microtiter plates were coated with 20 μg/ml α2 A domain. Increasing concentrations of divalent cations (Mn^{2+}, Mg^{2+}, Ca^{2+}) or 5 mM EDTA were incubated with biotinylated collagen I. Unbound ligand was washed off, ExtrAvidin-peroxidase was added and detection was carried out with ABTS. Absorbance readings were taken at 405 nm and corrected for non-specific binding. Absorbance values are the average of four wells, the error bars show the standard deviation of the four readings.

4.1.4 The activating I332G mutation in α2 increased collagen binding

To investigate the functional characteristics of the recombinant wt and CA α2 A domains produced in this study, collagen I binding over a range of concentrations was measured in solid-phase ligand-binding assays. Collagen I binding to the immobilised α2 A domains (coated in PBS9+)) was dose-dependent and could be saturated (Figure 4.8). Collagen I showed a higher maximal binding to the CA α2 A domain than to the wt in all concentrations tested (Figure 4.8). The data from three independent experiments testing the binding of biotinylated collagen to the wt and CA α2 A domains were analysed by curve fitting in Sigma Plot, version 8. The non-linear regression analysis program used to fit the specific binding data as a function of ligand concentration, determined the apparent affinity (K_d) for collagen as the concentration of collagen required to reach half-maximal binding. The apparent affinity of the CA α2 A domain for collagen was estimated at 2.3 ± 0.2 nM. The apparent affinity of the wt α2 A domain for collagen was 11.8 ± 0.14 nM. Thus the CA α2 A domain showed approximately a 5-fold increase in affinity for collagen compared to the wt α2 A domain.

Furthermore, to confirm the specificity of the CA α2 A domain, binding to the 50K fragment of fibronectin was examined. Fibronectin, over the same concentration range as collagen I, failed to bind to any of the recombinant α2 A domains, including the constitutive active mutant (data not shown). The lack of 50K binding to the α2 A domains was not surprising, as fibronectin is not a ligand for α2 A domains.

4.1.5 Summary

In this section I described the production of recombinant α2 A domain proteins in the glutathione S-transferase expression system. The DNA coding for the α2 A domains was generated by PCR amplification, sub-cloned into the pGEX-2T expression vector and expressed in bacteria. The two recombinant proteins produced to facilitate the present study are the α2 A domain$^{140\text{-}339}$ and the mutated α2 A domain$^{140\text{-}339}$[I332G]. Purification of the recombinant α2A domain proteins on affinity chromatography columns resulted in high yields of 10-20 mg/l.

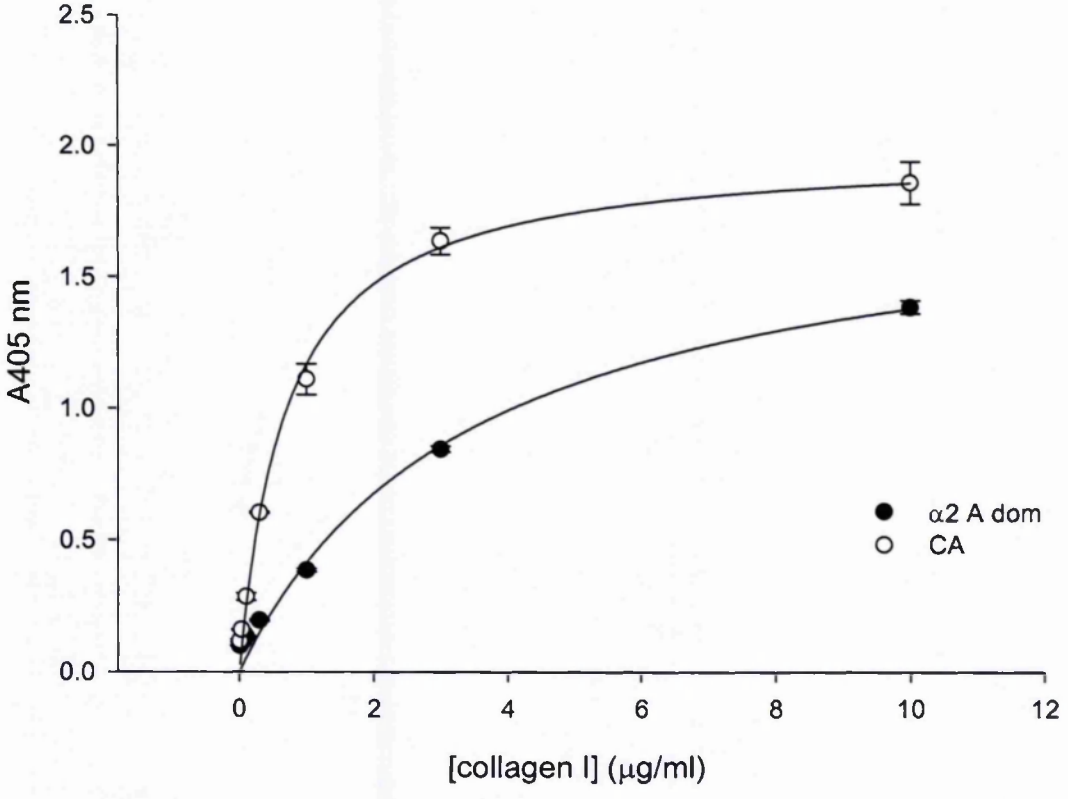

Figure 4.8. Apparent affinity (K_d) of α2 A domains for collagen I. Microtiter plates were coated with 10 µg/ml of GST-fusion α2 A domains in PBS(+). Biotinylated collagen I at varying concentrations was added in the presence of 1 mM Mn^{2+}. Bound biotinylated collagen was detected using ExtrAvidin-peroxidase, followed by ABTS development. Plates were read at 405 nm. Representative experiment showing the means (± S.D.) of three replicate wells. By non-linear regression analysis the K_d of the CA α2 A domain for collagen was 2.3 ± 0.2 nM, the K_d of the Wt α2 A domain for collagen was 11.8 ± 0.14 nM.

The isolated α2 A domain GST-fusion proteins were assayed for their folded state and ligand-binding abilities in solid-phase assays. A panel of five mAbs directed against the human α2 A domain was shown to recognise the recombinant α2 A domains. The initial weak collagen I -binding to the α2 A domain$^{140-339}$ observed in collagen I binding assays, was optimised by the addition of 5 mM Mn^{2+} cations in the solid-phase coating step. Moreover, engineering the Ile332 to Gly substitution in the α2 A domain resulted in high collagen I binding levels in the solid-phase assay. The I332G mutation resulted in a high affinity α2 A domain that did not require stimulation by additional Mn^{2+} cations. Therefore, based on the divalent cation dependency of each recombinant protein, solid-phase protocols were developed accordingly for each A domain to allow for detection of collagen binding to the isolated integrin α2 A domains.

In conclusion, the above experiments established that the recombinant α2 A domains were functional and had retained the functional characteristics of the parent α2β1 integrin. Undoubtedly, examining the activation state of the α2 A domain in isolation as well as in conjunction with the βA domain, in the context of this study will be instructive.

4.2 Production of α2-Fc mutants as soluble truncated α2β1-Fc proteins

4.2.1 Cloning of mutated pEE12.2hα2^{I806} constructs and expression of products in mammalian cells

Next, the I332G substitution was introduced in the context of α2β1-Fc, and the effect of the mutation on the collagen-binding ability of the α2β1-Fc was examined in Fc-capture ELISA type assays. Furthermore, the effect of other α2 subunit mutations on the functional ability of the soluble α2β1 holoreceptor were examined. Amino acids of particular interest in α2β1 integrins are conserved residues such as Glu336 and Phe345, located at the C-terminal end of the α2 A domain and the C-terminal loop linking the A domain to the α2 β-propeller, respectively. The conserved glutamate Glu310 in the αL A domain has been implicated in linking the αL to the β2 A domain with further implications in the indirect regulation of the αA domain function by the βA domain. An amino acid mutation disturbing the principal ligand-binding site in α2 A domain i.e. MIDAS (D151) was also included in the investigations as a negative control.

The mutations shown in Table 4.1 were introduced into the truncated α2 cDNA by PCR. The respective mutated $\alpha2^{I806*}$ fragments (asterisk denoting a mutated subunit) were inserted into the pEE12.2hFc plasmid as *Hind*III / *Sal*I fragments, likewise to the wt TR α2 expressing construct (Figure 4.9).

Table 4.1. Mutations introduced into the α2 subunit of TR α2β1-Fc integrin. Table also showing the equivalent mutation points on αL integrin subunit and the effect on ligand-binding integrin function.

Effect on αA domain activation	Mutation on αL	Equivalent a.a. on α2 (substitutions in parenthesis)
Inactive	D137A	D151(A) [Kamata *et al.*, 1994]
Constitutively active	I306G [Huth *et al.*, 2000]	I332(G)
Inactive	E310A [Yang *et al.*, 2004]	E336(A)
Not tested	F320A	F345(A)
Not tested	I306G/ E310A	I332(G) / E336(A)

For expression of the soluble α2-Fc mutants, pEE12.2hα2^{I806*} were co-transfected with pV16.hβ1^{P455} into CHO L761h mammalian cells. Briefly, the Lipofectamine 2000 method was used for small scale transient transfections; CHO cells were co-transfected with 2 μg DNA of pV.16hβ1^{P455} and with 2 μg DNA of each of the mutated pEE12.2hα2^{I806*} construct. Transfection with the wt TR α2β1-Fc or wt FL α2β1-Fc was used as a positive control in subsequent analysis. A mock transfection with no DNA added was performed in parallel, and used as a negative control. Culture supernatants were recovered from each transfectant well and the neat supernatants were assayed for α2β1-Fc protein expression, correct protein folding and ligand binding on 96-well plates solid-phase assays.

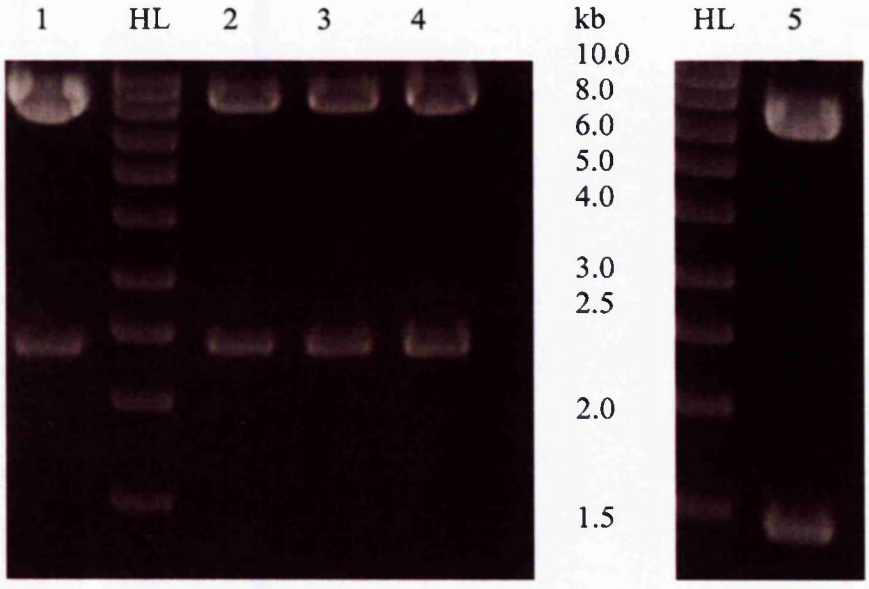

Lane	*Hind*III / *Sal*I digested fragments
1	pEE12.2hα^{I806} [I332G]
2	pEE12.2hα^{I806} [E336A]
3	pEE12.2hα^{I806} [F345A]
4	pEE12.2hα^{I806} [I332G/E336A]
5	pV16hβ1^{P455}

HL	HyperLadder I

Figure 4.9. Agarose gel analysis of the mutated α2-Fc expressing constructs in pEE12.2α2^{I806}. Mutations were introduced into the TR α2^{I806} cDNA by PCR. All fragments were ligated in the pEE12.2hFc vector likewise to the unmodified α2^{I806} as *Hind*III / *Sal*I fragments. Shown in lane 5, the TR wt β1 expressing construct utilised to co-transfect CHO L761h cells for the generation of TR α2^{I806*}β1^{P455}-Fc mutants.

4.2.2 Analysis of folding and ligand binding properties of α2 mutants in truncated α2β1-Fc integrins

To test for correct folding of the α2 mutants in α2β1-Fc, the binding of mAbs directed against both integrin subunits was assessed in Fc-capture assays. The anti-α2 integrin mAbs (JA218, 12F1), as well as the anti-β1 mAbs (12G10, TS2/16) recognised the α2 mutants in the TR α2β1-Fc integrin, comparable to the wt TR α2β1-Fc (Figure 4.10a) positive control. In addition, the anti-human Fc antibody binding levels indicated that all mutants were expressed at similar proteins levels to the positive control.

To examine ligand binding to the $\alpha2^{I806*}\beta1^{P455}$-Fc mutants, recombinant-Fc integrin from transfection supernatants were captured with anti-human Fc antibody, and biotinylated collagen I was added to the wells in the presence of 1 mM Mn^{2+}. Results demonstrated that the α2 [I332G] mutant bound collagen I (Figure 4.10b). It was also observed that whereas the E336A mutation resulted in loss of collagen binding, the double I332G / E336A mutant was able to bind collagen to a similar extent as seen for the wt integrin. In contrast, the remaining mutations introduced in the $\alpha2^{I806}$-Fc resulted in loss of the collagen binding ability of the TR α2β1-Fc heterodimer. To examine whether collagen binding could be induced by the addition of activating agents, the stimulating β1 integrin mAbs 12G10 and TS2/16 were utilised. However, there was no change observed in the ligand binding ability of the $\alpha2^{I806*}\beta1^{P455}$-Fc mutants, with the exception of the I332G α2β1-Fc mutant, as no collagen I binding was promoted under any experimental condition. The functionally active TR α2[I332G]β1-Fc mutant was chosen to continue the investigations.

4.2.3 Collagen I binding of α2[I332G]β1-Fc integrin

Next, collagen I solid-phase assays were used to study the ligand-binding properties of the TR α2[I332G]β1-Fc integrin in more detail. Experiments were carried out with neat culture supernatants from transfected mammalian cells, in the presence of 1 mM Mn^{2+} unless otherwise stated. The wt FL and wt TR α2β1-Fc proteins were included in the experiments to complete profiling of the ligand-binding properties of the recombinant α2β1-Fc integrins. As expected, collagen I bound to the α2β1 Fc-fusion integrins in the presence of 1 mM Mn^{2+} divalent cation alone, without external activating agents.

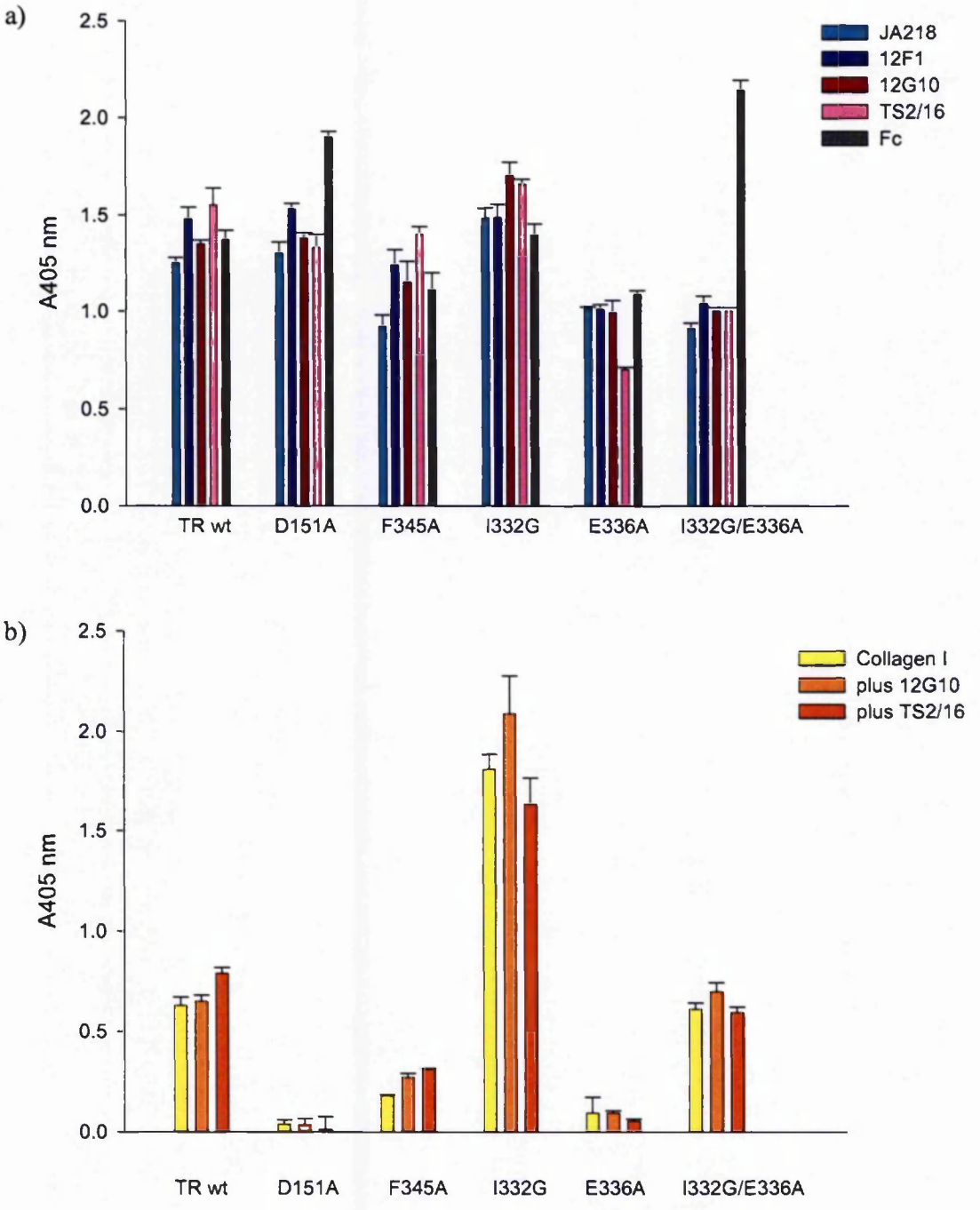

Figure 4.10. Antibody (a) and ligand (b) binding to soluble TR Fc-tagged α2β1 integrins with mutation(s) in the α2 subunit. Culture supernatants from $\alpha2^{I806*}\beta1^{P455}$ - Fc transient transfections were analysed in Fc-capture assays, performed in the presence of 1 mM Mn^{2+}. Binding was detected with 10 μg/ml integrin antibodies: anti-α2 (JA218, 12F1), anti-β1 (12G10, TS2/16), and 1 μg/ml anti-Fc antibody or biotinylated collagen I (1 μg/ml) in the presence of the integrin activating mAb TS2/16 or alone. Bound mAbs were detected with the appropriate HRP-conjugated secondary antibodies (1 μg/ml), whereas bound biotinylated collagen was detected using ExtrAvidin-peroxidase. Absorbance (405 nm) values and error bars represent the average and standard deviation of one experiment (n=4).

Moreover, in the presence of the stimulating TS2/16 β1 antibody collagen binding levels did not increase further but remained at the same levels as for Mn^{2+} only. These results indicated that all three α2β1-Fc proteins examine in Figure 4.11a are expressed in a constitutively active state. Surprisingly, in the presence of 12G10, a stimulating β1 LIBS mAb, there was a 20% decrease in the binding levels of collagen.

To examine the specificity of collagen binding to the α2β1-Fc integrins, ligand binding solid-phase assay was carried out in the presence of α2β1 inhibitors (Figure 4.11b). A potent inhibitory antibody of β1 integrins, mAb13, abrogated collagen binding to both the wt FL and wt TR α2β1 integrins to basal binding levels (as taken from the EDTA readings). However, mAb13 had only a minimal inhibitory effect (15%) on α2[I332G]β1-collagen binding. The Gi9 inhibitory α2 mAb was also effective in reducing collagen binding by 50% and 70% to the wt FL and wt TR α2β1-Fc proteins respectively; but for the α2 [I332G] β1-Fc integrin there was no more than a 28% decrease in the collagen binding levels. Rhodocetin, a snake venom inhibitor of α2β1 integrins (a gift from Dr. J. Eble, University of Munster, Germany), was the most effective agent in inhibiting collagen binding to all the Fc-fusion integrins. There was a 55% decrease in the collagen binding levels to the soluble α2[I332G]β1 integrin, and a complete blockage of ligand binding to the recombinant wt integrins. Collagen I binding was also dramatically reduced for the integrins examined in the presence of EDTA (Figure 4.11a), demonstrating a cation-dependent integrin-mediated ligand interaction. Taken together the above data demonstrated that the α2[I332G] mutant bound specifically to collagen I in a cation-dependent manner.

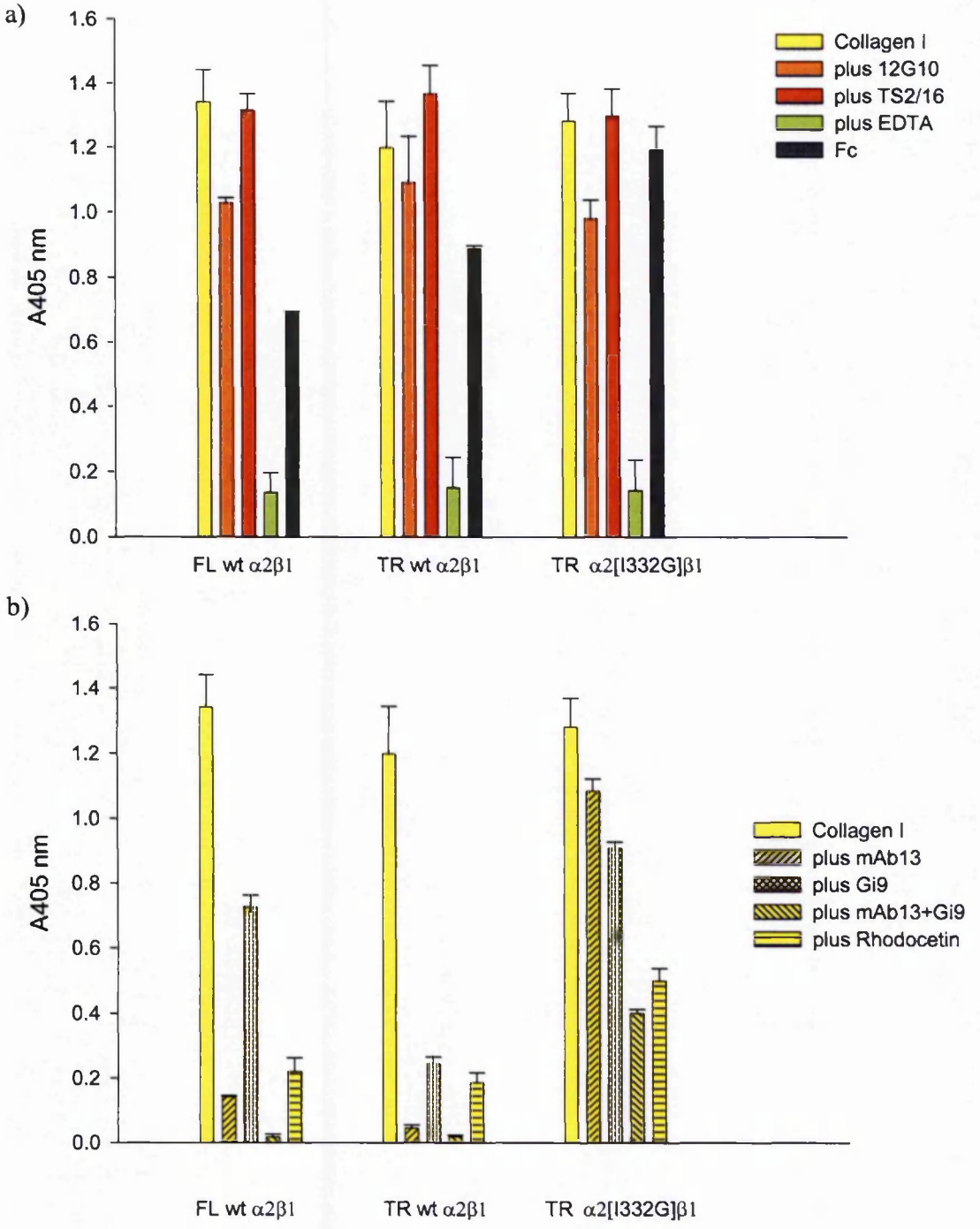

Figure 4.11. Effect of stimulatory (a) and inhibitory (b) reagents on the collagen I binding to α2β1-Fc variants. Culture supernatants from transfected CHO cells with $\alpha2^{E1129}\beta1^{D708}$, $\alpha2^{I806}\beta1^{P455}$ and $\alpha2^{I806}$[I332G]$\beta1^{P455}$ were analysed in Fc-capture assays, performed in the presence of 1 mM Mn^{2+}. In (a) the recombinant proteins were examined for their capacity to bind collagen in the presence of 10 μg/ml anti-β1 activating mAbs 12G10 and TS2/16. Binding to the anti-Fc antibody is included as an approximate indicative of the expression levels of each protein. In (b) the specificity binding of collagen I was examined in the presence of 10 μg/ml inhibitory anti-β1 (mAb13) and anti-α2 (Gi9) mAbs and 0.79 nM rhodocetin. Absorbance (405 nm) values and error bars represent the average and standard deviation from one experiment (n=4).

4.3 Analysis of the activatory effect of α2[I332G] mutation on α2β1-Fc function – the series of TR α2[I332G]β1*-Fc double mutants

4.3.1 Expression and folding of the TR α2[I332G]β1*-Fc double mutants

An activating α2 mutation as part of the whole α2β1 integrin heterodimer would be a useful tool to study further the inactivating β1 mutations examined in Chapter 3. If the I332G mutation regulates allosterically the collagen-binding α2 A domain activity, then the I332G substitution should rescue the ability of the β1 A domain mutants to bind to collagen I. In order to investigate this hypothesis, the TR α2[I332G]-Fc subunit was co-expressed with the mutated β1-Fc subunits in CHO L761h cells. The resulting six TR α2β1-Fc double mutants (shown in Figure 4.12) were examined for expression, correct folding and ligand binding ability in solid-phase assays.

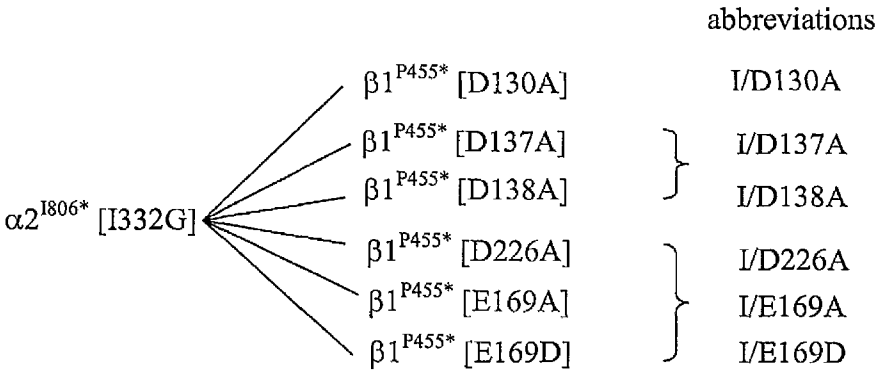

Figure 4.12. The series of the TR α2 [I332G] β1*-Fc double mutants. Residues in superscript denote the last amino acid of the human integrin α/β subunit in the cloned sequence. Asterisks identify mutated integrin subunit, residues in brackets specify the mutation. Each abbreviation describe the mutation in α / the mutation in the β subunit of the integrin heterodimer. The 'I' is for the I332G mutation in the α2 subunit.

ELISA sandwich assays were used as previously described to examine the Fc-capture integrins. Antibody binding to $\alpha2^{I806}$[I332G]$\beta1^{P455}$ -Fc is also shown as positive control. All six double integrin mutants expressed the epitopes for a panel of anti-α2 and anti-β1 mAbs (Figures 4.13). These results indicated that all TR α2β1-Fc double mutants were expressed in CHO transfectants and were folded correctly.

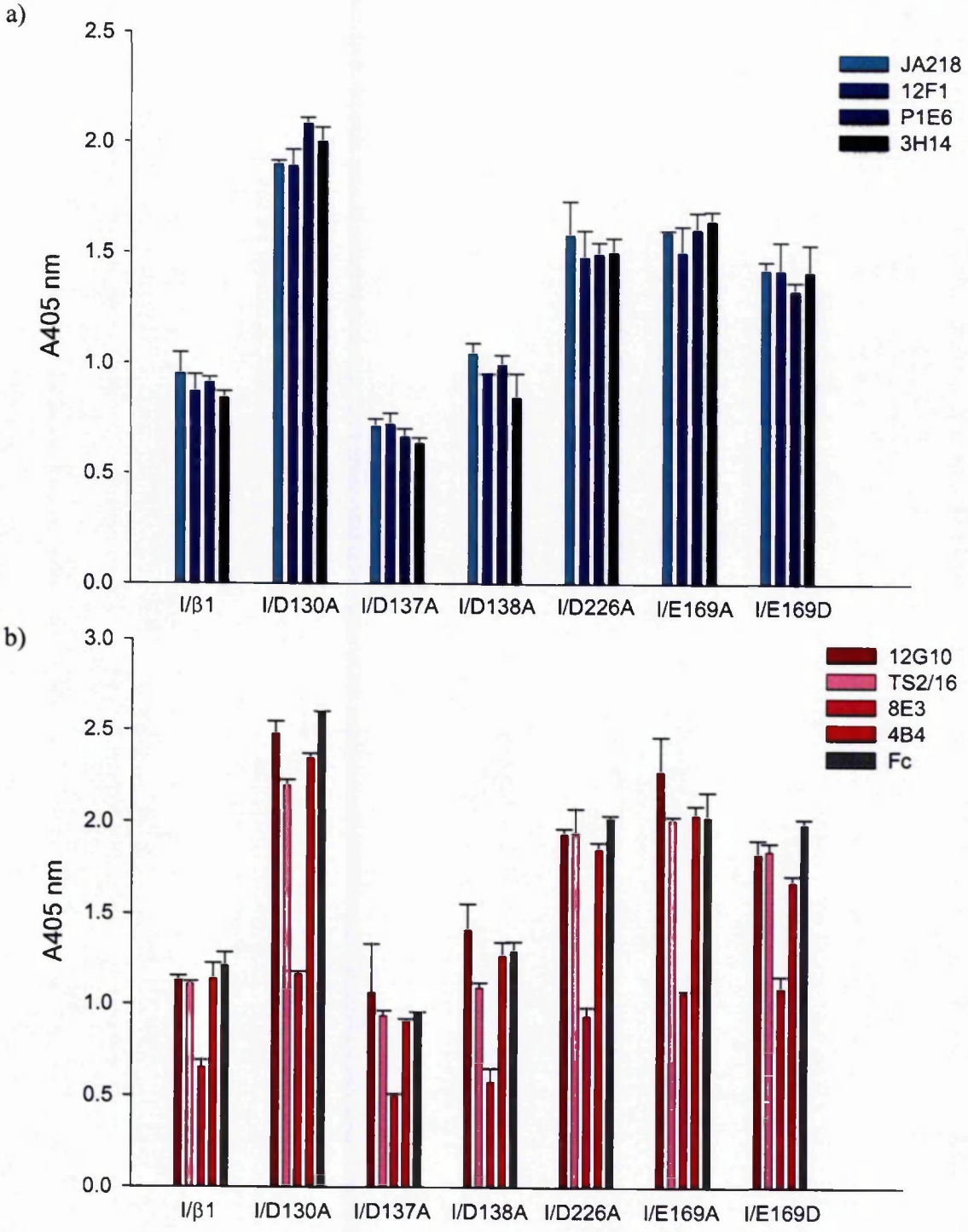

Figure 4.13. Antibody binding to soluble TR α2[I332G]β1-Fc integrin mutants. Culture supernatants from transfected CHO cells $\alpha 2^{I806}[I332G]\beta 1^{P455*}$ with the β1 MIDAS (D103A), ADMIDAS (D137A, D138A) or LIMBS (D226A, E169A, E169D) mutations were analysed in Fc-capture assays, performed in the presence of 1 mM Mn^{2+}. Recombinant Fc-fusion integrins were detected in a) with 5 μg/ml anti-α2 antibodies, and in b) with 5 μg/ml anti-β1 antibodies and 1 μg/ml anti-Fc antibody. Bound mAbs were detected with anti-mouse HRP-conjugated secondary antibodies (1 μg/ml). Absorbance (405 nm) values and error bars represent the average and standard deviation from one experiment (n=4). Non-specific binding as estimated from the mock transfection has been incorporated in the calculations.

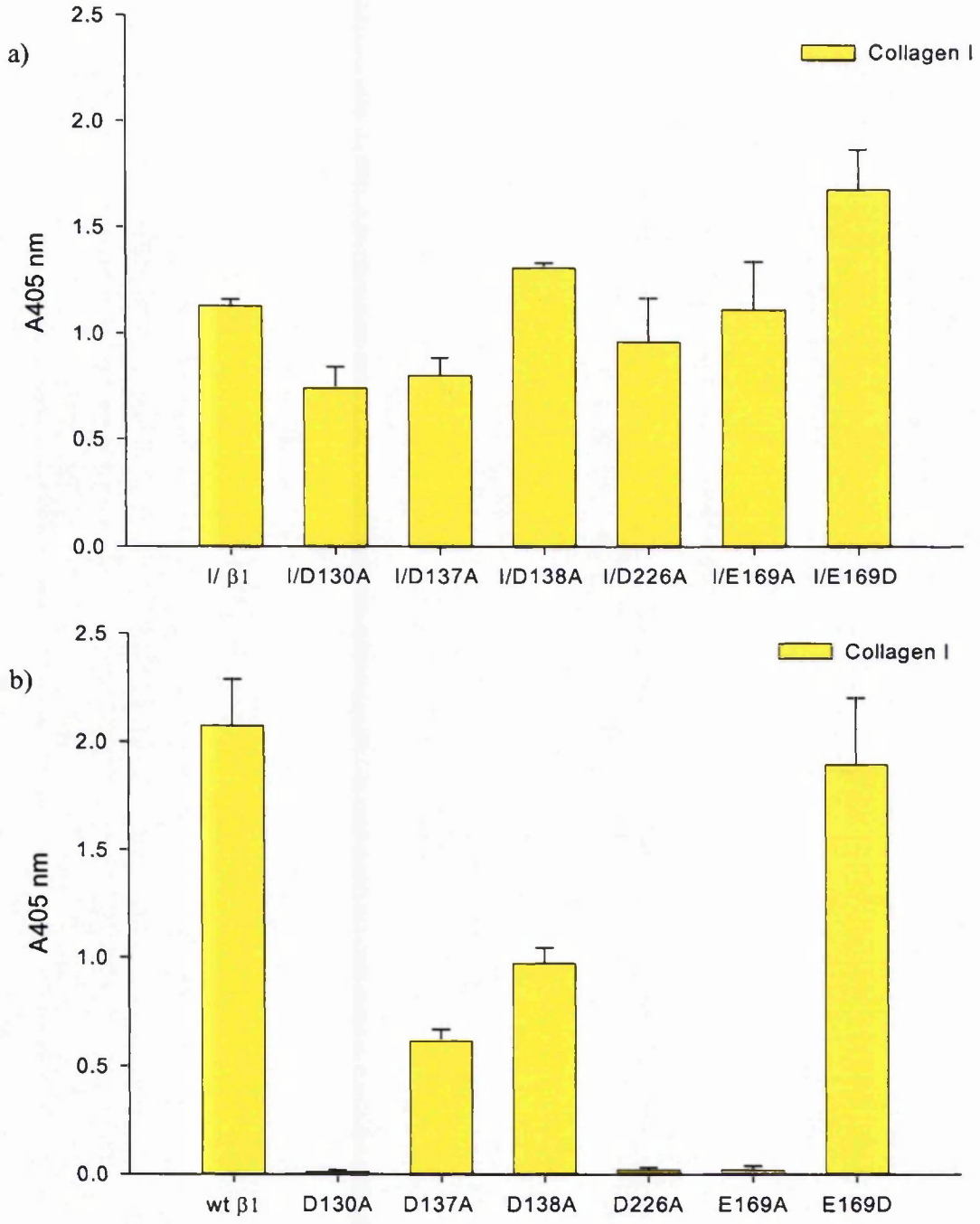

Figure 4.14. The α2[I332G] mutation rescued the collagen I ability of the TR α2[I332G]β1* integrin double mutants. a) Culture supernatants from transfected CHO cells with $\alpha2^{I806}$[I332G]$\beta1^{P455*}$ containing the β1 MIDAS (D103A), ADMIDAS (D137A, D138A) or LIMBS (D226A, E169A, E169D) mutations were analysed in Fc-capture assays, performed in the presence of 1 mM Mn^{2+}. b) The collagen I binding data for the mutated $\alpha2^{I806}$ [wt]$\beta1^{P455*}$-Fc integrins (replicated from Figure 3.10) are shown for comparisons with panel a). Recombinant Fc-fusion integrins were detected in with 1 μg/ml biotinylated collagen I. Bound biotinylated collagen was detected using ExtrAvidin-peroxidase. Absorbance (405 nm) values and error bars represent the average and standard deviation from one experiment (n=4). Non-specific binding as estimated from the mock transfection has been incorporated in the calculations.

4.3.2 Collagen I binding to the TR α2[I332G]β1*-Fc double mutants

Following confirmation of correct protein structure, the ability of the double mutants to bind collagen I was examined in solid-phase assays. CHO cell transfection culture supernatants were captured with anti-human Fc antibody and collagen I was added to the wells in 1 mM Mn^{2+}. As seen in Figure 4.14 the double I332G / β1 A domain α2β1-Fc mutants were able to support collagen I binding at comparable levels to the positive control. The α2[I332G]-Fc subunit combined with either of the β1 ADMIDAS mutants, D137A or D138A, enhanced the low collagen binding levels of the mutated α2β1-Fc dimer (described in Figure 3.10) to similar binding levels observed for the positive control. More importantly, the β1 MIDAS (D130A) and both the β1 LIMBS (D226A, E169A) mutants gained collagen I binding ability when expressed in conjunction with the TR α2[I332G]-Fc mutant. Ligand binding in the presence of the β1 mAbs 12G10 and TS2/16 was also examined in parallel (Figure 4.15). Upon addition of the LIBS mAb 12G10 there was a small decrease in the levels of collagen binding, whereas upon addition of the β1 stimulatory TS2/16 mAb the collagen binding levels for all α2β1-Fc variants were at the same order as collagen alone. Thus, upon addition of the TS2/16 there was no further stimulation of collagen binding.

The above results indicated that the I332G substitution is a gain-of-function mutation. Subsequent studies using the double I332G / β1 A domain α2β1-Fc mutants attempted to elucidate the role of the subtle conformational changes that occur in the βA domain of α2β1 and can regulate ligand binding.

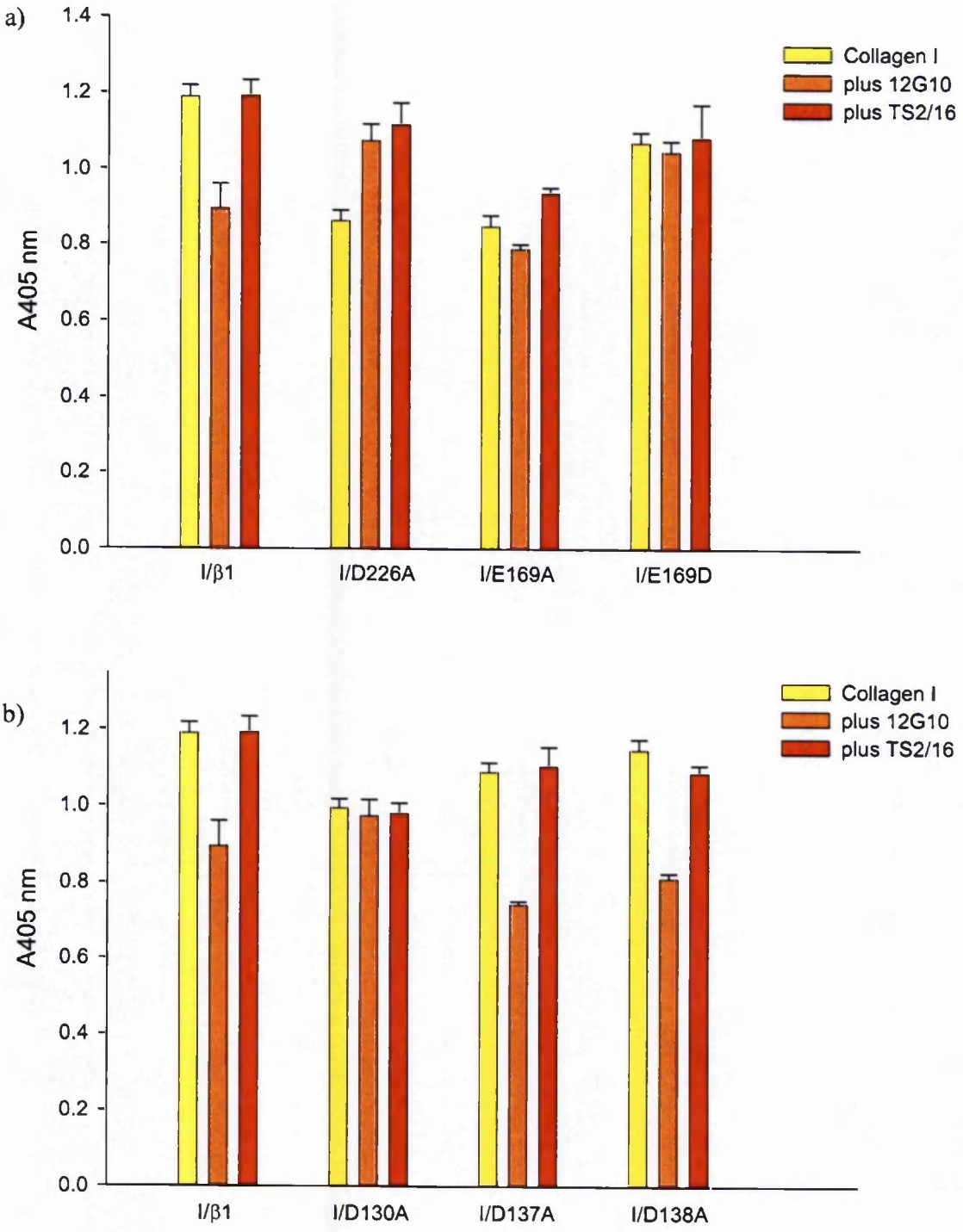

Figure 4.15. Collagen I binding to soluble TR α2[I332G]β1*-Fc integrin double mutants. Culture supernatants from transfected CHO cells $\alpha 2^{I806}$[I332G]$\beta 1^{P455*}$ with the β1 mutated at the LIMBS (D226A, E169A, E169D), MIDAS (D103A) or ADMIDAS (D137A, D138A) site were analysed in Fc-capture assays, performed in the presence of 1 mM Mn^{2+}. The capacity of collagen I binding was examined in the presence of 10 μg/ml activating anti-β1 antibodies, 12G10 and TS2/16. Bound biotinylated collagen was detected using ExtrAvidin-peroxidase. Absorbance (405 nm) values and error bars represent the average and standard deviation from one experiment (n=4). Non-specific binding as estimated from the mock transfection has been incorporated in the calculations.

4.3.3 Apparent affinities of TR α2[I332G]β1*-Fc variants for collagen

To estimate the apparent affinity (K_d) of recombinant integrin-collagen I interaction, Fc captured integrin variants from culture supernatant were tested in the collagen I binding ELISA. Collagen was added to the wells at a concentration range of 0.01 - 10 μg/ml, in the presence of 1 mM Mn^{2+}, and the absorbance readings corresponding to the collagen I binding levels were analysed by the one-site saturation, non-linear regression analysis program in Sigma Plot, version 8. Representative experiments are shown in Figure 4.16 and 4.17. The K_d values for the interactions were determined as the concentration of collagen to obtain half-maximal binding. The K_d values for the binding of recombinant soluble integrins to collagen varied from approximately 1.0 nM to 10 nM (summarised in Table 4.2).

Table 4.2. Apparent affinities for collagen I to solid-phase α2β1-Fc integrins. Apparent affinity (K_d) values were estimated by non-linear regression analysis and reflect the concentration of collagen required for half-maximal ligand binding. Data shown are the average values ± S.D. from three individual experiments for each recombinant integrin.

	K_d (nM)	± S.D.
FL	0.92	0.16
TR	1.52	0.23
α2[I332G] β1	1.07	0.06
α2[I332G]] β1[D130A]	9.92	1.32
α2[I332G] β1[D137A]	8.17	2.14
α2[I332G] β1[D138A]	2.94	0.29
α2[I332G] β1[D226A]	6.22	1.25
α2[I332G] β1[E169A]	4.87	0.69
α2[I332G] β1 E169D]	1.17	0.06

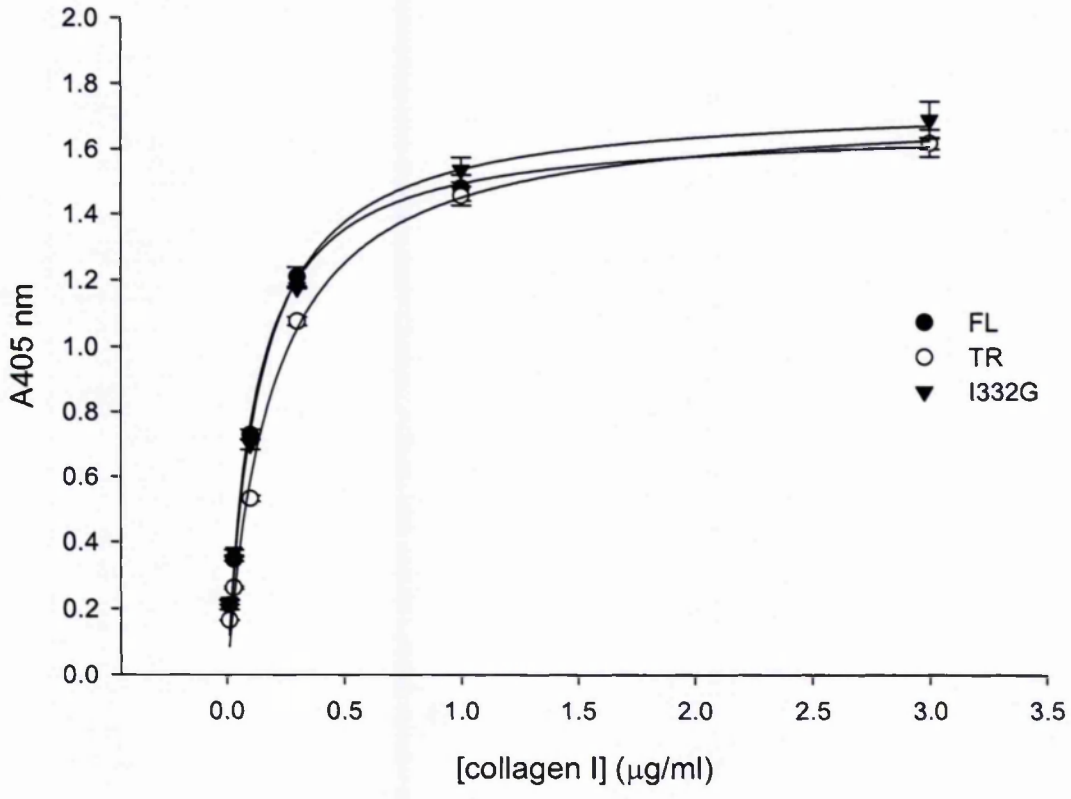

Figure 4.16. Apparent affinity (K_d) of soluble α2β1-Fc integrins for collagen I. Soluble integrins-Fc: $\alpha2^{E1129}\beta1^{D708}$, $\alpha2^{I806}\beta1^{P455}$ and $\alpha2^{I806}$[I332G]$\beta1^{P455}$, were captured into 96-well plates pre-coated with the anti-human Fc antibody. Biotinylated collagen I at varying concentrations was added in the presence of 1 mM Mn^{2+}. Bound biotinylated collagen was detected using ExtrAvidin-peroxidase. Representative experiment showing mean (± S.D.) of four replicate wells. By non-linear regression analysis the K_d values for collagen were: to FL wt α2β1-Fc, 0.92 ± 0.16 nM; to TR wt α2β1-Fc, 1.52 ± 0.23 nM; to TR α2[I332G]β1-Fc, 1.07 ± 0.06 nM.

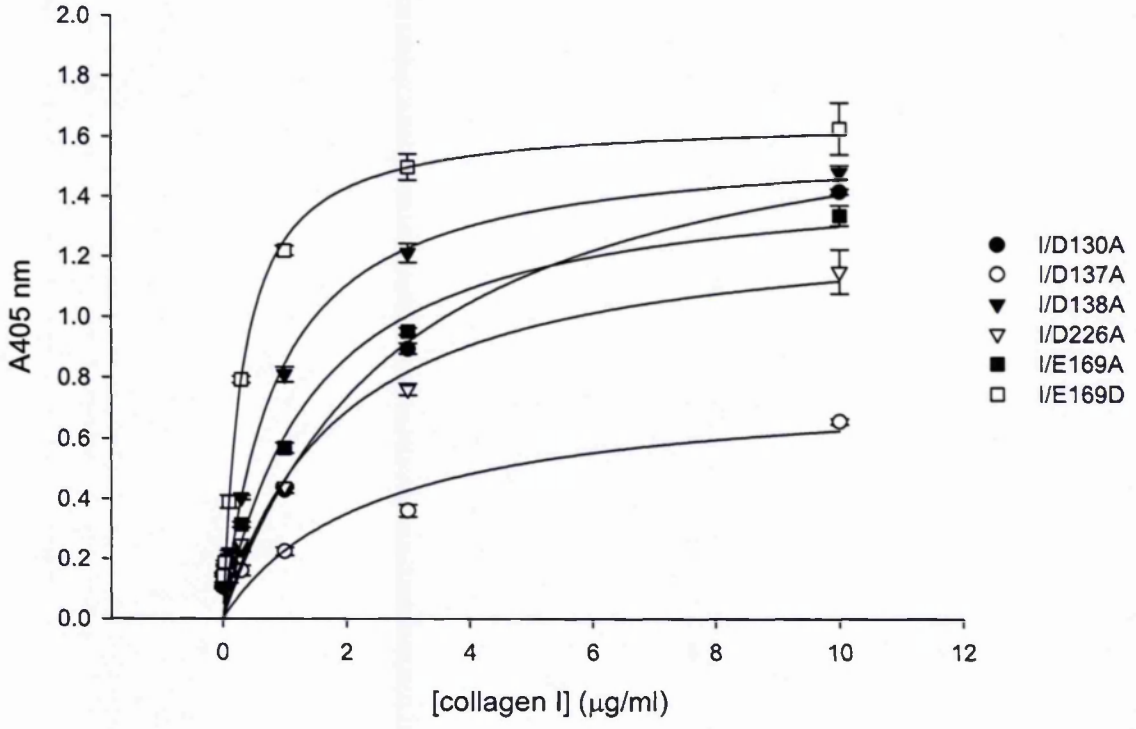

Figure 4.17. Apparent affinity (K_d) of I332G series of α2β1-Fc double mutants for collagen I. Mutated integrins-Fc in $\alpha2^{I806}$[I332G]$\beta1^{P455}$, were captured into 96-well plates pre-coated with the anti-human Fc antibody. Biotinylated collagen I at varying concentrations was added in the presence of 1 mM Mn^{2+}. Bound biotinylated collagen was detected using ExtrAvidin-peroxidase. Representative experiment showing mean (± S.D.) of four replicate wells. The apparent affinities for collagen are summarised in Table 4.2.

The apparent affinities of the wt FL and wt TR α2β1-Fc for collagen were estimated at 0.92 ± 0.16 nM and 1.52 ± 0.23 nM, respectively. Thus, the truncation of the C-terminal extracellular α2 and β1 subunits decreased the affinity of the wt soluble integrin for collagen by approximately a two-fold. In the case of the I332G mutant, which is also a truncated α2β1-Fc integrin, the affinity for collagen was estimated at 1.07 ± 0.06 nM. This suggested that the wt FL α2β1-Fc and α2[I332G]β1-Fc integrins interacted with collagen with a similar affinity.

In contrast, the broad range (1.0 - 10 nM) of K_d values for collagen to the double α2β1-Fc mutants suggested a great variation in affinities between the different β1 A domain mutants. The β1 MIDAS and D137A ADMIDAS α2[I332G]β1-Fc double mutants required the highest concentrations of collagen to reach saturation, as taken from K_d values of 9.9 ± 1.32 nM and 8.1 ± 2.1 nM, respectively. That is an 8–fold decrease in collagen-binding affinity relative to the α2[I332G]β1-Fc integrin, though, the D138A ADMIDAS mutant (K_d ~ 2.9 nM) showed only a 2.7-fold decrease in collagen affinity compared to α2[I332G]β1-Fc. Moreover, with an estimated K_d for collagen at 1.17 ± 0.06 nM, the E169D α2[I332G]β1-Fc LIMBS integrin revealed a similar affinity for collagen to the α2[I332G]β1-Fc (K_d ~ 1.07 nM). However, the concentration of collagen that gave 50% binding for the D226A and E169A α2[I332G] β1[LIMBS]-Fc mutants were estimated at 6.2 ± 1.2 nM and 4.8 ± 0.7 nM. These results showed that the β1 A domain mutations which disrupted the cation-binding sites, had a significant negative effect on the apparent affinity of the α2β1 integrin for collagen.

The above data also suggested that collagen I at around 1.0 μg/ml is the ideal concentration for further testing. The binding of collagen type I to Fc captured α2β1 increased with increasing concentrations of collagen and reached saturation at approximate 2 μg/ml collagen I. At 0.5 -1 μg/ml collagen I, the binding to the α2β1 variants was not saturated but corresponded approximately to the half-maximal level of binding. This would allow for optimal promotion or inhibition of binding by cations to be observed.

4.4 Summary

The collagen-binding abilities of α2β1 variants carrying mutations in the α2 integrin subunit were examined in this section. The I332G activating mutation, which resulted in high collagen binding to the isolated α2 A domain, was shown to affect the concentration of collagen required for half-maximal ligand binding. This activating mutation in the α2 subunit was co-expressed with each of the inactivating β1 cation-binding mutations, described in Chapter 3, as soluble α2β1-Fc integrins. The I332G / β1 A domain double mutants were analysed for their ability to support ligand binding in Fc-capture ELISA type assays. The results showed that the I332G mutation rescued the ability of the double mutants to bind collagen. Thus, the effect of allosteric activation of α2β1-collagen binding was shown to dominate the inhibitory modulation by the βA domain.

A summary of the collagen binding ability of the recombinant integrins is shown in Table 4.3.

Table 4.3. Summary of the collagen I binding ability of the single and double α2β1 integrin-Fc mutants. The β1 A domain single mutants compromised or abolished collagen I binding. The double I332G / β1 A domain α2β1 mutants gained the collagen I binding function. Symbols indicate '+', ability to bind; '-', no binding ability; '-/+' weak interaction.

TR α2-Fc		Integrin-Fc
wt	I332G	
+	+	wt β1–Fc
-	+	β1 [D130A] –Fc
-/+	+	β1 [D137A] –Fc
-/+	+	β1 [D138A] –Fc
-	+	β1 [D226A] –Fc
-	+	β1 [E169A] –Fc
+	+	β1 [E169D] –Fc

Chapter

5.0 Effect of cations on collagen I binding to α2β1-Fc integrins

In this study, a soluble form of α2β1 integrin has been generated in a mammalian expression system as an Fc-fusion protein. The recombinant integrin retained the structure and most importantly the function of the whole α2β1 integrin. Following the successful production of wild-type recombinant integrin variants, mutations were introduced in either or both integrin subunits to study the interactions between the α2 and β1 subunits of this heteroreceptor. In chapter 3, single mutations in the MIDAS, ADMIDAS and LIMBS cation-binding sites of β1 A domain were shown to perturb type I collagen binding to the α2β1-Fc mutants. Thus, the functional properties of the single β1 A domain α2β1 mutants could not be studied further in solid phase collagen-binding assays. However, a mutation in the α2 A domain, Ile332Gly, described in chapter 4, was shown to have an activating effect in the context of β1 A domain α2β1-Fc mutants. The resulting double I332G / β1 A domain α2β1-Fc mutants offered the opportunity to examine the functional significance of the β1 A domain cation-binding sites in relation to the collagen-binding activity of an αA-containing integrin such as α2β1. The effect of the β1 cation-binding site mutations on the specificity and requirement for cations in collagen binding is examined in this chapter, and compared to the wt α2β1 integrin.

5.1 The effect of Mn^{2+}, Mg^{2+} or Ca^{2+} on collagen I binding

Having shown that the recombinant α2β1 interaction with collagen required divalent cations, I investigated in greater detail the ability of the α2β1-Fc integrins to bind collagen I in the presence of Mn^{2+}, Mg^{2+} or Ca^{2+} cations. To study the divalent cation dependency/specificity on integrin-ligand interactions these experiments were conducted with buffers that have been filtered through a Chelex column to ensure removal of minute traces of cations from the assay buffers (Methods, 2.2.6c). Binding measured for immobilised integrins to 1-2 μg/ml biotinylated collagen I alone, without the addition of divalent cations in the collagen preparation, was minimal and was assumed as background binding. This was subtracted from all readings used for the statistical analysis.

The ability of each integrin to bind collagen was measured across a range of increasing Mn^{2+}, Mg^{2+} or Ca^{2+} cation concentrations and the collagen-binding data were processed by a computer-based, non-linear regression analysis program in Sigma Plot, version 8. The one-site saturation equation was used to fit the data to binding curves and calculate the apparent affinity (K_d) of each cation, which reflects the concentration of cation required for half-maximal ligand binding. Representative examples of the binding curves from single experiments are shown in Figures 5.1 - 5.6.

First, the binding of intact, native α2β1 integrin to collagen in the presence of different divalent cations was examined. In a typical integrin-ligand interaction, binding was supported by Mn^{2+} and Mg^{2+} divalent cations, but not by Ca^{2+} (Figure 5.1a). The binding curve of α2β1 reached a plateau at a much lower concentration of Mn^{2+} than that of Mg^{2+}. The K_d values of α2β1 were determined at 34 ± 16 μM for Mn^{2+} and 2.6 ± 1 mM for Mg^{2+}. Thus, integrin α2β1 showed a 75–fold greater affinity when 1 μg/ml collagen was added in the presence of Mn^{2+} in comparison to Mg^{2+}. Purified wt α2 A domain was examined next. Compared to the whole α2β1 integrin, the cation binding profile of the α2 A domain-collagen (Figure 5.1b) showed a clear difference in the Mg^{2+}-supported collagen binding. One-site saturation statistical analysis of the data estimated that the amount of Mn^{2+} and Mg^{2+} required for half-maximal collagen binding was approximately 25 ± 8 μM and 45 ± 14 μM, respectively. Thus, the MIDAS on the α2 A domain bound Mn^{2+} and Mg^{2+} with similar affinities.

The Fc-captured integrins were then examined for their collagen-binding properties in the presence of increasing concentrations of divalent cations by Fc-capture ELISA type assays. For all functional recombinant α2β1 integrins examined, collagen-binding in the presence of Mn^{2+} or Mg^{2+} was dose-dependent and saturable, which allowed for the estimation of K_d values. However, as observed for the intact α2β1, Ca^{2+} ions did not support the binding of collagen to any of the soluble α2β1-Fc integrins. Hence, it was not possible to obtain an indication of the relative affinity of recombinant α2β1 integrins for collagen in the presence of Ca^{2+}.

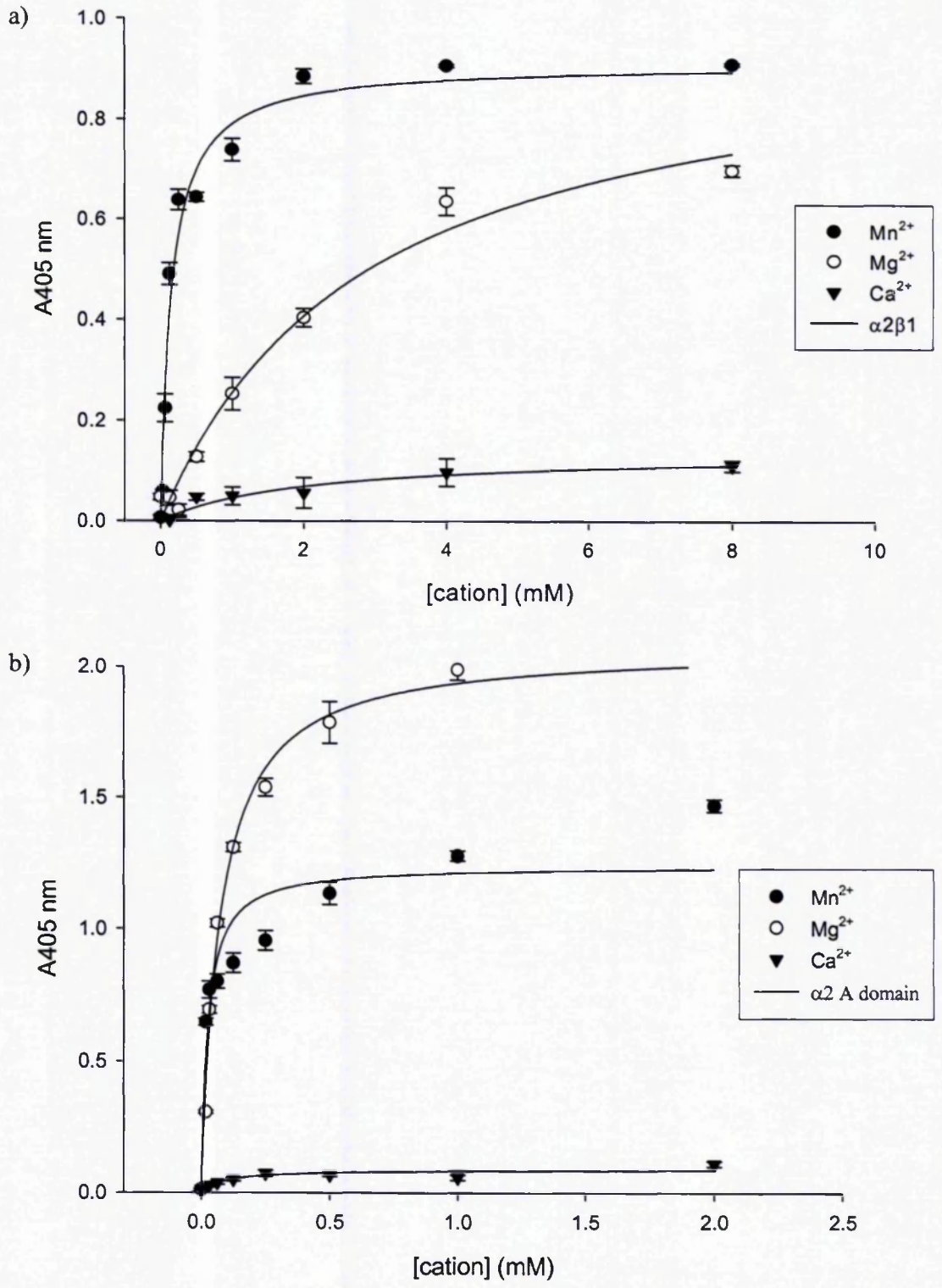

Figure 5.1. Effect of divalent cations on the binding of collagen I to purified α2β1 (a) and GST-α2 A domain (b). Assays were performed using purified whole α2β1 integrin and GST-α2 A domain. Binding of collagen I was measured in the presence of varying concentrations of Mn^{2+}, Mg^{2+}, or Ca^{2+}. Absorbance values and error bars represent the average and S.D. of four readings. By non-linear regression analyses the mean K_d values of α2β1 were: for Mn^{2+} = 0.0344 ± 0.01 mM; for Mg^{2+} = 2.67 ± 1.0 mM; of α2 A domain for Mn^{2+} = 0.025 ± 0.008 mM, for Mg^{2+} = 0.045 ± 0.01 mM.

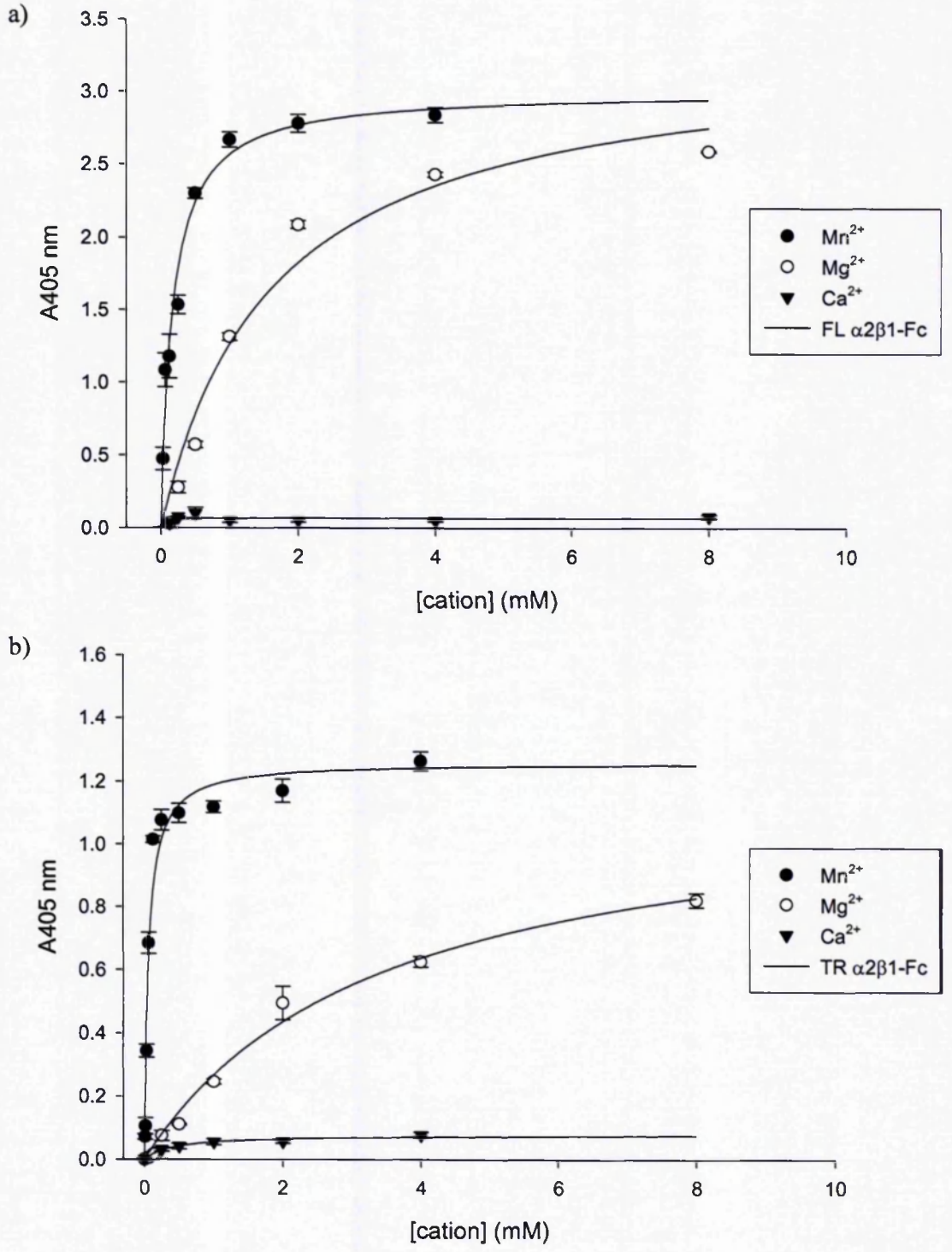

Figure 5.2. Effect of divalent cations on the binding of collagen I to FL wt α2β1-Fc (a) and TR α2β1-Fc (b). Assays were performed using Fc-captured integrin from culture supernatants. Binding of collagen I was measured in the presence of varying concentrations of Mn^{2+}, Mg^{2+}, or Ca^{2+}. Absorbance values and error bars represent the average and S.D. of four readings. By non-linear regression analyses the mean K_d values of FL α2β1-Fc were for $Mn^{2+} = 0.063 \pm 0.007$ mM; for $Mg^{2+} = 1.67 \pm 0.23$ mM; of TR α2β1-Fc were for $Mn^{2+} = 0.109 \pm 0.031$ mM, $Mg^{2+} = 4.0 \pm 1.1$ mM.

A similar profile of cation binding was observed for the wt FL and wt TR α2β1-Fc, relative to each other and to the whole α2β1 integrin. The binding curves for the wt α2β1-Fc integrins (Figure 5.2) showed that Mn^{2+} supported the highest levels of binding, with a significant difference compared to the Mg^{2+}-supported collagen-binding levels. In particular, Mn^{2+}-supported collagen binding to wt FL and wt TR α2β1-Fc showed half-maximal binding at 63 ± 7 μM and 100 ± 31 μM Mn^{2+}, respectively. The K_d value of wt FL α2β1-collagen for Mg^{2+} was calculated at 1.6 ± 0.2 mM. Yet, increasing Mg^{2+} concentrations up to 8.0 mM increased collagen binding to the TR soluble integrin in a dose-dependent manner but reached saturation at the highest concentration tested, resulting in a K_d of approximately 4.0 ± 1.1 mM Mg^{2+} for wt TR α2β1-Fc. This is in agreement to the solid phase assay results for the intact α2β1 integrin, whereby both divalent cations supported binding of the recombinant wt α2β1-Fc integrins to collagen I although Mn^{2+} was more effective than Mg^{2+}. Thus, the results showed that ligand binding to the Fc-fusion wt integrins was modulated by divalent cations in a very similar manner to the parent α2β1 integrin.

Next, the effect of these ions on collagen binding to the mutated α2β1-Fc integrins was examined over a range of divalent cation concentrations (Figure 5.3 –5.6). 100 μM Mn^{2+} strongly induced collagen binding at maximum levels for all I332G mutants examined. Mn^{2+} cations supported binding of the TR α2 [I332G] β1[wt] -Fc to collagen with a K_d value of 45 ± 27 μM Mn^{2+}. This value resembled the K_d measurements of Mn^{2+} for all the double I332G mutants, which had K_d values ranging from 20 to 60 μM. Thus, the I332G in the α2 integrin subunit had no significant effect on the apparent affinity of Mn^{2+} binding to the MIDAS.

Likewise to the results for Mn^{2+}-supported binding, 100-150 μM Mg^{2+} greatly induced collagen binding to the α2[I332G] β1 mutants. The I332G mutants bound collagen with similar K_d values, relative to each other, in the presence of Mg^{2+}. With the exception of the α2 [I332G] β1[D137A] -Fc mutant which had a K_d of 600 ± 200 μM for Mg^{2+}, the remaining I332G mutants showed an average K_d value of 100-150 μM in the presence of Mg^{2+}. Hence, ligand binding was already maximal (near 60%) for all I332G mutants when 1 μg/ml collagen was added in the presence of 1 mM Mg^{2+}.

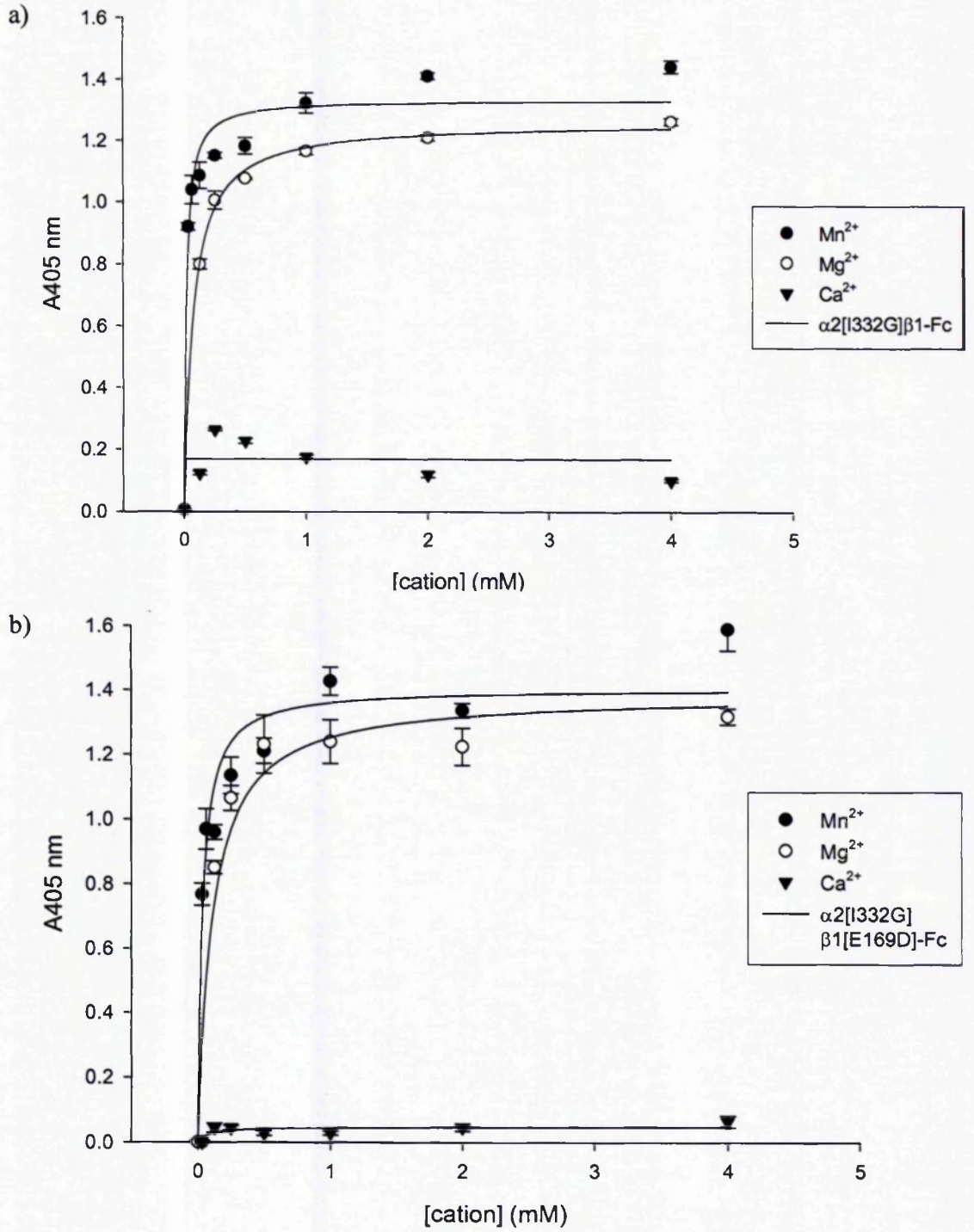

Figure 5.3. Effect of divalent cations on the binding of collagen I to TR α2[I332G] β1-Fc (a) and TR α2[I332G]β1[E169D]-Fc (b). Assays were performed using Fc-captured integrin from culture supernatants. Binding of collagen I was measured in the presence of varying concentrations of Mn^{2+}, Mg^{2+}, or Ca^{2+}. Absorbance values and error bars represent the average and S.D. of four readings. By non-linear regression analyses the mean K_d values of α2[I322G] β1-Fc were: for Mn^{2+} = 0.045 ±0.02 mM; for Mg^{2+} = 0.063 ±0.33 mM; of α2[I322G] β1[E169D]-Fc for Mn^{2+}= 0.041 ± 0.02 mM, for Mg^{2+} = 0.1 ± 0.05 mM.

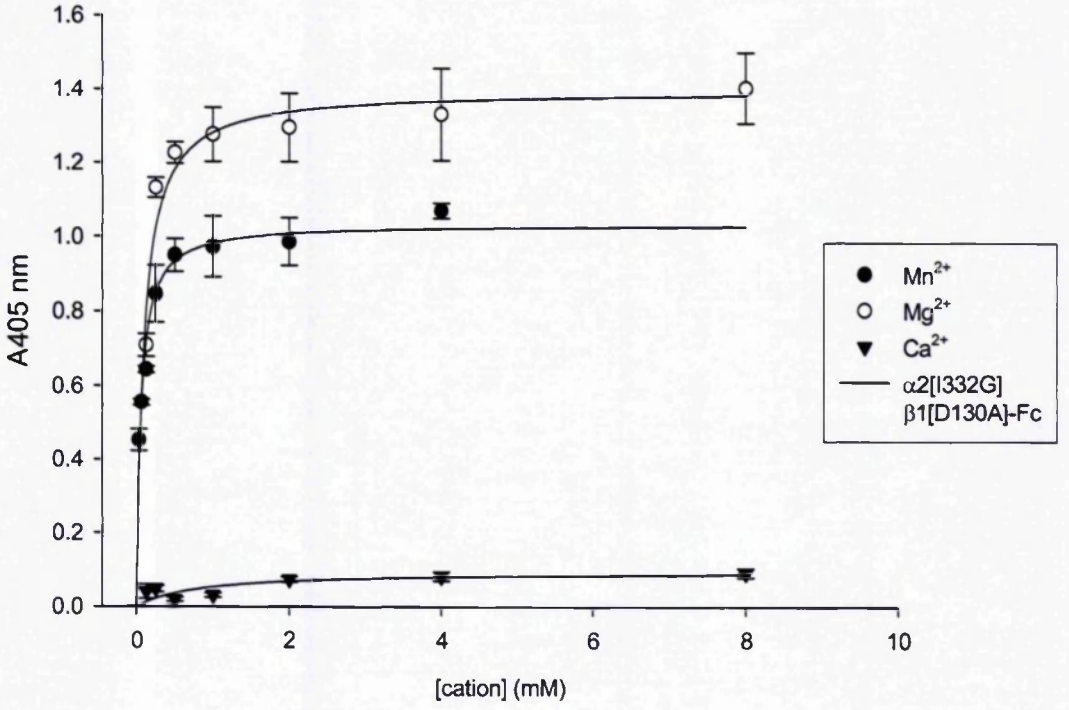

Figure 5.4. Effect of divalent cations on the binding of collagen I to TR α2[I332G] β1[D130A]-Fc. Assays were performed using Fc-captured integrin from culture supernatants. Binding of collagen I was measured in the presence of varying concentrations of Mn^{2+}, Mg^{2+}, or Ca^{2+}. Absorbance values and error bars represent the average and S.D. of four readings. By non-linear regression analyses the mean K_d values of α2[I322G] β1[D130A]-Fc were: for Mn^{2+} = 0.067 ±0.02 mM; for Mg^{2+} = 0.136 ±0.42 mM.

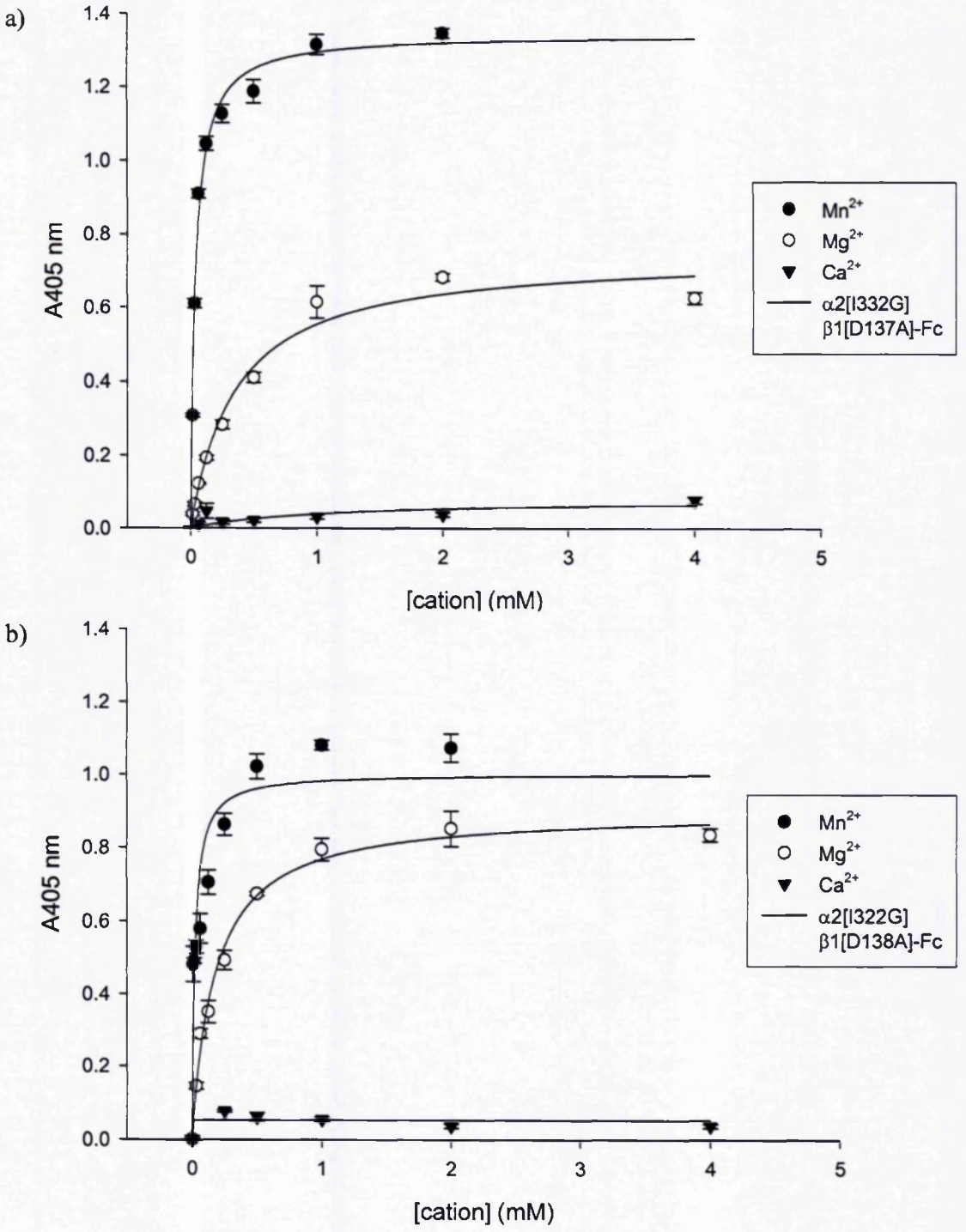

Figure 5.5. Effect of divalent cations on the binding of collagen I to TR α2[I332G] β1[D137A]-Fc (a) and TR α2[I332G] β1[D138A]-Fc (b). Assays were performed using Fc-captured integrin from culture supernatants. Binding of collagen I was measured in the presence of varying concentrations of Mn^{2+}, Mg^{2+}, or Ca^{2+}. Absorbance values and error bars represent the average and standard deviation of four readings. By non-linear regression analyses the mean K_d values of α2[I322G] β1[D137A]-Fc were: for Mn^{2+} = 0.028 ±0.01 mM; for Mg^{2+}= 0.639 ±0.19 mM; of α2[I322G] β1[D138A]-Fc for Mn^{2+} = 0.023 ± 0.01 mM, for Mg^{2+} = 0.159 ± 0.05 mM.

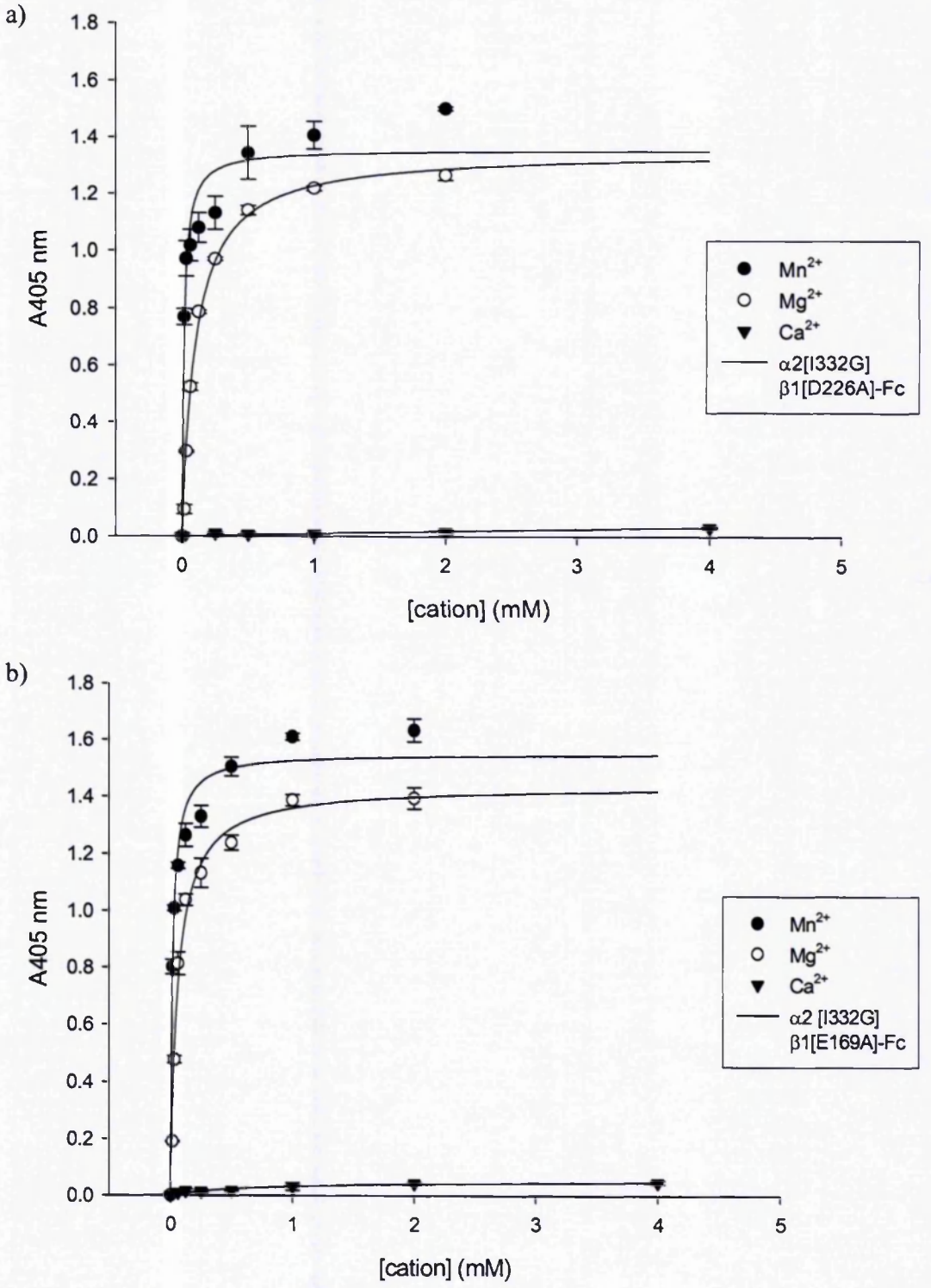

Figure 5.6. Effect of divalent cations on the binding of collagen I to TR α2[I332G] β1[D226A]-Fc (a) and TR α2[I332G] β1[E169A]-Fc (b). Assays were performed using Fc-captured integrin from culture supernatants. Binding of collagen I was measured in the presence of varying concentrations of Mn^{2+}, Mg^{2+}, or Ca^{2+}. By non-linear regression analyses the mean K_d values of α2[I322G] β1[D226A]-Fc were: for Mn^{2+} = 0.023 ±0.006 mM; for Mg^{2+} = 0.122 ±0.046 mM; of α2[I322G] β1[E169A]-Fc for Mn^{2+} = 0.042 ± 0.008 mM, for Mg^{2+} = 0.134 ± 0.05 mM.

Also, it should be noted that the double I332G / MIDAS mutant, α2[I332G] β1[D130A]-Fc (Figure 5.4), exhibited a similar cation-binding profile to the isolated α2 A domain (Figure 5.1b). In the above plots the Mg^{2+}-supported collagen-binding levels corresponded to higher readings than the Mn^{2+}-supported binding values, for the same ion concentration. Taken together the above results demonstrated that Mg^{2+} ions showed an enhanced ability to support ligand binding to the double I332G / βA domain α2β1-Fc mutants.

Finally, whereas 0.1-1 mM Mn^{2+} or Mg^{2+} strongly stimulated ligand binding to soluble α2[I332G]β1 integrins, Ca^{2+}concentrations of up to 10 mM failed to induce collagen binding (Figures 5.2-5.6). Consistent with the data for the wt, either Mn^{2+} or Mg^{2+}, but not Ca^{2+}, supported collagen binding to the series of TR α2 [I332G] β1-Fc mutants.

To summarise, the K_d values for Mn^{2+}- and Mg^{2+}-supported collagen binding to the I332G double mutants were calculated at similar μM values. In marked contrast, the β1 A domain α2[I332G] β1-Fc mutants showed significantly higher binding affinities for Mg^{2+} compared to wt TR, wt FL α2β1-Fc or native α2β1 integrin, all of which showed K_d values between 2 and 4 mM for Mg^{2+} (Table 5.1). Consequently, the series of mutated α2 [I332G]β1 integrins and the unmodified α2β1 integrins behaved differently with respect to Mg^{2+} -supported collagen binding. Yet again, Mn^{2+} bound better than Mg^{2+} in the presence of collagen.

The K_d values for Mn^{2+} and Mg^{2+}, for all integrins tested, are summarised in Table 5.1.

Integrin	K_d (mM)	
	Mn^{2+}	Mg^{2+}
α2β1	0.034 ± 0.016 (n = 4)	2.671 ± 1.0 (n = 3)
GST–α2 A domain	0.025 ± 0.008 (n = 4)	0.045 ± 0.014 (n = 4)
FL wt α2β1–Fc	0.063 ± 0.007 (n = 3)	1.676 ± 0.234 (n = 3)
TR wt α2β1–Fc	0.109 ± 0.031 (n = 6)	4.003 ± 1.1 (n = 4)
α2 [I332G] β1–Fc	0.045 ± 0.027 (n = 5)	0.063 ± 0.033 (n = 5)
α2 [I332G] β1[D130A]–Fc	0.067 ± 0.024 (n = 4)	0.136 ± 0.042 (n = 4)
α2 [I332G] β1[D137A]–Fc	0.028 ± 0.014 (n = 8)	0.639 ± 0.198 (n = 7)
α2 [I332G] β1[D138A]-Fc	0.023 ± 0.013 (n = 5)	0.159 ± 0.054 (n = 5)
α2 [I332G] β1[D226A]–Fc	0.023 ± 0.006 (n = 5)	0.122 ± 0.046 (n = 6)
α2 [I332G] β1[E169A]–Fc	0.020 ± 0.008 (n = 6)	0.134 ± 0.050 (n = 8)
α2 [I332G] β1[E169D]–Fc	0.041 ± 0.022 (n = 3)	0.100 ± 0.054 (n = 4)

Table 5.1. Apparent affinities (K_d) of α2β1 integrins for divalent cations. Collagen binding was measured in the presence of increasing concentration of Mn^{2+}or Mg^{2+} divalent cation. The K_d values were estimated by non-linear regression analysis in Sigma Plot, version 8. These K_d values correspond to the concentration of cation required for half-maximal binding. Data are presented as the mean ± S.D., in parenthesis are the number of experiments utilised for analysis.

5.2 The effect of Ca^{2+} on Mg^{2+}-supported collagen I binding

The presence of at least two distinct regulatory Ca^{2+} binding sites have been reported for αA domain-containing and non-αA domain-containing integrins including α2β1 and α5β1, respectively. Studies on integrins have revealed competition between Ca^{2+} and Mn^{2+} (inhibitory site) and synergy between Ca^{2+} and Mg^{2+} (stimulatory site). Early studies on α2β1-mediated adhesion observed the inhibitory effect of Ca^{2+} on Mg^{2+}-dependent ligand binding [Santoro S.A, 1986; Staatz *et al.*, 1989]. The site necessary for Ca^{2+} to inhibit Mg^{2+}-supported collagen binding was shown not to involve the MIDAS of the α2 A domain [Dickeson *et al.*, 1997]. Moreover, a study examining collagen binding to purified α2β1 integrin, as well as α2β1-mediated platelet adhesion, showed that there was a Ca^{2+}-dependent element of collagen binding to α2β1, which could not be demonstrated for the isolated α2 A domain [Onley *et al.*, 2000]. Thus, the stimulatory Ca^{2+} site, as well as the inhibitory Ca^{2+} site, was suggested to lie outside the α2 A domain. Recent data from αA domain-lacking integrins have demonstrated that the ADMIDAS site is the inhibitory Ca^{2+} site [Mould *et al.*, 2003b]. Additionally, the LIMBS site may be the Ca^{2+}-binding site that synergistically enhances ligand binding [Dr. A.P. Mould, personal communication].

To define the function of the LIMBS cation-binding site in α2β1, the I332G / β1 cation-binding mutants were used to examine the ability of Ca^{2+} ions to enhance Mg^{2+}-dependent collagen binding to recombinant α2β1 integrins.

For this set of experiments a constant concentration of Mg^{2+} was used while the concentration of Ca^{2+} was increased from 0 - 2 mM. For comparison I examined the effect of the mixed divalent cations on binding of collagen to purified whole α2β1 (Figure 5.7a), FL wt α2β1-Fc (Figure 5.7b) and TR wt α2β1-Fc (Figure 5.8a). In agreement to previous reports, low μM Ca^{2+} concentrations increased the Mg^{2+}-dependent collagen binding to the whole α2β1 integrin, while Ca^{2+} ions at above 0.25 mM had an inhibitory effect on ligand binding. In a similar manner, Ca^{2+} concentrations between 0.625 mM to 0.25 mM reproducibly increased Mg^{2+}-dependent collagen binding to both unmodified, recombinant α2β1-Fc integrins.

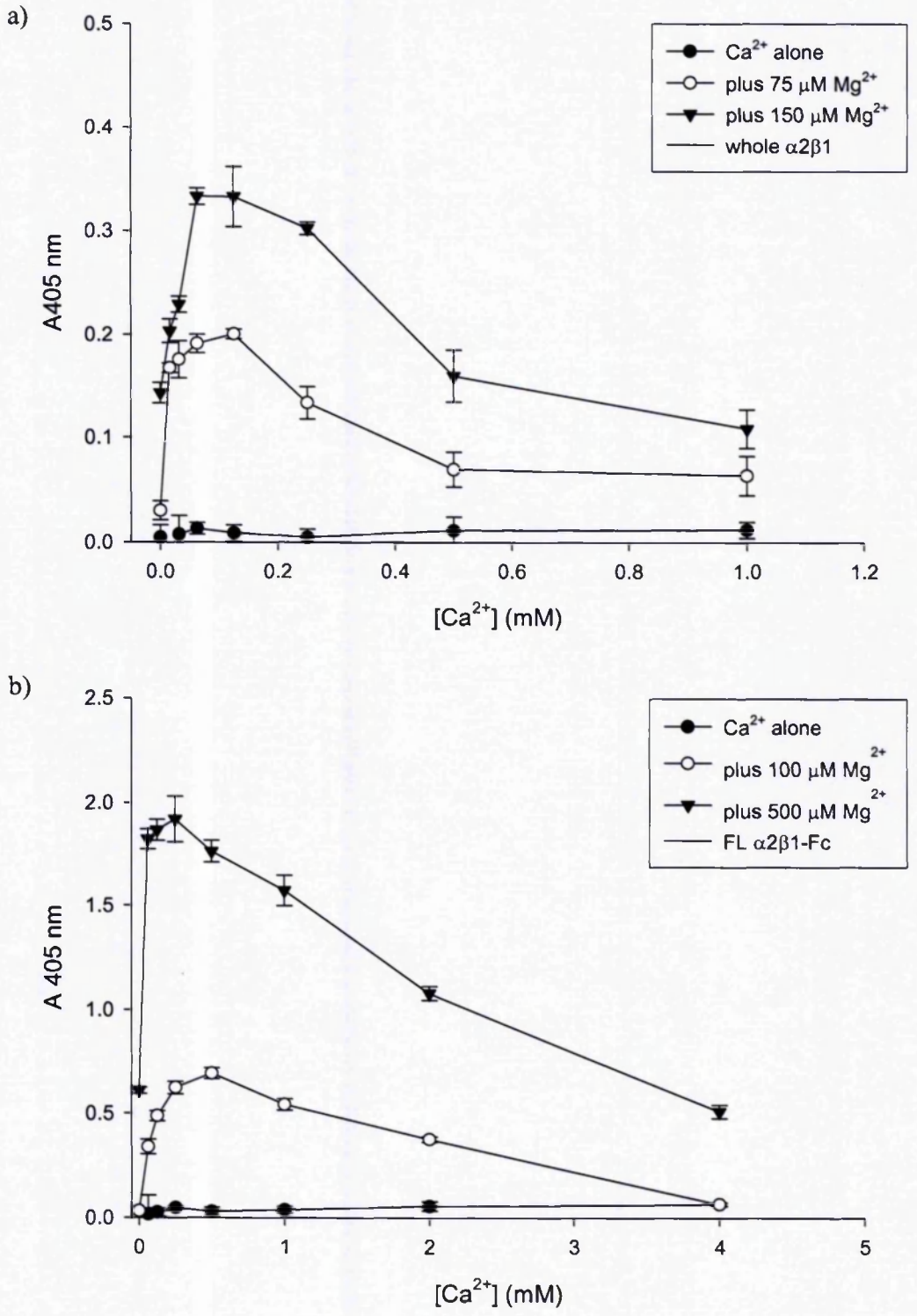

Figure 5.7. Effect of Ca^{2+} on Mg^{2+}-dependent collagen I binding to whole α2β1 (a) and FL wt α2β1-Fc (b). Assays were performed using Fc-captured integrin from culture supernatants. Binding of collagen I was measured in the presence of a constant concentration of Mg^{2+} with varying concentrations of Ca^{2+}. The level of ligand binding supported by Ca^{2+} alone is also shown. Absorbance values and error bars represent the average and S.D. of four readings.

a)

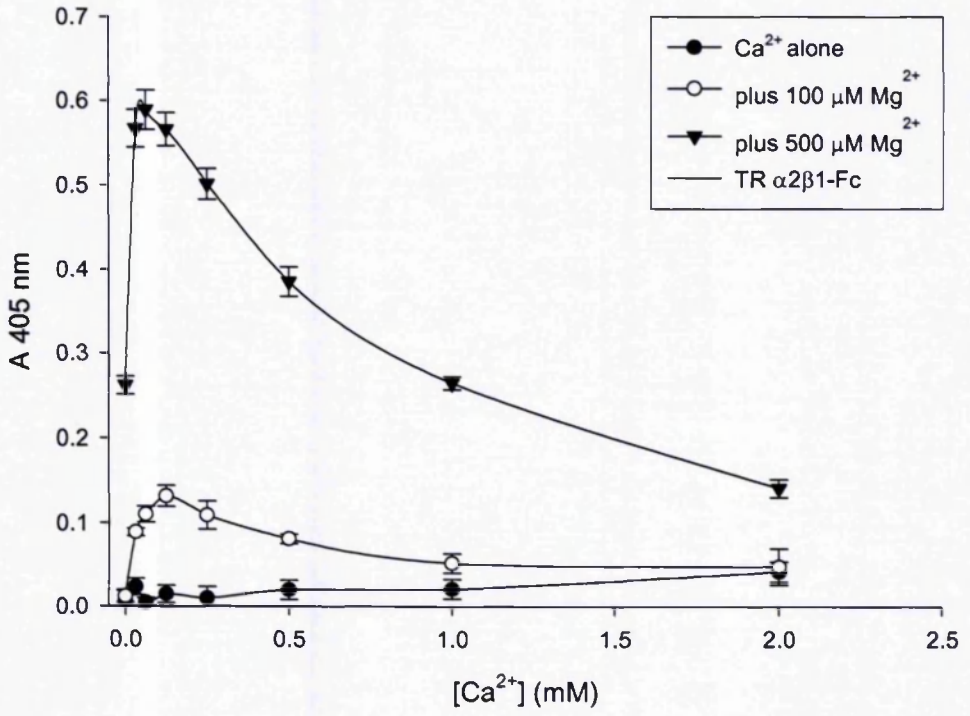

b)

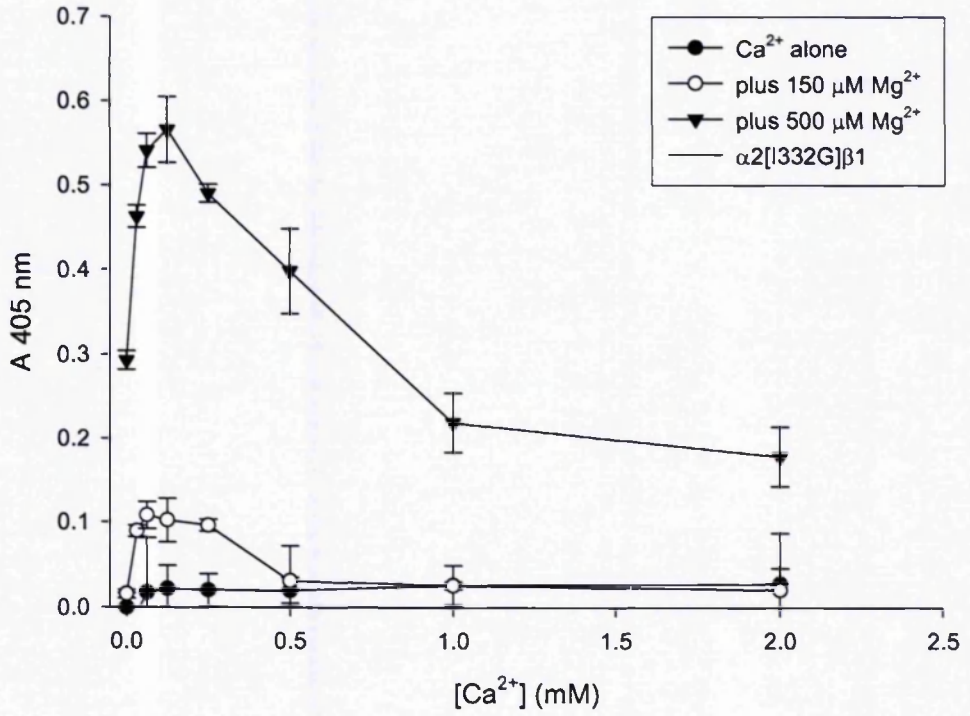

Figure 5.8. Effect of Ca^{2+} on Mg^{2+}-dependent collagen I binding to TR wt α2β1-Fc (a) and TR α2[I332G]β1-Fc (b). Assays were performed using Fc-captured integrin from culture supernatants. Binding of collagen I was measured in the presence of a constant concentration of Mg^{2+} with varying concentrations of Ca^{2+}. The level of ligand binding supported by Ca^{2+} alone is also shown. Absorbance values and error bars represent the average and S.D. of four readings.

However, increasing the Ca^{2+} concentration above 0.25 mM decreased collagen binding and subsequently resulted in inhibition of Mg^{2+}-supported collagen binding by 2 mM Ca^{2+}. Thus, in agreement to the reported regulatory effect of Ca^{2+} for the whole α2β1 integrin, low μM Ca^{2+} concentrations also stimulated the Mg^{2+}-dependent collagen binding to the recombinant wt α2β1-Fc integrins, while Ca^{2+} at higher concentrations inhibited binding.

The effect of Ca^{2+} on Mg^{2+}-dependent collagen binding to the TR α2[I332G]β1 integrin was also examined, and a representative experiment is shown in Figure 5.8. In the presence of both Ca^{2+} and Mg^{2+} cations, collagen binding to the TR α2[I332G]β1-Fc had a biphasic pattern, similar to that for the TR wt α2β1-Fc integrin. Ca^{2+} at 0.125 mM stimulated the Mg^{2+}-dependent collagen binding, whereas higher concentrations of 0.5 - 2 mM Ca^{2+} inhibited collagen binding supported by 0.5 mM Mg^{2+} (Figure 5.8b).

By contrast, Ca^{2+} did not have a stimulatory effect on the Mg^{2+}-dependent collagen binding to the double I332G / D226A α2β1-Fc mutant (Figure 5.9a). Lower micromolar concentrations of Ca^{2+} did not activate binding to collagen in the presence of sub-optimal (50 μM, data not shown) to optimal (0.15 - 0.5 mM) Mg^{2+} concentrations. Moreover, Ca^{2+} ions, even in the low micromolar range, inhibited collagen binding supported by Mg^{2+}. Similar data were obtained for the α2[I332G] β1[E169A]-Fc (Figure 5.9b). Thus, Ca^{2+} failed to synergistically enhance the binding of collagen to either of the I332G / LIMBS mutants in the presence of Mg^{2+}.

The double I332G / D137A α2β1-Fc mutant bound collagen better in the presence of Ca^{2+} and Mg^{2+} than Mg^{2+} alone (Figure 5.10a). The results for I332G / D138A were similar to I332G / D137A α2β1-Fc (data not shown). There is a clear stimulatory peak present in the collagen-binding curve for the I332G / ADMIDAS mutants. Thus, the addition of Ca^{2+} had a positive effect on the Mg^{2+}-supported collagen binding. Taken together, Ca^{2+} ions promoted Mg^{2+}-supported collagen binding when the ADMIDAS site was mutated. However, this positive effect was lost in the I332G / D130A integrin – collagen binding (Figure 5.10b). It was also observed that Ca^{2+} concentrations in the range of 0.5 - 2 mM did not inhibit significantly the integrin-collagen interaction. Thus, Ca^{2+} ions were less effective in inhibiting collagen binding to the double I332G / MIDAS mutant, as a result of Mg^{2+} ions binding to the α2 A domain inclusively.

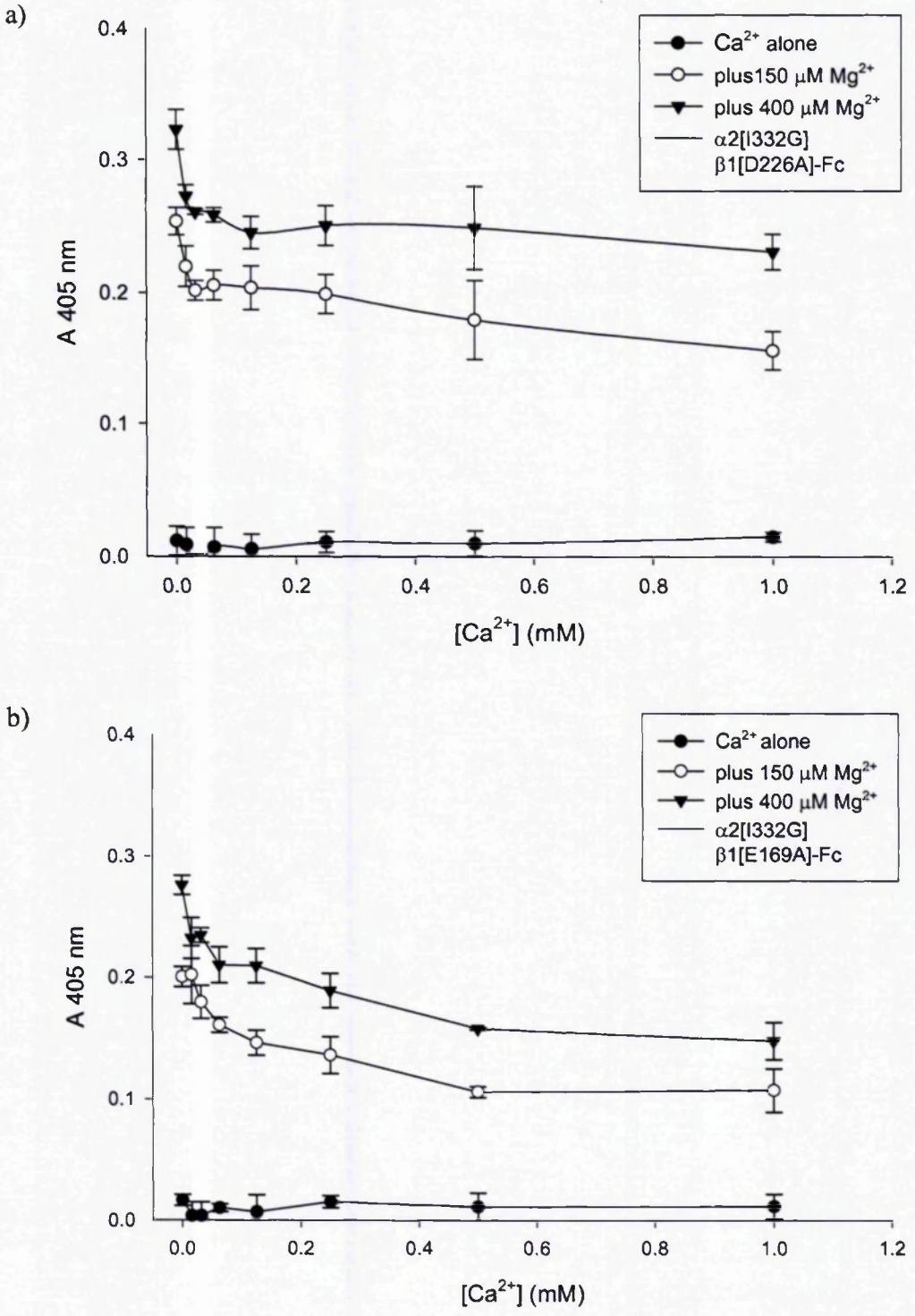

Figure 5.9. Effect of Ca^{2+} on Mg^{2+}-dependent collagen I binding to α2[I332G]β1[D226A]-Fc (a) and α2[I332G]β1[E169A]-Fc (b). Assays were performed using Fc-captured integrin from culture supernatants. Binding of collagen I was measured in the presence of a constant concentration of Mg^{2+} with varying concentrations of Ca^{2+}. The level of ligand binding supported by Ca^{2+} alone is also shown. Absorbance values and error bars represent the average and S.D. of four readings.

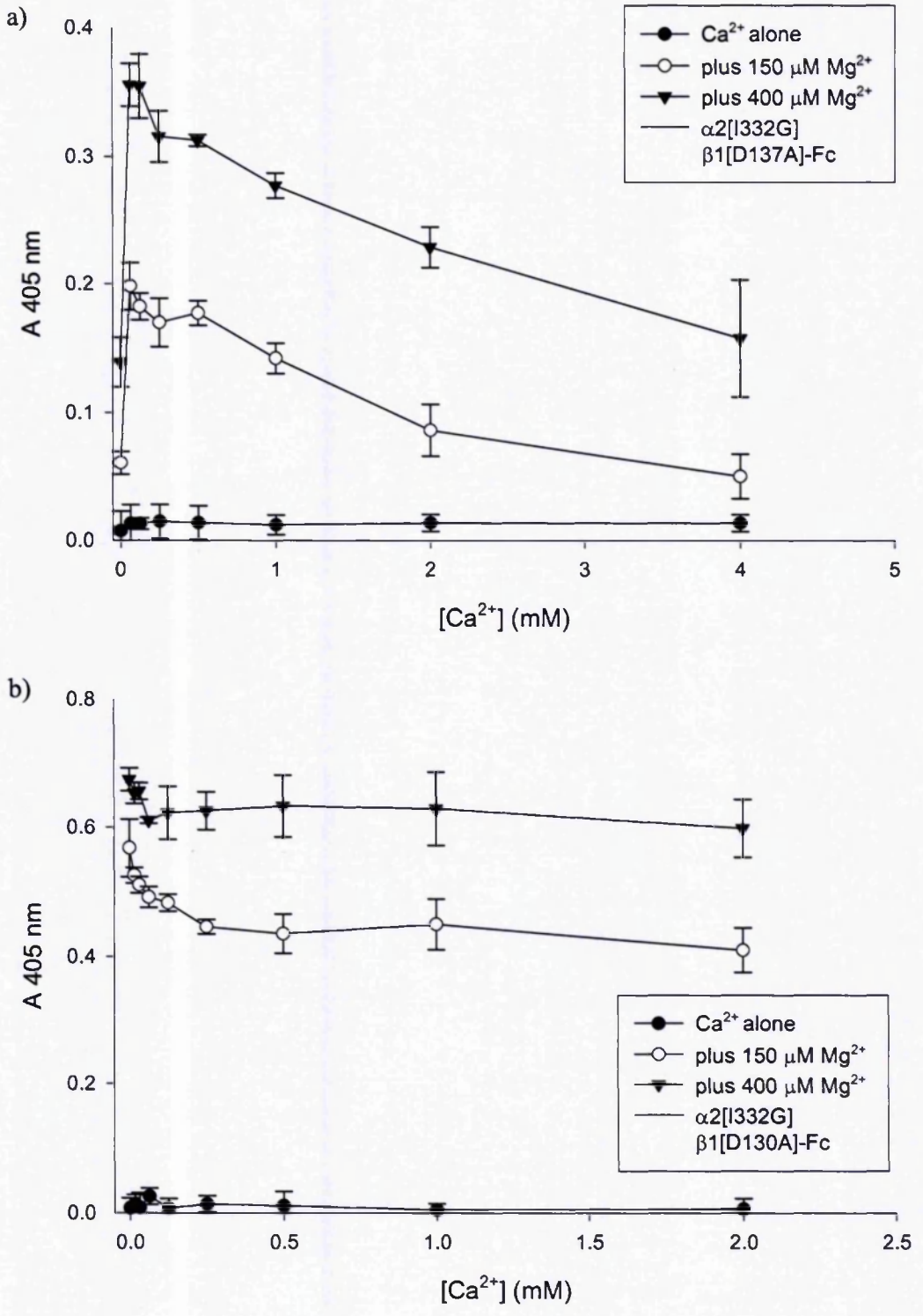

Figure 5.10. Effect of Ca^{2+} on Mg^{2+}-dependent collagen I binding to α2[I332G]β1[D137A]-Fc (a) and α2[I332G]β1[E130A]-Fc (b). Assays were performed using Fc-captured integrin from culture supernatants. Binding of collagen I was measured in the presence of a constant concentration of Mg^{2+} with varying concentrations of Ca^{2+}. The level of ligand binding supported by Ca^{2+} alone is also shown. Absorbance values and error bars represent the average and S.D. of four readings.

5.3 Summary

The data described above was aimed to asses the relative contributions of distinct cation-binding sites present in the β1 integrin subunit to the collagen-binding activity of α2β1 integrin. To approach this, divalent ions were examined for their ability to support collagen binding to the double I332G / β1 A domain α2β1-Fc mutants. The binding of biotinylated collagen I to immobilised α2β1-Fc integrins was measured in the presence of increasing concentrations of Mn^{2+}, Mg^{2+}or Ca^{2+} cations, in solid phase assays. The cation-binding profile for the mutated integrins was similar to that for the whole α2β1 integrin. Mn^{2+} and Mg^{2+} cations supported collagen binding to the recombinant integrins, but Ca^{2+} ions failed to support collagen interacting with α2β1-Fc. In general, μM concentrations of Mn^{2+} ions were sufficient to induce collagen binding to the wt α2β1-Fc and the I332G series of mutants. However, a significant difference was observed in collagen binding supported by Mg^{2+}. In the presence of Mg^{2+} ions the I332G mutants showed a dramatic enhancement in the affinity for collagen that differed greatly compared to that of the unmodified α2β1 integrins.

Finally, to elucidate the location of the reported stimulatory Ca^{2+} site on α2β1 integrin, the collagen-binding assays were conducted in the presence of both Ca^{2+} and Mg^{2+} ions, and the effect of Ca^{2+} on Mg^{2+}-supported collagen binding was examined for the mutated integrins. Positive regulation by low Ca^{2+} concentrations was lost when the LIMBS site or MIDAS was mutated, but could still be observed when the ADMIDAS was mutated.

The role of A domain metal-ion site in the integrin α2 subunit is well established. However, eight additional cation-binding sites, (nine in total) on α2β1 integrin signify a complex manner of regulation. As observed in this study, the A domain cation-binding sites in the β subunit also implement regulation of the function of the αA domain metal ion-binding site, by mechanisms that are not fully understood. This study aimed to reveal the roles of the individual, single cation-binding sites. In the ligand-binding solid-phase assays, the metal-ion dependencies were studied in the presence of tight ligand binding. The high affinity of cations for activated integrin provided the means to assess the K_d affinity values of metal ions indirectly by the ligand-binding measurements. However, the estimation of apparent K_d affinity values of cations for the integrin, but not actual affinity

constants for instance, reflected a limitation of this method for studying cation activation. Moreover, although the overall data indicated that cation regulation is a complex, cooperative event, when the data were fitted to a single-binding class model or a two-binding class model by non-linear regression analysis (data comparisons were not shown), the one-binding class model appeared to be a good working model. In general, fitting the binding model to the titration results generated hyperbolic curve fits. These indicated that a simple association model provided a good approximation to the experimental data for the majority of the recombinant integrins. However, comparisons of the estimated K_d values (Table 5.1) with the experimental data as taken from the simulated binding curves (Figures 5.1-5.6) did not appear without discrepancies. For example, although the experimentally-determined K_d values of Mg^{2+}-binding fitted the one-binding class model, the affinities of Mn^{2+} for the recombinant integrins were too strong ($\leq$50 μM) to be determined accurately by solid phase binding curves. This was the case for all recombinant integrins because the interaction with Mn^{2+} was fast and of high affinity. Therefore, the results from the single-binding model, non-linear regression analysis should be interpreted with caution. In the present study, the individual cation saturation curves described a hyperbola because one cation was saturating the reaction. An alternative explanation may be that the majority of the data correlated well to a quadratic shape of binding curve because the cation-binding sites are not equivalent but have differentiated roles in integrin regulation and function. This would also reflect the fact that the affinity for a cation is not a fixed number but varies as a result of ligand concentration and integrin activation. This was clearly observed in the presence of more that one divalent cation, i.e. where Mg^{2+} and Ca^2 both influenced the interaction (Figures 5.7-5.8). The cooperative binding of multiple metal ions by partial occupancy of these sites by Ca^{2+} increased the affinity of the remaining sites for Mg^{2+}. On the whole, regulation of integrin function by cations is not a simple process but requires coordination of multiple classes of metal ions with different affinities.

Chapter
6.0 Discussion

6.1 Overview

The overall objective of this study was to gain an understanding of the molecular mechanisms used to modulate α2β1-collagen binding. To achieve this objective, a mammalian expression system was established for the production of recombinant soluble α2β1 integrin. This system enabled the production of soluble full-length (FL) and truncated (TR) α2β1 variants containing the extracellular domains, but lacking the transmembrane and cytoplasmic segments. Each integrin subunit was expressed fused to the human IgG γ chain to promote heterodimer formation at sufficient quantities to undertake functional analysis of recombinant proteins. Using a mutagenesis-based approach, different integrin variants were produced in the TR heterodimer and the effects of the mutations were examined relative to the ligand-binding ability of the wt α2β1-Fc. These recombinant soluble α2β1 integrins were utilised as substrates in solid-phase assays and compared with isolated α2 A domains and purified, native human α2β1 integrin. In particular, the expression of β1 A domain cation-binding mutants enabled in-depth investigations of the divalent-cation preferences of the mutated receptors. This approach also made it possible to determine the regulatory role of individual cation sites in ligand binding. A different set of mutations in the C-terminal helix of α2 A domain and the C-terminal linker (C-linker) sequence connecting the αA domain to the β-propeller were designed to test the current model of αA domain-containing integrin activation, which proposes that the βA domain binds directly to the αA domain in a MIDAS-ligand fashion to regulate αA domain activation.

In this model system for studying α2β1-collagen interactions it was demonstrated that:

- integrin α2β1 can be expressed as full-length and truncated Fc-fusion protein for utilisation in functional, biochemical studies

- the I332G mutation at the C-terminal of α7-helix induced the open α2 A domain conformation and stabilised α2β1 in the active, high affinity form

- mutating the C-linker in α2 A domain inhibited functional interaction(s) with the β1 A domain, and resulted in inactivating the ligand-binding ability of the α2β1

- local structural rearrangements in the β1 A domain regulated indirectly the activation state of the α2 A domain, these included changes in coordination of the β1 MIDAS but also of the LIMBS and ADMIDAS sites

- mutations in the β1 metal ion-binding sites decreased the affinity of α2β1 for collagen

- LIMBS is the stimulatory Ca^{2+} regulatory site

6.2 Structure and function of soluble heterodimeric α2β1 integrins

In order to study the mechanisms of α2β1-ligand binding modulation by the β1 A domain it was necessary to produce a recombinant soluble α2β1 integrin heterodimer that retained the structure and function of the parent integrin. The strategy employed the generation of α and β integrins subunits as Fc-fusion proteins that would favour heterodimerisation and secretion into the culture medium. The full-length ectodomain of human integrin α2 subunit was cloned into the pEE12.2hFc mammalian expression vector. The recombinant soluble α2 and an existing β1 construct, in pV.16hFc [Stephens *et al.*, 2000], were co-transfected in CHO L671h cells, which have been modified to facilitate protein secretion into the culture medium [Cockett *et al.*, 1991]. Culture supernatants were examined directly in Fc-capture ELISA assays for expression of α2β1-Fc, confirming correct protein structure. Collagen type I (the principal α2β1 ligand), binding was examined in the Fc-capture type solid-phase assays to test for the functional ability of the soluble FL α2β1 protein. The recombinant wt FL α2β1-Fc heterodimer was shown to be functional as it retained collagen I-binding ability in a divalent cation-dependent manner. On the contrary, expression of the α2-Fc subunit on its own failed to demonstrate collagen-binding ability, despite maintaining structural integrity (Figure 3.5). Therefore, whereas the combination of α and β integrin chains determined ligand specificity, correct heterodimer formation was

critical for ligand binding. Although α4β1-Fc [Stephens *et al.*, 2000], α5β1-Fc [Coe *et al.*, 2001] and α4β7-Fc [M. Travis, Ph.D. thesis 2004] have previously been described, this is the first soluble αA domain-containing integrin heterodimer to be expressed as a functional Fc-fusion protein. The above results demonstrated the successful utilisation of the Fc mammalian expression system for the production of functional soluble integrin heterodimers, for both αA domain-lacking and αA domain-containing integrins.

To address the possibility of the distal, membrane-proximal structural constraints modulating activation and ligand binding in the N-terminal extracellular integrin domains, the Fc-expression system was utilised for the production of functional TR α2β1 integrin variants that lacked the leg domains. Investigations into the absolute domain requirements for heterodimer formation have suggested that the integrin headpiece is sufficient for receptor formation without impairing the ligand-binding ability of the minimal α5β1 integrin [A. Coe, Ph.D. thesis 2000, University of Manchester]. Truncation sites were identified by sequence alignments of α2 with α5 and αV chains and carried out in the α2-expressing construct. Truncated α2 subunits that differed in the length of the C-terminal thigh domain were co-expressed with a truncated β1 subunit. The latter truncated β1 subunit, containing the βA domain and the hybrid domain, has been previously utilised in the successful production of TR α5β1 integrins [Mould *et al.*, 2002; 2003a,b]. Subsequently, a minimal truncated construct was produced, containing in the α2 headpiece the β-propeller and the thigh domains including the genu site up to residue I806 of α2. Analysis of the neat culture supernatant of the TR α2β1-Fc transfected cells in Fc-capture ELISA assays showed that the recombinant α2β1-Fc was recognised specifically by a panel of conformation-sensitive mAbs directed against the α2β1 (Figure 3.7). Thus, soluble TR α2β1-Fc integrin was considered to fold properly. The successful generation of a second TR integrin heterodimer, especially one containing an αA domain, demonstrated that the leg domains of either integrin subunit are not required for the correct heterodimer formation.

Moreover, the TR protein bound collagen I in a cation-dependent manner. Like the soluble FL integrin, the interaction of TR integrin with collagen was specific, as it could be inhibited by EDTA as well as by anti-functional α2β1 mAbs and rhodocetin (Figure 4.11).

This is the first report of a functional TR α2 A domain-containing integrin. Furthermore, the expression of both FL and TR α2β1 integrins was equally efficient, being produced at levels of ~1 μg/ml recombinant FL or TR α2β1 in the culture medium. These amounts were comparable to expression levels reported for α5β1 [A. Coe, Ph.D. thesis 2000], and considerably higher than expression levels of the recombinant α4β7 integrin which was limited to 20 ng/ml [M. Travis, Ph.D. thesis 2004]. Thus, the expression of soluble TR α2β1 integrin-Fc was at excellent levels to enable the analysis of the recombinant proteins in solid-phase assays. Interestingly, both FL and TR α2β1 integrins were expressed in an active, high affinity state and did not require further activation. In contrast, the TR α5β1 integrin had a constitutive low activity when Fc-captured, but not when directly coated on microtiter plates. So in the prototype α5β1-fibronectin system, the recombinant integrins had to be purified through the Fc-tag. For the α2β1-Fc the purification step was not required and the proteins were used directly in Fc-capture assays for functional analysis in a rapid format. Overall, the α2β1-Fc expression system and the solid-phase binding assays comprised a model system for studying the activation mechanisms of the collagen-binding integrin family.

Supernatants containing a chimera of the FL α2 subunit combined with the TR β1 subunit, were also analysed for reactivity with anti-α2 and anti-β1 mAbs (Figure 3.7). In all cases, the α and β subunits of each mutant protein folded correctly, as shown from mAb epitope mapping. This is surprising as it might be expected that the longer α subunit would not align correctly with the much shorter truncated β1 subunit. However, the overall data suggested correct heterodimer formation. Results from recombinant α5β1 dimers also suggested that the FL α5 subunit formed functional receptors with the TR β1 subunit variants [Coe *et al.*, 2001]. Taken together the data suggested that even though the heterodimer formation is driven by the Fc domains, the C-terminal Fc-domain did not impose on the N-terminal domain alignment; the α and β integrin heads were still able to associate correctly with each other and retain the correct protein architecture. Thus, it would appear, that the integrin knee in the α chain is very flexible and allows intra-subunit rearrangement to a great extent.

6.3 The allosteric I332G-based, gain-of-function switch in α2 A domain

In the present study, the C-terminus of α7-helix in α2 A domain was targeted to show that a single amino acid substitution of an α2 A domain residue distal from the ligand-binding site at the MIDAS markedly increased activation-dependent ligand binding. Within α2β1 integrin, the α2 A domain (a.a. 140-349) contains the principal binding site for collagen. The α2 A domain has been the focus of numerous investigations and several groups have described the production and characterisation of recombinant αA domain proteins in isolation. For example, the α2 A domain has been expressed as a bacterial glutathione S-transferase (GST), maltose binding protein or hexahistidine fusion protein [Tuckwell *et al.*, 1995; Depraetere *et al.*, 1997; Smith *et al.*, 2000]. These recombinant α2 A domains differed with respect to the length of the coding sequence expressed, the methods of purification and the methods of functional characterisation used. An isolated α2 A domain fused to the GST domain has been shown to specifically bind to collagen in solid-phase assays in a cation-dependent manner similar to the parent α2β1 integrin [Tuckwell *et al.*, 1995].

Whereas α2 A domain isoforms of the native protein expressed in isolation have been previously described [Emsley *et al.*, 1997; 2000], a novel high affinity α2 A domain mutant was generated in the current study to explore allosteric affinity regulation of α2 A domain in the context of the α2β1 receptor. In total, the coding sequences for three α2 A domain variants were cloned into the pGEX-2T bacterial expression vector and expressed as GST-fusion proteins to facilitate purification. These α2 A domains encoded native α2 A domains a.a.124-339 (Fl) and a.a.140-339 (Wt), and the mutated α2 A domain a.a.140-339 [I332G] (CA). All GST-fusion α2 A domain variants were folded properly, as demonstrated by ELISA assays. More importantly, all three α2 A domains bound to type I collagen, the main α2β1 protein ligand. Examination of the collagen binding properties of the recombinant α2 A domains revealed that the proteins required divalent cations to support collagen I binding. Increasing amounts of Mn^{2+} ions, a potent activator of α2β1 resulted in a dose-dependent increase of the collagen I binding to the native recombinant α2 A domains. Identical investigations using the CA α2 A domain showed that the I332G mutation affected the ability of the αA domain to bind cations (Figure 4.6). Whereas the unmodified α2 A domains could be activated further by Mn^{2+} ions, the CA variant

displayed binding of collagen almost at maximum levels. This indicated that the unmodified α2 A domain isoforms were constitutively in a low affinity state, whereas the CA α2 A domain variant was present in a high affinity state.

To estimate the affinity for collagen to the immobilised CA, Fl, and Wt α2 A domains, binding of biotinylated collagen I over a range of concentrations was measured in solid-phase assays. The I332G mutation increased by approximately five-fold the apparent affinity of the CA α2 A domain-collagen interactions, compared to the unmodified α2 A domains. This is in excellent agreement to findings from a different gain-of-function mutation recently described for the α2 A domain [Aquilina *et al.*, 2002]. In this study, the substitution of a residue that lies at the N-terminal end of the α7-helix, E318, by a tryptophan enhanced binding to collagen I by approximately six-fold, and also led to increased binding to collagen VI and several other non-collagenous α2β1 ligands. This mutation was based on the observation that with the transition from the closed to the open α2 A domain, the preceding α7-helix loop also moved in concert to the downward shift of α7-helix and E318 moved from a buried to a solvent-exposed position.

The I332G mutation was based on three independent mutagenesis studies of this invariable isoleucine in the C-terminus of α7-helix in other integrin αA domains. The I314 substitution to glycine increased the affinity of the isolated αX A domain mutant by 200-fold relative to wild-type αX A domain [Vorup-Jensen *et al.*, 2003]. Similar data were described for the αA domain partners of other β2 integrins and extended in the context of the holoreceptors. For example, substitution of I316 in αM A domain [Xiong *et al.*, 2000] and I306 in αL A domain [Huth *et al.*, 2000] by a glycine residue were reported to activate ligand binding for the complete receptors. Furthermore, crystallisation of the αM [I316G] A domain demonstrated that this high affinity conformer is generated by unlocking the invariant Ile from a hydrophobic pocket that would coordinate this residue in the closed form [Xiong *et al.*, 2000]. In the current study it was also shown that the equivalent I332G mutation in the α2 A domain generated a constitutively active α2 A domain with respect to collagen I binding. Taken together, the data suggested that the same allosteric regulation is intrinsic for all αA domains and this modulation also takes place in the allosteric activation of the complete receptor.

Having examined the consequences of mutation of the isolated α2 A domain, it was hypothesised that including the same I332G mutation in the α2β1 dimer would also cause activation. Indeed, the results presented in this thesis showed that the α2 I332G mutation stabilised the open α2 A domain conformation and rescued the collagen-binding ability of inactivating mutations in α2β1, hence overriding modulation by the inactive / low affinity βA domain. This is the first report in which a high affinity, locked open α2β1 receptor has been engineered. This constitutively active α2β1 integrin can be used to discriminate between inhibitors with direct / competitive and indirect / non-competitive modes of inhibition and therefore will be useful in high-throughput screens for the development of effective α2β1–collagen antagonists.

6.4 Activation-regulatory C-linker sequence in the α2 A domain

Another notable finding from the α2 mutagenesis studies was that both activating and inactivating mutations were found at the C-linker of the α2 A domain. Similar experimental evidence have been published from mutagenesis studies of members of the leukocyte integrin subfamily. Alanine substitution of the invariant Glu residue in αM (E320) integrin resulted in loss of ligand binding [Alonso *et al.*, 2002]. Alonso *et al.* proposed that this conserved acidic Glu residue at the C-linker sequence of all αA domains interacts with the βA MIDAS cation directly and therefore acts as a ligand mimetic, and as a relay coupling ligand binding at the αA domain to activation of the β A domain (Figure 6.1). The E320A αM receptor also failed to express the activation and cation-sensitive epitope for mAb24, which binds to open βA domain but not to βA MIDAS mutants of αMβ2 [Alonso *et al.*, 2002]. Likewise, in αLβ2 integrin, alanine substitution of E310 impaired binding to activation-dependent ligands without affecting αL A domain interactions with activation-independent ligands [Huth *et al.*, 2000; Salas *et al.*, 2004].

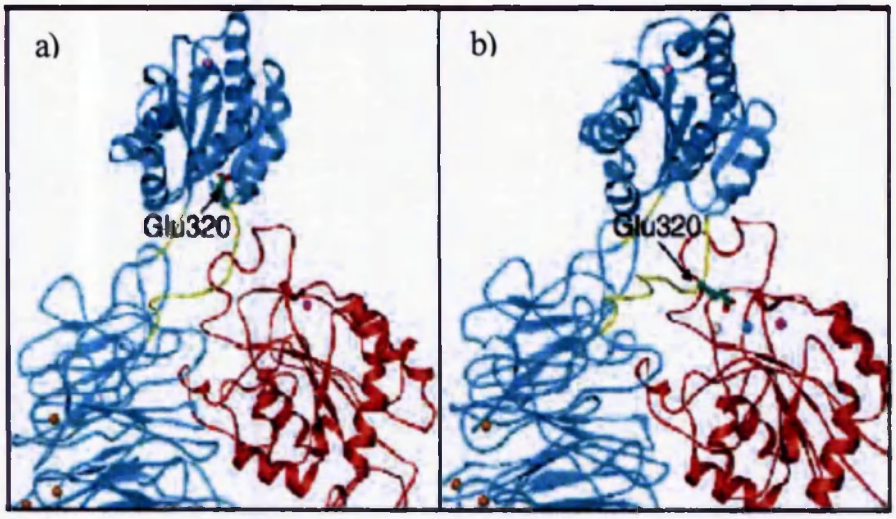

Figure 6.1. A hypothetical model of the αA domain-containing integrin αMβ2 in its inactive (a) and active (b) states. The model shows the αA domain invariant Glu (green side chain) to coordinate the MIDAS ion (cyan) of the active βA domain. This interaction is mediated by the large downward movement of the α7-helix in the αM A domain, which follows the from transition from closed to open αA domain. The αA MIDAS is in pink, the orange spheres represent the metal ions at the bottom of the propeller. The LIMBS and ADMIDAS are in grey and magenta. No structural information is available on the linker sequence connecting the N- and C-termini of αA to the propeller, thus the model predicts one of the potential positions of the αA domain relative to the location of the βA domain. As taken from Xiong *et al.*, 2003b.

If the conserved Glu in α2, residue E336, is the ligand mimic for the β1 A domain, it should be possible to test this hypothesis by mutating this residue to alanine. It was also hypothesised that mutating an invariant Phe residue within a conserved motif that follows the α7-helix would sever the link to the βA MIDAS, and hence inactivate the receptor. Indeed the results presented here showed that for α2β1 the E336A and the F345A mutations inactivated the integrin even in the presence of Mn^{2+}.This effect could be rescued by the activating I332G mutation which stabilises the downward displacement of α7-helix and is therefore located upstream of the connection to the βA domain. It would appear that removing the charge of the acidic Glu residue or severing the flexible C-linker in αA domain interfered with the interactions to the βA MIDAS site and prevented the αA domain from stably assuming the open conformation. Likewise, the inactivating effect of the β1 A domain mutations in the α2β1-collagen binding activity would suggest that there

is structural communication between the principal collagen I binding α2 A domain and the upper face of β1 A domain where the metal cation-binding sites form. A direct structural link would account for the influential role of the β1 A domain, of β1 MIDAS in particular, in the activation state of the α2 A domain. However, validation of such mechanism will require the 3-D structure determination of a whole integrin.

6.5 Cooperative binding of multiple ions in the β1 A domain modulates the ligand-binding activity of α2β1

To study the roles of the β1 A domain LMA (LIMBS, MIDAS, ADMIDAS) cation-binding sites in α2β1 function, a mutagenesis-based approach was adopted whereby conserved β1 residues were substituted for alanines and collagen I binding of the mutated receptor was examined in solid-phase assays. The current study utilised β1 A domain mutations that were designed to disrupt the formation of the β1 cation-binding sites and have been shown to be critical for ligand binding to α5β1 integrin in solid-phase assays [Mould *et al.*, 2002; 2003a,b]. Briefly, the existing mutated β1-expressing constructs were co-expressed with the recombinant α2 subunits in the established Fc-expression system. Cell-culture supernatants were directly tested for binding of reporter anti-human antibodies directed against the α2β1 and it was shown that the reactivity of the mAbs was unaffected by the mutations. Thus, it was concluded that the structural integrity of the α2β1 was not disturbed by the mutations. The specific mutations included the MIDAS D130A substitution, two ADMIDAS substitutions, D137A and D138A, and two LIMBS mutations, D226A and E169A. A different LIMBS mutation, E169D, was utilised as a control mutation since an Asp residue rather than a Glu is found in all other β subunits other than β1.

The D130A mutation, designed to disrupt the highly conserved β1 DxSxS motif, resulted in a complete loss of collagen I binding to α2β1, which could not be rescued by stimulatory anti-β1 mAbs. The loss of ligand binding by the α2 A domain-containing integrin was expected as several studies from the β2 integrins have previously suggested the indirect regulatory role of the βA MIDAS in αA domain-ligand binding. Mutations of the β2 MIDAS residues abolished the binding of αL and αM integrins to their cation-

dependent ligands [Bajt *et al.*, 1995; Hogg *et al.*, 1999; Mathew *et al.*, 2000]. The liganded β3 crystals structures demonstrated that in integrins that lack an αA domain, the β subunit MIDAS cation directly coordinates the acidic ligand residue to the ligand-binding pocket. Thus, mutating the β1 MIDAS cation would be expected to abolish integrin-ligand binding. Indeed, in α5β1, a different β1 integrin that does not contain an αA domain, the D130A MIDAS mutation completely abrogated fibronectin binding to α5β1 in solid-phase assays. In line with this, the epitope for the activation-sensitive, cation-dependent 12G10 mAb was also perturbed [Mould *et al.*, 2002].

In the present study, both of the β1 LIMBS E169A and D226A mutations also resulted in complete loss of collagen I binding, despite high expression levels of correct folded protein. The collagen-binding activity of the β1 LIMBS mutants could not be restored by the addition of 12G10 or TS2/16 stimulatory mAbs (Figure 4.15) which activate the βA domain. Thus, although the α2 MIDAS site was not defective in cation binding, the malfunction of the LIMBS cation-binding site in the β1 A domain indicates its importance in the regulation of α2 A domain-ligand binding. Similarly, in the context of α5β1 the LIMBS mutations blocked ligand binding while not preventing the binding of Mn^{2+}/ Mg^{2+} ions to the β1 MIDAS (Mould P.A., manuscript in preparation). In the liganded αVβ3 / αIIb3 crystal structures, the LIMBS cation did not participate directly in forming contacts with the ligand. However, occupancy of LIMBS site resulted in the reorientation of the E220 residue, opening up space for the accommodation of the cation in the MIDAS site. Therefore, it could be suggested that the presence of the LIMBS site is required to strengthen the structural integrity of βA MIDAS for coordination of its cation upon ligand binding, with an end result of stabilising the high affinity open βA domain structure. The conservative E169D mutation showed collagen-binding activity similar to the wt. This was expected as residue E169 in β1 corresponds to an Asp residue (D158) in β3. Therefore, it would appear that this 'conserved' mutation retained the ability to form the LIMBS site subsequently allowing coordination of a cation at the MIDAS and the normal geometry of all the cation-binding sites in the β1 A domain.

Furthermore, two β1 ADMIDAS mutations were examined in the frame of α2β1. Both ADMIDAS mutations, D137A and D138A, compromised the collagen-binding activity of the mutated α2β1, with the D137A mutation causing a more severe overall effect in

ligand-binding activity (Figure 4.17). Disorder of the ADMIDAS site appeared to allow coordination of the β1 MIDAS cation, albeit retaining the receptor in a low / intermediate affinity state (Table 4.2). High concentrations of Mn^{2+} (above 4 mM) completely restored collagen binding to ADMIDAS mutants (data not shown). In addition, the stimulatory anti-β1 mAbs 12G10 and TS2/16 were also capable of inducing a further increase in ligand binding, to similar levels to the wt proteins. This can be explained because the mode of action of these mAbs is known. The ADMIDAS mutations probably prevented the full movement of the activation-sensitive α1-helix, whereas both function-modulatory antibodies (12G10 or TS2/16) were able to induce the shift in the α1-helix. In keeping with this, the mAbs restored the ligand-binding affinity to the ADMIDAS mutants because they stabilised the active βA conformation. In the α5β1 study, the two ADMIDAS mutants also had low ligand-binding activity [Mould *et al.*, 2003b], which could be improved by the stimulating mAbs. The ADMIDAS is the ligand-independent metal-binding site [Xiong *et al.*, 2001] and it is not surprising that it is not required for ligand recognition in α5β1 or α2β1. However, repositioning of the ADMIDAS cation upon activation was required to stabilise further the formation of the ligand-occupied state of the integrin.

All the above results are in excellent agreement for the α2β1 and the α5β1 integrins. Thus, the mechanisms underlying activation appear to be conserved for both αA domain-containing and αA domain-lacking integrins.

6.6 β1 A domain conformation can alter the affinity of α2β1 for collagen

In the past, structure-based mutational studies targeted the highly conserved βA DxSxS motif, and revealed a complete abrogation of ligand binding activity. While underscoring the importance of the βA domain in αA domain-containing integrin function, this loss of activity prevented further analysis of conformational regulation [Kamata *et al.*, 1995b; Puzon-McLaughlin & Takada, 1996]. At the time there was a lack of structural knowledge of the β subunit, and therefore the presence of the LMA cation-binding cluster was not recognised. Some residues contributing to these sites had been mutated, but the implications of the studies were not appreciated. For example, the equivalent of LIMBS D226A and E169A mutations in β2 (D209A and D151A respectively) blocked ligand

binding as well as the epitope for mAb24, which was utilised as a reporter of β2 integrin activation [Kamata *et al.*, 2002]. Similar results were described for the equivalent D138A ADMIDAS mutation in β2 (D120A) [Kamata *et al.*, 2002]. Moreover, such mutagenesis-based approaches of the LMA sites also revealed an inhibitory effect on ligand binding, which hindered subsequent analyses.

The present study is the first study to include deliberate mutations in the LMA sites of an αA domain-containing integrin so as to examine the effect of the β1 LMA metal ion-binding sites in ligand binding and integrin activation. Briefly, it was shown that mutations in the βA domain residues did not affect α2β1 expression, but the β1 cation-binding mutants inactivated α2β1 function. Engineering the I332G mutation (at the bottom of α7-helix) in the α2 subunit rescued the collagen binding ability of the β1 A domain mutants (Figure 4.14, 4.15) allowing for further studies on the collagen-binding properties of α2β1 mutants to be conducted. By releasing the α7-helix, which has been shown to undergo a large conformational shift upon activation, the I332G-based integrin mutants may be considered as locked into an active αA domain conformation similar to when the α2 A domain binds to collagen [Emsley *et al.*, 2000]. Consistent with this scenario, the FL, the TR and the I332G α2β1 integrins showed similar apparent affinities for collagen to each other when compared under the same cation conditions (the apparent affinities of the double α2β1 I332G / β1 LMA mutants for collagen were measured in the presence of Mn^{2+} ions, Table 4.2). In parallel, the βA cation-binding mutants overall induced the inactive conformation in the βA MIDAS, primarily by lowering the affinity of β1 MIDAS for its ligand but essentially by decreasing the α2 MIDAS affinity for collagen. Thus, the estimated apparent collagen affinity of each double I332G / β1 mutant demonstrated the magnitude of each inactivating mutation in the overall ligand-binding activity of the α2β1 receptor. The β1 MIDAS mutant required the highest collagen concentration for αA domain activation, as taken by the ten-fold increase in half-maximal collagen concentration. The effect of the ADMIDAS D137A mutation also revealed a significant impact on collagen binding, by lowering the apparent affinity for collagen by eight-fold compared to the wt control. The LIMBS mutations affected the affinity for collagen to a lesser degree than the ADMIDAS mutations. The D226A LIMBS mutation, which appeared to be a more severe mutation than E169A mutation, lowered the affinity for collagen by five-fold relative to the wt integrins. Thus, the magnitude of the

ADMIDAS inhibitory effect on the ligand-binding activity of α2β1 suggested that ADMIDAS has a greater importance than LIMBS for regulating the activity of the open αA domain. This pointed towards the critical role of the activation-sensitive α1-helix in the upper face of the βA domain, while additional interactions between the βA and αA domains cannot be ruled out.

In summary, it was demonstrated that the mutations in the conserved βA domain residues did not affect α2β1 expression, but the β1 cation-binding mutants perturbed the ligand-binding activity of α2β1, primarily by altering the apparent affinity of the MIDAS (Table 4.2) for its ligand. The loss of collagen function by the β1 cation-binding mutants demonstrated a) the β1 A domain had an indirect regulatory role in α2 A domain-collagen binding primarily through the β1 MIDAS, but also via the ADMIDAS and LIMBS that modulated MIDAS, b) that the β1 A domain affinity state contributed to the α2β1 affinity modulation; the inactive / low affinity β1 A domain impaired ligand binding of the locked open α2 A domain, as observed by the differences in the apparent affinities of the mutants for collagen, but did not dominate over the allosteric I332G switch at the C-terminal of the α2 A domain, c) the β1 A domain remained in the inactive / low affinity state unless cation occupancy at the LIMBS and ADMIDAS sites coordinated simultaneously the MIDAS cation and d) that there was an absolute requirement for metal-ion occupancy in MIDAS of both the α and β A domains for complete integrin activation.

6.7 Activation-dependent metal ion binding to α2β1-collagen

To study further the effect of the LMA mutations on the ligand- and cation-binding properties of α2β1 integrin, the cation-dependency of collagen binding was examined for each I332G / β1 A domain mutant and compared to that of the cell-surface purified α2β1, isolated α2 A domain and soluble wt α2β1 integrins. The results for the soluble wt proteins were consistent with the cation-dependency studies of the isolated α2 A domain described by Tuckwell *et al.* (1995) and in agreement to the cation-binding profile for the whole, cell-surface purified α2β1 [Santoro S.A., 1986; Kern *et al.*, 1993]. In general, Mn^{2+} displayed higher affinities than Mg^{2+} that also supported collagen binding to the wt receptors, whereas Ca^{2+} did not support binding or was inhibitory. Collagen binding to the

mutated integrins was also specific, cation dependent and modulated by cations in an analogous manner to the unmodified integrins. The I332G mutation and the nature of the metal ion had a significant effect on cation dependency to the α2 MIDAS. The wt TR α2β1 integrin had a high (μM) binding affinity for Mn^{2+} but very low (mM) affinity for Mg^{2+} (Table 5.1). In comparison, the TR α2[I332G]β1 integrin had high affinity (μM) for both supporting divalent cations. Notably, the enhanced ability of Mg^{2+} ions to support collagen binding to the I332G variant was at comparable levels to the Mn^{2+} ions. All TR I332G mutants were much more efficient at binding Mg^{2+} ions than the wt integrins. Thus, it was concluded that the I332G mutation increased the affinity of the α2 MIDAS to Mg^{2+}.

However, there was segregation in the data within the series of the I332G / β1 A domain double mutants; the I332G / MIDAS and the I332G / LIMBS mutants showed a reduced ability to support Mg^{2+} binding compared to the TR α2[I332G]β1, while the ADMIDAS site displayed even lower affinity for Mg^{2+} compared to all the other β1 A domain mutants. So, largely the ADMIDAS but also the MIDAS and LIMBS mutations affected the affinity of Mg^{2+} ions binding to the α2 MIDAS. The mutations also led to changes in the affinity for Mn^{2+}, but to a lesser extent relative to Mg^{2+}. Reduced affinity for Mn^{2+} ions was displayed primarily by the β1 MIDAS mutant, as expected based on its established role of a ligand-competent Mn^{2+} site [Mould *et al.*, 2002; Xiong *et al.*, 2002]. The above findings provided further evidence that occupancy of the βA LMA sites influenced the affinity of cation binding to the active αA MIDAS, with effects reflected prominently in the apparent affinity for Mg^{2+} ions than for Mn^{2+} ions. Overall, alterations in the cation-dependency of the mutated βA domains were reflected in the changes of the apparent affinity of cation binding to the αA domain MIDAS, in line with the notion that the β1 A domain mutants differentially modulated the α2 A MIDAS activity.

The above conclusions are in agreement with a recent study that investigated the binding affinity of Mn^{2+}, Mg^{2+}, and Ca^{2+} cations in the active and inactive αM A domain [Ajroud *et al.*, 2004]. It was demonstrated that whereas Mn^{2+} ions bound with high affinity (~0.03 mM) to active or inactive αA domain, the activation state of the αA domain influenced the binding affinity of Mg^{2+} and Ca^{2+} ions, with activation increasing the affinity of MIDAS to Mg^{2+} from mM by approximately 10-fold to 0.1mM, but the inactive αM A domain highly favouring the binding of the generally inhibitory Ca^{2+}. In line with the above, the binding

affinity of Mg^{2+} to the α2[I332G]β1 integrin was significantly higher (μM range) compared to wt TR α2β1-Fc (mM), as the activating I332G mutation induced the high affinity conformation of the α2 A domain. Thus, the same principle appeared to be true for the α2 A domain which is interacting with a functional β1 A domain, as seen in the α2[I332G]β1 integrin. Consequently linking the αA domain to the inactivating β1 A domain lowered the affinity for collagen, which was reflected on the apparent affinity of binding cations to the α2 MIDAS, especially Mg^{2+} ions. Therefore, as ligand binding enhanced metal ion binding at the α2 MIDAS, metal ion binding at β1 MIDAS but also at the LIMBS and ADMIDAS sites enhanced collagen binding.

6.8 Cation regulation at the LIMBS stimulatory site

Like most integrins, the β1 integrins contain several cation-binding sites and these have been described as ligand-competent, stimulatory and inhibitory sites [Mould *et al.*, 1995a]. Whereas the ligand-competent sites typically bind Mn^{2+} or Mg^{2+}, the stimulatory and inhibitory sites appear to bind Ca^{2+} selectively [Hu *et al.*, 1996; Labadia *et al.*, 1998]. In particular, the β1 A domain MIDAS site has been shown to bind Mn^{2+}/ Mg^{2+} preferentially [Mould *et al.*, 2002; Xiong *et al.*, 2002]. In support of this, the liganded β3 crystals explained a preference of Ca^{2+} to bind at sites other than the βA MIDAS based on the chemistry of the coordinating oxygen atoms at the LMA sites. In view of the higher propensity of Ca^{2+} to coordinate carbonyl oxygen atoms [Harding M.M., 2001], Ca^{2+} binds to ADMIDAS and LIMBS rather than MIDAS, which has no carbonyl oxygen coordinations (Figure 6.2). Experimental proof of the above has been presented from the findings by Mould *et al.*, (1995a, 2002, 2003b) who previously reported that for α5β1 interaction to fibronectin, higher concentrations of Ca^{2+} ions inhibited ligand binding by Mn^{2+} in an allosteric manner [Mould *et al.*, 1995a]. However, it was not until recently shown that the ADMIDAS is the Ca^{2+}-binding site involved in the allosteric inhibition of Mn^{2+}-supported ligand binding; as the ADMIDAS mutations D137A and D138A reduced the ability of Ca^{2+} to compete with Mn^{2+} [Mould *et al.*, 2003b].

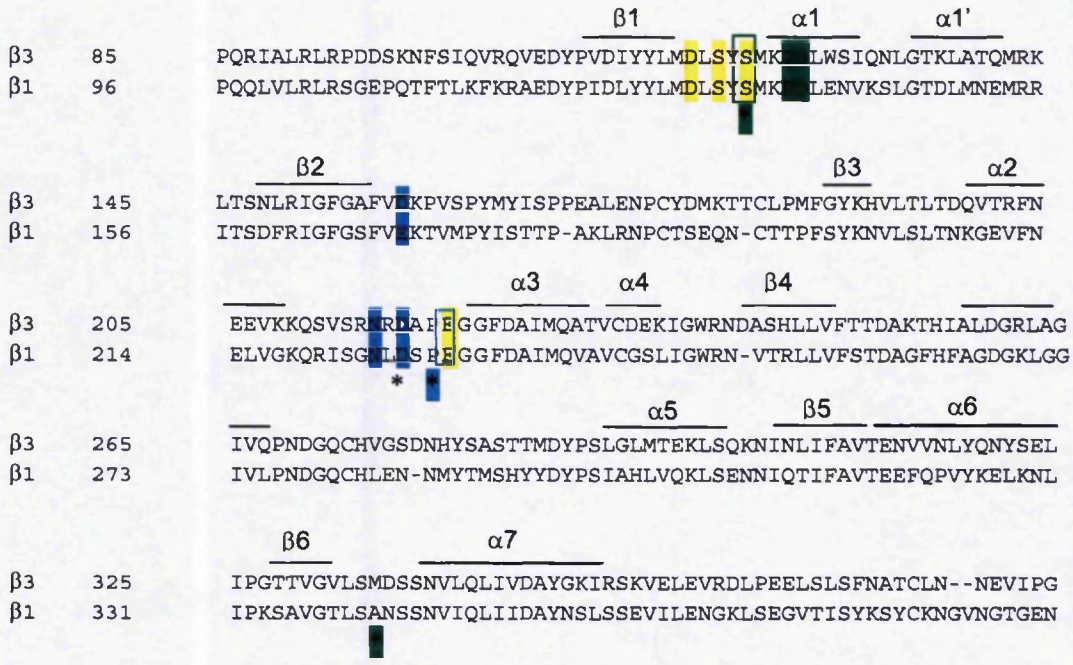

Figure 6.2. Sequence alignment of human integrin β3 and β1 A domains. Highlighted are residues with metal-coordinating side chain oxygen atoms. Marked with an asterisk are residues with metal-coordinating backbone carbonyl oxygen atoms. MIDAS coordinating residues in yellow, ADMIDAS in green, LIMBS in cyan, boxed in two colours are residues forming both metal-ion binding sites.

Moreover, the data presented here revealed that the LIMBS site has a critical role in α2β1 activation as both D226A and E169A mutations perturbed collagen binding. Similar results were obtained for α5β1 but as ligand binding could not be restored by the stimulatory β1 mAbs further studies were prevented (Dr. P.A. Mould, personal communication). Therefore, investigations in this study were focused at elucidating the role of the LIMBS cation-binding site in integrin activation. Since Ca^{2+} has both stimulatory and inhibitory regulatory effect on integrins and the evidence from the α5β1 investigations showed that the ADMIDAS was the negative regulatory Ca^{2+}-binding site, the LIMBS was predicted to be a good candidate for the stimulatory Ca^{2+}-binding site. Whereas the unmodified TR α2β1 and the TR α2[I332G]β1 mutants showed an enhancement of Mg^{2+}-supported collagen binding when the Ca^{2+} concentration remained low (Figure 5.9), both LIMBS mutations prevented the augmentation of Mg^{2+}-induced collagen binding by Ca^{2+}. Under similar experimental conditions, the ADMIDAS mutant had no effect on the Ca^{2+} stimulation of Mg^{2+}-induced collagen binding, as observed for

the TR integrin. These findings indicated that the LIMBS site was the stimulatory Ca^{2+}-binding site in $\alpha 2\beta 1$. Since the integrin stimulatory and inhibitory sites bind Ca^{2+} selectively [Mould *et al.*, 1995a] and the MIDAS binds Mg^{2+}[Mould *et al.*, 2002], the loss of higher binding activity in the LIMBS mutants suggested that the synergism between low concentrations of Ca^{2+} and Mg^{2+} resulted from their binding to the LIMBS and MIDAS in the βA domain, respectively.

The positive Ca^{2+}-regulatory role of LIMBS has been supported by data presented for cell-surface expressed $\alpha 4\beta 7$ integrins (a non-αA domain-containing integrin) in a different experimental system [Chen *et al.*, 2003]. This study examined the strength of cell adhesion mediated by $\alpha 4\beta 7$ on ligand-coated vessels under shear stress by measuring the resistance to detachment as shear stress increased incrementally. Consistent with the observation that low Ca^{2+} concentrations increased Mg^{2+}-mediated adhesion, this synergistic regulation required the LIMBS but not the ADMIDAS site. In the same study, disruption of the LIMBS site in β7 impaired the firm adhesion of cells on MAdCAM coated surfaces to rolling adhesion, independent of the divalent cation conditions. The firm and rolling $\alpha 4\beta 7$-mediated adhesion was equated to the high affinity and low $\alpha 4\beta 7$ affinity states respectively [Chen *et al.*, 2003]. The LIMBS mutants, including an equivalent to β1 D226A mutant, rolled in Mn^{2+}, in contrast to wild-type behaviour of firm adhesion in Mn^{2+}. Thus the loss of the LIMBS site converted the integrin to a lower affinity receptor.

Keeping in mind that in the β3 crystals, the MIDAS directly participated in ligand binding, and that this site is formed in the middle of the LMA array, it would appear that regulation of the β1 MIDAS cation is guarded at either side by a positive and a negative regulatory site. The interplay of the metal-binding sites in the ligand-binding surface of the β1 A domain determines the affinity for the MIDAS cation; the ADMIDAS stabilises the inactive (in the absence of ligand) or the low-affinity MIDAS configuration, whereas the LIMBS induces binding favouring the high-affinity configuration (Figure 6.3).

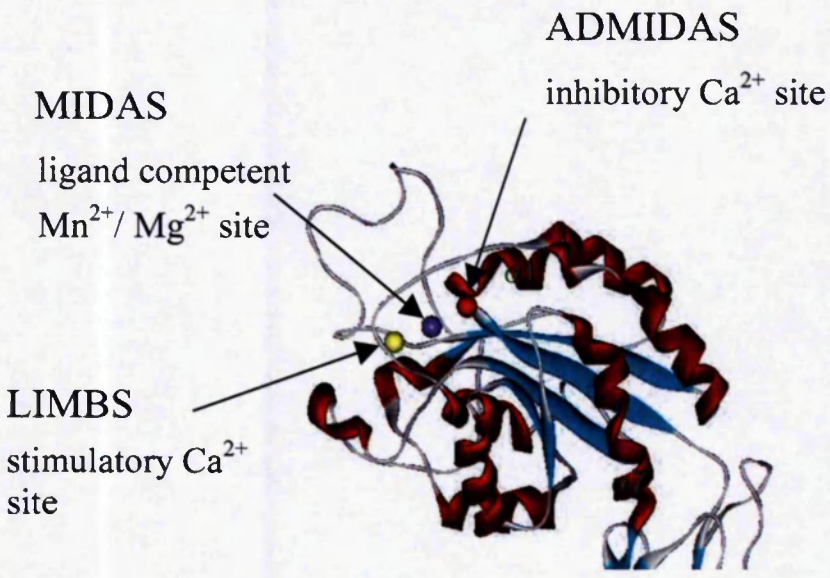

Figure 6.3. The role of βA domain cation-binding sites in integrin activation. The divalent ions at the LIMBS, MIDAS and ADMIDAS are shown as yellow, purple and red spheres respectively. In the open βA domain conformation α-helices are shown in orange, β-strands in cyan. With permission from Dr. P.A. Mould.

6.9 Summary and conclusions

The initial aim of this project was the production of the αA domain-containing integrin α2β1 as a soluble functional heterodimer to carry out biochemical studies. Soluble α2β1 integrins were expressed as FL and TR Fc-fusion proteins. Overall, the Fc-expression system facilitated a) expression of novel soluble truncated αA domain-containing integrins, in quantities appropriate for functional analyses, b) purification of the recombinant proteins by affinity chromatography, c) manipulation of the recombinant α2β1 e.g. by introduction of mutations in either integrin subunit, and expression of a series of α2β1 variants, d) rapid analysis of the collagen-binding activity of the recombinant proteins in solid-phase ligand-binding assays. These assays were used to examine the cation-binding properties of the TR α2β1 integrin in a cell-free system, eliminating implications by other than integrin-ligand contacts. Moreover, this strategy permitted direct comparisons of the mechanisms of activation of α2β1 to those of α5β1 integrin. This is the first report into the regulation of cation-dependent ligand binding of an αA domain-containing integrin by deliberate targeting of the LIMBS, MIDAS and ADMIDAS cations in the β subunit.

Integrin α5β1 lacks an αA domain and therefore the principal ligand-binding participant is the β1 A domain. In the α5β1 solid-phase fibronectin-binding studies it was shown that loss of metal occupancy at any one of the three β1 LMA cation-binding sites had an inhibitory effect on the integrin ligand-binding activity. Here, these results are extended to the α2β1 integrin that binds to non-RGD ligands in the αA domain. Thus, in α2β1 the β1 A domain has a regulatory role in integrin function through cation binding, conformational changes and / or intra-domain interactions. Moreover, by examining the interplay of the three cations (LIMBS, MIDAS, ADMIDAS) at the LMA cluster, it was shown that the LIMBS cation has a critical role in ligand recognition in both αA domain-containing and αA domain-lacking integrins. The ADMIDAS is essential for the disengagement of helices α1-α7 for complete integrin activation. Furthermore, the cooperative binding of MIDAS, LIMBS and ADMIDAS cations is required to stabilise the MIDAS cation and activate the open conformation of the βA domain to mediate integrin-ligand binding. Hence, the β1 A domain MIDAS has a fundamental role in integrin function, regulating

activation directly in the αA domain-lacking integrins and in an allosteric manner in the αA domain-containing integrins.

The overall objective of this study was to enhance the understanding of the β1 A domain regulation of α2β1-collagen binding. The principal research scheme involved around the cation-mediated regulation of collagen binding to the α2β1 and in particular of the role of the individual β1 LMA cation-binding sites in activation. These findings contribute to the understanding of the role of cations in the regulation of α2β1 activation and function. Evidently, occupancy of the cation-binding sites regulates integrin conformation in a complex manner, but the mechanisms by which metal ions regulate ligand binding to integrins that contain or lack an αA domain are conserved.

Chapter

7.0 References

Abrams C., Deng Y. J., Steiner B., O'Toole T. and Shattil S. J. (1994) Determinants of specificity of a baculovirus-expressed antibody Fab fragment that binds selectively to the activated form of integrin alpha IIb beta 3. *J. Biol. Chem.* **269,** 18781-18788.

Ajroud K., Sugimori T., Goldmann W. H., Fathallah D. M., Xiong J. P. and Arnaout M. A. (2004) Binding Affinity of Metal Ions to the CD11b A-domain Is Regulated by Integrin Activation and Ligands. *J. Biol. Chem.* **279,** 25483-25488.

Alonso J. L., Essafi M., Xiong J. P., Stehle T. and Arnaout M. A. (2002) Does the Integrin alphaA Domain Act as a Ligand for its betaA Domain? *Curr. Biol.* **12,** 340-342.

Aota S., Nomizu M. and Yamada K. M. (1994) The short amino acid sequence Pro-His-Ser-Arg-Asn in human fibronectin enhances cell-adhesive function. *J. Biol. Chem.* **269,** 24756-24761.

Aquilina A., Korda M., Bergelson J. M., Humphries M. J., Farndale R. W. and Tuckwell D. (2002) A novel gain-of-function mutation of the integrin alpha2 VWFA domain. *Eur. J. Biochem.* **269,** 1136-1144.

Armulik A., Nilsson I., von H. G. and Johansson S. (1999) Determination of the border between the transmembrane and cytoplasmic domains of human integrin subunits. *J. Biol. Chem.* **274,** 37030-37034.

Arnaout M. A., Mahalingam B. and Xiong J. P. (2005) Integrin Structure, Allostery, and Bidirectional Signaling. *Annu. Rev. Cell Dev. Biol.* **21,** 381-410.

Bader B. L., Rayburn H., Crowley D. and Hynes R. O. (1998) Extensive vasculogenesis, angiogenesis, and organogenesis precede lethality in mice lacking all alpha v integrins. *Cell* **95,** 507-519.

Bajt M. L. and Loftus J. C. (1994) Mutation of a ligand binding domain of beta 3 integrin. Integral role of oxygenated residues in alpha IIb beta 3 (GPIIb-IIIa) receptor function. *J. Biol. Chem.* **269,** 20913-20919.

Bajt M. L., Goodman T. and McGuire S. L. (1995) Beta 2 (CD18) mutations abolish ligand recognition by I domain integrins LFA-1 (alpha L beta 2, CD11a/CD18) and MAC-1 (alpha M beta 2, CD11b/CD18). *J. Biol. Chem.* **270,** 94-98.

Barton S. J., Travis M. A., Askari J. A., Buckley P. A., Craig S. E., Humphries M. J. and Mould A. P. (2004) Novel activating and inactivating mutations in the integrin beta1 subunit A domain. *Biochem. J.* **380,** 401-407.

Bazzoni G., Shih D. T., Buck C. A. and Hemler M. E. (1995) Monoclonal antibody 9EG7 defines a novel beta 1 integrin epitope induced by soluble ligand and manganese, but inhibited by calcium. *J. Biol. Chem.* **270,** 25570-25577.

Beglova N., Blacklow S. C., Takagi J. and Springer T. A. (2002) Cysteine-rich module structure reveals a fulcrum for integrin rearrangement upon activation. *Nat. Struct. Biol.* **9,** 282-287.

Bennett J. S. and Vilaire G. (1979) Exposure of platelet fibrinogen receptors by ADP and epinephrine. *J. Clin. Invest* **64,** 1393-1401.

Bergelson J. M., Chan B. M., Finberg R. W. and Hemler M. E. (1993) The integrin VLA-2 binds echovirus 1 and extracellular matrix ligands by different mechanisms. *J. Clin. Invest* **92,** 232-239.

Bokel C. and Brown N. H. (2002) Integrins in development: moving on, responding to, and sticking to the extracellular matrix. *Dev. Cell* **3,** 311-321.

Bork P., Doerks T., Springer T. A. and Snel B. (1999) Domains in plexins: links to integrins and transcription factors. *Trends Biochem. Sci.* **24,** 261-263.

Bouvard D., Brakebusch C., Gustafsson E., Aszodi A., Bengtsson T., Berna A. and Fassler R. (2001) Functional consequences of integrin gene mutations in mice. *Circ. Res.* **89,** 211-223.

Brakebusch C. and Fassler R. (2003) The integrin-actin connection, an eternal love affair. *EMBO J.* **22,** 2324-2333.

Brown N. H. (1993) Integrins hold Drosophila together. *Bioessays* **15,** 383-390.

Brown N. H. (2000) Cell-cell adhesion via the ECM: integrin genetics in fly and worm. *Matrix Biol.* **19,** 191-201.

Brunton V. G., MacPherson I. R. and Frame M. C. (2004) Cell adhesion receptors, tyrosine kinases and actin modulators: a complex three-way circuitry. *Biochim. Biophys. Acta* **1692,** 121-144.

Burrows L., Clark K., Mould A. P. and Humphries M. J. (1999) Fine mapping of inhibitory anti-alpha5 monoclonal antibody epitopes that differentially affect integrin-ligand binding. *Biochem. J.* **344,** 527-533.

Byzova T. V., Rabbani R., D'Souza S. E. and Plow E. F. (1998) Role of integrin alpha(v)beta3 in vascular biology. *Thromb. Haemost.* **80,** 726-734.

Calderwood D. A., Tuckwell D. S., Eble J., Kuhn K. and Humphries M. J. (1997) The integrin alpha1 A-domain is a ligand binding site for collagens and laminin. *J. Biol. Chem.* **272,** 12311-12317.

Calderwood D. A., Zent R., Grant R., Rees D. J., Hynes R. O. and Ginsberg M. H. (1999) The Talin head domain binds to integrin beta subunit cytoplasmic tails and regulates integrin activation. *J. Biol. Chem.* **274,** 28071-28074.

Calderwood D. A., Yan B., de Pereda J. M., Alvarez B. G., Fujioka Y., Liddington R. C. and Ginsberg M. H. (2002) The phosphotyrosine binding-like domain of talin activates integrins. *J. Biol. Chem.* **277,** 21749-21758.

Calderwood D. A., Fujioka Y., de Pereda J. M., Garcia-Alvarez B., Nakamoto T., Margolis B., McGlade C. J., Liddington R. C. and Ginsberg M. H. (2003) Integrin beta cytoplasmic domain interactions with phosphotyrosine-binding domains: a structural prototype for diversity in integrin signaling. *Proc. Natl. Acad. Sci. U. S. A* **100,** 2272-2277.

Calderwood D. A. (2004) Integrin activation. *J. Cell Sci.* **117,** 657-666.

Calderwood D. A., Tai V., Di P. G., De C. P. and Ginsberg M. H. (2004) Competition for talin results in trans-dominant inhibition of integrin activation. *J. Biol. Chem.* **279,** 28889-28895.

Calvete J. J., Henschen A. and Gonzalez-Rodriguez J. (1991) Assignment of disulphide bonds in human platelet GPIIIa. A disulphide pattern for the beta-subunits of the integrin family. *Biochem. J.* **274,** 63-71.

Calvete J. J. (1999) Platelet integrin GPIIb/IIIa: structure-function correlations. An update and lessons from other integrins. *Proc. Soc. Exp. Biol. Med.* **222,** 29-38.

Calvete J. J. (2004) Structures of integrin domains and concerted conformational changes in the bidirectional signaling mechanism of alphaIIbbeta3. *Exp. Biol. Med. (Maywood.)* **229,** 732-744.

Carlsson L. E., Santoso S., Spitzer C., Kessler C. and Greinacher A. (1999) The alpha2 gene coding sequence T807/A873 of the platelet collagen receptor integrin alpha2beta1 might be a genetic risk factor for the development of stroke in younger patients. *Blood* **93,** 3583-3586.

Carrell N. A., Fitzgerald L. A., Steiner B., Erickson H. P. and Phillips D. R. (1985) Structure of human platelet membrane glycoproteins IIb and IIIa as determined by electron microscopy. *J. Biol. Chem.* **260,** 1743-1749.

Casasnovas J. M., Pieroni C. and Springer T. A. (1999) Lymphocyte function-associated antigen-1 binding residues in intercellular adhesion molecule-2 (ICAM-2) and the integrin binding surface in the ICAM subfamily. *Proc. Natl. Acad. Sci. U. S. A* **96,** 3017-3022.

Champe M., McIntyre B. W. and Berman P. W. (1995) Monoclonal antibodies that block the activity of leukocyte function-associated antigen 1 recognize three discrete epitopes in the inserted domain of CD11a. *J. Biol. Chem.* **270,** 1388-1394.

Chen J., Diacovo T. G., Grenache D. G., Santoro S. A. and Zutter M. M. (2002) The alpha(2) integrin subunit-deficient mouse: a multifaceted phenotype including defects of branching morphogenesis and hemostasis. *Am. J. Pathol.* **161,** 337-344.

Chen J., Salas A. and Springer T. A. (2003) Bistable regulation of integrin adhesiveness by a bipolar metal ion cluster. *Nat. Struct. Biol.* **10,** 995-1001.

Chen J., Takagi J., Xie C., Xiao T., Luo B. H. and Springer T. A. (2004) The relative influence of metal ion binding sites in the I-like domain and the interface with the hybrid domain on rolling and firm adhesion by integrin alpha4beta7. *J. Biol. Chem.* **279,** 55556-55561.

Chigaev A., Blenc A. M., Braaten J. V., Kumaraswamy N., Kepley C. L., Andrews R. P., Oliver J. M., Edwards B. S., Prossnitz E. R., Larson R. S. and Sklar L. A. (2001) Real time analysis of the affinity regulation of alpha 4-integrin. The physiologically activated receptor is intermediate in affinity between resting and Mn^{2+} or antibody activation. *J. Biol. Chem.* **276,** 48670-48678.

Cierniewski C. S., Haas T. A., Smith J. W. and Plow E. F. (1994) Characterization of cation-binding sequences in the platelet integrin GPIIb-IIIa (alpha IIb beta 3) by terbium luminescence. *Biochemistry* **33,** 12238-12246.

Cierniewski C. S., Byzova T., Papierak M., Haas T. A., Niewiarowska J., Zhang L., Cieslak M. and Plow E. F. (1999) Peptide ligands can bind to distinct sites in integrin alphaIIbbeta3 and elicit different functional responses. *J. Biol. Chem.* **274,** 16923-16932.

Clark E. A. and Brugge J. S. (1995) Integrins and signal transduction pathways: the road taken. *Science* **268,** 233-239.

Clemetson K. J. and Clemetson J. M. (1998) Integrins and cardiovascular disease. *Cell Mol. Life Sci.* **54,** 502-513.

Clemetson K. J. and Clemetson J. M. (2004) Platelet receptor signalling. *Hematol. J.* **5** 159-163.

Cockett M. I., Bebbington C. R. and Yarranton G. T. (1991) The use of engineered E1A genes to transactivate the hCMV-MIE promoter in permanent CHO cell lines. *Nucleic Acids Res.* **19,** 319-325.

Coe A. P., Askari J. A., Kline A. D., Robinson M. K., Kirby H., Stephens P. E. and Humphries M. J. (2001) Generation of a minimal alpha5beta1 integrin-Fc fragment. *J. Biol. Chem.* **276,** 35854-35866.

Colombatti A. and Bonaldo P. (1991) The superfamily of proteins with von Willebrand factor type A-like domains: one theme common to components of extracellular matrix, hemostasis, cellular adhesion, and defense mechanisms. *Blood* **77,** 2305-2315.

Coppolino M. G. and Dedhar S. (2000) Bi-directional signal transduction by integrin receptors. *Int. J. Biochem. Cell Biol.* **32,** 171-188.

Critchley D. R. (2000) Focal adhesions - the cytoskeletal connection. *Curr. Opin. Cell Biol.* **12,** 133-139.

D'Souza S. E., Ginsberg M. H., Burke T. A., Lam S. C. and Plow E. F. (1988) Localization of an Arg-Gly-Asp recognition site within an integrin adhesion receptor. *Science* **242,** 91-93.

D'Souza S. E., Ginsberg M. H., Burke T. A. and Plow E. F. (1990) The ligand binding site of the platelet integrin receptor GPIIb-IIIa is proximal to the second calcium binding domain of its alpha subunit. *J. Biol. Chem.* **265,** 3440-3446.

D'Souza S. E., Haas T. A., Piotrowicz R. S., Byers-Ward V., McGrath D. E., Soule H. R., Cierniewski C., Plow E. F. and Smith J. W. (1994) Ligand and cation binding are dual

functions of a discrete segment of the integrin beta 3 subunit: cation displacement is involved in ligand binding. *Cell* **79,** 659-667.

Dechantsreiter M. A., Planker E., Matha B., Lohof E., Holzemann G., Jonczyk A., Goodman S. L. and Kessler H. (1999) N-Methylated cyclic RGD peptides as highly active and selective alpha(V)beta(3) integrin antagonists. *J. Med. Chem.* **42,** 3033-3040.

Deckmyn H., Chew S. L. and Vermylen J. (1990) Lack of platelet response to collagen associated with an autoantibody against glycoprotein Ia: a novel cause of acquired qualitative platelet dysfunction. *Thromb. Haemost.* **64,** 74-79.

Depraetere H., Wille C., Gansemans Y., Stanssens P., Lauwereys M., Baruch D., De R. S. and Deckmyn H. (1997) The integrin alpha 2 beta 1 (GPIa/IIa)-I-domain inhibits platelet-collagen interaction. *Thromb. Haemost.* 77, 981-985.

Di P. J., Federici A. B., Mannucci P. M., Canciani M. T., Kritzik M., Kunicki T. J. and Nugent D. (1999) Low platelet alpha2beta1 levels in type I von Willebrand disease correlate with impaired platelet function in a high shear stress system. *Blood* **93,** 3578-3582.

Dickeson S. K., Walsh J. J. and Santoro S. A. (1997) Contributions of the I and EF hand domains to the divalent cation-dependent collagen binding activity of the alpha2beta1 integrin. *J. Biol. Chem.* **272,** 7661-7668.

Du X., Gu M., Weisel J. W., Nagaswami C., Bennett J. S., Bowditch R. and Ginsberg M. H. (1993) Long range propagation of conformational changes in integrin alpha IIb beta 3. *J. Biol. Chem.* **268,** 23087-23092.

Eble J. A., Wucherpfennig K. W., Gauthier L., Dersch P., Krukonis E., Isberg R. R. and Hemler M. E. (1998) Recombinant soluble human alpha 3 beta 1 integrin: purification, processing, regulation, and specific binding to laminin-5 and invasin in a mutually exclusive manner. *Biochemistry* **37,** 10945-10955.

Elices M. J. and Hemler M. E. (1989) The human integrin VLA-2 is a collagen receptor on some cells and a collagen/laminin receptor on others. *Proc. Natl. Acad. Sci. U. S. A* **86,** 9906-9910.

Emsley J., King S. L., Bergelson J. M. and Liddington R. C. (1997) Crystal structure of the I domain from integrin alpha2beta1. *J. Biol. Chem.* **272,** 28512-28517.

Emsley J., Knight C. G., Farndale R. W., Barnes M. J. and Liddington R. C. (2000) Structural basis of collagen recognition by integrin alpha2beta1. *Cell* **101,** 47-56.

Etzioni A., Doerschuk C. M. and Harlan J. M. (2000) Similarities and dissimilarities between humans and mice looking at adhesion molecules defects. *Adv. Exp. Med. Biol.* **479,** 147-161.

Fenczik C. A., Sethi T., Ramos J. W., Hughes P. E. and Ginsberg M. H. (1997) Complementation of dominant suppression implicates CD98 in integrin activation. *Nature* **390,** 81-85.

ffrench-Constant C. and Colognato H. (2004) Integrins: versatile integrators of extracellular signals. *Trends Cell Biol.* **14,** 678-686.

Gadek T. R., Burdick D. J., McDowell R. S., Stanley M. S., Marsters J. C., Jr., Paris K. J., Oare D. A., Reynolds M. E., Ladner C., Zioncheck K. A., Lee W. P., Gribling P., Dennis M. S., Skelton N. J., Tumas D. B., Clark K. R., Keating S. M., Beresini M. H., Tilley J. W., Presta L. G. and Bodary S. C. (2002) Generation of an LFA-1 antagonist by the transfer of the ICAM-1 immunoregulatory epitope to a small molecule. *Science* **295,** 1086-1089.

Garcia-Alvarez B., de Pereda J. M., Calderwood D. A., Ulmer T. S., Critchley D., Campbell I. D., Ginsberg M. H. and Liddington R. C. (2003) Structural determinants of integrin recognition by talin. *Mol. Cell* **11,** 49-58.

Geiger B., Bershadsky A., Pankov R. and Yamada K. M. (2001) Transmembrane crosstalk between the extracellular matrix--cytoskeleton crosstalk. *Nat. Rev. Mol. Cell Biol.* **2,** 793-805.

Gibbins J. M. (2004) Platelet adhesion signalling and the regulation of thrombus formation. *J. Cell Sci.* **117,** 3415-3425.

Ginsberg M. H., Yaspan B., Forsyth J., Ulmer T. S., Campbell I. D. and Slepak M. (2001) A membrane-distal segment of the integrin alpha IIb cytoplasmic domain regulates integrin activation. *J. Biol. Chem.* **276,** 22514-22521.

Goodman T. G. and Bajt M. L. (1996) Identifying the putative metal ion-dependent adhesion site in the beta2 (CD18) subunit required for alphaLbeta2 and alphaMbeta2 ligand interactions. *J. Biol. Chem.* **271,** 23729-23736.

Guo W. and Giancotti F. G. (2004) Integrin signalling during tumour progression. *Nat. Rev. Mol. Cell Biol.* **5,** 816-826.

Haas T. A. and Plow E. F. (1996) The cytoplasmic domain of alphaIIb beta3. A ternary complex of the integrin alpha and beta subunits and a divalent cation. *J. Biol. Chem.* **271,** 6017-6026.

Hangan D., Uniyal S., Morris V. L., MacDonald I. C., von B. C., Chau T., Schmidt E. E., Chambers A. F., Groom A. C. and Chan B. M. (1996) Integrin VLA-2 (alpha2beta1) function in postextravasation movement of human rhabdomyosarcoma RD cells in the liver. *Cancer Res.* **56,** 3142-3149.

Harding M. M. (2001) Geometry of metal-ligand interactions in proteins. *Acta Crystallogr. D. Biol. Crystallogr.* **57,** 401-411.

Harris E. S., McIntyre T. M., Prescott S. M. and Zimmerman G. A. (2000) The leukocyte integrins. *J. Biol. Chem.* **275,** 23409-23412.

Hayashi Y. K., Chou F. L., Engvall E., Ogawa M., Matsuda C., Hirabayashi S., Yokochi K., Ziober B. L., Kramer R. H., Kaufman S. J., Ozawa E., Goto Y., Nonaka I., Tsukahara T., Wang J. Z., Hoffman E. P. and Arahata K. (1998) Mutations in the integrin alpha7 gene cause congenital myopathy. *Nat. Genet.* **19,** 94-97.

He L., Pappan L. K., Grenache D. G., Li Z., Tollefsen D. M., Santoro S. A. and Zutter M. M. (2003) The contributions of the alpha 2 beta 1 integrin to vascular thrombosis in vivo. *Blood* **102,** 3652-3657.

Hemmings L., Rees D. J., Ohanian V., Bolton S. J., Gilmore A. P., Patel B., Priddle H., Trevithick J. E., Hynes R. O. and Critchley D. R. (1996) Talin contains three actin-binding sites each of which is adjacent to a vinculin-binding site. *J. Cell Sci.* **109,** 2715-2726.

Hogg N., Stewart M. P., Scarth S. L., Newton R., Shaw J. M., Law S. K. and Klein N. (1999) A novel leukocyte adhesion deficiency caused by expressed but nonfunctional beta2 integrins Mac-1 and LFA-1. *J. Clin. Invest* **103,** 97-106.

Hogg N. and Bates P. A. (2000) Genetic analysis of integrin function in man: LAD-1 and other syndromes. *Matrix Biol.* **19,** 211-222.

Hu D. D., Barbas C. F. and Smith J. W. (1996) An allosteric Ca^{2+} binding site on the beta3-integrins that regulates the dissociation rate for RGD ligands. *J. Biol. Chem.* **271,** 21745-21751.

Huang C., Zang Q., Takagi J. and Springer T. A. (2000) Structural and functional studies with antibodies to the integrin beta 2 subunit. A model for the I-like domain. *J. Biol. Chem.* **275,** 21514-21524.

Hughes P. E., O'Toole T. E., Ylanne J., Shattil S. J. and Ginsberg M. H. (1995) The conserved membrane-proximal region of an integrin cytoplasmic domain specifies ligand binding affinity. *J. Biol. Chem.* **270,** 12411-12417.

Hughes P. E., az-Gonzalez F., Leong L., Wu C., McDonald J. A., Shattil S. J. and Ginsberg M. H. (1996) Breaking the integrin hinge. A defined structural constraint regulates integrin signaling. *J. Biol. Chem.* **271,** 6571-6574.

Hughes P. E. and Pfaff M. (1998) Integrin affinity modulation. *Trends Cell Biol.* **8,** 359-364.

Humphries J. D., Askari J. A., Zhang X. P., Takada Y., Humphries M. J. and Mould A. P. (2000) Molecular basis of ligand recognition by integrin alpha5beta 1. II. Specificity of arg-gly-Asp binding is determined by Trp157 OF THE alpha subunit. *J. Biol. Chem.* **275,** 20337-20345.

Humphries M. J. (1990) The molecular basis and specificity of integrin-ligand interactions. *J. Cell Sci.* **97,** 585-592.

Humphries M. J. (2000) Integrin structure. *Biochem. Soc. Trans.* **28,** 311-339.

Humphries M. J. (2002) Insights into integrin-ligand binding and activation from the first crystal structure. *Arthritis Res.* 3, 69-78.

Humphries M. J., McEwan P. A., Barton S. J., Buckley P. A., Bella J. and Mould A. P. (2003) Integrin structure: heady advances in ligand binding, but activation still makes the knees wobble. *Trends Biochem. Sci.* **28,** 313-320.

Humphries M. J. (2004) Monoclonal antibodies as probes of integrin priming and activation. *Biochem. Soc. Trans.* **32,** 407-411.

Huth J. R., Olejniczak E. T., Mendoza R., Liang H., Harris E. A., Lupher M. L., Jr., Wilson A. E., Fesik S. W. and Staunton D. E. (2000) NMR and mutagenesis evidence for an I domain allosteric site that regulates lymphocyte function-associated antigen 1 ligand binding. *Proc. Natl. Acad. Sci. U. S. A* **97,** 5231-5236.

Hynes R. O. (1992) Integrins: versatility, modulation, and signaling in cell adhesion. *Cell* **69,** 11-25.

Hynes R. O. (2002) Integrins: bidirectional, allosteric signaling machines. *Cell* **110,** 673-687.

Irie A., Kamata T. and Takada Y. (1997) Multiple loop structures critical for ligand binding of the integrin alpha4 subunit in the upper face of the beta-propeller mode 1. *Proc. Natl. Acad. Sci. U. S. A* **94,** 7198-7203.

Kainoh M. and Tanaka T. (2002) Production of soluble integrin alpha2beta1 heterodimer complex functionally active in vitro and in vivo. *Biochem. Biophys. Res. Commun.* **290,** 305-310.

Kallen J., Welzenbach K., Ramage P., Geyl D., Kriwacki R., Legge G., Cottens S., Weitz-Schmidt G. and Hommel U. (1999) Structural basis for LFA-1 inhibition upon lovastatin binding to the CD11a I-domain. *J. Mol. Biol.* **292,** 1-9.

Kamata T., Puzon W. and Takada Y. (1994) Identification of putative ligand binding sites within I domain of integrin alpha 2 beta 1 (VLA-2, CD49b/CD29). *J. Biol. Chem.* **269,** 9659-9663.

Kamata T., Wright R. and Takada Y. (1995a) Critical threonine and aspartic acid residues within the I domains of beta 2 integrins for interactions with intercellular adhesion molecule 1 (ICAM-1) and C3bi. *J. Biol. Chem.* **270,** 12531-12535.

Kamata T., Puzon W. and Takada Y. (1995b) Identification of putative ligand-binding sites of the integrin alpha 4 beta 1 (VLA-4, CD49d/CD29). *Biochem. J.* **305,** 945-951.

Kamata T., Liddington R. C. and Takada Y. (1999) Interaction between collagen and the alpha(2) I-domain of integrin alpha(2)beta(1). Critical role of conserved residues in the metal ion-dependent adhesion site (MIDAS) region. *J. Biol. Chem.* **274,** 32108-32111.

Kamata T., Tieu K. K., Irie A., Springer T. A. and Takada Y. (2001) Amino acid residues in the alpha IIb subunit that are critical for ligand binding to integrin alpha IIbbeta 3 are clustered in the beta-propeller model. *J. Biol. Chem.* **276,** 44275-44283.

Kamata T., Tieu K. K., Tarui T., Puzon-McLaughlin W., Hogg N. and Takada Y. (2002) The role of the CPNKEKEC sequence in the beta(2) subunit I domain in regulation of integrin alpha(L)beta(2) (LFA-1). *J. Immunol.* **168,** 2296-2301.

Kamata T., Handa M., Sato Y., Ikeda Y. and Aiso S. (2005) Membrane-proximal {alpha}/{beta} stalk interactions differentially regulate integrin activation. *J. Biol. Chem.* **280,** 24775-24783.

Kanner S. B., Grosmaire L. S., Ledbetter J. A. and Damle N. K. (1993) Beta 2-integrin LFA-1 signaling through phospholipase C-gamma 1 activation. *Proc. Natl. Acad. Sci. U. S. A* **90,** 7099-7103.

Karpusas M., Ferrant J., Weinreb P. H., Carmillo A., Taylor F. R. and Garber E. A. (2003) Crystal structure of the alpha1beta1 integrin I domain in complex with an antibody Fab fragment. *J. Mol. Biol.* **327,** 1031-1041.

Kashiwagi H., Schwartz M. A., Eigenthaler M., Davis K. A., Ginsberg M. H. and Shattil S. J. (1997) Affinity modulation of platelet integrin alphaIIbbeta3 by beta3-endonexin, a selective binding partner of the beta3 integrin cytoplasmic tail. *J. Cell Biol.* **137,** 1433-1443.

Kato A. (1997) The biologic and clinical spectrum of Glanzmann's thrombasthenia: implications of integrin alpha IIb beta 3 for its pathogenesis. *Crit Rev. Oncol. Hematol.* **26,** 1-23.

Kern A., Briesewitz R., Bank I. and Marcantonio E. E. (1994) The role of the I domain in ligand binding of the human integrin alpha 1 beta 1. *J. Biol. Chem.* **269,** 22811-22816.

Kerr J. R. (1999) Cell adhesion molecules in the pathogenesis of and host defence against microbial infection. *Mol. Pathol.* **52,** 220-230.

Kim M., Carman C. V. and Springer T. A. (2003) Bidirectional transmembrane signaling by cytoplasmic domain separation in integrins. *Science* **301,** 1720-1725.

Knezevic I., Leisner T. M. and Lam S. C. (1996) Direct binding of the platelet integrin alphaIIbbeta3 (GPIIb-IIIa) to talin. Evidence that interaction is mediated through the cytoplasmic domains of both alphaIIb and beta3. *J. Biol. Chem.* **271,** 16416-16421.

Knight C. G., Morton L. F., Onley D. J., Peachey A. R., Messent A. J., Smethurst P. A., Tuckwell D. S., Farndale R. W. and Barnes M. J. (1998) Identification in collagen type I of an integrin alpha2 beta1-binding site containing an essential GER sequence. *J. Biol. Chem.* **273,** 33287-33294.

Knight C. G., Morton L. F., Peachey A. R., Tuckwell D. S., Farndale R. W. and Barnes M. J. (2000) The collagen-binding A-domains of integrins alpha(1)beta(1) and alpha(2)beta(1) recognize the same specific amino acid sequence, GFOGER, in native (triple-helical) collagens. *J. Biol. Chem.* **275,** 35-40.

Kolanus W., Nagel W., Schiller B., Zeitlmann L., Godar S., Stockinger H. and Seed B. (1996) Alpha L beta 2 integrin/LFA-1 binding to ICAM-1 induced by cytohesin-1, a cytoplasmic regulatory molecule. *Cell* **86,** 233-242.

Komoriya A., Green L. J., Mervic M., Yamada S. S., Yamada K. M. and Humphries M. J. (1991) The minimal essential sequence for a major cell type-specific adhesion site (CS1) within the alternatively spliced type III connecting segment domain of fibronectin is leucine-aspartic acid-valine. *J. Biol. Chem.* **266,** 15075-15079.

Kozlowski J. M., Hart I. R., Fidler I. J. and Hanna N. (1984) A human melanoma line heterogeneous with respect to metastatic capacity in athymic nude mice. *J. Natl. Cancer Inst.* **72,** 913-917.

Kritzik M., Savage B., Nugent D. J., Santoso S., Ruggeri Z. M. and Kunicki T. J. (1998) Nucleotide polymorphisms in the alpha2 gene define multiple alleles that are associated with differences in platelet alpha2 beta1 density. *Blood* **92,** 2382-2388.

Labadia M. E., Jeanfavre D. D., Caviness G. O. and Morelock M. M. (1998) Molecular regulation of the interaction between leukocyte function-associated antigen-1 and soluble ICAM-1 by divalent metal cations. *J. Immunol.* **161,** 836-842.

Larson R. S., Davis T., Bologa C., Semenuk G., Vijayan S., Li Y., Oprea T., Chigaev A., Buranda T., Wagner C. R. and Sklar L. A. (2005) Dissociation of I domain and global conformational changes in LFA-1: refinement of small molecule-I domain structure-activity relationships. *Biochemistry* **44,** 4322-4331.

Last-Barney K., Davidson W., Cardozo M., Frye L. L., Grygon C. A., Hopkins J. L., Jeanfavre D. D., Pav S., Qian C., Stevenson J. M., Tong L., Zindell R. and Kelly T. A. (2001) Binding site elucidation of hydantoin-based antagonists of LFA-1 using multidisciplinary technologies: evidence for the allosteric inhibition of a protein--protein interaction. *J. Am. Chem. Soc.* **123,** 5643-5650.

Lee J. O., Bankston L. A., Arnaout M. A. and Liddington R. C. (1995a) Two conformations of the integrin A-domain (I-domain): a pathway for activation? *Structure* **3,** 1333-1340.

Lee J. O., Rieu P., Arnaout M. A. and Liddington R. (1995b) Crystal structure of the A domain from the alpha subunit of integrin CR3 (CD11b/CD18). *Cell* **80,** 631-638.

Li R., Rieu P., Griffith D. L., Scott D. and Arnaout M. A. (1998) Two functional states of the CD11b A-domain: correlations with key features of two Mn^{2+}-complexed crystal structures. *J. Cell Biol.* **143,** 1523-1534.

Li R., Mitra N., Gratkowski H., Vilaire G., Litvinov R., Nagasami C., Weisel J. W., Lear J. D., Degrado W. F. and Bennett J. S. (2003) Activation of integrin alphaIIbbeta3 by modulation of transmembrane helix associations. *Science* **300,** 795-798.

Li W., Metcalf D. G., Gorelik R., Li R., Mitra N., Nanda V., Law P. B., Lear J. D., Degrado W. F. and Bennett J. S. (2005) A push-pull mechanism for regulating integrin function. *Proc. Natl. Acad. Sci. U. S. A* **102,** 1424-1429.

Liddington R. C. and Ginsberg M. H. (2002) Integrin activation takes shape. *J. Cell Biol.* **158,** 833-839.

Liu G. (2001) Small molecule antagonists of the LFA-1 / ICAM-1 interactions as potential therapeutic agents. *Expert Opin. Ther. Patents* **11,** 1383-1393.

Liu G., Huth J. R., Olejniczak E. T., Mendoza R., DeVries P., Leitza S., Reilly E. B., Okasinski G. F., Fesik S. W. and von Geldern T. W. (2001) Novel p-arylthio cinnamides as antagonists of leukocyte function-associated antigen-1/intracellular adhesion molecule-1 interaction. 2. Mechanism of inhibition and structure-based improvement of pharmaceutical properties. *J. Med. Chem.* **44,** 1202-1210.

Loftus J. C., Halloran C. E., Ginsberg M. H., Feigen L. P., Zablocki J. A. and Smith J. W. (1996) The amino-terminal one-third of alpha IIb defines the ligand recognition specificity of integrin alpha IIb beta 3. *J. Biol. Chem.* **271,** 2033-2039.

Lu C., Oxvig C. and Springer T. A. (1998) The structure of the beta-propeller domain and C-terminal region of the integrin alphaM subunit. Dependence on beta subunit association and prediction of domains. *J. Biol. Chem.* **273,** 15138-15147.

Lu C., Ferzly M., Takagi J. and Springer T. A. (2001) Epitope mapping of antibodies to the C-terminal region of the integrin beta 2 subunit reveals regions that become exposed upon receptor activation. *J. Immunol.* **166,** 5629-5637.

Lu C., Takagi J. and Springer T. A. (2001a) Association of the membrane proximal regions of the alpha and beta subunit cytoplasmic domains constrains an integrin in the inactive state. *J. Biol. Chem.* **276,** 14642-14648.

Lu C., Shimaoka M., Zang Q., Takagi J. and Springer T. A. (2001b) Locking in alternate conformations of the integrin alphaLbeta2 I domain with disulfide bonds reveals functional relationships among integrin domains. *Proc. Natl. Acad. Sci. U. S. A* **98,** 2393-2398.

Lu C., Shimaoka M., Ferzly M., Oxvig C., Takagi J. and Springer T. A. (2001c) An isolated, surface-expressed I domain of the integrin alphaLbeta2 is sufficient for strong adhesive function when locked in the open conformation with a disulfide bond. *Proc. Natl. Acad. Sci. U. S. A* **98,** 2387-2392.

Lu C., Shimaoka M., Salas A. and Springer T. A. (2004) The binding sites for competitive antagonistic, allosteric antagonistic, and agonistic antibodies to the I domain of integrin LFA-1. *J. Immunol.* **173,** 3972-3978.

Luo B. H., Springer T. A. and Takagi J. (2003) High affinity ligand binding by integrins does not involve head separation. *J. Biol. Chem.* **278,** 17185-17189.

Luo B. H., Springer T. A. and Takagi J. (2003a) Stabilising the open conformation of the integrin headpiece with a glycan wedge increases affinity for ligand. *PNAS.* **100,** 2403-2408.

Luo B. H., Springer T. A. and Takagi J. (2004) A specific interface between integrin transmembrane helices and affinity for ligand. *PLoS. Biol.* **2,** e153.

Luo B. H., Carman C. V., Takagi J. and Springer T. A. (2005) Disrupting integrin transmembrane domain heterodimerization increases ligand binding affinity, not valency or clustering. *Proc. Natl. Acad. Sci. U. S. A* **102,** 3679-3684.

Lupher M. L., Jr., Harris E. A., Beals C. R., Sui L. M., Liddington R. C. and Staunton D. E. (2001) Cellular activation of leukocyte function-associated antigen-1 and its affinity are regulated at the I domain allosteric site. *J. Immunol.* **167,** 1431-1439.

Ma Q., Shimaoka M., Lu C., Jing H., Carman C. V. and Springer T. A. (2002) Activation-induced conformational changes in the I domain region of lymphocyte function-associated antigen 1. *J. Biol. Chem.* **277,** 10638-10641.

Mathew E. C., Shaw J. M., Bonilla F. A., Law S. K. and Wright D. A. (2000) A novel point mutation in CD18 causing the expression of dysfunctional CD11/CD18 leucocyte integrins in a patient with leucocyte adhesion deficiency (LAD). *Clin. Exp. Immunol.* **121,** 133-138.

Mathias P., Galleno M. and Nemerow G. R. (1998) Interactions of soluble recombinant integrin alphav beta5 with human adenoviruses. *J. Virol.* **72,** 8669-8675.

Matsubara Y., Murata M., Maruyama T., Handa M., Yamagata N., Watanabe G., Saruta T. and Ikeda Y. (2000) Association between diabetic retinopathy and genetic variations in alpha2beta1 integrin, a platelet receptor for collagen. *Blood* **95,** 1560-1564.

McCleverty C.J. and Liddington R.C. (2003) Engineering mutants of the integrin αMβ2 I domain: structural and functional studies. *Biochem.J.* **372,** 121-127.

Mehta R. J., Diefenbach B., Brown A., Cullen E., Jonczyk A., Gussow D., Luckenbach G. A. and Goodman S. L. (1998) Transmembrane-truncated alphavbeta3 integrin retains high affinity for ligand binding: evidence for an 'inside-out' suppressor? *Biochem. J.* **330,** 861-869.

Miao H., Li S., Hu Y. L., Yuan S., Zhao Y., Chen B. P., Puzon-McLaughlin W., Tarui T., Shyy J. Y., Takada Y., Usami S. and Chien S. (2002) Differential regulation of Rho GTPases by beta1 and beta3 integrins: the role of an extracellular domain of integrin in intracellular signaling. *J. Cell Sci.* **115,** 2199-2206.

Moshfegh K., Wuillemin W. A., Redondo M., Lammle B., Beer J. H., Liechti-Gallati S. and Meyer B. J. (1999) Association of two silent polymorphisms of platelet glycoprotein Ia/IIa receptor with risk of myocardial infarction: a case-control study. *Lancet* **353,** 351-354.

Mould A. P., Komoriya A., Yamada K. M. and Humphries M. J. (1991a) The CS5 peptide is a second site in the IIICS region of fibronectin recognized by the integrin alpha 4 beta 1. Inhibition of alpha 4 beta 1 function by RGD peptide homologues. *J. Biol. Chem.* **266,** 3579-3585.

Mould A. P. and Humphries M. J. (1991) Identification of a novel recognition sequence for the integrin alpha 4 beta 1 in the COOH-terminal heparin-binding domain of fibronectin. *EMBO J.* **10,** 4089-4095.

Mould A. P., Akiyama S. K. and Humphries M. J. (1995a) Regulation of integrin alpha 5 beta 1-fibronectin interactions by divalent cations. Evidence for distinct classes of binding sites for Mn^{2+}, Mg^{2+}, and Ca^{2+}. *J. Biol. Chem.* **270,** 26270-26277.

Mould A. P., Garratt A. N., Askari J. A., Akiyama S. K. and Humphries M. J. (1995b) Regulation of integrin alpha 5 beta 1 function by anti-integrin antibodies and divalent cations. *Biochem. Soc. Trans.* **23,** 395S.

Mould A. P., Garratt A. N., Askari J. A., Akiyama S. K. and Humphries M. J. (1995c) Identification of a novel anti-integrin monoclonal antibody that recognises a ligand-induced binding site epitope on the beta 1 subunit. *FEBS Lett.* **363,** 118-122.

Mould A. P., Akiyama S. K. and Humphries M. J. (1996) The inhibitory anti-beta1 integrin monoclonal antibody 13 recognizes an epitope that is attenuated by ligand occupancy. Evidence for allosteric inhibition of integrin function. *J. Biol. Chem.* **271,** 20365-20374.

Mould A. P. (1996) Getting integrins into shape: recent insights into how integrin activity is regulated by conformational changes. *J. Cell Sci.* **109,** 2613-2618.

Mould A. P., Askari J. A., Aota S., Yamada K. M., Irie A., Takada Y., Mardon H. J. and Humphries M. J. (1997) Defining the topology of integrin alpha5beta1-fibronectin interactions using inhibitory anti-alpha5 and anti-beta1 monoclonal antibodies. Evidence that the synergy sequence of fibronectin is recognized by the amino-terminal repeats of the alpha5 subunit. *J. Biol. Chem.* **272,** 17283-17292.

Mould A. P., Askari J. A. and Humphries M. J. (2000) Molecular basis of ligand recognition by integrin alpha 5beta 1. I. Specificity of ligand binding is determined by amino acid sequences in the second and third NH2-terminal repeats of the alpha subunit. *J. Biol. Chem.* **275,** 20324-20336.

Mould P.A.. (2002) Integrin purification. *In* Current Protocols in Cell Biology. Bonifacino J.S., Dasso M., Harford J.B., Lippinocott-Schwartz J. and Yamada K.M., editors. Wiley, Chichester, UK, **1;** 9.4.1-9.4.16

Mould A. P., Askari J. A., Barton S., Kline A. D., McEwan P. A., Craig S. E. and Humphries M. J. (2002) Integrin activation involves a conformational change in the alpha 1 helix of the beta subunit A-domain. *J. Biol. Chem.* **277,** 19800-19805.

Mould A. P., Barton S. J., Askari J. A., McEwan P. A., Buckley P. A., Craig S. E. and Humphries M. J. (2003a) Conformational changes in the integrin beta A domain provide a mechanism for signal transduction via hybrid domain movement. *J. Biol. Chem.* **278,** 17028-17035.

Mould A. P., Barton S. J., Askari J. A., Craig S. E. and Humphries M. J. (2003b) Role of ADMIDAS cation-binding site in ligand recognition by integrin alpha 5 beta 1. *J. Biol. Chem.* **278,** 51622-51629.

Mould A. P., Symonds E. J., Buckley P. A., Grossmann J. G., McEwan P. A., Barton S. J., Askari J. A., Craig S. E., Bella J. and Humphries M. J. (2003c) Structure of an integrin-ligand complex deduced from solution x-ray scattering and site-directed mutagenesis. *J. Biol. Chem.* **278,** 39993-39999.

Mould A. P., Travis M. A., Barton S. J., Hamilton J. A., Askari J. A., Craig S. E., Macdonald P. R., Kammerer R. A., Buckley P. A. and Humphries M. J. (2005) Evidence that monoclonal antibodies directed against the integrin beta subunit plexin/semaphorin/integrin domain stimulate function by inducing receptor extension. *J. Biol. Chem.* **280,** 4238-4246.

Munoz M., Serrador J., Sanchez-Madrid F. and Teixido J. (1996) A region of the integrin VLA alpha 4 subunit involved in homotypic cell aggregation and in fibronectin but not vascular cell adhesion molecule-1 binding. *J. Biol. Chem.* **271,** 2696-2702.

Munoz M., Serrador J., Nieto M., Luque A., Sanchez-Madrid F. and Teixido J. (1997) A novel region of the alpha4 integrin subunit with a modulatory role in VLA-4-mediated cell adhesion to fibronectin. *Biochem. J.* **327,** 727-733.

Nermut M. V., Green N. M., Eason P., Yamada S. S. and Yamada K. M. (1988) Electron microscopy and structural model of human fibronectin receptor. *EMBO J.* **20;7,** 4093-4099.

Ni H., Li A., Simonsen N. and Wilkins J. A. (1998) Integrin activation by dithiothreitol or Mn^{2+} induces a ligand-occupied conformation and exposure of a novel NH2-terminal regulatory site on the beta1 integrin chain. *J. Biol. Chem.* **273,** 7981-7987.

Nieswandt B., Brakebusch C., Bergmeier W., Schulte V., Bouvard D., Mokhtari-Nejad R., Lindhout T., Heemskerk J. W., Zirngibl H. and Fassler R. (2001) Glycoprotein VI but not alpha2beta1 integrin is essential for platelet interaction with collagen. *EMBO J.* **20,** 2120-2130.

Nieuwenhuis H. K., Akkerman J. W., Houdijk W. P. and Sixma J. J. (1985) Human blood platelets showing no response to collagen fail to express surface glycoprotein Ia. *Nature* **318,** 470-472.

Nolte M., Pepinsky R. B., Venyaminov S. Y., Koteliansky V., Gotwals P. J. and Karpusas M. (1999) Crystal structure of the alpha1beta1 integrin I-domain: insights into integrin I-domain function. *FEBS Lett.* **452,** 379-385.

O'Toole T. E., Mandelman D., Forsyth J., Shattil S. J., Plow E. F. and Ginsberg M. H. (1991) Modulation of the affinity of integrin alpha IIb beta 3 (GPIIb-IIIa) by the cytoplasmic domain of alpha IIb. *Science* **254,** 845-847.

O'Toole T. E., Katagiri Y., Faull R. J., Peter K., Tamura R., Quaranta V., Loftus J. C., Shattil S. J. and Ginsberg M. H. (1994) Integrin cytoplasmic domains mediate inside-out signal transduction. *J. Cell Biol.* **124,** 1047-1059.

O'Toole T. E., Ylanne J. and Culley B. M. (1995) Regulation of integrin affinity states through an NPXY motif in the beta subunit cytoplasmic domain. *J. Biol. Chem.* **270,** 8553-8558.

Onley D. J., Knight C. G., Tuckwell D. S., Barnes M. J. and Farndale R. W. (2000) Micromolar Ca^{2+} concentrations are essential for Mg^{2+}-dependent binding of collagen by the integrin alpha 2beta 1 in human platelets. *J. Biol. Chem.* **275,** 24560-24564.

Otey C. A., Pavalko F. M. and Burridge K. (1990) An interaction between alpha-actinin and the beta 1 integrin subunit in vitro. *J. Cell Biol.* **111,** 721-729.

Oxvig C., Lu C. and Springer T. A. (1999) Conformational changes in tertiary structure near the ligand binding site of an integrin I domain. *Proc. Natl. Acad. Sci. U. S. A* **96,** 2215-2220.

Pampori N., Hato T., Stupack D. G., Aidoudi S., Cheresh D. A., Nemerow G. R. and Shattil S. J. (1999) Mechanisms and consequences of affinity modulation of integrin alpha(V)beta(3) detected with a novel patch-engineered monovalent ligand. *J. Biol. Chem.* **274,** 21609-21616.

Parsons M., Keppler M. D., Kline A., Messent A., Humphries M. J., Gilchrist R., Hart I. R., Quittau-Prevostel C., Hughes W. E., Parker P. J. and Ng T. (2002) Site-directed perturbation of protein kinase C- integrin interaction blocks carcinoma cell chemotaxis. *Mol. Cell Biol.* **22,** 5897-5911.

Partridge A. W., Liu S., Kim S., Bowie J. U. and Ginsberg M. H. (2005) Transmembrane domain helix packing stabilizes integrin alphaIIbbeta3 in the low affinity state. *J. Biol. Chem.* **280,** 7294-7300.

Pfaff M., Liu S., Erle D. J. and Ginsberg M. H. (1998) Integrin beta cytoplasmic domains differentially bind to cytoskeletal proteins. *J. Biol. Chem.* **273,** 6104-6109.

Pierschbacher M. D. and Ruoslahti E. (1984) Variants of the cell recognition site of fibronectin that retain attachment-promoting activity. *Proc. Natl. Acad. Sci. U. S. A* **81,** 5985-5988.

Plow E. F., Haas T. A., Zhang L., Loftus J. and Smith J. W. (2000) Ligand binding to integrins. *J. Biol. Chem.* **275,** 21785-21788.

Puzon-McLaughlin W. and Takada Y. (1996) Critical residues for ligand binding in an I domain-like structure of the integrin beta1 subunit. *J. Biol. Chem.* **271,** 20438-20443.

Qu A. and Leahy D. J. (1996) The role of the divalent cation in the structure of the I domain from the CD11a/CD18 integrin. *Structure.* **4,** 931-942.

Randi A. M. and Hogg N. (1994) I domain of beta 2 integrin lymphocyte function-associated antigen-1 contains a binding site for ligand intercellular adhesion molecule-1. *J. Biol. Chem.* **269,** 12395-12398.

Ridgway J. B., Presta L. G. and Carter P. (1996) 'Knobs-into-holes' engineering of antibody CH3 domains for heavy chain heterodimerization. *Protein Eng.* **9,** 617-621.

Rivas G. A., Usobiaga P. and Gonzalez-Rodriguez J. (1991) Calcium and temperature regulation of the stability of the human platelet integrin GPIIb/IIIa in solution: an analytical ultracentrifugation study. *Eur. Biophys. J.* **20,** 287-292.

Salas A., Shimaoka M., Kogan A. N., Harwood C., von Andrian U. H. and Springer T. A. (2004) Rolling adhesion through an extended conformation of integrin alphaLbeta2 and relation to alpha I and beta I-like domain interaction. *Immunity.* **20,** 393-406.

Sampath R., Gallagher P. J. and Pavalko F. M. (1998) Cytoskeletal interactions with the leukocyte integrin beta2 cytoplasmic tail. Activation-dependent regulation of associations with talin and alpha-actinin. *J. Biol. Chem.* **273,** 33588-33594.

Santoro S. A. (1986) Identification of a 160,000 dalton platelet membrane protein that mediates the initial divalent cation-dependent adhesion of platelets to collagen. *Cell* **46,** 913-920.

Santoro S. A. and Zutter M. M. (1995) The alpha 2 beta 1 integrin: a collagen receptor on platelets and other cells. *Thromb. Haemost.* **74,** 813-821.

Schwartz M. A. and Ginsberg M. H. (2002) Networks and crosstalk: integrin signalling spreads. *Nat. Cell Biol.* **4,** 65-68.

Sells M. A., Pfaff A. and Chernoff J. (2000) Temporal and spatial distribution of activated Pak1 in fibroblasts. *J. Cell Biol.* **151,** 1449-1458.

Shattil S. J., Kashiwagi H. and Pampori N. (1998) Integrin signaling: the platelet paradigm. *Blood* **91,** 2645-2657.

Shih D. T., Edelman J. M., Horwitz A. F., Grunwald G. B. and Buck C. A. (1993) Structure/function analysis of the integrin beta 1 subunit by epitope mapping. *J. Cell Biol.* **122,** 1361-1371.

Shimaoka M., Shifman J. M., Jing H., Takagi J., Mayo S. L. and Springer T. A. (2000) Computational design of an integrin I domain stabilized in the open high affinity conformation. *Nat. Struct. Biol.* **7,** 674-678.

Shimaoka M., Lu C., Palframan R. T., von Andrian U. H., McCormack A., Takagi J. and Springer T. A. (2001) Reversibly locking a protein fold in an active conformation with a disulfide bond: integrin alphaL I domains with high affinity and antagonist activity in vivo. *Proc. Natl. Acad. Sci. U. S. A* **98,** 6009-6014.

Shimaoka M., Lu C., Salas A., Xiao T., Takagi J. and Springer T. A. (2002a) Stabilizing the integrin alpha M inserted domain in alternative conformations with a range of engineered disulfide bonds. *Proc. Natl. Acad. Sci. U. S. A* **99,** 16737-16741.

Shimaoka M., Takagi J. and Springer T. A. (2002b) Conformational regulation of integrin structure and function. *Annu. Rev. Biophys. Biomol. Struct.* **31,** 485-516.

Shimaoka M., Xiao T., Liu J. H., Yang Y., Dong Y., Jun C. D., McCormack A., Zhang R., Joachimiak A., Takagi J., Wang J. H. and Springer T. A. (2003a) Structures of the alpha L I domain and its complex with ICAM-1 reveal a shape-shifting pathway for integrin regulation. *Cell* **112,** 99-111.

Shimaoka M., Salas A., Yang W., Weitz-Schmidt G. and Springer T. A. (2003b) Small molecule integrin antagonists that bind to the beta2 subunit I-like domain and activate signals in one direction and block them in the other. *Immunity.* **19,** 391-402.

Smith C., Estavillo D., Emsley J., Bankston L. A., Liddington R. C. and Cruz M. A. (2000) Mapping the collagen-binding site in the I domain of the glycoprotein Ia/IIa (integrin alpha(2)beta(1)). *J. Biol. Chem.* **275,** 4205-4209.

Smith J. W. and Cheresh D. A. (1988) The Arg-Gly-Asp binding domain of the vitronectin receptor. Photoaffinity cross-linking implicates amino acid residues 61-203 of the beta subunit. *J. Biol. Chem.* **263,** 18726-18731.

Smith J. W. and Cheresh D. A. (1990) Integrin (alpha v beta 3)-ligand interaction. Identification of a heterodimeric RGD binding site on the vitronectin receptor. *J. Biol. Chem.* **265,** 2168-2172.

Staatz W. D., Rajpara S. M., Wayner E. A., Carter W. G. and Santoro S. A. (1989) The membrane glycoprotein Ia-IIa (VLA-2) complex mediates the Mg^{2+} dependent adhesion of platelets to collagen. *J. Cell Biol.* **108,** 1917-1924.

Stanley P. and Hogg N. (1998) The I domain of integrin LFA-1 interacts with ICAM-1 domain 1 at residue Glu-34 but not Gln-73. *J. Biol. Chem.* **273,** 3358-3362.

Steeber D. A., Venturi G. M. and Tedder T. F. (2005) A new twist to the leukocyte adhesion cascade: intimate cooperation is key. *Trends Immunol.* **26,** 9-12.

Stefansson A., Armulik A., Nilsson I., von H. G. and Johansson S. (2004) Determination of N- and C-terminal borders of the transmembrane domain of integrin subunits. *J. Biol. Chem.* **279,** 21200-21205.

Stephens P., Romer J. T., Spitali M., Shock A., Ortlepp S., Figdor C. G. and Robinson M. K. (1995) KIM127, an antibody that promotes adhesion, maps to a region of CD18 that includes cysteine-rich repeats. *Cell Adhes. Commun.* **3,** 375-384.

Stephens P. E. and Cockett M. I. (1989) The construction of a highly efficient and versatile set of mammalian expression vectors. *Nucleic Acids Res.* **17,** 7110.

Stephens P. E., Ortlepp S., Perkins V. C., Robinson M. K. and Kirby H. (2000) Expression of a soluble functional form of the integrin alpha4beta1 in mammalian cells. *Cell Adhes. Commun.* **7,** 377-390.

Stupack D. G. and Cheresh D. A. (2004) Integrins and angiogenesis. *Curr. Top. Dev. Biol.* **64,** 207-238.

Stupack D. G. (2005) Integrins as a distinct subtype of dependence receptors. *Cell Death Differ.* **12,** 1021-1030.

Takada Y. and Hemler M. E. (1989) The primary structure of the VLA-2/collagen receptor alpha 2 subunit (platelet GPIa): homology to other integrins and the presence of a possible collagen-binding domain. *J. Cell Biol.* **109,** 397-407.

Takada Y. and Puzon W. (1993) Identification of a regulatory region of integrin beta 1 subunit using activating and inhibiting antibodies. *J. Biol. Chem.* **268,** 17597-17601.

Takagi J., Kamata T., Meredith J., Puzon-McLaughlin W. and Takada Y. (1997) Changing ligand specificities of alphavbeta1 and alphavbeta3 integrins by swapping a short diverse sequence of the beta subunit. *J. Biol. Chem.* **272,** 19794-19800.

Takagi J., Beglova N., Yalamanchili P., Blacklow S. C. and Springer T. A. (2001a) Definition of EGF-like, closely interacting modules that bear activation epitopes in integrin beta subunits. *Proc. Natl. Acad. Sci. U. S. A* **98,** 11175-11180.

Takagi J., Erickson H. P. and Springer T. A. (2001b) C-terminal opening mimics 'inside-out' activation of integrin alpha5beta1. *Nat. Struct. Biol.* **8,** 412-416.

Takagi J. and Springer T. A. (2002) Integrin activation and structural rearrangement. *Immunol. Rev.* **186:141-63.,** 141-163.

Takagi J., Petre B. M., Walz T. and Springer T. A. (2002a) Global conformational rearrangements in integrin extracellular domains in outside-in and inside-out signaling. *Cell* **110,** 599-11.

Takagi J., DeBottis D. P., Erickson H. P. and Springer T. A. (2002b) The role of the specificity-determining loop of the integrin beta subunit I-like domain in autonomous expression, association with the alpha subunit, and ligand binding. *Biochemistry* **41,** 4339-4347.

Takagi J., Strokovich K., Springer T. A. and Walz T. (2003) Structure of integrin alpha5beta1 in complex with fibronectin. *EMBO J.* **22,** 4607-4615.

Takahashi N., Ueda S., Obata M., Nikaido T., Nakai S. and Honjo T. (1982) Structure of human immunoglobulin gamma genes: implications for evolution of a gene family. *Cell* **29,** 671-679.

Tan S. M., Walters S. E., Mathew E. C., Robinson M. K., Drbal K., Shaw J. M. and Law S. K. (2001) Defining the repeating elements in the cysteine-rich region (CRR) of the CD18 integrin beta 2 subunit. *FEBS Lett.* **505,** 27-30.

Tsuboi S. (2002) Calcium integrin-binding protein activates platelet integrin alphaIIb beta3. *J. Biol. Chem.* **277,** 1919-1923.

Tuckwell D., Calderwood D. A., Green L. J. and Humphries M. J. (1995) Integrin alpha 2 I-domain is a binding site for collagens. *J. Cell Sci.* **108,** 1629-1637.

Tuckwell D. S., Smith L., Korda M., Askari J. A., Santoso S., Barnes M. J., Farndale R. W. and Humphries M. J. (2000) Monoclonal antibodies identify residues 199-216 of the integrin alpha2 vWFA domain as a functionally important region within alpha2beta1. *Biochem. J.* **350,** 485-493.

Ueda T., Rieu P., Brayer J. and Arnaout M. A. (1994) Identification of the complement iC3b binding site in the beta 2 integrin CR3 (CD11b/CD18). *Proc. Natl. Acad. Sci. U. S. A* **91,** 10680-10684.

Vallar L., Melchior C., Plancon S., Drobecq H., Lippens G., Regnault V. and Kieffer N. (1999) Divalent cations differentially regulate integrin alphaIIb cytoplasmic tail binding to beta3 and to calcium- and integrin-binding protein. *J. Biol. Chem.* **274,** 17257-17266.

van der F. A. and Sonnenberg A. (2001) Function and interactions of integrins. *Cell Tissue Res.* **305,** 285-298.

Vandenberg P., Kern A., Ries A., Luckenbill-Edds L., Mann K. and Kuhn K. (1991) Characterization of a type IV collagen major cell binding site with affinity to the alpha 1 beta 1 and the alpha 2 beta 1 integrins. *J. Cell Biol.* **113,** 1475-1483.

Vidal F., Aberdam D., Miquel C., Christiano A. M., Pulkkinen L., Uitto J., Ortonne J. P. and Meneguzzi G. (1995) Integrin beta 4 mutations associated with junctional epidermolysis bullosa with pyloric atresia. *Nat. Genet.* **10,** 229-234.

Vinogradova O., Velyvis A., Velyviene A., Hu B., Haas T., Plow E. and Qin J. (2002) A structural mechanism of integrin alpha(IIb)beta(3) "inside-out" activation as regulated by its cytoplasmic face. *Cell* **110,** 587-597.

Vorup-Jensen T., Carman C. V., Shimaoka M., Schuck P., Svitel J. and Springer T. A. (2005) Exposure of acidic residues as a danger signal for recognition of fibrinogen and other macromolecules by integrin alphaXbeta2. *Proc. Natl. Acad. Sci. U. S. A* **102,** 1614-1619.

Weitz-Schmidt G., Welzenbach K., Brinkmann V., Kamata T., Kallen J., Bruns C., Cottens S., Takada Y. and Hommel U. (2001) Statins selectively inhibit leukocyte function antigen-1 by binding to a novel regulatory integrin site. *Nat. Med.* **7,** 687-692.

Weljie A. M., Hwang P. M. and Vogel H. J. (2002) Solution structures of the cytoplasmic tail complex from platelet integrin alpha IIb- and beta 3-subunits. *Proc. Natl. Acad. Sci. U. S. A* **99,** 5878-5883.

Welzenbach K., Hommel U. and Weitz-Schmidt G. (2002) Small molecule inhibitors induce conformational changes in the I domain and the I-like domain of lymphocyte function-associated antigen-1. Molecular insights into integrin inhibition. *J. Biol. Chem.* **277,** 10590-10598.

Williams B. D. and Waterston R. H. (1994) Genes critical for muscle development and function in Caenorhabditis elegans identified through lethal mutations. *J. Cell Biol.* **124,** 475-490.

Williams M. J., Hughes P. E., O'Toole T. E. and Ginsberg M. H. (1994) The inner world of cell adhesion: integrin cytoplasmic domains. *Trends Cell Biol.* **4,** 109-112.

Xiao T., Takagi J., Coller B. S., Wang J. H. and Springer T. A. (2004) Structural basis for allostery in integrins and binding to fibrinogen-mimetic therapeutics. *Nature* **432,** 59-67.

Xiong J. P., Li R., Essafi M., Stehle T. and Arnaout M. A. (2000) An isoleucine-based allosteric switch controls affinity and shape shifting in integrin CD11b A-domain. *J. Biol. Chem.* **275,** 38762-38767.

Xiong J. P., Stehle T., Diefenbach B., Zhang R., Dunker R., Scott D. L., Joachimiak A., Goodman S. L. and Arnaout M. A. (2001) Crystal structure of the extracellular segment of integrin alpha Vbeta3. *Science* **294,** 339-345.

Xiong J. P., Stehle T., Zhang R., Joachimiak A., Frech M., Goodman S. L. and Arnaout M. A. (2002) Crystal structure of the extracellular segment of integrin alpha Vbeta3 in complex with an Arg-Gly-Asp ligand. *Science* **296,** 151-155.

Xiong J. P., Stehle T., Goodman S. L. and Arnaout M. A. (2003a) New insights into the structural basis of integrin activation. *Blood* **102,** 1155-1159.

Xiong J. P., Stehle T., Goodman S. L. and Arnaout M. A. (2003b) Integrins, cations and ligands: making the connection. *J. Thromb. Haemost.* **1,** 1642-1654.

Xiong Y. M., Chen J. and Zhang L. (2003c) Modulation of CD11b/CD18 adhesive activity by its extracellular, membrane-proximal regions. *J. Immunol.* **171,** 1042-1050.

Yang W., Shimaoka M., Salas A., Takagi J. and Springer T. A. (2004) Intersubunit signal transmission in integrins by a receptor-like interaction with a pull spring. *Proc. Natl. Acad. Sci. U. S. A* **101,** 2906-2911.

Zamir E. and Geiger B. (2001) Components of cell-matrix adhesions. *J. Cell Sci.* **114,** 3577-3579.

Zang Q., Lu C., Huang C., Takagi J. and Springer T. A. (2000) The top of the inserted-like domain of the integrin lymphocyte function-associated antigen-1 beta subunit contacts the alpha subunit beta -propeller domain near beta-sheet 3. *J. Biol. Chem.* **275,** 22202-22212.

Zang Q. and Springer T. A. (2001) Amino acid residues in the PSI domain and cysteine-rich repeats of the integrin beta2 subunit that restrain activation of the integrin alpha(X)beta(2). *J. Biol. Chem.* **276,** 6922-6929.

Zent R., Fenczik C. A., Calderwood D. A., Liu S., Dellos M. and Ginsberg M. H. (2000) Class- and splice variant-specific association of CD98 with integrin beta cytoplasmic domains. *J. Biol. Chem.* **275,** 5059-5064.

Zent R., Fenczik C. A., Calderwood D. A., Liu S., Dellos M. and Ginsberg M. H. (2000) Class- and splice variant-specific association of CD98 with integrin beta cytoplasmic domains. *J. Biol. Chem.* **275,** 5059-5064.

Zhang L. and Plow E. F. (1999) Amino acid sequences within the alpha subunit of integrin alpha M beta 2 (Mac-1) critical for specific recognition of C3bi. *Biochemistry* **38,** 8064-8071.

Zhang X. P., Puzon-McLaughlin W., Irie A., Kovach N., Prokopishyn N. L., Laferte S., Takeuchi K., Tsuji T. and Takada Y. (1999) Alpha 3 beta 1 adhesion to laminin-5 and invasin: critical and differential role of integrin residues clustered at the boundary between alpha 3 N-terminal repeats 2 and 3. *Biochemistry* **38,** 14424-14431.

Zutter M. M. and Santoro S. A. (1990) Widespread histologic distribution of the alpha 2 beta 1 integrin cell-surface collagen receptor. *Am. J. Pathol.* **137,** 113-120.

AlGaN/GaN HIGH ELECTRON MOBILITY TRANSISTORS

A thesis submitted to The University of Manchester for the degree of
Doctor of Philosophy
in the Faculty of Engineering and Physical Sciences

2005

Alexander Morgan Wells

School of Electrical and Electronic Engineering

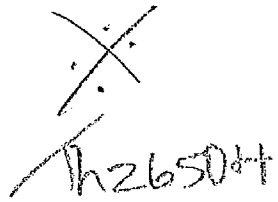
Th26501+

CONTENTS

Final Word count: 30,143 words.

LIST OF TABLES

LIST OF FIGURES

LIST OF ABBREVIATIONS AND ACRONYMS

2DEG	2-Dimensional Electron Gas
2HEG	2-Dimensional Hole Gas
CV	Capacitance-Voltage
CC	Current collapse
CW	Continuous Wave
DC	Direct Current
EL	Electroluminescence
FP	Field Plate
HEMT	High Electron Mobility Transistor
HDTV	High Definition Television
HT	High Temperature
IV	Current-Voltage
MBE	Molecular Beam Epitaxy
MESFET	Metal Semiconductor Field Effect Transistor
MOCVD	Metal Organic Chemical Vapour Deposition
MOVPE	Metal Organic Vapour Phase Epitaxy
MOSFET	Metal Oxide Semiconductor Field Effect Transistor
LED	Light Emitting Diode
LT	Low Temperature
PAE	Power Added Efficiency
PCC	Passivated current collapse
PECVD	Plasma Enhanced Chemical Vapour Deposition
RF	Radio Frequency
SBH	Schottky Barrier Height
SEM	Scanning Electron Micrograph
SI	Semi-insulating
TEM	Transmission Electron Microscopy
UCC	Un-passivated current collapse
UHV	Ultra High Vacuum

UID	Un-intentional Doping
UV	Ultra Violet
VSAT	Very Small Aperture Terminal
XRD	X-Ray Diffraction

LIST OF SYMBOLS

A**	Effective Richardson constant
a_L	Epilayer lattice constant
a_S	Substrate lattice constant
a_0	Lattice constant along the a-axis (the hexagonal edge)
c_0	Lattice constant along the c-axis (the height of the prism)
C_G	Gate capacitance
C_{ij}	Elastic constants
d_{il}	Piezoelectric moduli
e_{kl}	Piezoelectric constants
ε	Strain
ε_r	Dielectric constant
ε_{kl}	Crystal deformation strain forces
E_C	Conduction band energy
E_G	Bandgap
E_{POP}	Optical phonon energy
E_V	Valence band energy
f_τ	Unity-gain cut-off frequency
f_{max}	Maximum oscillating frequency
h_c	Critical thickness
h	Plank constant (6.626×10^{-34} Js)
γ	Scaling factor gamma
I_D	Drain current
I_{DS}	Drain-source current
I_{DSO}	Drain current at $V_{GS} = 0V$
I_{DSB}	Class B biased drain current
I_{DSZ}	Zero biased drain current

I_G	Gate current
I_{max}	Maximum drain current
I_S	Source current
I_{SAT}	Saturation current
J	Current density
k	Boltzmann constant (1.38×10^{-23} J.K^{-1})
κ	Thermal conductivity
L_{FP}	Field plate length
L_G	Gate length
L_{GAP}	Gap length
L_{GD}	Gate-drain length
L_{GS}	Gate-source length
m_e	Effect mass
μ	Mobility
n	Ideality factor
N	Electron number density
P·	Total polarisation
P_{OUT}	Power output
P_{PZ}	Piezoelectric polarisation
P_R	Passivation ratio
P_i^{pz}	Piezoelectric polarisation components
P_{SP}	Spontaneous polarisation
P_i^{SP}	Spontaneous polarisation components
q	Charge of an electron (1.6×10^{-19}C)
Q	Total charge
R	relative alloy scattering rate
r_1	Time independent scattering rate
r_2	Acoustic phonon scattering rate
r_3	Polar optical phonon scattering rate

r_A	Alloy scattering rate
r_{Q1}	Alloy scattering in Q1
r_{Q2}	Alloy scattering Q2
r_C	Coulomb scattering
r_{SR}	Surface roughness scattering rate
R_C	Contact resistance
$R_{CHANNEL}$	Channel resistance
R_D	Drain resistance
R_{GAP}	Gap resistance
R_S	Source resistance
R_{SP}	Specific contact resistance
ρ_{SH}	Sheet resistance
S	Schottky contact area
S_{ij}	Elastic compliance constants
S_{11}^*	Reciprocal Young's modulus
T	Temperature [K]
θ	Angle of stress
σ	Conductance
σ_{ij}	Stress forces
$\sigma(m)$	Total polarisation-induced charge sheet density
Φ_b	Schottky barrier height
V_{BASE}	Gate pulse base voltage
V_{Di}	Drain voltage inside the cryostat
V_{DS}	Drain-source voltage
V_G	Voltage dropped across the gate
V_{GS}	Gate-source voltage
V_P	Pinch-off voltage
V_{Si}	Source voltage inside the cryostat
W_G	Gate width

W_{GAP}	Gap width
$\psi(z)$	Electron subband wavefunction

ABSTRACT

AlGaN/GaN HEMTs have been the focus of intense research in recent years. Solid state GaN devices have consistently demonstrated power densities of 12W/mm, which were previously only possible using microwave vacuum tubes. However, there are some problems. The drain current collapses under negative gate bias, preventing high microwave power outputs being achieved. In addition, the 2DEG mobility falls at high carrier concentrations.

Current collapse has been investigated using gate lag and DC pulsed measurements. The effects of passivation have also been examined. Direct measurements of the un-gated surface resistances under pulsed gate conditions indicate that the virtual gate concept is the main cause of current collapse. Surface passivation has been found to reduce current collapse. DC pulsed measurements have indicated that passivation reduces the depth of surface traps allowing electrons to move on and off the device surface at an increased rate.

Drift mobility as a function of gate voltage has been measured in HFETs fabricated by MOVPE to a common 300Å AlGaN/ 1.2μm GaN layer structure. The mobility reached a peak of 2000 cm^2/Vs for the best samples, at room temperature. All wafers mobilities fell at high electron number densities. However, SiC based devices consistently showed higher mobilities than sapphire based devices.

The growth of an AlN exclusion layer between the AlGaN barrier and GaN buffer layers caused dramatic improvement in carrier drift mobility at high carrier concentrations. By extracting the alloy, polar optical and acoustic phonon scattering terms from the mobility as a function of temperature and number density, it was found that roughness and Coulomb scattering are insignificant at room temperature. Samples with and without an AlN layer at the AlGaN/GaN interface were compared and used to extract the alloy scattering. At room temperature the mobility was dominated by phonon scattering.

DECLARATION

No portion of the work referred to in this thesis has been submitted in support of an application for another degree or qualification of this or any other university or other institute of learning.

Alexander Morgan Wells

COPYRIGHT STATEMENT

ACKNOWLEDGEMENTS

I would like to thank my supervisors Prof. M. Missous and Dr. M. Uren for their support, encouragement and guidance. I thank R. Balmer, T. Martin and K. Hilton for growing and fabricating the devices. J. Sly, I Hawkins and M. McGowan are thanked for their assistance with all types of technical problems.

On a personal note, I wish to thank all my friends in Manchester and Worcester for their support, banter and occasional bed for a night/week. You have all helped to make my years in Manchester some of the best of my life.

Finally, I am forever indebted to my parents and family for their understanding, endless patience, support and encouragement when it was most required.

AUTHOR'S PUBLICATIONS

Listed below is a chronological list of the author's publications:

[1] M. J. Uren, T. Martin, B. T. Hughes, K. P. Hilton, A. Wells, R. S. Balmer, D. C. Herbert, A. M. Keir, D. J. Wallis, A. J. Pidduck, and M. Missous, "Channel mobility in AlGaN/GaN HFETs on SiC and sapphire substrates," *Physica Status Solidi C*, pp. 468-71, 2002.

[2] R. S. Balmer, D. E. J. Soley, K. P. Hilton, K. J. Nash, M. J. Uren, D. J. Wallis, A. Wells, M. Missous, and T. Martin, "AlGaN/GaN microwave HFET including a thin AlN carrier exclusion layer," presented at 10th European Workshop on MOVPE,, Lecce (Italy), 2003.

[3] R. Balmer, K. P. Hilton, K. J. Nash, M. J. Uren, D. J. Wallis, A. Wells, M. Missous, and T. Martin, "AlGaN/GaN microwave HFET including a thin AlN carrier exclusion layer," *Phys. Stat. Sol (c)*, vol. 0, pp. 2331-4, 2003.

[4] R. S. Balmer, K. P. Hilton, K. J. Nash, M. J. Uren, D. J. Wallis, D. Lee, A. Wells, M. Missous, and T. Martin, "Analysis of thin AlN carrier exclusion layers in AlGaN/GaN microwave heterojunction field-effect transistors," *Semiconductor Science and Technology*, vol. 19, pp. 65-7, 2004.

[5] A. M. Wells, M. J. Uren, R. Balmer, K. P. Hilton, T. Martin, and M. Missous, "Direct demonstration of the 'virtual gate' mechanism for current collapse in AlGaN/GaN HFETs," *Solid-State Electronics*, vol. 49, pp. 279-282, 2004.

[6] A. Wells, M. J. Uren, R. Balmer, K. J. Nash, T. Martin, and M. Missous, "Extraction of temperature and number dependent scattering rates for an AlGaN/GaN 2DEG," *Physica Status Solidi (A) Applied Research*, vol. 202, pp. 812-815, 2005.

1 INTRODUCTION

This PhD concentrates on research of Aluminium Gallium Nitride/ Gallium Nitride high electron mobility transistors (AlGaN/GaN HEMTs). All the measurements reported in this thesis were performed on QinetiQ-grown and fabricated AlGaN/GaN HEMT devices. The AlGaN/GaN HEMTs devices were grown by metal organic vapour phase epitaxy (MOVPE) on both Silicon Carbide (SiC) and Sapphire wafers. The standard AlGaN/GaN HEMT device used in this project is referred to as QinetiQ One (Q1) and has the following structure: 300Å AlGaN/ 1.2μm GaN on either SiC or Sapphire. Further details of the growth and fabrication of the devices are given later in Chapter 2.

The author was responsible for the measurement and analysis of the devices but didn't partake in any of the growth or fabrication of the AlGaN/GaN HEMTs devices. However, the author did gain an appreciation of device fabrication and mask design through the fabrication and measurement of Indium Gallium Phosphide psuedomorphic high electron mobility transistors (InGaP pHEMTs) at UMIST.

AlGaN/GaN HEMTs have, for the last few years, been the subject of intense research because they offer superior radio frequency (RF) power, typically at elevated temperatures, compared to conventional GaAs and Si devices. However, there are

numerous problems (described in subsection 1.3) that need to be addressed before the full potential of AlGaN/GaN HEMTs can be utilised.

1.1 Applications for AlGaN/GaN HEMTs

AlGaN/GaN HEMTs have numerous commercial and military applications. Current QinetiQ-made GaN HEMTs are intended for military applications such as radars (shipboard, airborne and ground) and high performance space electronics; because current research is Military of Defence funded. However, there are also numerous possible applications within the commercial sector. The high RF output-power capability of AlGaN/GaN HEMTs means they are ideal for commercial applications such as power amplifiers for base stations in mobile telecommunications, high definition television (HDTV) transmitters, Ku-K band (10-17GHz) very small aperture terminals (VSATs) and broadband satellites, C-band (4-8GHz) Satcom, and digital radio.

AlGaN/GaN HEMTs have demonstrated one-order of magnitude higher power density and higher efficiency than both current Si and GaAs based RF and microwave transistors. Thus, for the same power output, the GaN devices can be 1/10 of the size of the equivalent GaAs and Si based devices. High-power solid-state transmitters will be useful in many future applications because of their high reliability, small size and high resistance to radiation. AlGaN/GaN HEMTs will be specifically appealing for applications that require operation at high temperatures and/or in high radiation environments.

1.2 Advantages of AlGaN/GaN HEMTs

The most important and desirable properties of a semiconductor material include large band gap, high thermal conductivity, low value of dielectric constant , and high critical electric field for breakdown. When comparing GaN with other common semiconductors,

as shown in Table 1 it can be observed that GaN is best in nearly all the categories. The large 3.4eV band gap of GaN enables it to withstand large internal electric fields, which results in GaN having a critical breakdown voltage an order of magnitude greater than that of GaAs, and also provides enhanced resistance to radiation. High critical breakdown voltage results in a large power density and thus more compact devices, it also permits large radio frequency (RF) voltages to be applied which are necessary for high RF power generation.

Table 1: Material properties of common semiconductors [1]

Material	Band Gap (eV)	Dielectric constant (Unitless)	Thermal conductance (W/°Kcm)	Critical electric field (V/cm)
Si	1.12	11.9	1.5	3×10^5
GaAs	1.43	12.5	0.54	4×10^5
InP	1.34	12.4	0.67	4.5×10^5
4H-SiC	3.2	10.0	4	$(1\text{-}5) \times 10^6$
6H-SiC	3.0	10.0	4	$(1\text{-}5) \times 10^6$
GaN	3.4	9.5	1.3	$\sim 3.5 \times 10^6$

The low dielectric constant permits a larger area device for a given impedance, enabling a greater RF current and thus once again more RF power. The wide band gap materials have dielectric constants about 20% lower than conventional semiconductors. The good thermal conductivity of GaN and its substrate SiC allows the power dissipated in the devices to be extracted with ease, which prevents the device performance from being degraded through over heating. GaN has a thermal conductance comparable to Si, which is the best of conventional semiconductors. Although, GaN has a relatively poor room temperature bulk mobility of ~500cm^2/Vs, the low field 2DEG mobility of the AlGaN/GaN heterojunction has a room temperature mobility of >1500cm^2/Vs using sapphire substrates and ~2000cm^2/Vs using SiC substrates. This is greater than the critical mobility of 500cm^2/Vs required for field saturation and velocity saturation, and

thus efficient gate modulation. In addition, by using a high aluminium percentage AlGaN epilayer a 2DEG sheet carrier density of ~ 1 x 10^{13} cm^{-2} can regularly be achieved, which is about 5 times greater than conventional AlGaAs/GaAs structures. Moreover, GaN has a high saturation velocity ~2 x 10^7 cm/sec; twice that of bulk Si and GaAs. High saturation velocity is necessary for high-speed device operation.

1.3 Problems associated with AlGaN/GaN HEMTs

There were several major problems with GaN devices in 2001 (at the start of this research programme), which needed to be addressed. These were current collapse, self-heating, hysteresis and a fall in 2DEG mobility at high carrier number density. Detailed explanations of the problems are given along with prior art at the start of the appropriate result chapters.

1.3.1 Current collapse

Current collapse is the main problem hindering RF power operation. Current collapse is the name given to the discrepancy between actual measured RF power output and that predicted from direct current (DC) measurements. The low RF power output results from a collapse in device drain current. The collapse occurs when the device gate is negatively biased during microwave operation. A complete literature review of the problem is given in chapter 3.

1.3.2 Fall in mobility

An understanding of low field 2DEG mobility is crucial to take full advantage of the high electron number densities generated in the 2DEG of the AlGaN/GaN HEMTs. The 2DEG mobility is a good gauge of AlGaN/GaN interface quality and therefore the extent of electron scattering that occurs at the interface. The fall in mobility limits the device operating frequency. A full review of the literature is given in chapter 4.

1.3.3 Self –heating and hysteresis (trapping phenomenon)

Device self-heating and hysteresis were two additional problems found in AlGaN/GaN HEMTs. Device self-heating causes the drain current to reduce at high dissipated power, and is associated with the finite thermal conductivity of the device materials. Several papers were written on the ways of measuring self-heating [2-4] using Raman spectroscopy to determine device temperatures with a spatial resolution of approximately 1μm and temperature accuracy of 10°C. Self-heating can be clearly observed in Figure 1. Self-heating is most evident in the blue (V_{GS} = 0V) curve where the drain falls considerably as V_{DS} is increased from 5 to 20V. The devices also suffered from hysteresis, indicated in the current-voltage (IV) characteristics shown in Figure 1 as an undesirable second knee, found in the pink and yellow curves (V_{GS} = -1V and -2V) at approximately V_{DS} = 12V. Hysteresis limits the frequency of device operation and is due to the charging and discharging of deep level traps in the GaN buffer.

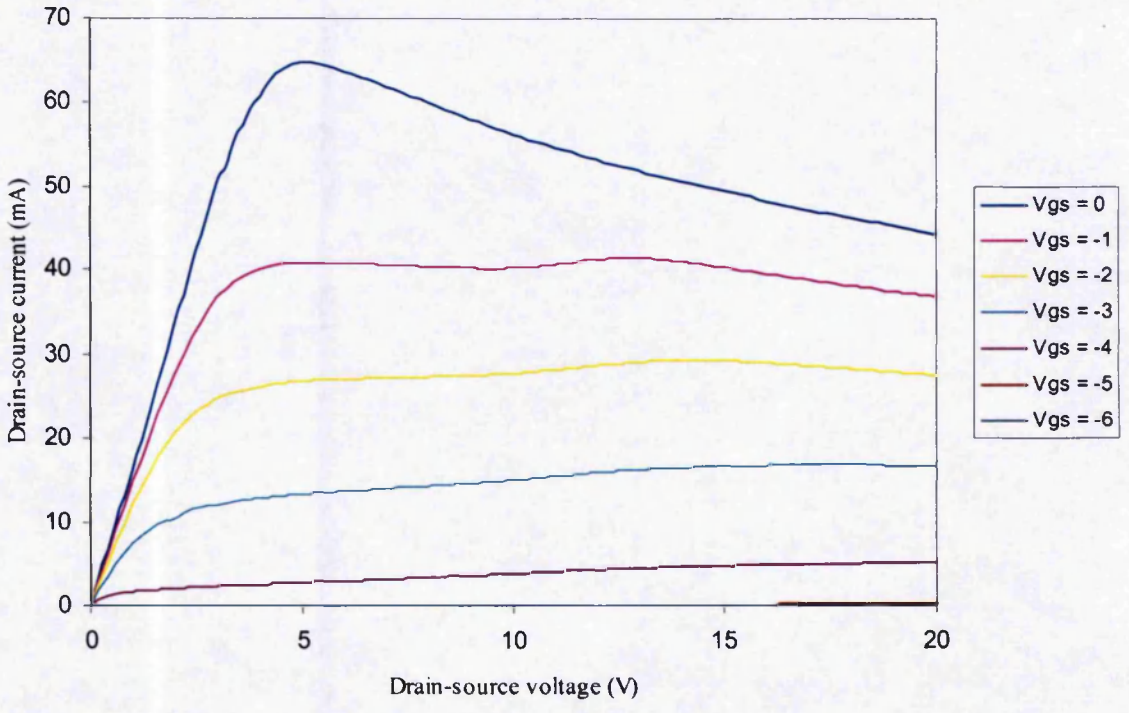

Figure 1 Example of hysteresis and self –heating in AlGaN/GaN HEMTs.

1.4 Thesis layout

Chapter 2 explains the physics required to understand the structure, fabrication and operation of AlGaN/GaN HEMTs. In addition, the development of devices over the last 20 years is reviewed.

The research presented in this thesis focuses on two main problems associated with AlGaN/GaN HEMTs; current collapse and the fall in two-dimensional gas (2DEG) mobility observed at high electron number density. Chapter 3 investigates current collapse within AlGaN/GaN HEMTs using pulsed DC measurement, a comparative study of different passivation types and finally gate lag measurements. The research presented successfully measures the origin on current collapse and gives indications of how it can minimised.

The 4th and 5th chapters both examine AlGaN/GaN HEMT 2DEG mobility. In chapter 4 the effects of the substrate and of a novel device structure on 2DEG mobility are analysed. Chapter 5 uses the temperature dependence of different scattering mechanisms to determine the form of scattering responsible for reducing the 2DEG mobility at high electron number density. Models are then used to accurately predict high temperature 2DEG mobility. Conclusions drawn from the research and future work are given in chapter 6.

2 BACKGROUND ON AlGaN/GaN HEMTs

The following chapter gives detailed information about the QinetiQ-produced AlGaN/GaN HEMT devices used in this research. This chapter begins by explaining the basic device physics that is required to understand the operation of AlGaN/GaN HEMTs. It then goes on to illustrate how pseudomorphic growth produces strain within the device layers and generates the piezoelectric properties of the device. This chapter also explains the device structure, the growth conditions, the role of each layer of the structure and the fabrication conditions and techniques used. Finally, this chapter gives the history of the devices and presents the state-of-the-art.

2.1 Basic device physics

In order to understand how AlGaN/GaN HEMTs operate, an understanding of pseudomorphic growth, and hence lattice constants, strain, critical thickness, piezoelectric and spontaneous polarisation, and heterojunctions is required.

2.1.1 Epitaxial growth

Semiconductor wafers are grown by a method called epitaxy. The word epitaxy comes from the Greek prefix *epi-* meaning 'outer, on and upon' and from the Greek *taxis* meaning 'arrangement'. There are many different forms of epitaxy, including Molecular Beam Epitaxy (MBE) and Metal Organic Chemical Vapour Deposition (MOCVD), also known as metal organic vapour phase epitaxy (MOVPE). During MBE the substrate is heated under Ultra High Vacuum (UHV) conditions. Once the substrate has been heated to the optimum growth temperature the required epilayer species, in this case Aluminium, Gallium and Nitrogen, are introduced to the growth chamber. In MBE this is done in the form of molecular beams which is directed at the substrate. In MOCVD the sources are introduced in the form of a vapour at temperatures and pressures higher than those in MBE. When the atoms or molecules react at the surface of the substrate they bond to one another and form bonds with the surface atoms. The nature of the layers formed by these interactions is dependent upon the lattice constants of the epilayer and substrate.

2.1.1.1 Lattice constant

The lattice constant of a solid (a_0) corresponds to the size of the conventional unit cell at equilibrium volume. It's usually obtained either experimentally, from low temperature X-ray diffraction measurements that are extrapolated to zero Kelvin, or computationally, using the local density approximation. The lattice constant of a material is a function slightly with temperature. Compounds can have more than one lattice constant depending on the structure, such as GaN and AlN (see 2.2.2.2)

2.1.1.2 Pseudomorphic layers and strain

When the lattice constant of an epilayer a_L is different from that of the substrate a_S, the

epilayer is forced, by the substrate's influence, to adjust its in-plane lattice constant to that of the substrate, as depicted in Figure 2. The word pseudomorphic meaning "false form", describes this type of layer grown having a different lattice constant from normal.

A pseudomorphic layer adopts the in-plane lattice constant of the substrate material on which it is grown. The pseudomorphic arrangement of the epilayer causes it to be under strain. The strain can be either tensile (if $a_L < a_S$) or compressive (if $a_L > a_S$). The strain, ε, between the two material layers is defined as:

$$\varepsilon = \frac{a_L - a_S}{a_S} \tag{2.1}$$

Where a_L is the lattice constant of the epilayer and a_S is the lattice constant of the substrate.

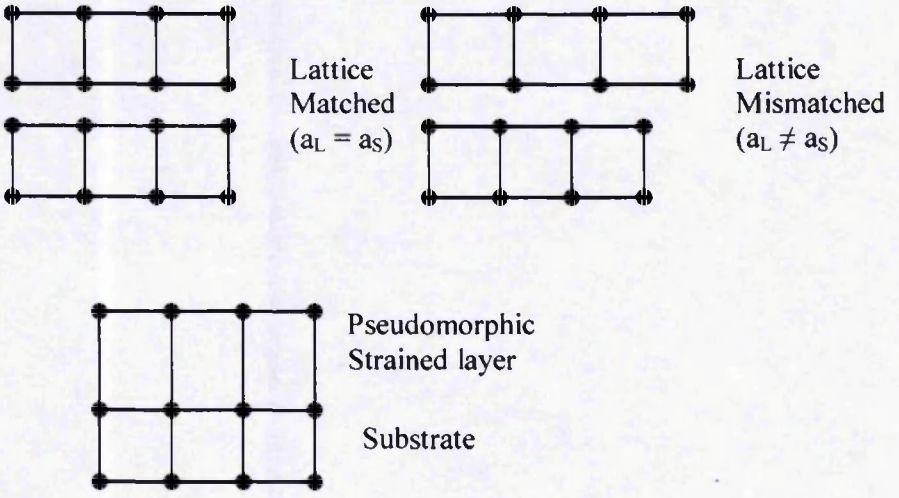

Figure 2: Lattice matched, mismatched and strained pseudomorphic layers

2.1.1.3 Critical thickness

The pseudomorphic influence of the substrate lattice diminishes as the growth plane moves away from the layer/substrate interface. When the influence of the substrate lattice becomes less than the strain within the pseudomorphic layer, the structure dislocates as illustrated in Figure 3. The finite thickness to which a pseudomorphic layer can be grown before it dislocates is referred to as the critical thickness h_c, and is defined as:

$$h_C = \frac{a_s}{2\varepsilon} \tag{2.2}$$

Where ε is strain and a_S is the substrate lattice constant. At the critical thickness where the dislocation occurs the strain is released and the epitaxially layer reverts to its true lattice constant. Defects in the form of edge dislocations often occur at the plane where the crystal regains its true lattice constant, as can be observed below in Figure 3.

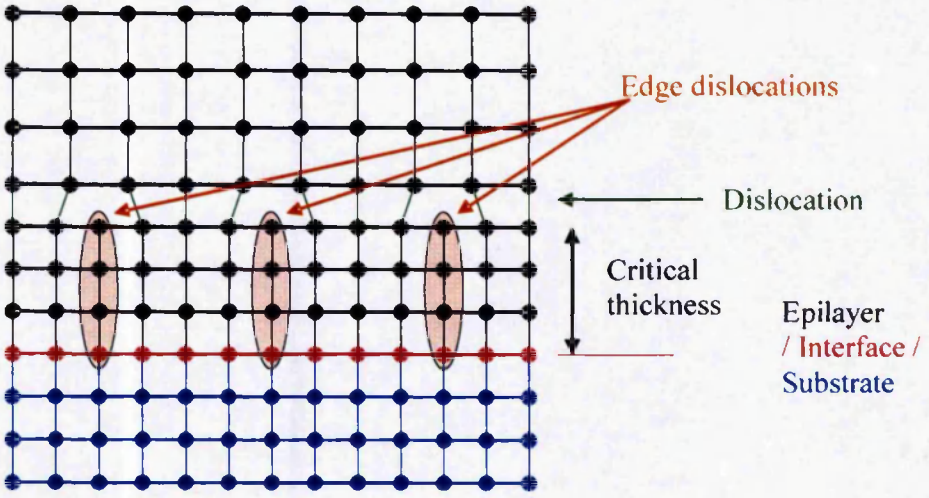

Figure 3: Dislocations in a pseudomorphic layer

2.1.1.4 Heterojunctions

At the interface of the substrate and epilayer a heterojunction is formed. The band structure of the heterojunction is determined by the band gaps of the two materials and the way the bands line up (the conduction and valence band discontinuities). The 'triangular' heterojunction formed in the conduction band at the AlGaN/GaN interface is shown in the energy band diagram below (Figure 4) [5]. The Fermi level is indicated by a red band. The piezoelectrically induced 2DEG typically has a electron number density of ~1 x10^{13} cm^{-2}. Computer modelling has shown the distribution to be as follows:

1st subband (red): 8.44 x 10^{12} cm^{-2}

2nd subband (green): 0.49 x 10^{12} cm^{-2}

Higher subbands: 0.04 x 10^{12} cm^{-2} – the 3rd subband is 111meV above the Fermi level with occupancy of ~3 x 10^{10} cm^{-2}.

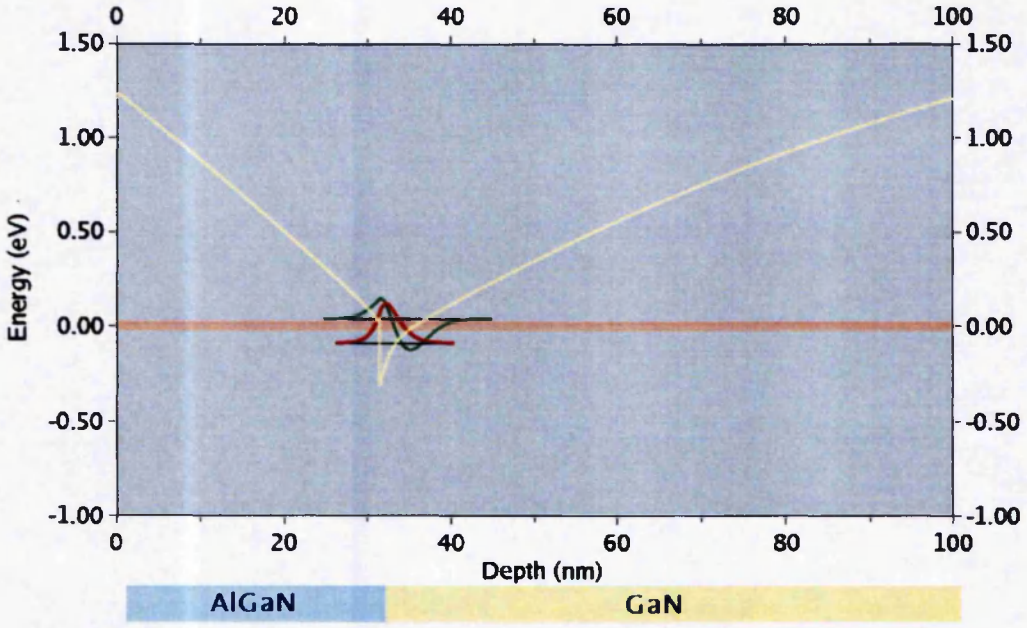

Figure 4: Band diagram for a entire AlGaN/GaN HEMT showing the 1st (red) and 2nd (green) subbands.

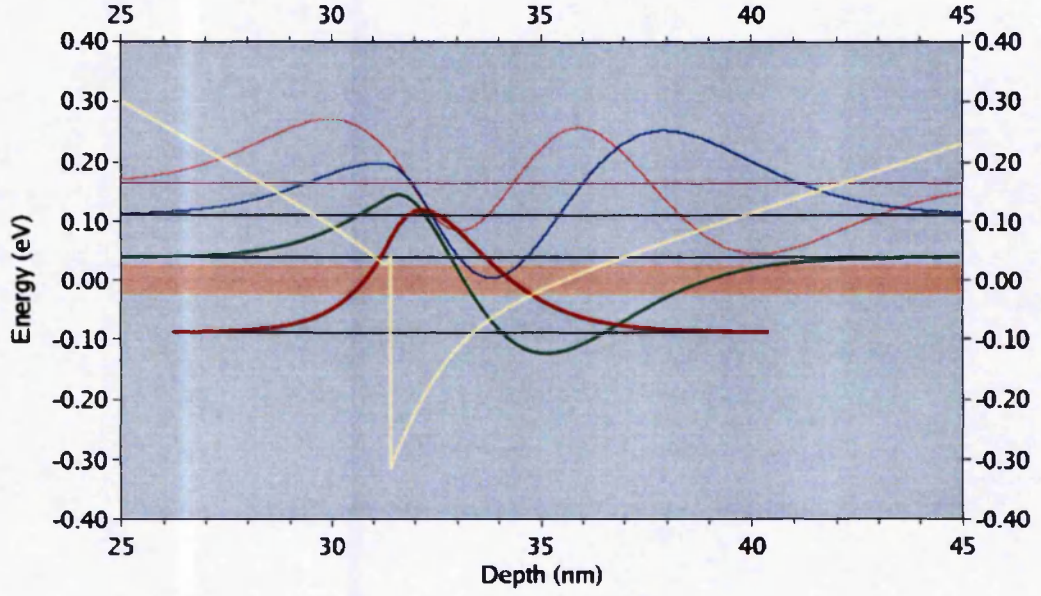

Figure 5: Band diagram for the 'triangular' AlGaN/GaN 2DEG showing 1st (red), 2nd (green), 3rd (blue) and 4th (pink) subbands.

2.2 The AlGaN/GaN HEMT device

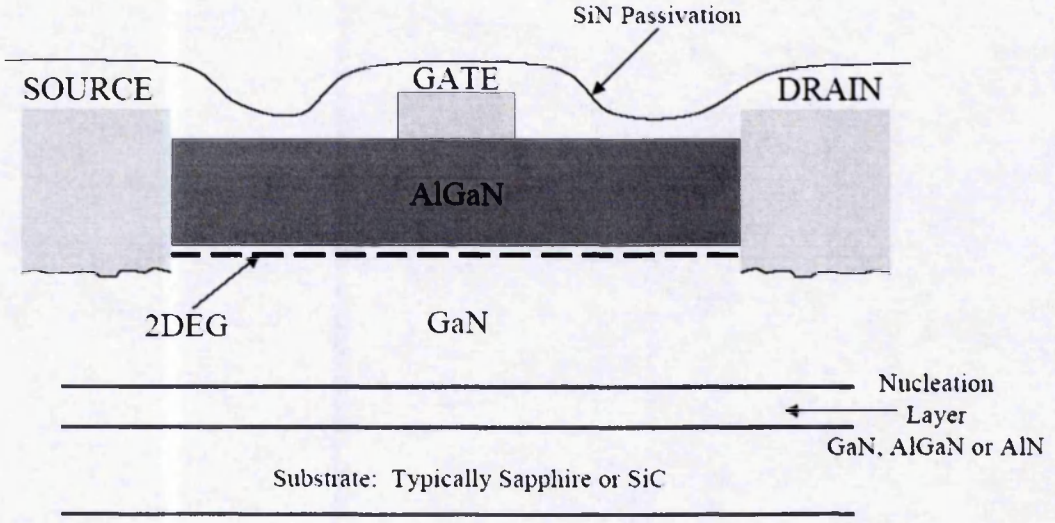

Figure 6: AlGaN/GaN HEMT structure [6]

2.2.1 Device operation

HEMTs operate in a similar manner to n-channel depletion mode Metal Oxide Semiconductor Field Effect Transistor (MOSFETs). They both operate using electrons as charge carriers, both devices are 'normally-on' (conducting when no bias is applied) and both are turned off by applying a negative voltage to the gate electrode. However, unlike in n-channel MOSFETs where the current flows through an n+ doped semiconductor, in a HEMT the current flows through the 2DEG situated in a potential well. 2DEG mobility (~2000cm^2/Vs in an AlGaN/GaN 2DEG) is significantly higher than bulk mobility (~500 cm^2/Vs) and therefore HEMTs can operate at higher frequencies than MOSFETs. In HEMTs the gate voltage controls the flow of electrons from the source to the drain by way of an electric field. When a negative voltage is applied to the gate contact the 2DEG under the gate starts to be depleted of electrons.

Once the gate voltage reaches the pinch-off voltage (~-6V in AlGaN/GaN HEMTs) the area under the gate is completely depleted of electrons and the device is turned off. In a conventional HEMT the 2DEG is generated from doping within the supply layer. However, in AlGaN/GaN HEMTs the 2DEG is formed by the piezoelectric dipole generated across the AlGaN layer as a result of the tensile strain induced during the growth process. The 2DEG is balanced by a net positive sheet charge at the surface of the device.

2.2.2 Piezoelectric effect

2.2.2.1 History of piezoelectric effect

Piezoelectricity was discovered by Pierre and Jacque Curie in 1880, when they were 21 and 24 respectively. They were researching crystallography at the University of Paris when they discovered that both quartz and Rochelle salt exhibited peculiar properties when placed under mechanical stress. They discovered that the crystals developed a voltage across them when squeezed and, conversely, changed shape under applied electrical field. Tension and compression developed voltage of opposite polarity, and in proportion to the applied force. These observed phenomena they named the piezoelectric effect and the inverse piezoelectric effect, from Greek *piezo* meaning "squeeze or pressure".

2.2.2.2 Structure of Gallium Nitride and Aluminium Nitride

Both GaN and AlN have a wurtzite crystal structure, tetrahedrally co-ordinated with a hexagonal Bravais lattice with four atoms per unit cell. The crystal growth orientation is an important factor in determining the polar nature of the GaN and AlGaN, which dominates the device behaviour and determines the carrier density in the 2DEG. Growth orientation is shown below, in Figure 7.

The crystal lattice can be defined using the length of the hexagonal edge a_0, the height of the prism c_0, and a microscopic dimensionless parameter u, which is defined as the length of the bond parallel to the c axis (parallel to [0001]), in units of c_0 [7]. The group III nitrides have lattice constants a_0 and c_0 of 3.11 and 4.98Å, respectively, for AlN and 3.19 and 5.18Å, respectively, for GaN [8, 9]. Compression along the c–axis and subsequent reduction in c_0, as a result of the growth of the AlGaN epilayer, causes the piezoelectric dipole across the AlGaN layer to be generated.

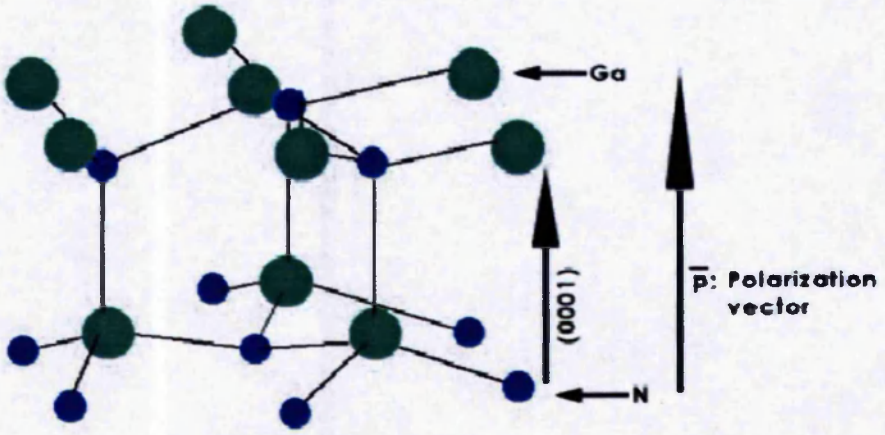

Figure 7: Growth occurs along the c-axis [0001] producing Ga-faced [0001] basal plane bilayers [10].

2.2.2.3 Polarisation

There are two forms of polarisation in this structure, spontaneous (due to the cation and anion positions present in the lattice as a result of hexagonal growth) and piezoelectric (due to lattice mismatch between the GaN and AlGaN layer). Spontaneous polarisation (the larger of the two) occurs along the crystallographic axis of noncentrosymmetric compound crystals when two difference sequences of atomic layering occur parallel to

that axis. The spontaneous polarity along the c-axis of AlGaN/GaN HEMTs arises from the fact that the GaN is grown in the hexagonal noncentrosymmetric wurtzite form, as opposed to the cubic form. When the GaN is grown along the [0001] basal plane, as shown in Figure 7, the GaN atoms are arranged in bilayers consisting of two closely spaced hexagonal layers of Ga^+ cations and N^- anions, which generates a dipole across the layer and induces a spontaneous polarisation along the c-axis of the crystal, towards the substrate.

Piezoelectric polarisation is produced between surfaces of a solid dielectric noncentrosymmetric material (non-conducting substance) when a mechanical stress is applied to it. In AlGaN/GaN HEMTs the mechanical stress is supplied by the strain induced through the pseudomorphic growth of the AlGaN epilayer. The tensile strain produced when $Al_xGa_{1-x}N$ is epitaxially grown on GaN results in a piezoelectric polarisation field being developed in the AlGaN layer. When stress is applied the metal lattice is displaced with respect to the nitrogen lattice, which causes variations in the cation-anion bond length and so increases polarisation. The larger the Al mole fraction is the smaller the AlGaN lattice constant becomes, which in turn increases the tensile strain at the AlGaN/GaN interface, increases the piezoelectric polarisation induced in the AlGaN epilayer and hence increases the 2DEG sheet carrier concentration [11].

2.2.2.3.1 Calculation of Piezoelectric polarization in the AlGaN layer

For a given crystal ε_{kl} the deformation due to external or internal forces or stresses σ_{ij} can be described using Hooke's law, which after simplification using Voigt notation gives the matrix of elastic constants C_{ij} for a wurtzite crystal structure [12].

$$C_{ij} = \begin{pmatrix} C_{11} & C_{12} & C_{13} & 0 & 0 & 0 \\ C_{12} & C_{11} & C_{13} & 0 & 0 & 0 \\ C_{13} & C_{13} & C_{33} & 0 & 0 & 0 \\ 0 & 0 & 0 & C_{44} & 0 & 0 \\ 0 & 0 & 0 & 0 & C_{44} & 0 \\ 0 & 0 & 0 & 0 & 0 & \frac{1}{2}(C_{11} - C_{12}) \end{pmatrix} \tag{2.3}$$

Through inversion on the C_{ij} matrix the elastic compliance constants can be calculated, and used to determine the reciprocal Young's modulus as a function of the crystal orientation. The reciprocal Young's modulus S_{11}^{*} along angle θ with respect to the [0001]-axis for hexagonal structures is given by [13]

$$S_{11}^{*} = S_{11}\sin^4(\theta) + S_{33}\cos^4(\theta) + (S_{44} + 2S_{13})\sin^2(\theta)\cos^2(\theta) \tag{2.4}$$

Where the elastic compliance constants S_{11}, S_{12}, S_{13} and S_{44} are given by:

$$S_{11} = \frac{C_{11}C_{33} - C_{13}^2}{(C_{11} - C_{12})[C_{33}(C_{11} + C_{12}) - 2C_{13}^2]} \tag{2.5}$$

$$S_{12} = \frac{C_{12}C_{33} - C_{13}^2}{(C_{11} - C_{12})[C_{33}(C_{11} + C_{12}) - 2C_{13}^2]} \tag{2.6}$$

$$S_{13} = \frac{C_{13}}{C_{33}(C_{11} + C_{12}) - 2C_{13}^2} \tag{2.7}$$

$$S_{44} = \frac{1}{C_{44}} \tag{2.8}$$

The basal plane is perpendicular to the principal axis (c-axis). Shown in Figure 8 is a plot of S_{11}^{*} for AlN, GaN and AlN as function of direction along the basal plane, it can be observed that since the reciprocal Young's modulus of GaN is a perfect circle, GaN is isotropic in the basal plane.

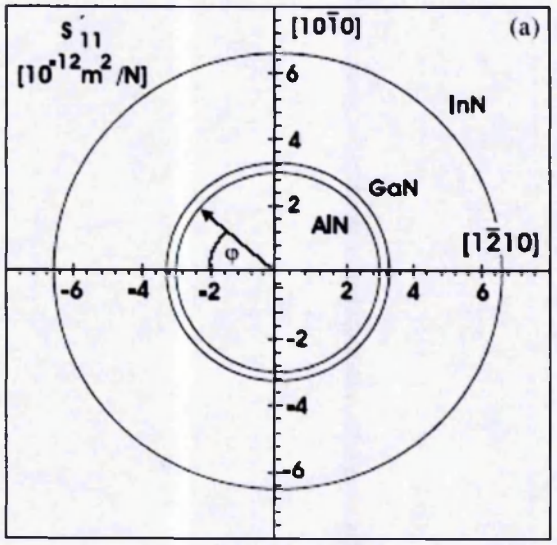

Figure 8: The reciprocal Young's moduli in the basal plane of InN, GaN and AlN.

The stiffness of AlN and GaN is more than twice that for InN. More importantly, the hardness of the wurtzite crystals is isotropic in the basal plane [12].

Since GaN is isotropic in the basal plane the strain is biaxial, therefore stresses $\sigma_1 = \sigma_2$. In addition, the crystal is relaxed in the growth direction since $\sigma_3 = 0$. From Hooke's law and matrix (2.3) the relationship between strain along the c-axis and along the basal plane can be determined as:

$$\varepsilon_3 = -2\frac{C_{13}}{C_{33}}\varepsilon_1 \tag{2.9}$$

Where

$$\nu(0001) = 2\frac{C_{13}}{C_{33}} \tag{2.10}$$

defines the Poisson ratio and

$$\varepsilon_1 = \frac{a - a_0}{a_0} \qquad \varepsilon_3 = \frac{c - c_0}{c_0} \tag{2.11}$$

are the relative variations in lattice constants a and c with respect to the relaxed lattice constants a_0 and c_0. The strain in the basal plane as a result of lattice mismatch is given by:

$$\sigma_1 = \varepsilon_1 (C_{11} + C_{12} - 2\frac{C_{13}^2}{C_{33}}) \tag{2.12}$$

Where

$$C_{11} + C_{12} - 2\frac{C_{13}^2}{C_{33}} > 0 \tag{2.13}$$

The piezoelectric polarisation for hexagonal materials belonging to the C_{6v} crystallographic point group [14] is given by:

$$P_i^{pz} = \sum_l d_{il}\sigma_l \quad i = 1,2,3 \quad l = 1,...,6 \tag{2.14}$$

where P_i^{pz} are the components of the piezoelectric polarisation and d_{il} are the piezoelectric moduli. Since, the strain is biaxial in the basal plane, that there is no strain in the growth direction because the layer is relaxed $(c = c_0)$ and assuming shear stresses to be negligible the piezoelectric polarisation can be simplified to a single component along the growth direction given by

$$P_3^{PZ} = 2d_{31}\sigma_1 = 2d_{31}\varepsilon_1 (C_{11} + C_{12} + 2\frac{C_{13}^2}{C_{33}}) \tag{2.15}$$

By converting the piezoelectric moduli (d_{il}) into piezoelectric constants (e_{kl}) [12], the piezoelectric polarisation in the c-axis associated with the biaxial basal tensile strain is given by

$$P_3^{PZ} = \varepsilon_1 e_{31} + \varepsilon_2 e_{32} + \varepsilon_3 e_{33} \tag{2.16}$$

$$= 2\varepsilon_1 e_{31} + \varepsilon_3 e_{33} \tag{2.17}$$

$$= 2\varepsilon_1 (e_{31} - e_{33} \frac{C_{13}}{C_{33}}) \tag{2.18}$$

Two important things should be noted; firstly, that P_3^{PE} is linearly dependant on ε_1 and hence variations in a_0; secondly, that P_3^{PE} is always negative for tensile biaxial strain and positive for compressive biaxial strain along the basal plane. Therefore when AlGaN is grown on GaN the spontaneous and piezoelectric polarisations always point in the same direction. It is for that reason that the total polarisation P found in an AlGaN/GaN HEMT is equal to the piezoelectric polarisation, P_3^{PE} (due to the lattice mismatch) plus the spontaneous polarisation, P_3^{SP} (due to the cation and anion positions present in the lattice). This is more usually written as

$$P = P_{PZ} + P_{SP} \tag{2.19}$$

The total polarisation-induced charge sheet density σ (m) is given by:

$$\sigma(m) = P_{sp}(Al_xGa_{1-x}N) - P_{sp}(GaN) + P_{pz}(Al_xGa_{1-x}N) - P_{pz}(GaN) \tag{2.20}$$

Where x is the aluminium mole fraction, $P_{SP}(Al_XGa_{1-x}N)$ and $P_{SP}(GaN)$ are the spontaneous polarisations in the AlGaN and GaN layers respectively and $P_{PZ}(Al_XGa_{1-x}N)$ and $P_{PZ}(GaN)$ are the piezoelectric polarisations in the AlGaN and GaN layers respectively. Since the GaN layer is assumed to be fully relaxed, which is a

reasonable assumption because the GaN layer is much thicker than the pseudomorphic AlGaN epilayer, [15] $P_{PZ}(GaN) = 0$. Equation (2.20) therefore becomes:

$$\sigma(m) = P_{sp}(Al_xGa_{1-x}N) - P_{sp}(GaN) + P_{pz}(Al_xGa_{1-x}N) \qquad (2.21)$$

The polarisation field results in a net positive sheet charge on the surface of the AlGaN which is balance by a net negative sheet charge to be formed in the GaN at the AlGaN/GaN interface.

2.2.3 Growth and role of device layers

Large high-purity single-crystal Gallium Nitride (GaN) substrates are difficult to obtain at present, resulting in alternative substrates often being used for thin film growth. The most commonly used substrates for the growth of hexagonal phase GaN are *c*-plane sapphire, and 6H and 4H polytypes of Silicon Carbide (SiC). However, there is significant interest in the use of Silicon (Si) as a substrate [16-21]. In addition to Si, there are other alternative substrate materials emerging e.g. Lithium Gallate [22]. Throughout 2001 and early 2002, sapphire was the substrate-of-choice because it was considerably cheaper that SiC. However, now nearly all state-of-the-art research is performed using SiC substrates because sapphire has a larger lattice mismatch with GaN of 14.8% compared to 3.3% for SiC. In addition, SiC has much higher thermal conductivity than sapphire, $\kappa = 4.9$W/cm°C compared to $\kappa = 0.3$W/cm°C, which leads to less self-heating in the devices and higher power outputs.

All the sample wafers used in this research were grown at QinetiQ, Malvern, on either SiC or *c*-plane sapphire substrates. The AlGaN/GaN HEMT's substrates were typically 250 to 350μm thick layers. The devices were grown by MOVPE using a "close-coupled showerhead" Thomas Swan reactor. Trimethyl gallium (TMGa – $[(CH_3)_3$ Ga]) and trimethyl aluminium (TMAl - $[(CH_3)_3$ Al]) were used as the group III precursor and ammonia was used as the group V precursor with hydrogen as the carrier gas. In order to

ensure that pre-reaction of the reagents was minimised, the group III and V gas flows were kept separate at room temperature until injection through the showerhead into the reaction chamber 16mm above the heated substrate. Throughout the AlGaN and GaN growth process was monitored *in-situ* using real-time spectral reflectrometry [23].

In order to obtain good quality, reproducible, specular surfaces and two-dimensional growth a well established growth procedure was used [23]. The routine begins with the nitrogen pre-treatment (nitridation) [24]. In which the substrate is exposed to NH_3 in order to increase the reflectance [23]. This is followed by low temperature (~550°C) nucleation [25], which forms an island film of GaN [23]. During the third stage, recystallisation, the temperature is ramped causing adjacent islands to merge to form larger islands. On sapphire substrates the nucleation layers normally consists of either GaN or AlGaN grown at a temperature of 600 °C. On SiC substrates the nucleation layer is often provided by AlN, which has been grown at 900 °C. The nucleation layer is typically 200Å thick and has the purpose of bridging the severe lattice mismatch between GaN and the substrate. In addition, it minimises parallel conduction through the substrate. An AlN sub-buffer has been shown to reduce the current transport through the substrate to just 100nA/mm [26].

During the high temperature GaN buffer growth phase (~1050°C at the rate of ~ 1μm/hr) the islands completely coalesce to form a smooth film. The GaN buffer layer is an unintentionally doped (UID) 1.2μm thick layer. The buffer layer needs to be resistive in order to prevent parallel conduction, ensuring full pinch-off, absence of punch-through and hence high efficiency, and also to provide good device isolation. Experimentally it has been seen that high temperature growth conditions result in insulating GaN. However, the mechanism or defect responsible for the insulating GaN is still unknown [27]. The quality of the GaN layer is very important because it influences the quality of the GaN/AlGaN interface which directly affects device mobility.

The final stage of the growth process is that of the $Al_xGa_{1-x}N$ channel layer, which is typically an un-doped 280Å thick layer grown at 1000 °C at a rate of ~ 1μm/hr, onto the

GaN buffer layer. More information on the growth process used at QinetiQ can be found in Balmer *et al* [23]. The AlGaN layer nominally contains 24% ± 1% aluminium. The greater the aluminium content, the smaller the lattice constant of the AlGaN compound; which increases the tensile strain in the epilayer (see section 2.1.1.2.). AlGaN/GaN HEMTs are normally passivated, using SiN or Si_3N_4, to try and reduce current collapse. The topic of passivation is covered in depth in chapter 3.

2.2.4 Device fabrication

The initial step of the fabrication process is the mesa isolation of the devices. Optical lithography is used to pattern Shipley S1818 photoresist. The mesas are then reactive ion etched using $SiCl_4$ with the patterned photoresist as a mask. The typically required mesa height is 0.1 - 0.2μm, taking about 18mins at an etch rate of 110Å/min. After photographing and testing the etch depth using a Dektak, a Titanium/Aluminium/Gold (Ti/Al/Au) ohmic alloy which consists of 500Å of Ti and 3000Å of Au is deposited by thermal evaporation at a pressure of 5×10^{-7} Torr. This is then alloyed at 900° C. Next, an optical lithography alignment etch is performed using patterned Shipley S1818 and RIE $SiCl_4$ to improve the contrast in preparation for the E-beam gate alignment stage. The feed metal is then defined using a PMGISF11/S1818 double-photoresist process (with MF-319 as developer). The feed metal of Ti 500Å /Au 8000Å / Ni 300Å / Au 3000Å is deposited at 5×10^{-7} Torr, followed by a conventional lift off process. After an E-beam resist process, the Schottky gates of Ni 300Å and Au 3000Å are deposited at 5×10^{-7} Torr, followed by another conventional lift off process. The final step is the deposition of silicon nitride passivation at 300°C and 200mT by plasma enhanced chemical vapour deposition (PECVD).

2.3 History of the GaN based devices

The history of GaN FET devices started in 1993 when Khan *et al* [28] reported the fabrication and characterization of a metal semiconductor field effect transistor

(MESFET) based on single crystal GaN. The first GaN–based MESFET was grown on sapphire substrates using low-pressure metal organic chemical vapour deposition (MOCVD). The device consisted of a 6000Å thick un-intentionally doped (UID) n-GaN layer deposited on a thin AlN layer on a (0001) basal sapphire substrate. The n-GaN layer was used as the transistor channel, which had a doping density and low field mobility of 1 x $10^{17}cm^{-3}$ and $350cm^2/Vs$, respectively. The 4μm-gate-length device had a current density of 180mA/mm and a peak transconductance of 23mS/mm. The devices performances were limited almost entirely by the poor GaN channel mobility, and Khan soon surpassed it, later that year, using a GaN HEMT based on a n-GaN/$Al_{0.14}G_{0.86}N$ heterojunction [29]. The addition of 1000Å $Al_{0.14}G_{0.86}N$ layer resulted in an AlGaN/GaN HEMT structure with a two dimensional electron gas (2DEG) with an improved mobility of $563cm^2/$ Vs. A year later Khan [30] published the first microwave performance results of AlGaN/GaN, 0.25μm gate-length HEMT, with an f_τ of 11GHz and an f_{max} of 35GHz; comparable to more mature SiC MESFETs at that time.

As the technology improved, dislocation densities in the GaN epilayers were reduced and the ohmic contacts changed from Ti/Au to Ti/Al. Better bulk and 2DEG mobilities of 600 and $1500cm^2/Vs$ respectively, were attained. At the same time, devices with useful current densities of 330mA/mm, breakdown voltages greater than 220V and cut-off frequencies of f_τ = 6GHz and f_{max} = 10GHz were demonstrated by Wu [31]. This progress led to the first report of large-signal performances of a GaN FET in 1996 by Wu [32]. The device structure was composed of an $Al_{0.15}Ga_{0.85}N$ epilayer on 0.3μm GaN channel, grown on c-plane sapphire substrate. The $Al_{0.15}Ga_{0.85}N$ epilayer consisted of a 3nm spacer, a 15nm Si doped layer (3 x $10^{18}cm^{-3}$) and a 12 nm cap, with background doping density of approximately 1 x $10^{18}cm^{-}3$ in the 'undoped' region. A 1μm gate-length, 4μm source-drain separation and 500μm gate-width MODFET yielded a peak output power of 550mW, or a power density of 1.1W/mm at 2GHz with a power-added efficiency (PAE) of 18.6%; surpassing the usual 1W/mm achieved by GaAs FETs. The problem of self heating was identified [32] as the limiting factor of sapphire-based power devices.

2.3.1 High Al-content devices

Devices continued to improve, leading to 1μm gate-length MODFETs with current over 500mA/mm and a 220V-plus breakdown. A unity-gain cutoff frequency (f_τ) of 19 GHz at 100V and a continuous wave (CW) power density of 1.57W/mm at 4GHz when biased at 28 V and 205 mA/mm was achieved [33]. Short-channel (0.2μm) MODFETs [34] achieved a mobility of 1200cm^2/Vs, f_τ of 50GHz, saturation current and transconductance of 800mA and 240mS/mm, respectively and breakdown fields of 80V/μm gate-drain spacing; leading to a CW output power density of 1.7W/mm at 10GHz. However, the next large breakthrough [35] came from the use of high-aluminium content AlGaN layers, which gave rise to numerous devices with gate-widths of 76μm and 100μm achieving CW output power of greater than 3W/mm at 18GHz, the best being 3.3W/mm and a with power-added efficiency (PAE) of 18.2% using an $Al_{0.5}Ga_{0.5}N$ epilayer [36]. These power densities are three times those of GaAs MESFETS and twice that of lower Al-content AlGaN/GaN devices. An AlGaN layer with a large percentage of aluminium has a larger band gap and hence can withstand a larger electric field before avalanche breakdown occurs. In addition, the resultant larger conduction band discontinuity (ΔE_c) enhances electron carrier confinement, resulting in high 2DEG mobility. Moreover, the increase in lattice mismatch between GaN and AlGaN layer increases the polarisation field in the devices which in turn, increases the electron carrier density in the 2DEG. In conclusion, the high aluminium concentration enabled high mobility and large electron number density. However, high aluminium content leads to poor ohmic contact resistance, which has meant that most modern devices use no more than 30% Al in the AlGaN layer.

2.3.2 Introduction of SiC substrate devices

The next significant innovation came from the rekindling of an idea first introduced by Binari *et al* [37]; the use of SiC as substrate instead of c-plane sapphire. The use of SiC negated the problem of poor thermal conductance found in sapphire. Although SiC is a lot more expensive, it is now the preferred substrate material for GaN based technology

because, firstly, it has a very high thermal conductivity of $\kappa = 4.9$W/cm°C compared to $\kappa = 0.3$W/cm°C (although most devices used in this project were grown on vanadium-doped material, with a thermal conductivity of 3.3W/mK). Secondly, the lattice mismatch between GaN and SiC is only ~ 3% (tension) compared to ~13% (compression) between GaN and sapphire. Sullivan *et al* [38] reported the first large-signal performance of $Al_{0.2}Ga_{0.8}N$/GaN HEMTs on 4H insulating SiC. Although the Al/Ti, 950°C annealed, ohmic contacts were poor, with contact resistances of 2.6-3.5 Ω.mm the 0.7μm gate-length, 40μm gate-width devices showed a high current density of 1.1A/mm and f_τ and f_{max} of 15GHz and 42GHz, respectively. At 10GHz, 320μm gate-width devices showed an output power of 0.9W, or 2.8W/mm, along with an associated gain of 6.5dB and PAE of 17.3%.

Through the use of SiC substrates there was steady improvement in reported power densities. Sheppard *et al* in 1999 [39] achieved 0.125-0.25mm gate periphery devices with high CW power output densities of between 5.3 and 6.9W/mm, with typical PAE of 35.4% and 9.2dB of gain, using semi-insulating (SI) 4H-SiC. He also produced a 3mm HEMT that gave 9.1W of CW output power at 7.4GHz, with a PAE of 29.6% and a gain of 7.1 dB. Wu *et al* [40] achieved 6.5W/mm on sapphire, 9.8W/mm on SiC and 9.2-9.8W of output power from 2mm wide devices flip-chip mounted onto AlN substrates. However, the highest power densities published by 2001 [41] were 10.7W/mm, with a PAE of 40%, from a 1 x 150 x 0.3μm AlGaN/GaN/SiC HEMT, after passivation, at 10GHz. Meanwhile, 32mm periphery devices on thinned sapphire [42] showed 113W (3.5W/mm) of CW output power, through the use of a 120nm thick SiN passivation PECVD. Wu [43] reported 51W total output power at 6GHz from a AlGaN/GaN HEMT amplifier. Kasahara [44] reported a 0.25μm AlGaN/GaN/SiC FET generating 2.3W output power at 30GHz, while Sandhu [45] published results from a 0.2μm gate-length AlGaN/GaN HEMT, operating at 29GHz, with a power density of 1.6W/mm and 26% PAE. This was followed by [46] a 500μm device operating 20GHz with a power density of 3.2W/mm and 71% PAE.

While most groups had changed to SiC, Kumar continued using sapphire substrates and

produced some high speed devices; 0.25μm gate-length devices with an f_τ of 67GHz and a maximum oscillating frequency (f_{max}) of 136GHz [47] (using MBE) and 0.15μm recessed gate devices with an f_τ of 107GHz and an f_{max} of 148GHz and 0.25μm gate-length devices with an f_τ of 85GHz and an f_{max} of 151GHz [48, 49] (using MOCVD). When Kumar finally moved onto SiC substrates [50-52] the devices improved to an f_τ of 121GHz and an f_{max} of 162GHz.

2.3.3 Devices with field plates

The next leap in progress came from the introduction of field plates (FP), as shown in Figure 9, which dramatically increased the power density of the devices. Field plates were first used on AlGaAs/GaAs HFETs in 1998 by Asano at NEC in Japan [53] where the idea improved power densities to 1.7W/mm. N-Q Zhang *et al* was the first [54] to use the field plate idea (or overlapping gate) on AlGaN/GaN HEMTs in 2000 to produce a record breakdown voltage of 570V. The field plate reduces the peak electric field found at the gate edge, as shown in Figure 10.

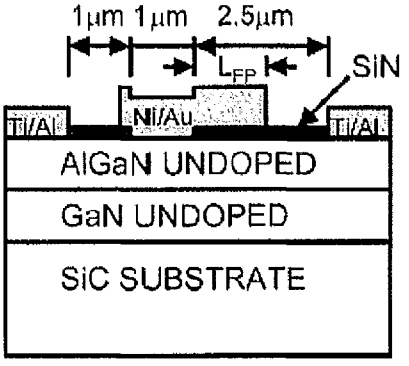

Figure 9: Schematic of AlGaN/GaN FP-FET structure[55].

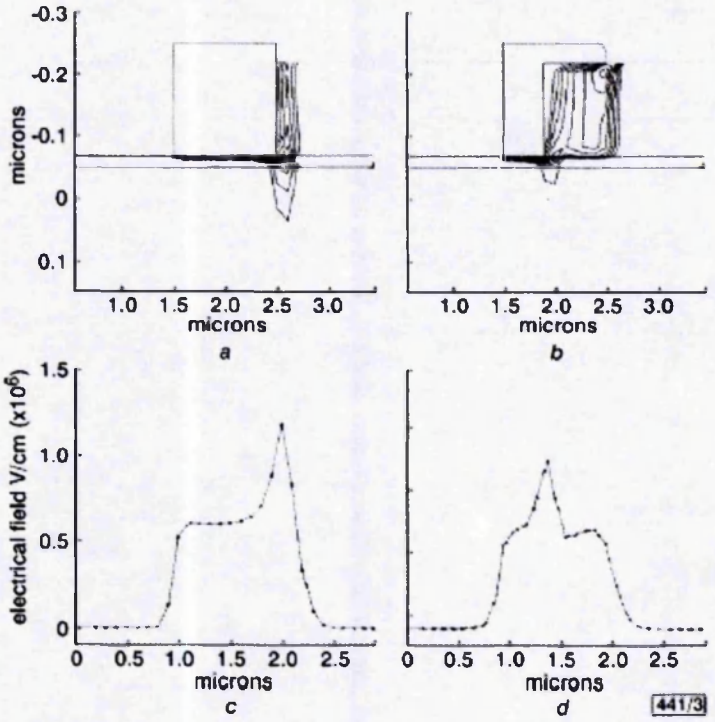

Figure 10: Simulation results of a conventional GaN HFET and a GaN FP-HFET [56].

Field strength is softened with a field plate. Degree of improvement depends on thickness of Si_3N_4 layer and extension of field plate as well device parameters. *a* Normal gate simulation structure *b* Gamma gate simulation structure. Innermost field line indicates highest electrical field (1.2 $\times 10^6$V/cm) while outermost field line indicates lowest electrical field (4 $\times 10^5$ V/cm). *c* Electrical field from source to drain, normal gate. *d* Electrical field from source to drain, gamma gate.

Using the FP idea over the last two years, the Ando and Okamoto group, also working for NEC in Japan, have published several papers [55, 57-61] on high power-density and high CW output-power large peripheral devices. Beginning with a 1mm wide gate which showed a CW output power of 10.3W at 2GHz [55]. Then soon after they developed a 1mm wide gate which showed a CW output power of 12W at 2GHz [57] by recessing the gate 14nm using BCl_3 plasma etching. Earlier this year they reported a single 24mm wide recessed-gate FET chip which generated 179W (3.7W/mm) of saturated output power, 64% PAE, and 9.3dB linear gain at a drain bias of 46V [58]. The group started to fabricate 24mm gate-width devices, starting with a non-recessed gates which generated

80W (3.3W/mm), 42% PAE, and a linear gain of 8.5dB at 2GHz [59]. Then by extending the plate length L_{FP} to 0.7μm, they produced a device that exhibited 96W (4.0 W/mm) output power, 54% power-added efficiency and 8.5 dB linear gain at a drain bias of 32 V at 2GHz [60]. Moving further to using a 32 mm wide recessed gate they reported an output power of 149W (4.7W/mm) with 64% power-added efficiency and 8.7 dB linear gain with a drain bias of 47V [61].

2.4 State-of-the-art

The largest power generated from a single chip is reported earlier this year by Ando *et al* [58] using a single 48mm wide recessed-gate FET chip which generated 179W (3.7W/mm) of saturated output power, 64% PAE, and 9.3dB linear gain at a drain bias of 46V.

The highest power density on sapphire substrates to date has been reported by Chini *et al* [62]. Chini used a novel design structure of field plate where the field plate is deposited on a layer of SiN as shown below in Figure 11. Such devices achieved a power density of 12W/mm.

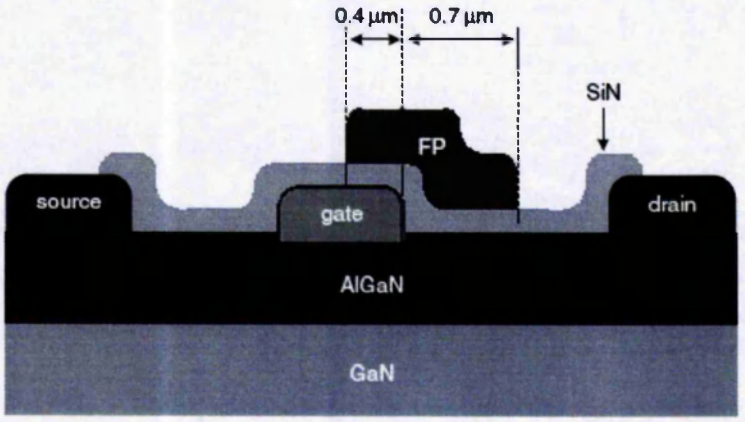

Figure 11: Novel field plate structure [62].

After SiN PECVD deposition a second gate is evaporated on the dielectric layer, acting as a field plate. The two gates are electrically shorted through the device pad and gate feeders.

The highest power density on SiC currently obtained is by Wu *et al* [63], 30W/mm with PAE of 49.6% at 8GHz, using devices with dimensions of 0.55 x 246µm^2 and a field plate length of 1.1µm. Wu used the same field plate design as Chini [62].

The fastest reported devices are by Kumar [52]. The 0.12µm gate-length grown by MOCVD onto 4H-SiC substrates demonstrated a f_t of 121GHz and an f_{max} of 162GHz.

The highest current density reported to date [64] is 1798mA/mm from MBE-grown AlGaN/GaN HEMTs on 6H-SiC.

3 CURRENT COLLAPSE

3.1 Introduction

This chapter describes an investigation of the causes of current collapse using gate lag and DC pulsed measurements. The wafer ID and numbers, device types and numbers and substrates used in the measurements are detailed below.

Table 2: Wafer details for current collapse measurements

Wafer Details			Device Details		
ID	Number	Substrate	Type	Number	Measurement
Japan	1194SC12A	SiC	E	numerous	Pulsed DC
Bravo	1218AN68A	Sapphire	Hall Bar	L 1	Gate lag

The wafers are standard Q1 structures, grown and fabricated using the techniques explained in the previous the chapter. The work described in this chapter resulted in the presentation of a poster at the Institute of Physics and a paper published in Solid-state Electronics [65].

3.2 Current collapse related literature

Despite their impressive performance, many AlGaN/GaN HEMTs show discrepancies between the predicted output power from static current-voltage curves (see below) and the actual load pull output power. 'Current collapse' is the term used to describe the shortfall in drain current and hence output power between the microwave frequency output power and the output power predicted from DC drain characteristics. Current collapse, which was first reported by Khan *et al* in 1994 [66], is also known as current slump [67], current compression [68] or dispersion [69, 70], and is the main obstacle preventing high power-output performance being obtained at microwave frequencies for AlGaN/GaN HEMTs. Ideal drain characteristics and the ideal load line are shown in Figure 12.

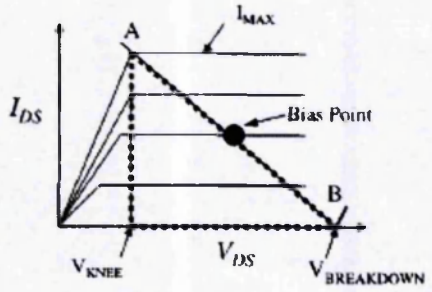

Figure 12: Ideal IV characteristics showing load line drawn to maximise output power [71].

It is possible to predict microwave frequency output power (P_{OUT}) from DC drain CV measurements using the following equation:

$$P_{OUT} = \frac{(\Delta V \Delta I)}{8} \tag{3.1}$$

Where the maximum current swing ΔI is equal to saturation current, I_{max} and the maximum voltage swing ΔV is given by ($V_{BREAKDOWN} - V_{KNEE}$), as shown in Figure 12.

Current collapse occurs when the gate of the devices are highly negatively biased [72]. This occurs, for example, when devices are biased in class B operation. Class B operation being when the devices are biased at point B as indicated on Figure 12 (i.e. V_{GS} = –6V and V_{DS} = 20V). When operating at class B the maximum drain saturation current I_{max} of the device decreases dramatically due to a large increase in the knee voltage. Current collapse is often observed using GaAscode (explained in subsection 3.3.1) pulse measurements (as shown in Figure 13) because pulse measurements help to prevent self-heating within the devices and therefore give a better indication of future device performance at microwave frequencies than standard DC measurements.

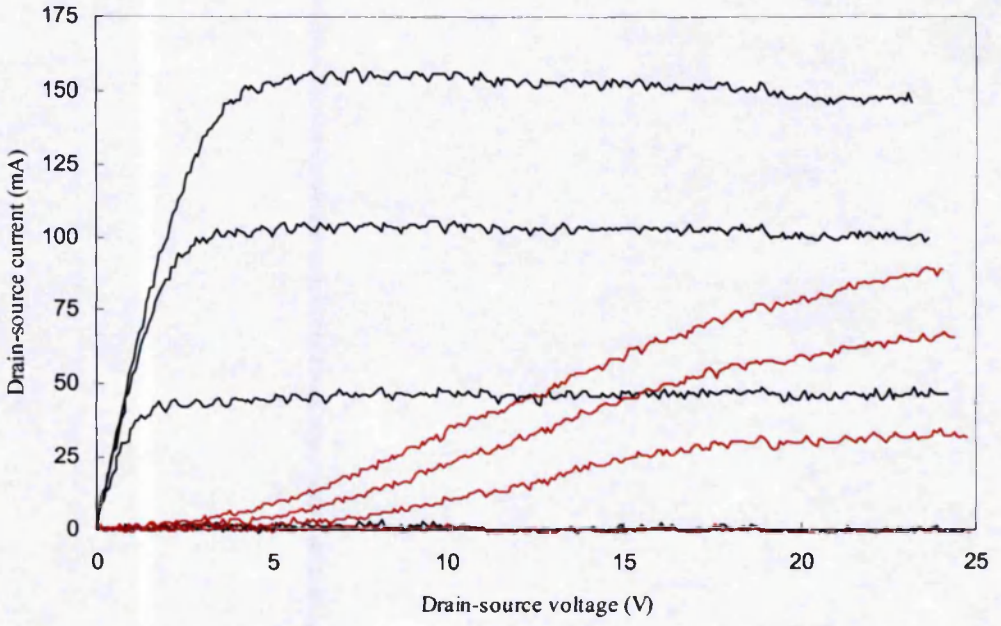

Figure 13: Pulsed measurements showing current collapse.

Black (biased at V_{GS} = 0V, V_{DS} = 0V) Red (biased at V_{GS} = -6V, V_{DS} = 20V). For V_{GS} = 0 to -6V, with -2V step.

3.2.1 Possible causes of current collapse

It is generally agreed that current collapse is caused by electron trapping. However, the location of the traps and the source of the electrons are hotly debated. There are three possible mechanisms of current collapse.

Firstly, hot electrons (from the 2DEG) could be trapped in the GaN buffer layer. This idea is spearheaded mainly by P.B. Klein [73-76] and S.C. Binari [37, 77-80]. They suggest that drain lag [78] occurs without surface involvement. Only gate lag is attributed to surface trapping. Their measurements were performed on 250Å AlGaN (30%) / 3μm SI GaN / 200Å AlN / Sapphire HEMTs with (PtAu) gate lengths of 0.2 to 1μm. Using the optical reversibility of current collapse, the photoionisation spectra of the traps involved were determined to be at 1.8 and 2.85eV below the conduction band [73-75, 79]. Through the reduction of the trapping effects Binari was able to fabricate 0.4μm device with a f_τ of 30GHz and a f_{max} of 70GHz, a CW power density of 3.3W/mm and a pulsed power density of 6.7W/mm at 3.8GHz.

The second possible mechanism is variation in the charge trapped in the AlGaN layer under the gate. Tarakji *et al* [81] concluded from their comparative study of MOSHFET [82] and HFET current-voltage transfer characteristics (under dc and short-pulsed drain and gate voltage biasing) that changes in the transverse electric field between gate and channel caused changes in the trapped charge beneath the gate, resulting in current collapse. They ruled out gate leakage and surface states as possible mechanisms of current collapse because both device types suffered from current collapse despite having different surface conditions. A similar effect on the device properties has been reported from trapping of electrons in states in the AlGaN close to the gate corner of unpassivated devices [83]. In this case the trapping was non-linear in drain voltage and obeyed a Poole-Frenkel law. Since the charge trapping (to either surface states or AlGaN traps) is a non-linear function of applied voltage, the model suggests that under RF excitation (or in pulse operation) the charge state of the virtual gate becomes characteristic of the most negative applied gate voltage. This leads to a reduction in drain current which is a strong

function of RF input power, explaining the difference between DC and RF operation.

The third, and most widely accepted [68, 71, 84-95], explanation of current collapse is the trapping of gate electrons on the device surface and the subsequent formation of a 'virtual gate'. The virtual gate concept has been examined in many different ways, such as, drain lag [84], gate lag [71, 85] thermal drain current recovery [86] and through ultra violet (UV) illuminated drain current recovery [84, 87-89] measurements. It has been previously shown [7] that sheet charges are induced by piezoelectric polarization, and that the polarization dipole alone is not sufficient to create a 2DEG [96]. In order for 2DEG formation to occur in the GaN channel, a positive sheet charge must exist at the AlGaN surface. In the virtual gate model, when the gate is under large negative bias, electrons can be injected from the gate onto the surface of the device at the gate edges, changing the occupation of surface states. The virtual gate formed on the surface depletes the 2DEG of electrons and increases the parasitic source and/or drain resistance of the device. The movement of the electrons onto the surface and subsequent current collapse is depicted in Figure 14.

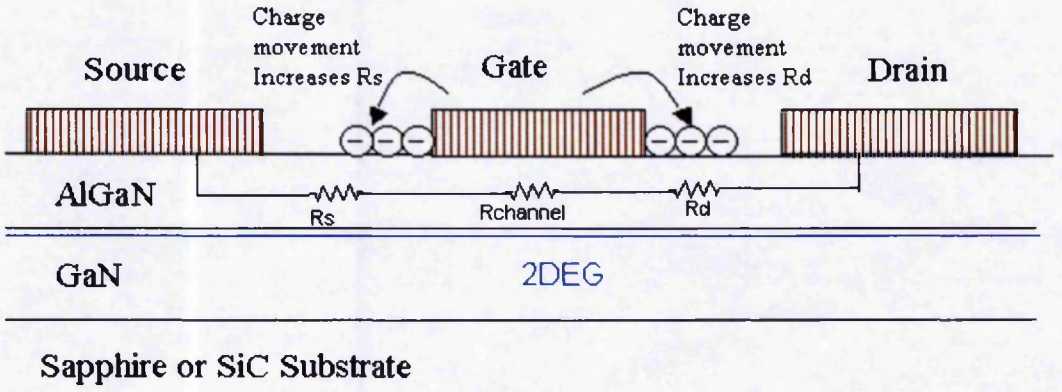

Figure 14: Charge transferring onto the surface form a 'virtual' gate.

3.2.1.1 Drain lag measurements

The 'virtual gate' effect has been elegantly demonstrated using a Kelvin probe technique [84]. Charge was found to spread up to a micron across the surface of unpassivated devices. Simultaneous measurements of the drain current and the surface potential (using the Kelvin probe technique) clearly indicated that the surface potential variations were responsible for the collapse in drain current. UV illumination totally eliminated current collapse whilst silicon nitride passivation reduced the magnitude of the surface and drain current transients.

3.2.1.2 Gate lag measurements

Gate lag measurements by Vetury *et al* [71] and Verzellesi *et al* [85] both clearly indicated that the traps located on the ungated surfaces explain all dispersion effects. By measuring the maximum drain current of devices operating with and without ultra violet (UV) exposure, Vetury *et al* [71] showed that the devices had a higher maximum drain current when operated under UV. They concluded that the incident photons of UV light, which have energies greater than the GaN bandgap (3.4 eV), induce the formation of electron–hole pairs. The holes are then pulled to the surface by the electric field where they neutralise the virtual gate. A Japanese group, Ohno *et al* [86-89] using Micro-Raman scattering spectroscopy, Electroluminescence (EL) and a spatially-resolved illumination technique discovered a high-field region at the drain edge, caused by a high-density surface traps. The high field region that they discovered is shown below in Figure 15. When the devices were illuminated (using their spatially-resolved illumination technique) the current collapse was reduced greatly. They concluded that the current collapse was caused by the virtual gate mechanism. They also studied the effect of surface passivation on current collapse [89]. They found that by depositing a 100nm thick film of Si_3N_4 passivation using electron-cyclotron-resonance (ECR) sputtering, current collapse was eliminated, giving further evidence that surface states were the cause of current collapse.

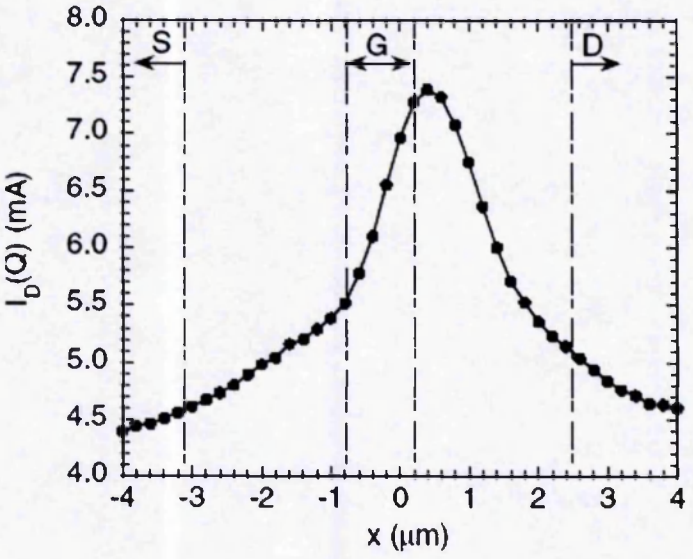

Figure 15: Drain current as a function of UV illumination [89].

3.2.1.3 Surface passivation

Passivation has been found by numerous groups [84, 89-95, 97] to improve device characteristics. DLTS measurements by Vertiatchikh *et al* [90] clearly show the reduction of two surface traps through Si_3N_4 passivation. Passivation experiments performed by B.M. Green *et al* [91] showed that the addition of a Si_3N_4 passivation layer to undoped AlGaN/GaN HEMTs increased the saturated power density by up to 100% at 4GHz and increased the breakdown voltage by an average of 25%. Hence, they concluded that a surface-layer mechanism was the main factor limiting the maximum RF current. A comparative study [92] of different surface passivations on AlGaN/GaN HFETs showed that Si_3N_4 and SiO_2 gave a 25% improvement in device drain current performance. SiO only gave a 15% improvement. However, both Si_3N_4 and SiO_2 increased gate leakage of the samples from 0.1mA to 1mA whilst the gate leakage of the SiO sample remained at 0.1mA. Probably the best results reported in terms of dispersion-free transistors are from a US group from Yale university, N-Q Zhang *et al* [93], who use a JVD (Jet Vapour Deposition) double passivation technique. They found

that Si_3N_4 reduced current collapse (by introducing shallow donors into the AlGaN surface) but caused a large increase in gate leakage current. They also found that SiO_2 passivation dramatically reduced gate leakage (by introducing deep level donors) but caused severe current collapse. In order to combine both advantages of SiO_2 and Si_3N_4 a double gate dielectric scheme was devised (shown in Figure 16). This led to devices with no current collapse and without gate leakage.

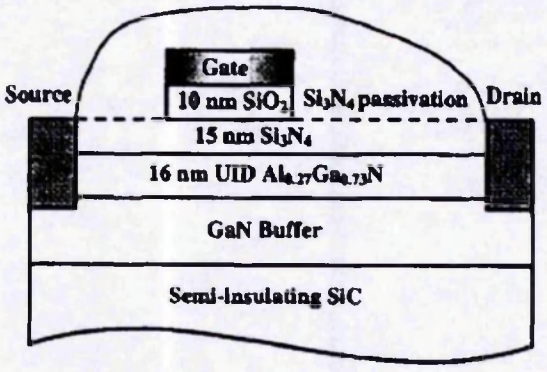

Figure 16: Double gate-dielectric insulated GaN HEMT structure [93].

3.2.1.4 GaN caps

Several groups in an attempt to reduce current collapse have investigated the use of a GaN cap layer (typically 5nm thick). Using a GaN cap layer reduces the electric field at the surface and hence possibly reduces the migration of electrons from the gate onto the surface. However, to date there have been contradictory results. A German/Korean collaboration [94] found that SiN passivation had less effect when deposited on a GaN cap layer, where as a Japanese group [95] achieved extremely good devices without current collapse or transconductance dispersion, using an n^+ doped GaN cap layer with strongly stressed SiN passivation. Tilak *et al* [41] report that variation in barrier thickness also affects the electric field at the surface and consequentially current collapse. It is reported that the current collapse effect is increased if the barrier

thickness is decreased, due to the increase in electric fields in thin barrier structure.

3.2.1.5 AlGaN/GaN double barrier structure

The AlGaN/GaN double barrier structure is a novel design by Neuburger *et al* [98] which attempts to prevent current collapse by hiding the positive sheet charge within the structure of the device. The AlGaN/GaN double structure is shown below in Figure 17, it results in an ambipolar device that has both a 2DEG at the usual AlGaN/GAN interface and a two-dimensional hole gas (2DHG) at the GaN/AlGaN interface.

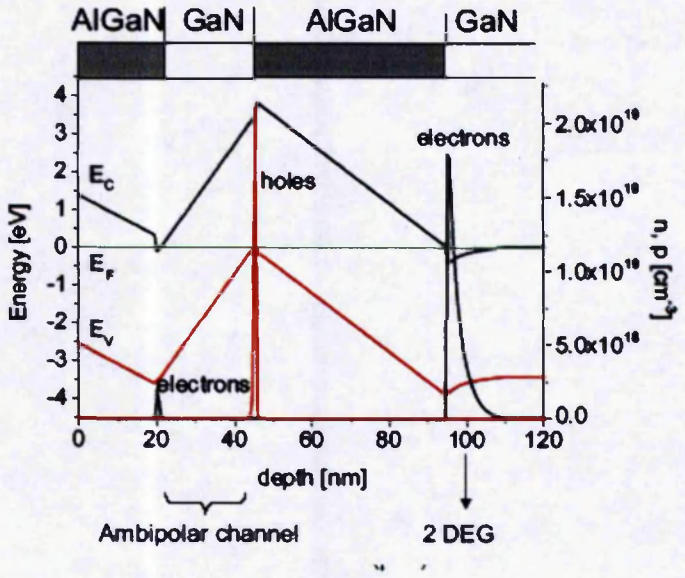

Figure 17: AlGaN/GaN double barrier structure [98].

In order to obtain a unipolar device, acceptor and donor doping spikes are used to neutralise the rear 2DEG and 2DHG, respectively. The doping profile of the resulting structure, from capacitance-voltage (CV) measurements, is shown below.

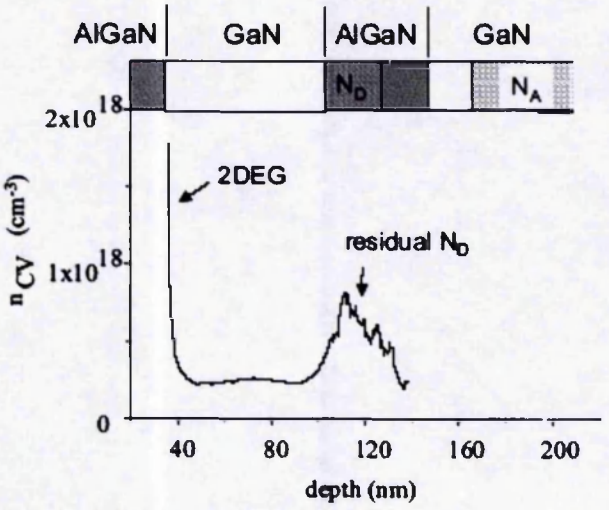

Figure 18: Doping profile of a AlGaN/GaN double barrier structure from CV measurements [98].

Following their initial processing a residual parallel donor path remained, however their concept was verified.

3.3 Passivation experiments

As mentioned, device passivation has been found by many groups, at best remove or, at least, to reduce current collapse. In order to investigate these claims, and to optimise the silicon nitride deposition process, the effect of different passivation conditions on drain current was measured.

3.3.1 Experimental

An unpassivated wafer (1194SC12A) was sawn into 10 samples. Three co-planar 200μm T-gate type E devices (Figure 19) were chosen from each of the samples. Current collapse in each of the 30 devices was measured, using a GaAscode pulse kit, before and after passivation, thus allowing the effect of the passivation to be determined as a ratio (3.3). Each sample was passivated under different conditions, as shown in

Table 3. The passivation results were then compared to determine which passivation conditions improved the devices (reduced current collapse) the most.

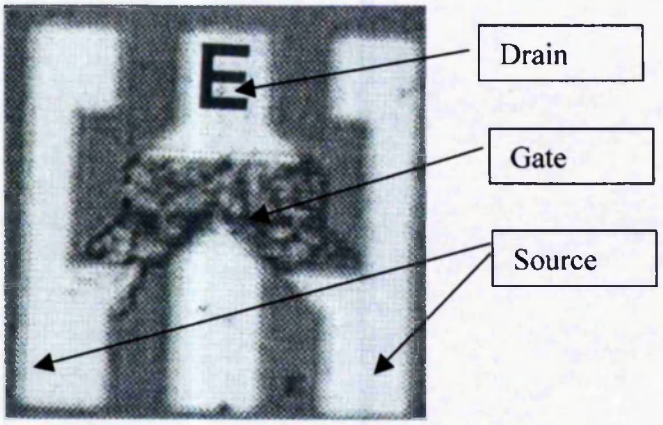

Figure 19: A co-planar 200μm T-gate type E device.

The GaAscode pulse kit enables the device to be biased at any gate-source and drain-source voltage point (i.e. at V_{GS} = 0V and V_{DS} = 0V). From that bias point the device is then pulsed at a programmable rate to the measurement points. As mentioned previously current collapse is the fall in saturation current observed in high frequency measurements as compared to the DC behaviour. For the purpose of these measurements the high frequency measurements were class B biased pulse measurements while the DC measurements were represented by standard zero biased pulse measurements. The maximum saturation current of the device (indicated as I_{max} on Figure 12) was used as the figure of merit. Thus the current collapse (CC) of the devices was given by the ratio between the zero biased saturation current (I_{DSZ}) and the class B biased saturation current (I_{DSB}).

$$CC = \frac{I_{DSB}}{I_{DSZ}} \tag{3.2}$$

Therefore, a single current collapse measurement consisted of two separate measurement sweeps one biased at zero and another biased at point B. For each sweep, V_{GS} was swept

from 0 to -7V in 1V steps while V_{DS} was swept from 0 to 25V in 100mV steps at a pulse length of 0.5µs and pulse separation of 0.5ms, as shown in Figure 20.

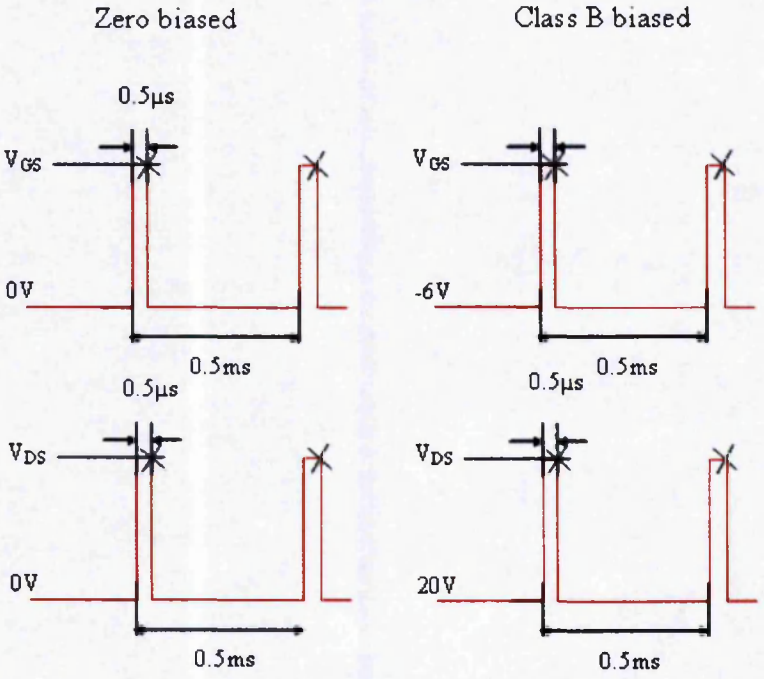

Figure 20: Zero and Classed B biased pulse measurement waveforms.

After they were measured each piece was individually passivated under different conditions, shown in Table 3. Each sample was used to test a single variable of the passivation process. The control sample, C, was passivated using the currently preferred passivation conditions.

Table 3: Passivation experiment matrix (by PECVD)

Sample	2%SiH_4 flow	N_2 flow	Pressure	Power	Temp	Time	Test
F	100	135	200	5	300	20	High Silane
B	N_2 preplasma	135	200	5	300	10	N_2 plasma
	35	135	200	5	300	40	
C	35	135	200	5	300	40	Control
E	35	135	200	5	300	80	Thickness
G	35	135	200	5	300	20	Thickness
J	35	135	200	5	300	10	Thickness
K	35	135	200	10	300	40	Power
L	35	135	400	5	300	40	Pressure
N	35	135	600	5	300	40	Pressure
O	35	135	200	5	350	30	Temperature

After passivation the pulse measurements were repeated on the same devices that had been measured before passivation. The direct comparison of current collapse after passivation doesn't give a true indication of the improvement in the devices due to passivation because it doesn't take into account the state of the devices before passivation. Therefore, the ratio of passivated current collapse (PCC) at V_{DS} = 10V to unpassivated current collapse (UCC) at V_{DS} = 10V was also calculated for each device.

$$P_R = \frac{PCC}{UCC} \tag{3.3}$$

A passivation ratio (P_R) of 1 indicates no improvement, greater than 1 indicates that the device is improved and less than 1 indicates that the device has deteriorated. The results of the passivation experiments (UCC, UCC standard deviation, PCC, PCC standard deviation and P_R for each device, and their average for each sample) are given below in Table 4. The standard deviation values where calculated using the un-biased (n-1) method, where n is the number of samples, in this case n = 3.

Table 4: Average UCC, UCC standard deviation, PCC, PCC standard deviation and P_R (2dp).

Sample	UCC	UCC SD	PCC	PCC SD	P_R
F	0.31	0.07	0.67	0.04	2.16
B	0.15	0.13	0.13	0.04	0.87
C	0.27	0.1	0.34	0.12	1.26
E	0.50	0.15	0.67	0.21	1.34
G	0.21	0.12	0.41	0.13	1.95
J	0.23	0.72	0.30	0.04	1.30
K	0.27	0.06	0.42	0.07	1.56
L	0.51	0.27	0.65	0.25	1.27
N	0.26	0.15	0.57	0.07	2.19
O	0.32	0.16	0.49	0.04	1.53

As can be observed from Table 4, there wasn't a single outstanding result, since ideally the PCC ratio should be 1 (i.e. zero current collapse after passivation) and the P_R should be high, to indicate that the device wasn't good previous to passivation. However, passivation F was found to have significantly better results than the control C, while passivation B was found to give the worst results. The device uniformity, indicated by the standard deviation, generally improved after passivation. The high and high average UCC and PCC values of samples L and E are as a result of a single good transistor, indicated by the high standard deviation of the samples. Passivation F had an average passivation ratio of 2.16, meaning that on average the maximum drain current of the devices more than double after passivation. Passivation B had an average passivation ratio of 0.87, meaning that the drain current of an average device is approximately a 1/10 less than before passivation, in other words passivation B causes more current collapse. A comparative study between conditions F and B was then undertaken to explain why condition B passivation increased current collapse and why condition F reduced current collapse. Although passivation N improved the devices greatly (2.19 times) the devices still had a considerable current collapse after passivation (0.57). The large variation in passivation results lead to a comparative study of the passivation types in order to

distinguish their differences, and hence why passivation could both increase and decrease current collapse.

3.3.2 Differences in passivation

In order to test the hypothesis proposed by the virtual gate concept that current collapse is a surface trapping phenomena, pulsed IV characteristics of a type F and B passivated device where taken at various pulse lengths with constant separation. If the current collapse was a surface trapping issue, as the pulse width increased the parasitic drain resistance (R_D) should decrease because there will be more time for surface trapped electrons to return to the gate. Figure 21 and Figure 22 show the pulsed IV measurements of the type B and F passivated devices as the pulse width was varied from 1µs to 1ms at constant 0.5ms pulse separation.

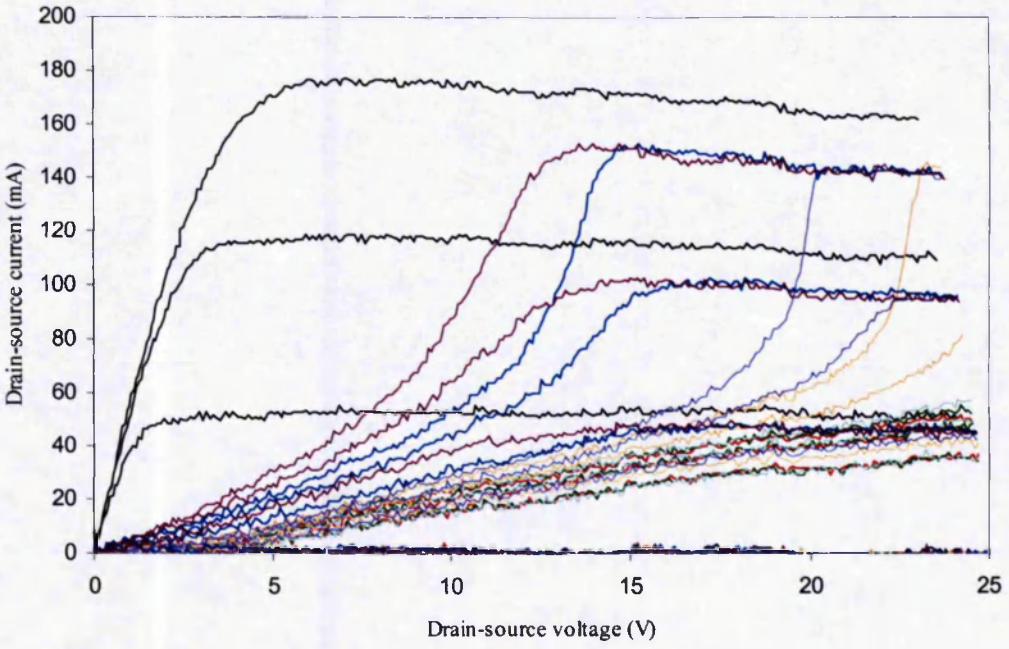

Figure 21: Current collapse of device 2110 with type B passivation.

Each sweep has a constant pulse separation of 0.5ms, pulse widths vary. Zero biased (V_{GS} = 0V and V_{DS} = 0V) – Black (1µs), Class B biased (V_{GS} = -6V and V_{DS} = 20V) – Red (1µs), Green (5µs), Light blue (10µs), Peach (50µs), Lilac (100µs), Blue (500µs) and Purple (1ms).

From both Figure 21 and Figure 22 it can be seen that 1ms pulse width measurements show significantly less current collapse than 1μs measurements, which is in-keeping with the initial hypothesis. From examination of the (poor) type- B passivated device results it can be observed that, at a critical voltage/pulse-width product, the drain current rapidly increases to saturation at approximately 150mA. Therefore, the movement of electrons from the surface to the gate is a function of the electric field at the surface and the amount of time the electrons have to migrate (i.e. pulse width), which is as expected. The mass exodus of electrons from the surface at the critical voltage-pulse-width results in a rapid and dramatic reduction in R_D and hence an equally rapid increase in drain current, as observed. For a given pulse width the electric field required after type F passivation to move the electrons from the surface back to the gate is less than after type B passivation. It can thus be concluded that the main difference between passivation F and B is that traps made by passivation F are shallower than those made by passivation B.

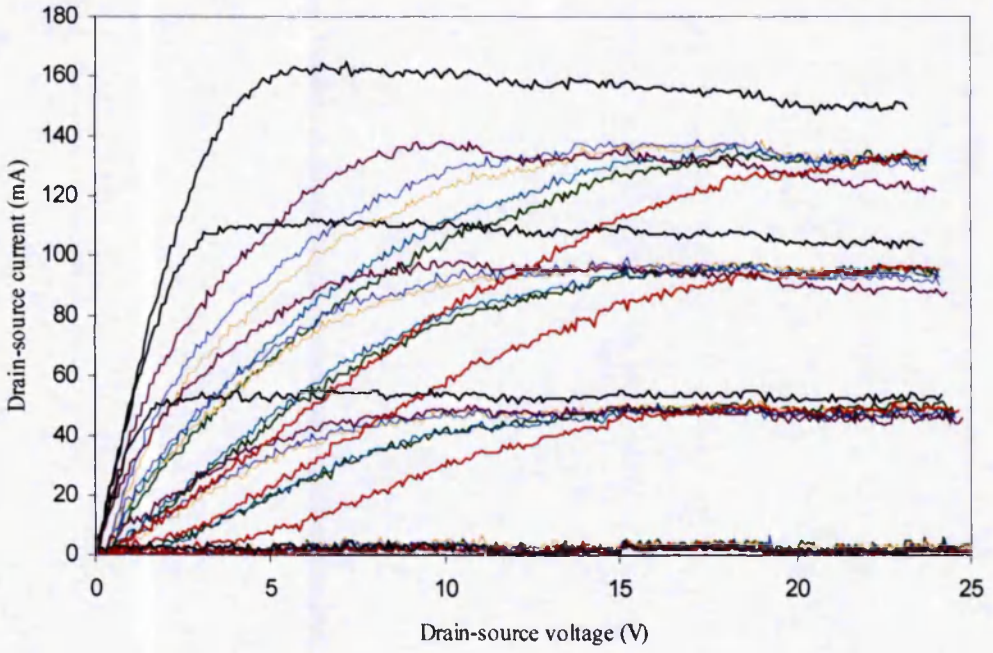

Figure 22: Current collapse of device 1414 with type F passivation.

Each sweep has a constant pulse separation of 0.5ms, pulse widths vary. Zero biased (V_{GS} = 0V and V_{DS} = 0V) – Black (1µs), Class B biased (V_{GS} = -6V and V_{DS} = 20V) – Red (1µs), Green (5µs), Light blue (10µs), Peach (50µs), Lilac (100µs) and Purple (1ms).

N-Q Zhang *et al* [93] reported that, although shallow traps inducing passivation (like type F) reduce current collapse, they also increase device gate leakage. Unfortunately, the gate leakage was not measured before passivation and therefore the affect of the passivation on gate leakage couldn't be determined.

3.3.3 Passivation conclusions

The passivation experiments showed that under the right conditions current collapse could be reduced by passivation. This strongly suggested that current collapse was directly affected by the condition of the device surface. However, since none of the passivation condition were able to eliminate current collapse entirely, either the passivation processing procedure required further optimization or there was an

additional cause of current collapse, such as hot electrons trapping in the GaN and / or the AlGaN layers. Passivation type F was found to reduce current collapse, but the pulse length variation experiment suggested that instead of preventing the migration of electrons onto the device surface, as hoped, the passivation merely provided shallower traps, allowing the electrons to move on and off the surface faster. Therefore, control passivation scheme C, remained the QinetiQ standard.

3.4 Gate lag measurements

The gate lag measurements were performed in order to further investigate the surface induced current collapse. Potential probes to the channel of a long channel AlGaN/GaN HFET were used to directly measure the increase in resistance of the ungated regions at the source and drain that were suspected as being responsible for current collapse under pulsed conditions. Due to the fact that no bias was applied to the substrate and that the measurements were performed on long channel devices, bulk trapping effects in these devices could be assumed to be negligible, which left only the possibility of surface trapping or trapping at the gate corner. Combined with surface passivation, these experiments were able to focus solely on surface trapping in AlGaN/GaN HFETs.

3.4.1 Measurements and discussion

The layer structure used in this work was fabricated by metal organic vapour phase epitaxy in a Thomas-Swan reactor. The epilayer consisted of 30nm AlGaN (~25% Al) and 1nm AlN on 1.2μm GaN (all undoped) on a sapphire substrate. The AlN layer, as explained in chapters 4 and 5, reduces alloy scattering and increases the mobility of the 2DEG up to a peak value of about 1800cm^2/Vs [99]. The device used was a gated Hall bar as shown in Figure 23 with 100μm x 300μm Ni/Au gate and 100μm square Ti/Al/Ti/Au ohmic contacts. The gate-source and gate-drain spacings were 5μm. Equally spaced contacts to the channel allowed the potential drop along the channel to be probed in measurements discussed later. Measurements were made on the devices before and

after passivation with silicon nitride (Si_3N_4).

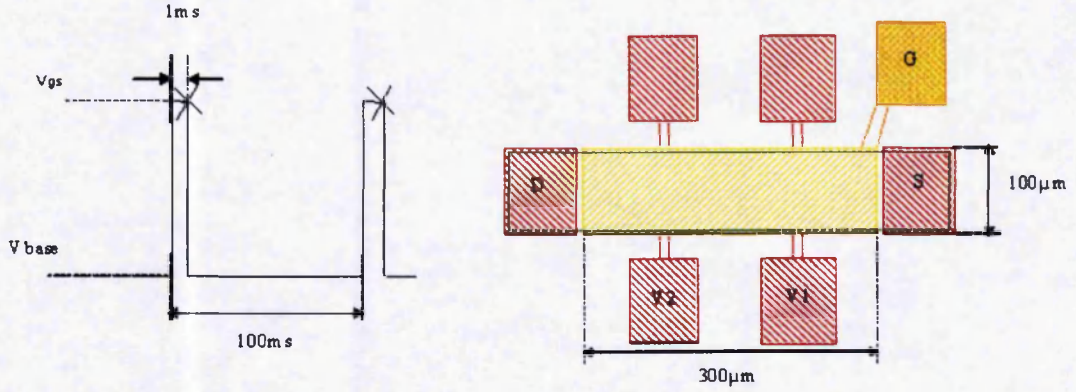

Figure 23: The voltage waveform applied to the gate and a schematic plan view of the Hall bar structure. Ohmic contacts to the 2DEG under the gate (Red), Schottky gate contact (Yellow), gate feed metal (Orange) and mesa (green).

Pulsed gate-lag measurements were performed using a HP4156A precision semiconductor parameter analyser. The gate voltage was held at the pulse base voltage (V_{BASE}) for 99ms and then pulsed to the measurement voltage, V_{GS}, for 1ms while the measurement was taken on the falling edge, as shown in Figure 23. The drain voltage, V_{DS}, was held at only 100mV in order to ensure the transistor was in the linear regime and to prevent any possibility of hot electron trapping under the gate. V_{BASE} was made increasingly negative (0V to -30V) to simulate the high electric field that occurs at the surface at the gate edge in normal operation with large V_{DS}. Under these conditions for V_{GS} below pinch-off, the only current flow in the channel was from a small gate leakage of a few microamps. For each V_{BASE} value, V_{GS} was swept from 1V to -8V at 100mV steps.

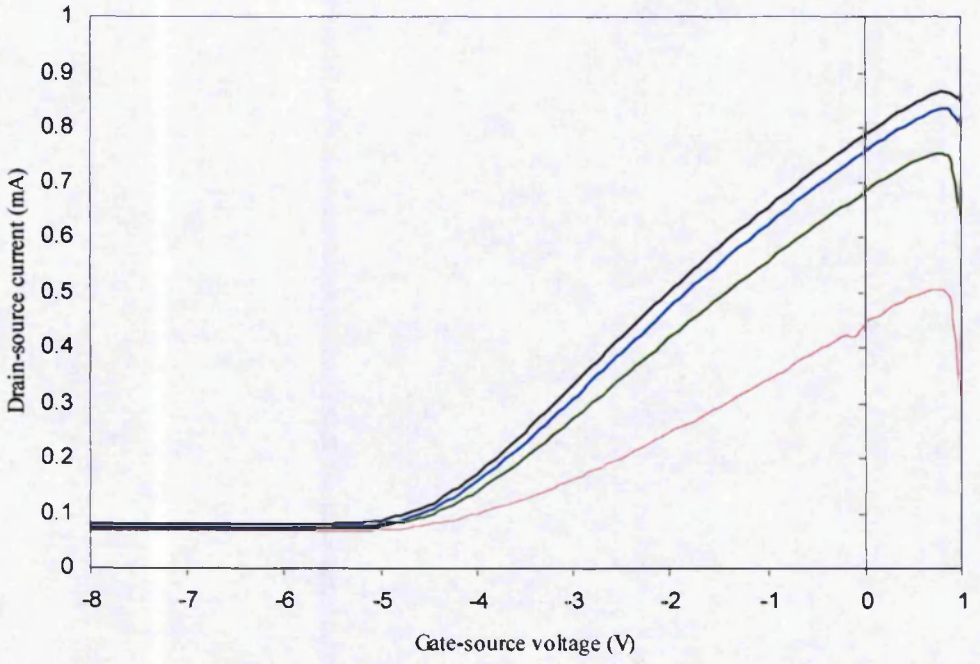

Figure 24: Gate lag measurements for an unpassivated device.

V_{BASE} = 0V (Black), V_{BASE} = -10V (Blue), V_{BASE} = -20V (Green) and V_{BASE} = -30V (Red).

As shown in Figure 24 V_{BASE} had a dramatic effect on device transport for an unpassivated device. As V_{BASE} became more negative (corresponding to an increase in the peak electric field at the gate corner) there was a fall in the conductance of the device. Note there was no shift in the pinch off voltage, indicating there was no change in the electron number density under the gate. This confirmed the previous assumption that electron trapping under the gate was negligible. After passivation of the surface with a silicon nitride layer, it was found that the base voltage had almost no effect on the drain conductance - for measurement times accessible with the parameter analyser (see Figure 25). The fall in conductance seen in Figure 24 can easily arise from an increase in the source and drain resistance of the ungated regions without any change in the transport properties under the gate.

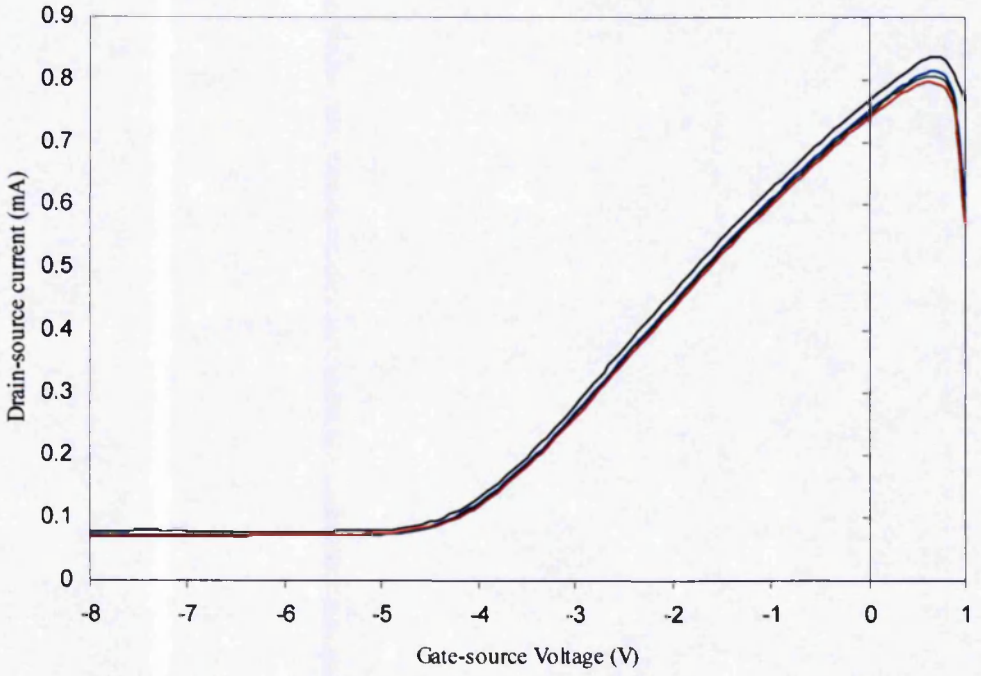

Figure 25: Gate lag measurements for a passivated device.

V_{BASE} = 0V (Black), V_{BASE} = -10V (Blue), V_{BASE} = -20V (Green) and V_{BASE} = -30V (Red).

In order to demonstrate the increase in source and drain resistance directly, a second set of gate lag measurements were carried out. V_{GS} was pulsed from increasingly negative V_{BASE} values to a fixed gate voltage of 0V, at which the channel conductivity was measured. V_{DS} was swept from 0.5V to -0.5V with 100mV steps to determine the channel conductivity at V_{GS} = 0V and V_{DS} = 0V. Two Hall voltage probes situated at 1/3 and 2/3 of the total gate length were used to determine the voltage gradient in the 2DEG under the gate. Assuming the voltage gradient to be constant under the gate and using the known geometry of the device, the resistance of the channel and the ungated regions between the gate and source/drain were extracted using the following equations.

$$R_S = \frac{\frac{\Delta V1}{\Delta V_{DS}} - \left(\frac{\Delta V2 - \Delta V1}{\Delta V_{DS}}\right)}{\frac{\Delta I_{DS}}{\Delta V_{DS}}} \tag{3.4}$$

$$R_D = 1 - \left(\frac{\frac{\Delta V2}{\Delta V_{DS}} + \left(\frac{\Delta V2 - \Delta V1}{\Delta V_{DS}}\right)}{\frac{\Delta I_{DS}}{\Delta V_{DS}}}\right) \tag{3.5}$$

$$R_{CHANNEL} = \frac{3\left(\frac{\Delta V2 - \Delta V1}{\Delta V_{DS}}\right)}{\frac{\Delta I_{DS}}{\Delta V_{DS}}} \tag{3.6}$$

The resistance of each of the ungated regions and any associated contact resistance were lumped together as a source and a drain resistance. For the unpassivated device in Figure 26, it can be observed that the source and drain resistances increased from 3Ωmm to 30Ωmm as V_{base} was changed whereas the channel resistance was constant at ~400 Ω/□. There was no significant change in the channel resistance, which further confirms the expectation that bulk trapping is insignificant under these experimental conditions. The increase in R_S and R_D is entirely consistent with the virtual gate mechanism and clearly demonstrates that there was trapping of electrons at the gate corners when the gate was held at negative bias.

After silicon nitride passivation, there was no longer any variation in the resistances of the ungated regions for varying V_{BASE}, as shown in Figure 27 This is consistent with the widely reported [90-92] benefits of silicon nitride as a means of controlling current collapse. Since, in this case, surface passivation completely suppressed the gate lag, it seems that trapping in the AlGaN layer was insignificant compared to trapping at the surface.

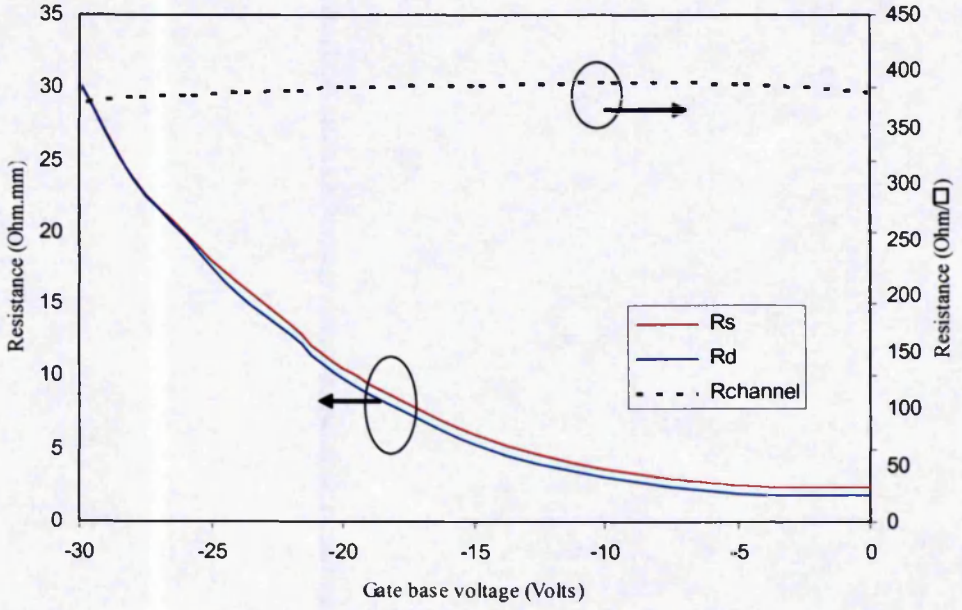

Figure 26: Source, drain and channel resistance variation as a function of gate base-voltage for an unpassivated device. At V_{GS} = 0V.

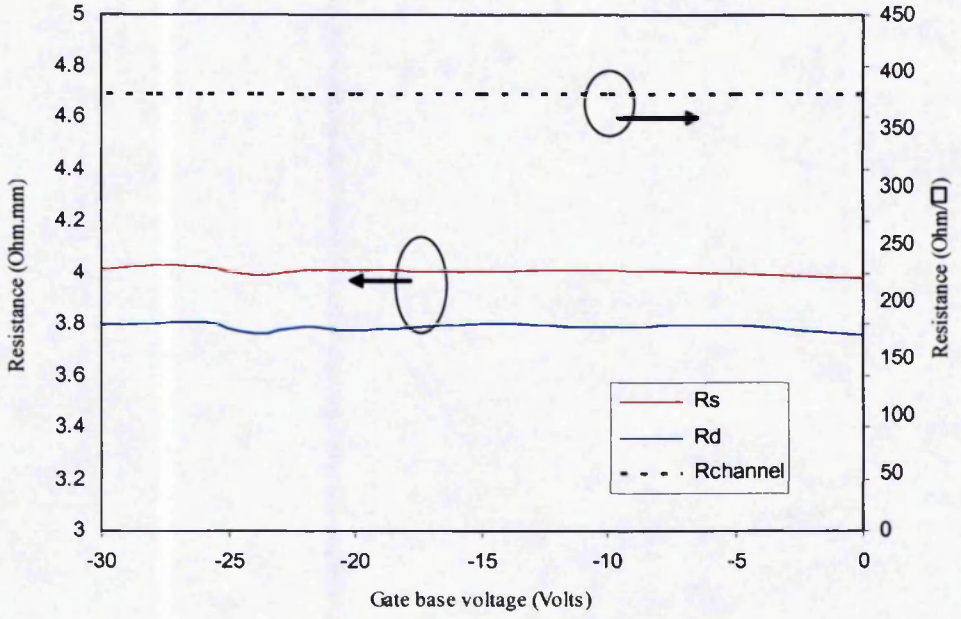

Figure 27: Source, drain and channel resistance variation as a function of gate base voltage for a passivated device. At V_{GS} = 0V.

3.4.2 Gate lag conclusions

Measurements of the potential drop in a large area gate device directly showed that the current collapse seen in GaN/AlGaN HEMTs could be caused by the virtual gate effect. When the gate was stressed with a large negative bias, electrons migrated onto the ungated regions of the device, producing an increased parasitic resistance and a decreased drain current. After Si_3N_4 passivation of the device, transport of electrons onto the surface and subsequent formation of a virtual gate was prevented and consequently the reduction in device transconductance was avoided.

3.5 Conclusions

Current collapse is a surface-related phenomenon. It is caused by mass movement of electrons onto the surface of the device when the gate base voltage is reduced and off the surface when the gate base voltage is increased. Passivation can help or hinder the movement and thereby reduce or increase the current collapse accordingly. The movement of electrons is dependent on the pulse length and the electric field applied. The hall structure measurements indicated that current collapse is not associated with the trapping of electrons in either the GaN or AlGaN layers.

4 ROOM TEMPERATURE MOBILITY

4.1 Introduction

Knowledge of the mechanisms controlling and limiting the formation and the mobility of the 2DEG is crucial in order that the full potential of AlGaN/GaN HEMTs can be realised. Low field 2DEG mobility is a useful figure of merit with which to compare transistors. In particular, low field 2DEG mobility gives a good indication of the quality of the GaN buffer layer and the AlGaN/GaN interface. Mobility is greatly affected by scattering mechanisms, such as interface roughness scattering, dislocation scattering, impurity scattering by remote donors and due to interface charge, acoustic deformation potential scattering, piezoelectric scattering and polar optical phonon scattering. By measuring mobility with respect to carrier concentration, an indication into the variation and types of the scattering mechanisms affecting the 2DEG during device operation can be determined.

The following chapter describes research relating to the fall in room temperature low field 2D electron gas drift mobility at large charge carrier densities ($1x10^{13}$ cm^{-2}). The drift mobility was determined in a novel way from separate measurements of

conductance and electron number density, as explained in subsection 4.3.2. Initially, substrate type was investigated; it was observed that the mobilities of SiC based devices were consistently higher than those of Sapphire based devices. In addition, an overlaying regime was observed in the mobilities regardless of substrate that suggested there was a universal field dependant dominant scattering mechanism at high electron number density.

4.2 Mobility related literature review part 1

4.2.1 Number density dependence

Before the publication of this PhD there was substantial research using mobility as a figure of merit [100-114]. However, the majority of the literature examined mobility with respect to temperature [100-114] both theoretically [100-104] and/or experimentally [105-114]. The vast majority of the mobility based experimental research was performed on Van der Pauw mobility structures [105-111], which are un-gated structures making 2DEG carrier concentration variation impossible. For this reason, there was limited research into the electron number density dependence of 2DEG mobility [110, 112-114]. And even when number density dependence was reported it was more of an afterthought and by-product of temperature dependant measurements.

Although the research was limited, all reported measurements [110, 112-114] indicated a fall in mobility with respect to increasing number density. Through capacitance-voltage (C-V) profiling of Si-doped $Al_{0.15}Ga_{0.85}N$ GaN HEMTs at low temperatures Dang *et al* [112] found that low field mobility decreased with increasing positive gate bias voltage and hence number density. Carrier concentration dependent measurements on $Al_{0.2}Ga_{0.8}N$/GaN HEMTs using gated Hall bar structures with geometry factor of $\gamma = 7$ (ratio of bar length to bar width) published by Gaska *et al* [113, 114] found that mobility first increases with an increase in the sheet carrier density, up to approximately $1x10^{13}$ cm^{-2} and decreases with further increase in carrier density. The highest mobility reported

by Gaska *et al* was 2019 cm^2/Vs at a number density of $1x10^{13}$ cm^{-2}, using a modulation doped $Al_{0.2}Ga_{0.8}N$/GaN HEMT on 6H-SiC, at room temperature. Both Dang *et al* and Gaska *et al* attributed the mobility decrease to the spilling of hot 2DEG electrons into a parallel conducting low mobility channel formed by the AlGaN layer [112] and delocalized states in the device channel [113, 114].

An alternative explanation was suggested Zhang *et al* [110] who through Van der Pauw Hall measurements on numerous wafers with different aluminium concentrations was able to demonstrate a correlation between number density and mobility. Zhang *et al* attributed the fall in mobility to the fact that the "electron gas is squeezed closer to the interface and senses the disorder more".

The only theoretical investigation into room temperature mobility dependence on carrier concentration was published by Ridley *et al* [100], who predicted that the 300K mobility should go through a weak peak of about 2000 cm^2/Vs at a density of about $2x10^{12}$ cm^{-2} dropping to about 1300 cm^2/Vs at 10^{13} cm^{-2}. This prediction was based on the acoustic and polar optical phonon scattering and the transition from 2DEG to bulk mobility as carrier concentration increased.

4.2.2 Substrate dependence

Gaska *et al* [113, 114] also investigated substrate dependence, finding that 4H-SiC based devices had higher mobilities than sapphire based devices but lower than 6H-SiC based devices. This they attributed to a better quality of GaN grown on SiC substrates because of the much smaller lattice mismatch between GaN and SiC, resulting in a smaller dislocation density and/or a less pronounced columnar structure. This is supported by a comparison of transistors grown on AlN/SiC with sapphire based devices by Johnson *et al* [115] which reported that structures grown on AlN/SiC showed significantly less defects.

4.3 Mobility measurement and calculation

4.3.1 Mobility measurement

The 2DEG low field drift mobility was measured using a combination of conductance and capacitance measurements. Most of the conductance-capacitance mobility measurements were performed on the following FatFET devices, shown in Figure 28. The FatFET devices have a nominal 100 x 160μm gate, 160 x 160μm ohmic contacts with a gate to source and gate to drain spacing of 10μm.

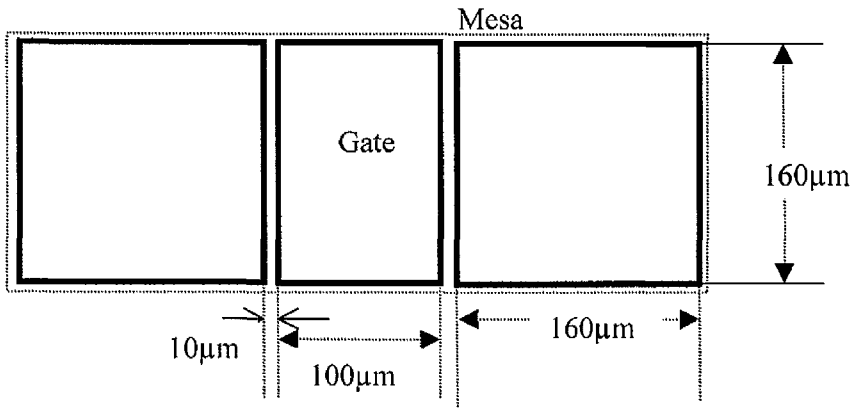

Figure 28: FatFET device dimensions.

The capacitance measurements were performed using a HP4191A and control workstation. The gate capacitance was measured as V_{GS} was swept from 1 to -7, -8 or -9V at 100mV steps using probing frequencies of 1k, 10k, 100k and 1MHz. The current measurements were performed on a HP4145A semi-conductor parameter analyser. The drain current was measured while V_{GS} was swept from 1 to -7 or -8 or -9V at 100mV steps. From the I_{DS} - V_{GS} measurements the channel conductance, σ, was calculated, whilst the CV measurements were used to calculate the 2DEG electron number density N (by integration). A typical I_{DS} - V_{GS} graph for a SiC wafer is shown in Figure 29.

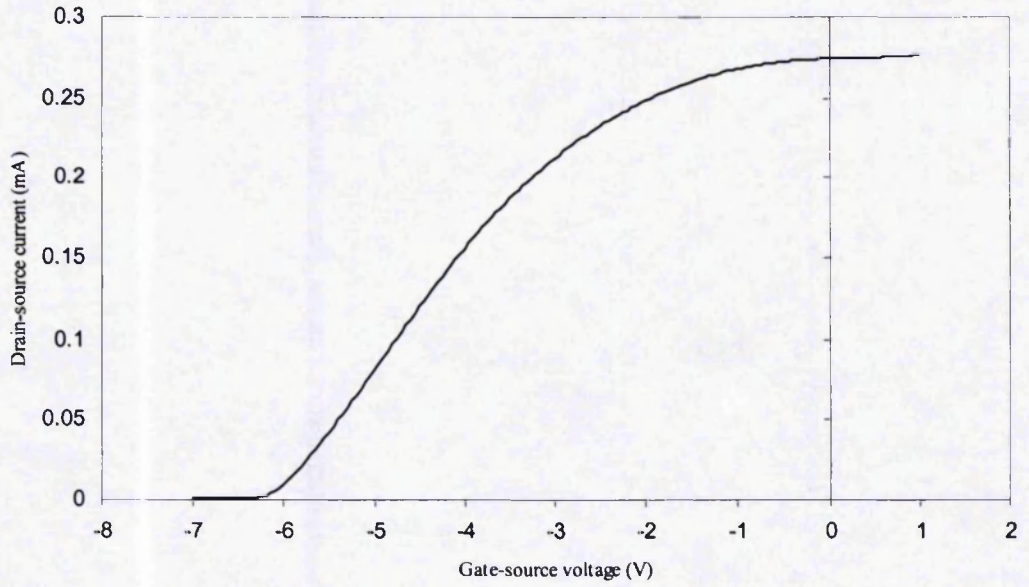

Figure 29: Example of drain-source current of FatFET device against gate-source voltage at a constant drain-source voltage of 100mV.

Any gate leakage indicated at pinch-off by the drain current sweep was corrected. The corrected drain current was calculated using:

$$corrected\ I_D = \frac{(I_D - I_S)}{2} \tag{3.7}$$

Where: I_D is the measured drain current and I_S is the source current. This method of correction assumes that the current is equally distributed between the source and drain contacts. As shown in Figure 30, $\frac{I_D - I_S}{2} = 0$ at pinch off and therefore this assumption is valid. A comparison of the correct drain current and the measured current at pinch-off is shown in Figure 31.

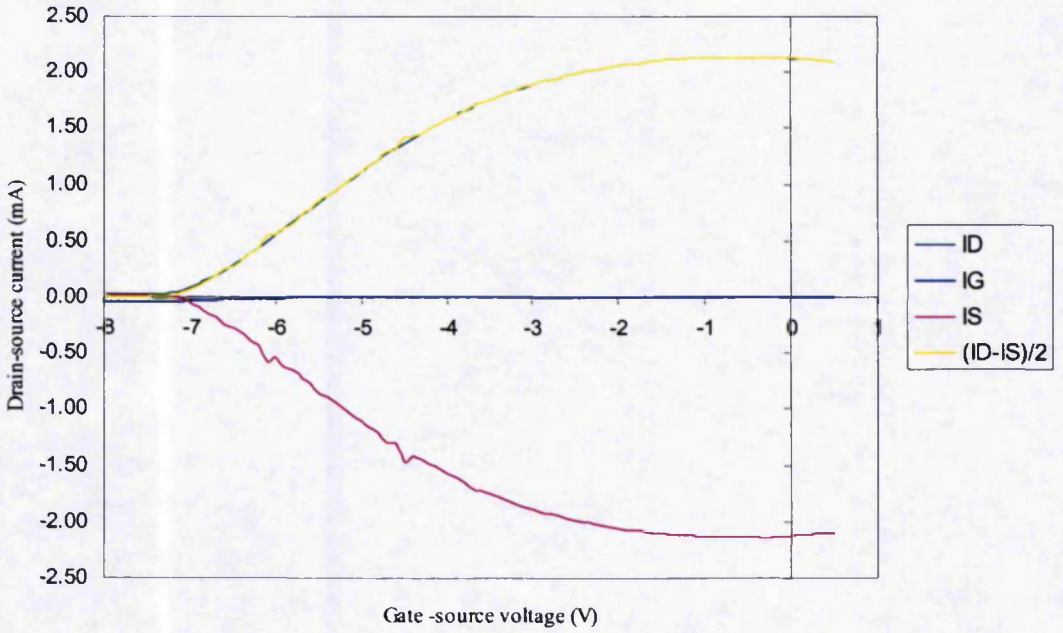

Figure 30: An example of drain current, gate current, source current and corrected drain current against gate -source voltage.

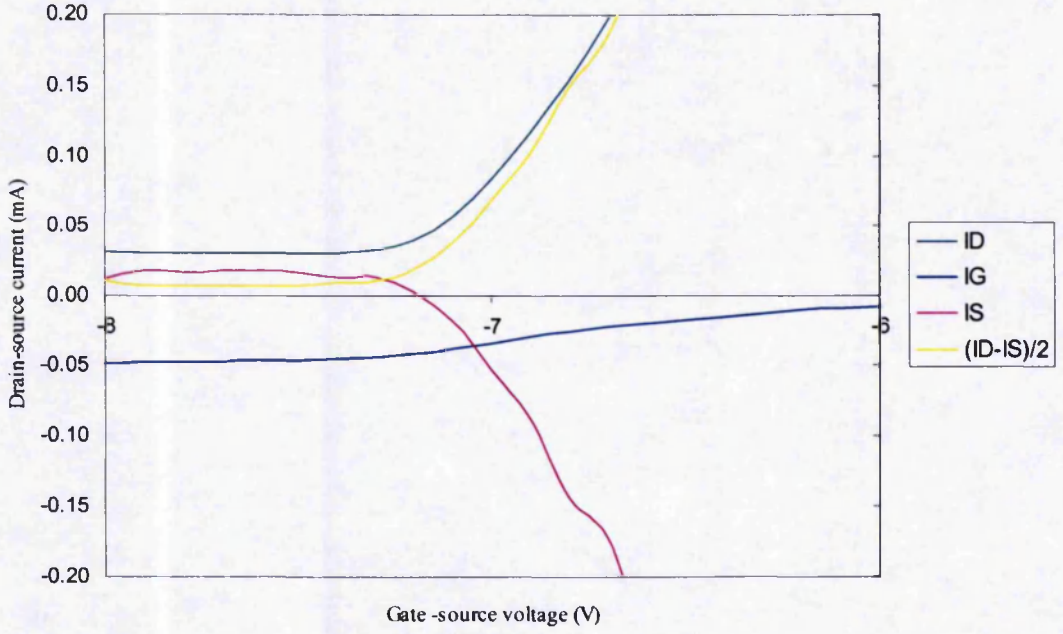

Figure 31: Corrected and measured drain currents at pinch-off.

Given in Figure 32 is a typical C_G against V_{GS} graph. Clearly this measurement technique measures all the charge induced at the AlGaN/GaN interface and includes any charge stored in traps which can respond at the measurement frequency. However, the abrupt turn-off and lack of dispersion seen in Figure 32 indicates that the density of traps active on the measurement timescale is low.

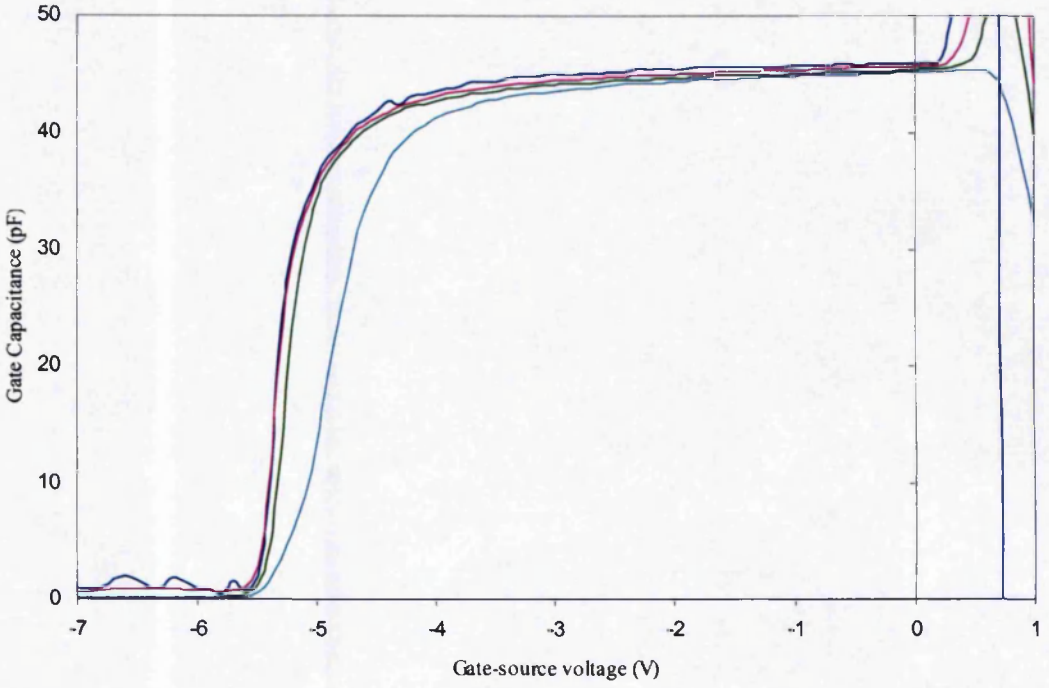

Figure 32: Example of capacitance of FatFET device against gate-source voltage at a constant drain-source voltage of 100mV.

Probing frequencies: 1k (dark blue), 10k (pink), 100k (green) and 1MHz (light blue).

At high probing frequencies the gate capacitance reactance is reduced. Which results in gate capacitance reactance becoming comparable to the drain and source resistances. As shown in Figure 32 by the light blue 1MHz line the fall in gate capacitance reactance enables the device to turn off at a lower gate voltage. Thus the measurement taken using the 1MHz probing frequency doesn't give an accurate indication of the gate capacitance. For this reason the data measured at a probing frequency of 100kHz was used in the

subsequent mobility calculations. The 100kHz data is preferable to the 10kHz data because it is less susceptible to errors that result from parallel leakage.

4.3.2 Mobility calculation

4.3.2.1 Conductance calculation

From the I_{DS} - V_{GS} graph the I_{DS} value at V_{GS} = 0V, referred to as I_{DS0} was read, and used to calculate the sheet resistance using:

$$\rho_{SH} = \frac{V_{DS} W_G}{I_{DS0} L_G} \tag{3.8}$$

where W_G was the gate-width and L_G was the gate-length. The channel resistance was then calculated using ohm's law. Then, using the sheet resistance and the device dimensions, the total resistance of the un-gated regions (or gap resistance) was calculated as follows:

$$R_{GAP} = \frac{\rho_{SH}}{W_G}(L_{GS} + L_{GD}) \tag{3.9}$$

Using an auto-prober, the measured contact resistance R_C, the gap resistance R_G and the channel resistance R_{CH}, the voltage dropped across the gate V_G was calculated using:

$$V_G = \frac{V_{DS}(R_{CH} - (R_C + R_G)}{R_{CH}} \tag{3.10}$$

The conductance under the gate was then calculated using:

$$\sigma = \frac{I_{DS}}{V_G} \tag{3.11}$$

4.3.2.2 2DEG number density calculation

Firstly from the capacitance measurements the total amount of charge under the gate was calculated by integrating the capacitance from open channel to pinch off with respect to the gate-source voltage, using :

$$Q = \int_0^{V_P} C_G dV_{GS} \tag{3.12}$$

The total charge was then divided by the charge of an electron to get the number of electrons, which in turn was divided by the gate area (in cm^2) to get the number density N.

$$N = \frac{Q}{qA} \tag{3.13}$$

Then finally drift mobility was calculated using:

$$\mu = \frac{\sigma}{Nq} \tag{3.14}$$

This method of estimating mobility counts all of the gate-controlled electrons and hence counts any electrons that are in the channel - irrespective of whether they are trapped or free electrons. So there is a possibility that the free electron mobility will be slightly underestimated particularly near pinch-off. It should be noted that this method also relies on stable pinch-off voltage between the capacitance and conductance measurements. If the current measurements pinch-off first the mobility will tend to zero.

If the capacitance measurements pinch-off first the mobility will tend to infinity. For these reasons the accuracy of the mobility estimation is best above a number density of about $1x10^{12}$ cm^{-2}.

4.4 Comparison of Sapphire and SiC drift mobility

4.4.1 Experimental

For a comparison of sapphire-based devices against SiC-based devices the room temperature drift mobility of two sapphire and five SiC wafers were measured. The details of which are given in Table 5 below. All layers were Q1 structures, that being 30nm of undoped AlGaN (23%) on 1.2μm on GaN, on an appropriate nucleation layer for growth on insulating on-axis 4H-SiC or sapphire. All the wafers were grown and fabricated in the fashion explained earlier, in section 2.2.4. The Ti/Al/Ti/Au ohmic contacts, measured by an auto-prober were found to have an average contact resistance of ~ 1Ωmm (4×10^{-5} Ω cm^{-2}). X-ray measurements performed by other members of the QinetiQ group indicated that the AlGaN layers on SiC were pseudomorphic with the GaN, but up to 25% relaxation was seen in some layers on sapphire.

Table 5: Wafer and device numbers used in room temperature mobility measurements.

Wafer Number	Device Number	Substrate Type
1035SCO3	S 1011	Silicon Carbide
1093SCO3	S 0611	Silicon Carbide
1088SCO3	S 0625	Silicon Carbide
1135SCO5A	S 1021	Silicon Carbide
1137SCO6A	S 1029	Silicon Carbide
1028AN28C	S 0717	Sapphire
1117AN47A	S 1031	Sapphire

Three or more FatFET type S devices were chosen and measured (as described in 4.3) on each wafer. A representative (device indicated in Table 5) of each wafer is shown below in Figure 34 against electron number density and in Figure 35 against gate-source voltage. As can be observed from Figure 33 the devices were consistent across the wafer. The variation in the electron mobility between devices was found to be approximately 100cm^2/Vs.

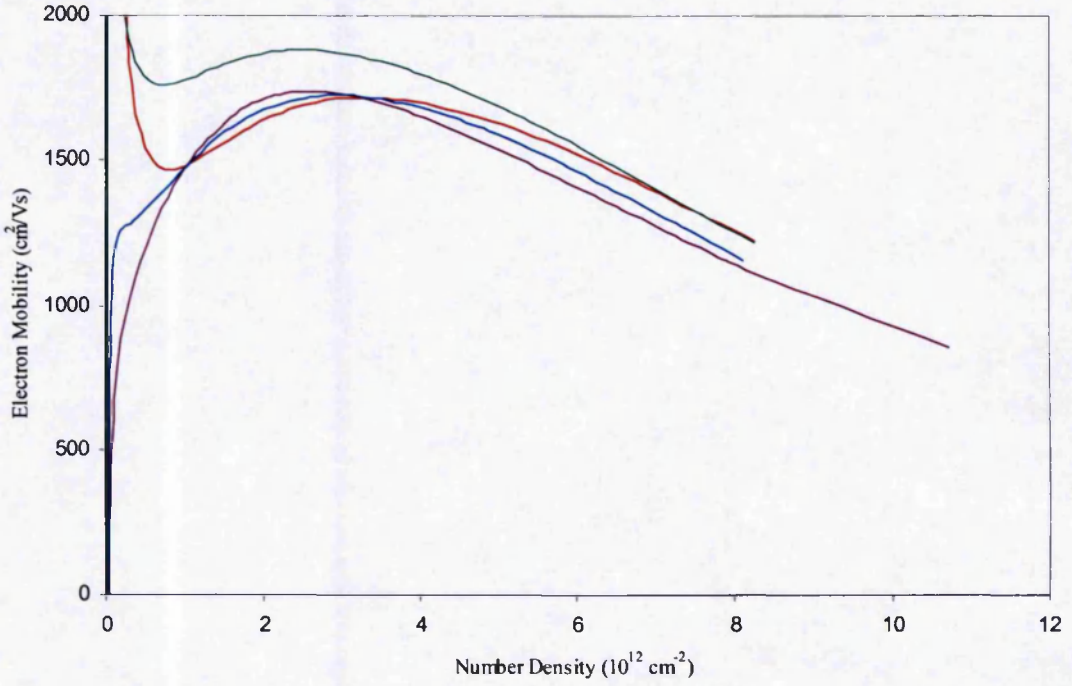

Figure 33: Electron mobility against number density for devices S 1023 (red), S 1022 (green), S 0921 (purple) and S 1021 (blue) from wafer 1135SCO5A

4.4.2 Results

The pinch –off voltage was found to vary from -6.5 to -4V. The capacitance- voltage (C-V) measurements showed that the layers were fully pinched-off and that there was no parallel leakage path through the insulating GaN substrate, and that the layers were of high quality [116]. As expected, for all the wafers the mobility rose to a peak before

falling smoothly against number density. These results were in keeping with numerous theoretical and experimental measurements [112-114] that report a rise and fall in mobility with respect to number density. The highest peak mobility at low electron number density was found to be as high as ~2000 cm^2/Vs, but in open channel (high carrier concentration, zero gate voltage) it fell to nearer 1400 cm^2/Vs.

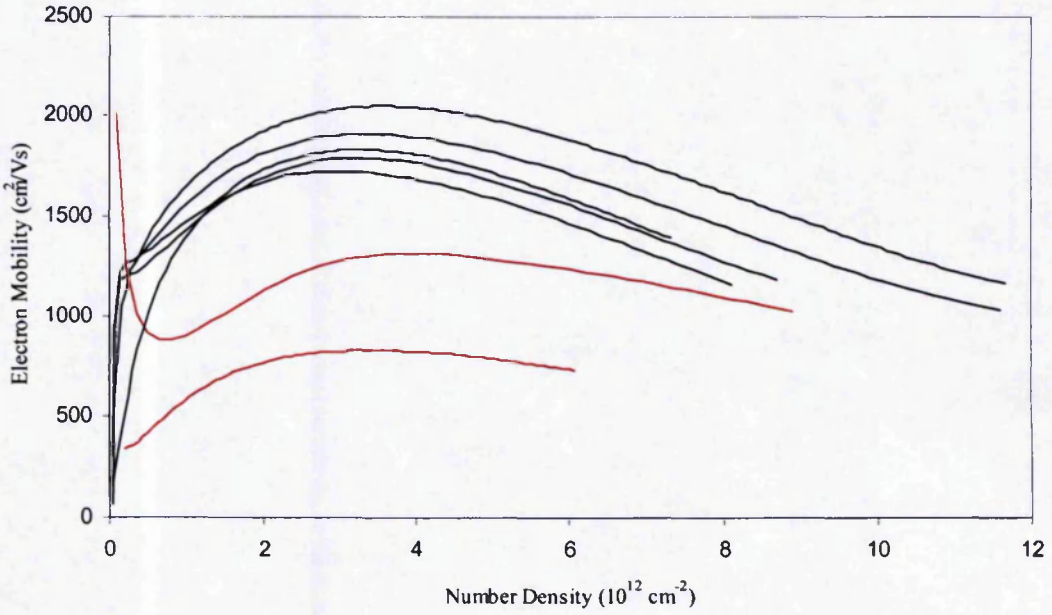

Figure 34: Mobility against electron number density for device with SiC (black) and Sapphire (red) substrates.

It can be observed from Figure 34 that all SiC wafers showed significantly higher peak mobilities (1500-2000 cm^2/Vs) than the Sapphire wafers (750-1300 cm^2/Vs). This is consistent with Gaska *et al* [113, 114] and is ascribed to poorer AlGaN/GaN interfaces in the sapphire devices. Sapphire has a significantly larger lattice mismatch with GaN (14.8%) than there is between SiC and GaN (3.3%). Consequently growth on sapphire is more difficult and usually that results in dislocation density being typically a factor of 5-10 times higher than those on SiC substrates.

Although all the mobility curves showed a similar smooth peak they did not overlay in any regime. Interestingly however, when plotted against gate voltage, as shown in Figure 35, all the curves (except the poorest sapphire wafer) tended to a common curve at gate voltages around zero, despite large variations in number density of 6 x 10^{12} to 1 x10^{13}cm^{-2}. This suggests that a common scattering mechanism dominates the mobilities at low negative gate voltages / high sheet carrier density in open channel conditions.

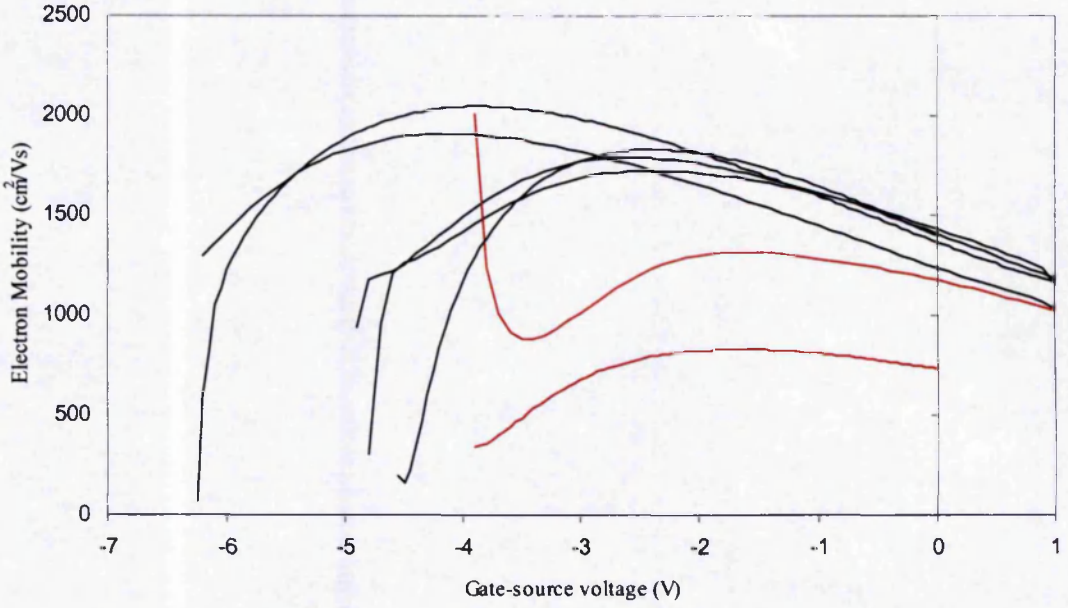

Figure 35: Mobility of SiC (black) and Sapphire (red) based devices against gate-source voltage. They follow a common curve in open channel conditions, due to a common dominant scattering mechanism.

4.4.3 Discussion

As a result of the fact that all the wafers are identical in terms of AlGaN layer aluminium concentrations, thicknesses and strain (no relaxation on SiC substrates and only slightly on sapphire substrates) it is reasonable to assume that they all have the same spontaneous and piezoelectrically induced charge. Hence, the observed variations

in pinch-off voltage are mostly to be associated with variations in charge stored in deep levels in the GaN layer. The deep levels may be due to point defects or dislocations but, unfortunately, they must exist to ensure that the GaN layer is insulating, preventing parallel leakage. The experimentally observed pinch-off variation was ~ 2.5V, corresponding to a variation of ~ 4 x $10^{12}cm^{-2}$ in 2DEG concentration. Previous wafers, of a similar quality, had been measured at QinetiQ [117] and found to have deep level acceptor density of around $10^{17}cm^{-3}$, which is consistent with roughly $10^{12}cm^{-2}$ of charge in the depletion layer for the best layers.

At the time, the rise in mobility at low carrier concentration was ascribed to screening of ionised impurities by the surface [110] and/or phonon scattering dominated at high electron carrier concentration. Polar optical and acoustic phonon scattering were concluded to be the dominant scattering mechanisms at room temperature.

Due to the remarkable similarities between the results and the theoretical predictions by Ridley *et al* [100] the fall in mobility with respect to increasing number density was ascribed to phonon scattering; since then that conclusion has been found to be incorrect, as shown later, in chapter 5.

Following the publication of this research [118] the measurement technique was adopted by Marso *et al* [119]. From their comparison of doped and undoped AlGaN/GaN HEMTs with respect to number density they found that doping increased carrier concentration from $6.8x10^{12}$ to $1x10^{13}cm^{-2}$, but at the same time reduced the mobility from 1800 to 1620 cm^2/Vs.

4.5 Mobility related literature review part 2

4.5.1 Introduction of low temperature Aluminum Nitride layers

Low temperature AlN (LT-AlN) layers where first introduced into GaN based devices in

1986 by Amano *et al* [120] as an effective nucleation layer for sapphire substrates. A number of years later, in 1999, Amano *et al* [121] rekindled the idea so that thick, crack-free, high-aluminium AlGaN layers could be grown for UV light emitting diodes (LEDs), UV photo-detectors and other optoelectronic applications. Amano *et al* [121, 122] reported Scanning Electron Micrograph (SEM), X-Ray Diffraction (XRD) and Transmission Electron Microscopy (TEM) evidence that the crystalline quality of $Al_{0.45}Ga_{0.55}N$ films grown on LT-AlN layers was substantially better than that grown on either LT-GaN or high temperature GaN (HT-GaN), by reducing the biaxial tensile stress within the GaN.

Numerous groups [104, 105, 123-129] now use LT-AlN interlayers because they prevent the GaN layer from cracking and reduce the dislocation threading density. In fact Bourgrioua *et al* [123] states that by just adding two LT AlN interlayers the dislocation threading density can be reduced by a factor of 10. Germain *et al* [124] in 2004 used low temperature (LT) grown AlN interlayers within the GaN buffer layer to greatly reduce the sheet resistance and to lower the dislocation threading density, resulting in a better quality AlGaN/GaN interface resulting in a mobility value of 2050 cm^2/Vs on sapphire.

The UCSB group [104, 105] introduced a novel device with a 1nm AlN interlayer between the GaN and AlGaN layers, shown in Figure 36. The AlN interlayer improved the low temperature 2DEG mobility in comparison with standard AlGaN/GaN HEMTs. The improvement was attributed to a reduction in alloy scattering, since mobility was found to increase with decreasing alloy composition x, as shown in Figure 37. The effect of the AlN interlayer on mobility with respect to number density was not reported. The effect of an AlN interlayer was researched as part of this PhD study by comparing structures with and without the AlN interlayer, firstly at room temperature (shown in subsection 4.6), and then later against temperature (shown in chapter 5).

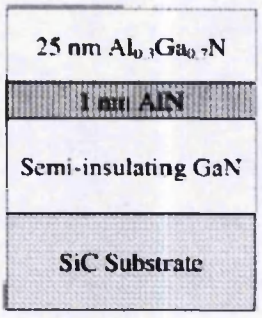

Figure 36: Schematic cross-section of an AlGaN/AlN/GaN HEMT [105].

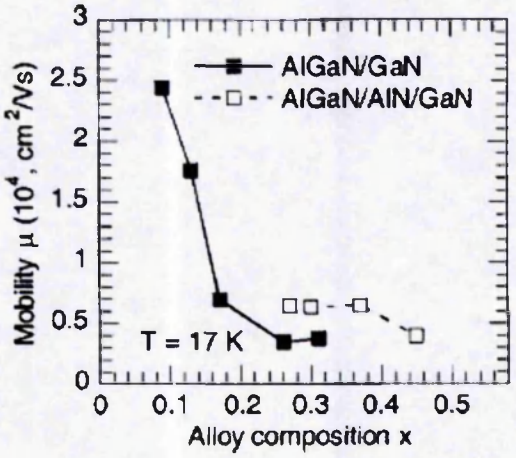

Figure 37: Low temperature mobility in $Al_xGa_{1-x}N$ /GaN (dark squares) and $Al_xGa_{1-x}N$ /AlN/GaN (open squares) 2DEG structures as a function of alloy composition x. [104]

4.6 Effect of AlN layer

4.6.1 Experimental

A promise of progress in reducing electron scattering mechanism came from a novel AlGaN/AlN/GaN HEMT proposed by Shen *et al* from UCSB [105]. They hypothesised that the inserted AlN layer reduced Alloy scattering – but gave no evidence to support their hypothesis.

In order to properly evaluate the benefits of the AlN layer, a second device standard was produced. The QinetiQ 2 (Q2) device structure consists of the appropriate nucleation layer for the sapphire or SiC substrate, followed by a 12,000Å GaN layer, next a 1nm AlN exclusion layer, followed by a 29nm of $Al_xGa_{1-x}N$ ($x = 0.25$). The optimum growth time of the AlN layer was found to be 20 seconds, giving a Lehighton sheet resistivity [116] of 430Ω/sq. on sapphire and 280Ω/sq. on SI-SiC [130, 131]. The in-process carrier densities of the wafers were estimated from mercury probe CV measurements [116], and were found to be relatively insensitive to the AlN layer at about 1.0×10^{13} cm^{-2} (± 10% experimental error), and thus the large difference in sheet resistivity was attributed to improvement in channel mobility for the SiC structures.

A series of Q1 and Q2 structures on SiC and sapphire substrates (details shown in Table 6) were then grown at QinetiQ by low pressure MOVPE using a Thomas Swan Close-Coupled showerhead reactor and in-situ optical monitoring [23] while the devices were fabricated with Ti/Al/Ti/Au ohmic source and drain contacts and Ni/Au Schottky gate contacts using the conventional process described in chapter 2.

Table 6: Wafer and device numbers used in the Q1/Q2 comparison measurements.

Wafer Number	Device Number	Substrate Type	AlN Layer
1230SC13B	S 1231	Silicon Carbide	With AlN layer
1229SC11A	F2 1210	Silicon Carbide	Without AlN layer
1218AN68C	S 1113	Sapphire	With AlN layer
1117AN7A	S 1031	Sapphire	Without AlN layer

Several FatFET devices (as shown in Figure 28) from each wafer were measured on-wafer at room temperature (as described in 4.3.1) and the capacitance and conductance results were then used to determine the variation of drift mobility (as described in 4.3.2) as a function of sheet carrier density.

4.6.2 Results

The room temperature CV and drift mobilities of the various wafers are shown in Figure 38 and Figure 39, respectively. Although 3 devices were measured on each of the 4 wafers only one device (measured as 100 kHz probing frequency) is plotted to represent each wafer. It can be observed from Figure 38 and from Table 7 that the pinch-off voltages of Q2 devices are 0.5 to 1.0V higher than the Q1 equivalent devices. In addition, in Q1 samples (without AlN layer) a significant increase in capacitance can be observed at low gate bias, which shall be referred to as the 'turn up effect'.

Table 7: Pinch-off voltages for various wafer types.

Device Structure	Substrate	Pinch-off voltage V
Q1	Sapphire	4.9
Q2	Sapphire	5.6
Q1	SiC	6.1
Q2	SiC	7.1

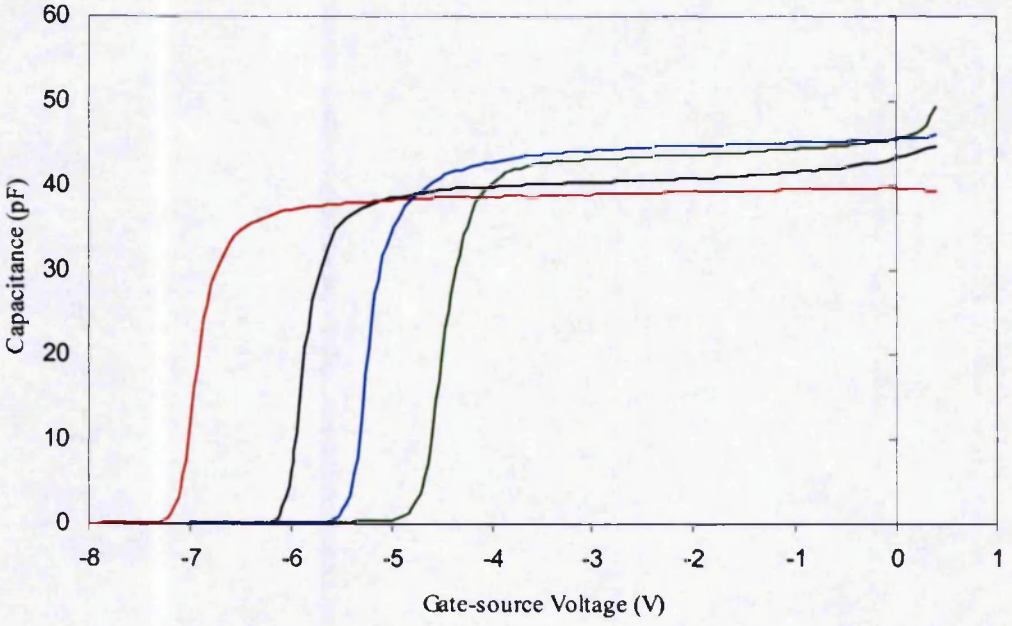

Figure 38: Capacitance-Voltage profiles of Q2-SiC (red), Q2-Sapphire (blue), Q1-SiC (black) and Q1-sapphire (green).

It can be observed from Figure 39 below, that at low carrier concentrations, towards device pinch-off, both structures were comparable with a drift mobility of about 2300 cm^2/Vs. However, at large concentrations they were no longer comparable. At large carrier concentrations the Q1 devices (without the AlN exclusion layer) fell rapidly with increasing number density, but the Q2 devices (with the AlN exclusion layer) maintained high mobility at high number densities. At open channel the drift mobility for devices from two representative samples grown on SiC with and without the AlN exclusion layer were 2177 and 1308 cm^2/Vs, respectively. For sapphire with and without the AlN exclusion layer, these values were 1677 and 1174 cm^2/Vs, respectively. In addition, SiC based devices are again shown to have higher mobilities than the equivalent sapphire based devices. Although there are not shown on the graph, several other wafers were measured to test reproducibility. All the wafers were found to follow the same trend i.e. the order of highest mobility at zero bias was Q2-SiC, Q2-sapphire, Q1-SiC and finally Q1-sapphire, as shown below in Figure 39.

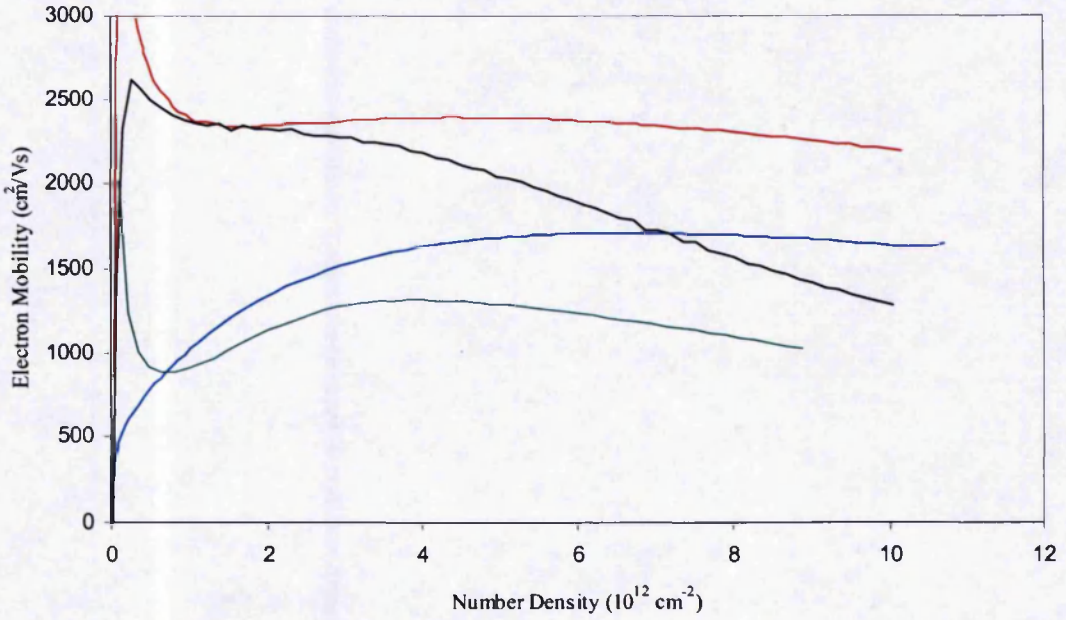

Figure 39: Drift mobility against number density for Q2-SiC (red), Q2-Sapphire (blue), Q1-SiC (black) and Q1-sapphire (green).

4.6.3 Discussion

The increase in pinch-off voltage of Q2 devices compared with the equivalent Q1 device can be attributed to two phenomena. Firstly, AlN produces more spontaneous polarisation than GaN and hence AlGaN. Secondly, the AlN interlayer reduces the electric field in the AlGaN layer for a given voltage. This is supported by reports in the literature of high aluminium content AlGaN layer devices [35, 103, 132] producing larger 2DEG concentrations. Shown in Figure 40 are results for an AlN/GaN device and an example of a maximum aluminium percentage AlGaN/GaN device. The results clearly show that carrier concentration increases with increasing Aluminium concentration.

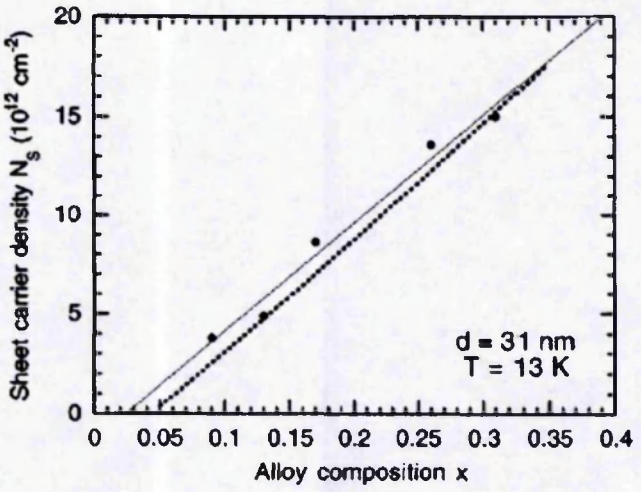

Figure 40: 2DEG sheet carrier density in the $Al_xGA_{1-x}N$/GaN structures as a function of AlGaN barrier composition x.

The thin solid line represents a least-squares linear fit to the experimental data. The dotted line corresponds to the theoretically calculated 2DEG density, assuming a constant surface barrier height of 1.42 V [103].

The insertion of the AlN interlayer between the AlGaN and GaN layers has two main effects on the device 2DEG, as shown in the following group of energy band diagrams where the 1st subband (red) occupancy of 8.44 x 10^{12} cm^{-2} and the 2nd subband (green) has an occupancy of 0.49 x 10^{12} cm^{-2} [5].

Firstly, as shown by the comparison of Figure 41 with Figure 42, the AlN layer dramatically increases the conduction band far above (1.2eV) the Fermi level creating a higher barrier to electron movement from the 2DEG to the AlGaN layer. Secondly, as a result of the increase in the energy gap between the conduction band and the Fermi level there is reduction in 2DEG waveform penetration into the AlGaN. As shown by the comparison of Figure 43 with Figure 44 the AlN layer reduces the penetration of the 2DEG waveform into the barrier from about 9.5nm (~13% of the wave function) to about 2.5nm (~3% of the wave function).

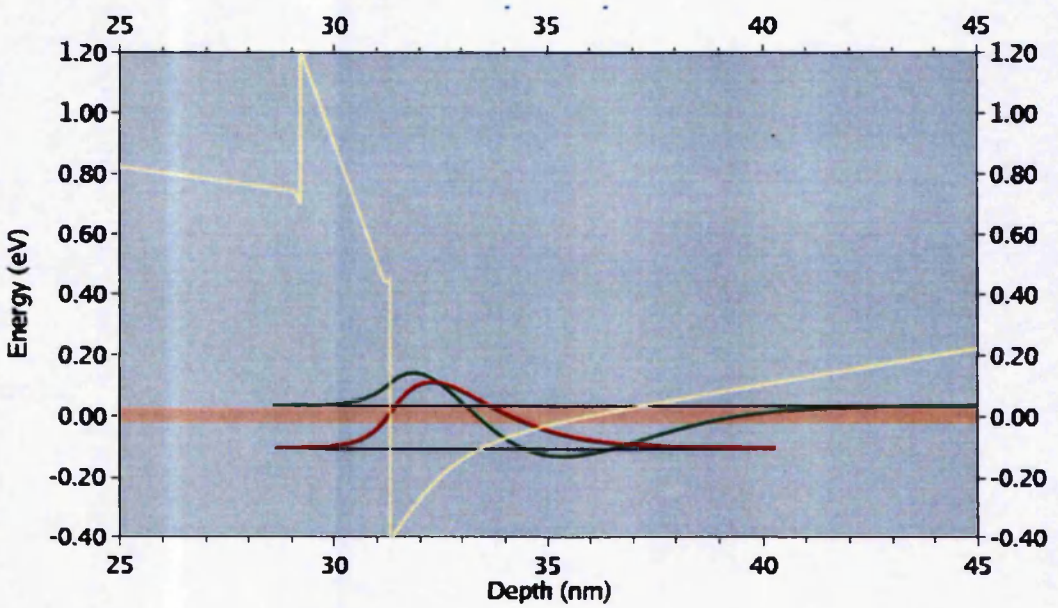

Figure 41: AlGaN/AlN/GAN interface energy band diagram. 1st subband (red), 2nd subband (green) [5].

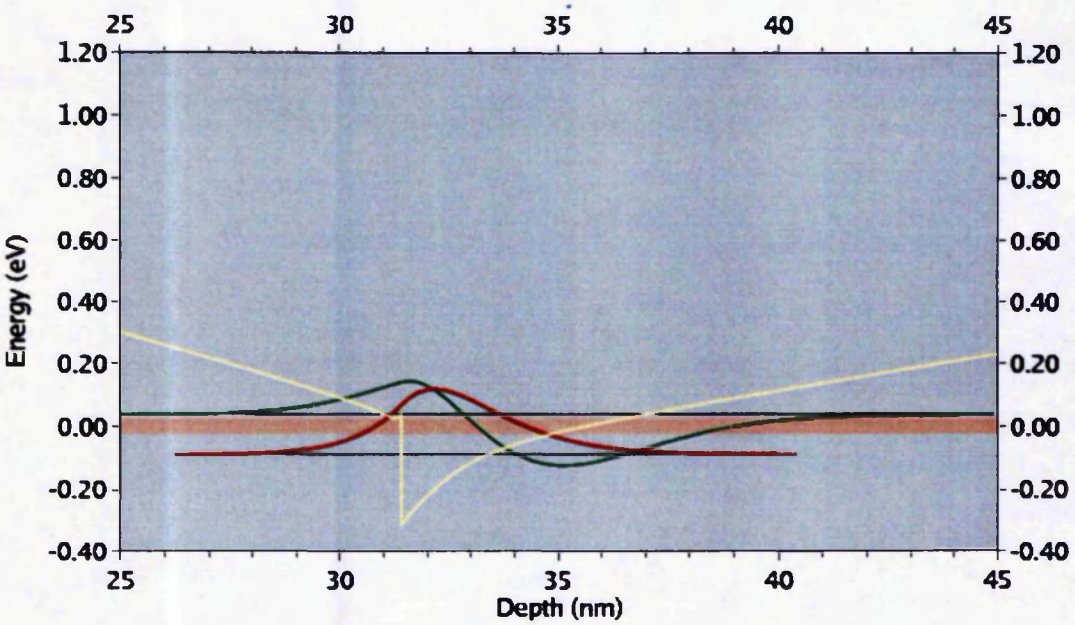

Figure 42: AlGaN/GaN interface energy band diagram. 1st subband (red), 2nd subband (green) [5].

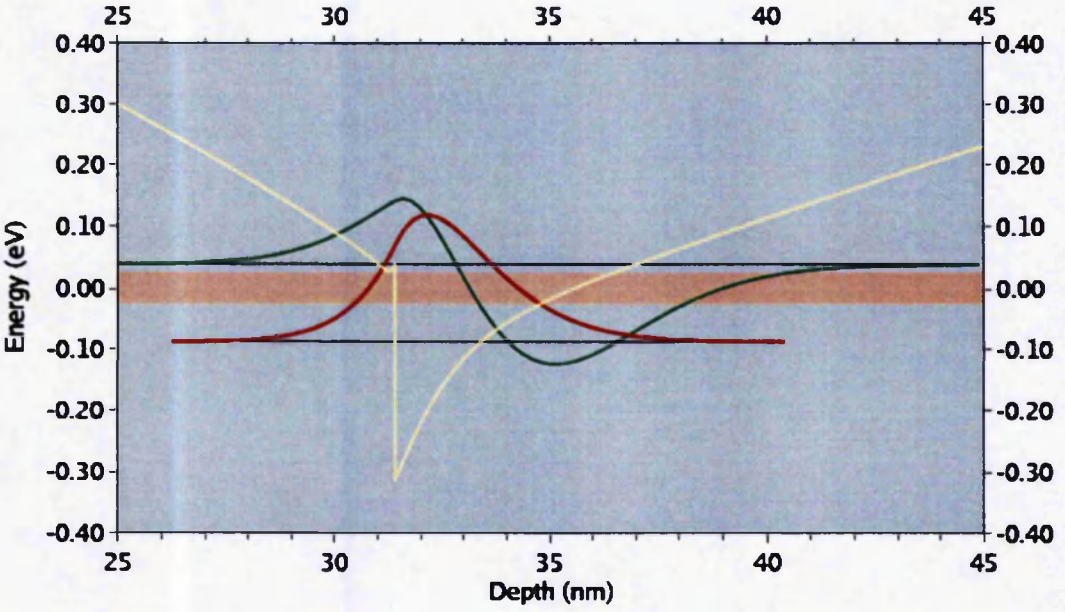

Figure 43: Waveform penetration at AlGaN/GaN interface. 1st subband (red), 2nd subband (green) [5].

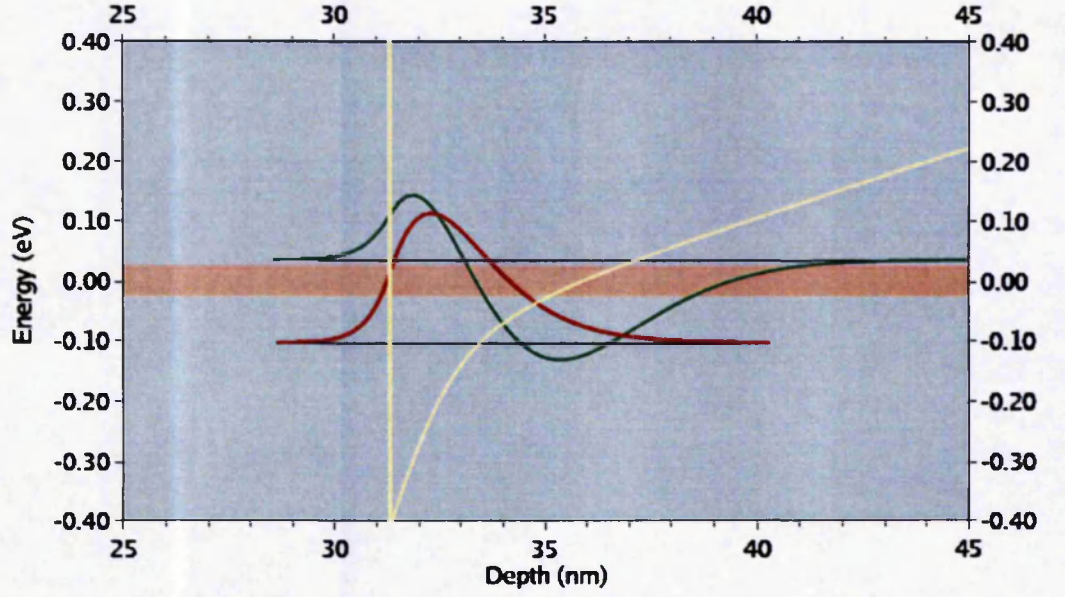

Figure 44: Waveform penetration at AlN/GaN interface. 1st subband (red), 2nd subband (green) [5].

The 'turn up effect' was found to be too large to be solely attributable to either

waveform overlap into the AlGaN conduction band or to tunnelling into the AlGaN bandgap. However, the 'turn up effect' could be reproduced in simulations, by adding deep level donors in the AlGaN barrier [5]. The 'turn up effect' is therefore attributed to donor states in the AlGaN being populated as a result of the minimal energy difference between the AlGaN conduction band and the Fermi level at low gate bias. Since the introduction of the AlN layer removes the 'turn up effect' the maximum depth of the donors is limited to ~0.8eV below the AlGaN conduction band, as shown in Figure 41.

4.7 Conclusions

Both experiments have given evidence that SiC devices have higher mobilities than sapphire based devices. This is attributed to SiC being a better thermal conductor reducing the self-heating within the device and thus reducing the phonon scattering of the 2DEG at AlGaN/GAN interface. Thus experimental data confirms the theoretical predictions [100] that maximum room temperature mobility is limited by polar optical phonon scattering.

It has been found that the fall in mobility at high number density can be prevented by inserting an AlN interlayer. The AlN layer dramatically increases the conduction offset and offers a substantial barrier to electron movement into the AlGaN. In addition the binary structure of the AlN reduces scattering at the interface. The 2DEG wavefunction penetration into the barrier is significantly less in the Q2 structure. The dominant scattering mechanism at large carrier concentration is most likely due to alloy scattering, not phonon scattering as previously suggested.

The 'turn up effect' observed in the Q1 structure was attributed to the populating of one or more defect donor levels with in the AlGaN layer at low gate biases. The introduction of an AlN layer in the Q2 structure prevented the defect donor levels being occupied and thereby prevented the 'turn up effect' That implies that the defect donor levels have a maximum depth of ~0.8eV below the AlGaN conduction band.

5 TEMPERATURE DEPENDENT MOBILITY

5.1 Introduction

The following chapter describes a comparative study of a Q1 (without-AlN layer) wafer and a Q2 (with-AlN layer) wafer with regard to the temperature dependency of both structures. The relationship was investigated in order to determine the scattering mechanism that is reduced by the AlN layer, as observed in the previous chapter. By measuring the two structures against temperature, the temperature dependent and independent scattering terms could be extracted. From the extracted temperature dependence two models were generated. From the first model a better understanding of the Q2 structure was gained. However, a second more accurate model was required so that high temperature mobility predictions could be made. In addition, the effect of temperature on the barrier height, the capacitance and the ideality factor of the Schottky contact was examined. The details of the wafers and devices used in the experiments are given in Table 8.

Table 8: Temperature dependent mobility measurement - device details

Wafer	Q1/Q2	Device	Dye
1093SCO3A	Q1	FatFET	0923
1093SCO3A	Q1	TLM pattern	1223
1230SC13A	Q2	FatFET	1905
1230SC13A	Q2	TLM pattern	1707
1318SC13B	Q2	FatFET	0419

5.2 Temperature dependent mobility measurements

5.2.1 Experimental

As in measurements in the previous chapter, the low field mobility was calculated from a combination of capacitance and conductance measurements performed on 100 x 160μm FatFET devices. The devices were measured (using the Kelvin measurement technique – explained in 5.2.1.1) at 50K intervals between 300 and 100K and then at 80, 60 40 and 24K. The low temperatures were reached using a close cycle helium cryostat. The capacitance and conductance were measured using a HP4191A via a control workstation and a HP4145B, respectively. Due to practical probing difficulties, the devices where diced and glued onto chip carriers. The device bondpads were then fine-wire bonded, at QinetiQ, to the carrier bondpads. A picture of a carrier with three devices bonded to it is shown in Figure 45. Initially, numerous fine wire bonds were broken accidentally, because of the practical difficulties of manoeuvring the relatively large cryostat probes, causing time delays and additional cost because they could only be re-bonded at QinetiQ. Therefore, in later experiments only one device was bonded to each carrier. The carrier bondpads were then bonded together (using more robust bonds) to enable the drain, source and gate to be probed from several different bondpads. Hence, the cryostat probes could then be placed a safe distance away from the fine bonds attached to the device, and yet still probe the device through the inter-carrier

bondpad bonds which bridged the distance.

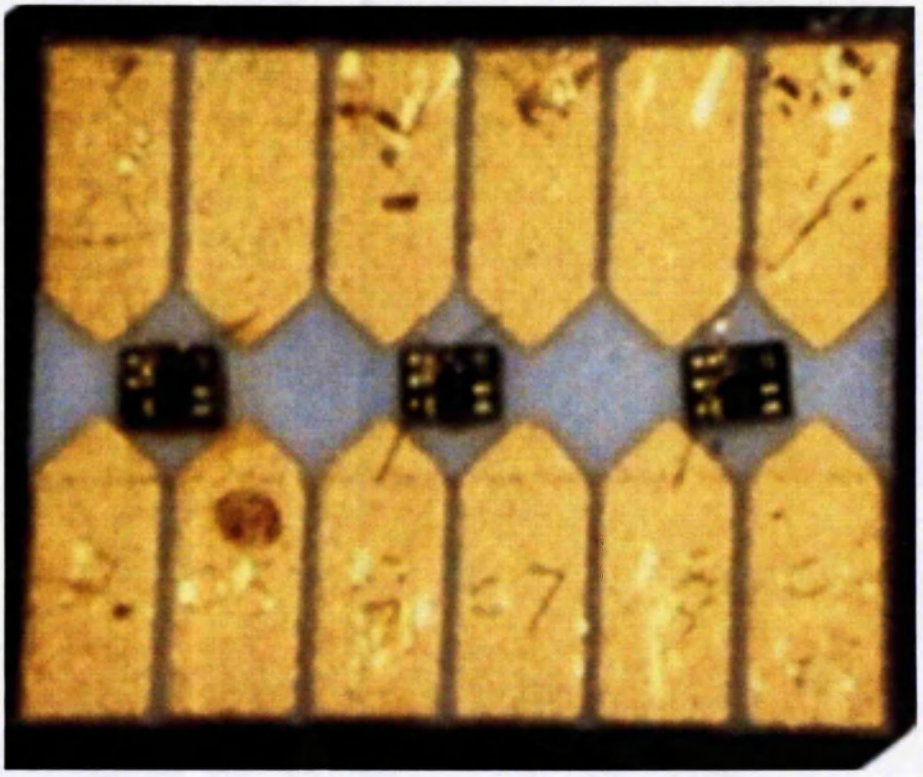

Figure 45: Fine-wire bonding of devices onto a carrier

In order to calculate the mobility accurately, knowledge of contact resistance and sheet resistivity variation with respect to temperature was required. Therefore transmission line measurements were performed at each temperature, from which contact resistance and sheet resistivity were extracted.

5.2.1.1 TLM measurements

The Transmission Line Measurements were performed over the temperature range of 20K to 300k using a close circuit helium cryostat. Four-terminal Kelvin measurements (see Figure 46) were used so the resistance of wires to the bottom of the cryostat could be calculated and later subtracted from the experimental data. The TLM pattern

contained five 100x160μm ohmic (Al/Au/Ti/Au) pads. The four gaps had nominal values of 5, 10, 15, and 20μm. However, the actual gap sizes used in the final calculations were measured using a graduated microscope.

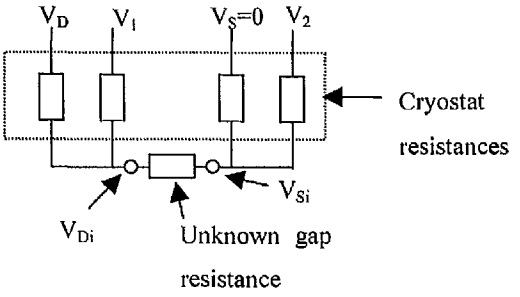

Figure 46: Diagram of TLM Kelvin measurements

The resistance of the wires within the cryostat were large in comparison with the device resistances and varied with temperature. Therefore, in order to accurately measure the device resistances, the effect to the cryostat wires had to be accounted for. This was achieved by using the Kelvin measurement technique, where by the unknown resistance, (be it gap resistance in the case of the TLMs or channel resistance in the case of mobility measurements), was measured by sourcing zero current to terminals V_1 and V_2, whilst applying V_D and V_S to their respective terminals. Since, zero current was sourced to terminal V_1 the voltage measured at V_1 was equal to V_{Di}, the same was true for V_2 and V_{Si}. Therefore, the unknown resistance could be calculated using

$$R_{UNKNOWN} = \frac{V_{Di} - V_{Si}}{I_D} = \frac{V_1 - V_2}{I_D} \tag{5.1}$$

The TLM measurements were performed on the same wafers, on structures as close as possible to the FatFET devices used in the mobility measurements. The exact device details are given in Table 8. The best Q1 and Q2 experimental data was used to plot graphs of gap resistance against gap length (shown in Figure 47 and Figure 48) from

which several parameters were extracted.

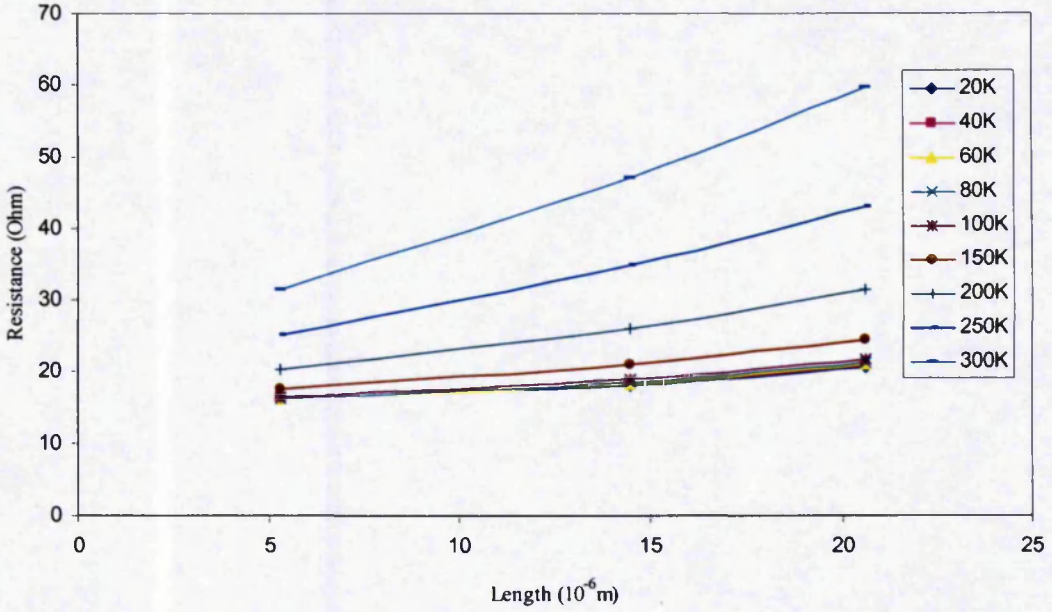

Figure 47: Resistance against length for the Q2 structure (with AlN) wafer 1230SC13A

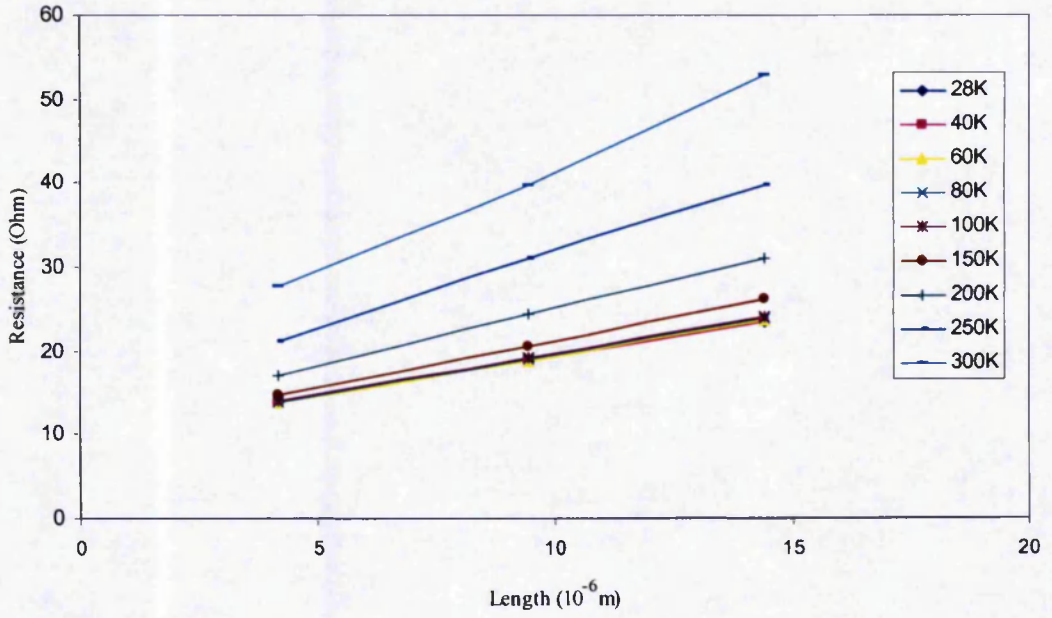

Figure 48: Resistance against length for the Q1 structure (without AlN) wafer 1093SCO3A

The contact resistance for each wafer, R_C [Ω.mm] was calculated from intercept with the y-axis (L_Y) and gap width (W_G) using:

$$R_C = W_{GAP}\frac{L_Y}{2} \tag{5.2}$$

The sheet resistance, R_{SH} [Ω/□] for each wafer was calculated from the gradient using:

$$R_{SH} = \frac{dR_{GAP}}{dL_{GAP}}W_{GAP} \tag{5.3}$$

The transfer length (L_T) for each wafer was calculated from the extrapolated intercept with the x-axis (L_X) using:

$$L_X = 2L_T \tag{5.4}$$

The contact and sheet resistance of both the Q1 and Q2 structure were found to be directly proportional with respect to temperature, whilst the transfer lengths of both the Q1 and Q2 structure were found to be inversely proportional with respect to temperature.

The transfer length (L_T) and gap width (W_G) was then used to calculate the specific contact resistance for each wafer, R_{SP} [Ω.cm^2] using:

$$R_{SP} = R_C W_{GAP} L_T \tag{5.5}$$

In addition, approximate sheet resistance from (5.6) were calculated.

$$R_{SH} \approx \frac{V_{DS}}{I_{DS}} \tag{5.6}$$

All the Q1 and Q2 TLM results (2d.p.) are tabulated below.

Table 9: TLM results for the Q1 device

Temperature (K)	Contact resistance (Ω.mm)	Transfer length (μm)	Specific Contact resistance ($\Omega.cm^2$)	Experimental Sheet resistance (Ω/□)	Theoretical Sheet resistance (Ω/□)
28	0.77	5	$3.88x10^{-5}$	152.36	140.10
40	0.77	5	$3.88x10^{-5}$	152.64	140.10
60	0.77	5	$3.85x10^{-5}$	155.23	141.16
80	0.77	5	$3.89x10^{-5}$	156.56	141.35
100	0.78	5	$3.93x10^{-5}$	157.92	146.06
150	0.81	4.5	$3.65x10^{-5}$	176.01	163.90
200	0.91	4.1	$3.75x10^{-5}$	217.42	212.90
250	1.09	3.75	$4.09x10^{-5}$	289.08	283.47
300	1.37	3.5	$4.81x10^{-5}$	391.45	400.00

Table 10: TLM results for the Q2 device

Temperature (K)	Contact resistance (Ω.mm)	Transfer length (μm)	Specific Contact resistance ($\Omega.cm^2$)	Experimental Sheet resistance (Ω/□)	Theoretical Sheet resistance (Ω/□)
20	1.14	25	$2.87x10^{-4}$	45.91	62.59
40	1.14	25	$2.87x10^{-4}$	46.87	62.59
60	1.14	25	$2.86x10^{-4}$	48.60	65.57
80	1.14	25	$2.86x10^{-4}$	51.33	68.02
100	1.15	25	$2.89x10^{-4}$	53.69	71.22
150	1.19	17	$2.03x10^{-4}$	71.08	85.50
200	1.29	11	$1.43x10^{-4}$	113.92	123.34
250	1.49	9	$1.35x10^{-4}$	184.59	185.92
300	1.71	6	$1.03x10^{-4}$	291.56	280.66

The contact resistances are poor in comparison with those reported in the literature. Desmaris et al [133] reported Si/Ti/Al/Ni/Au ohmics contacts with R_C values of 0.23Ω.mm and specific contact resistances of 1.06×10^{-6} Ωcm^2. The results given above were used in the calculation of the 1093SCO3A and 1230SC13A device mobilities.

5.2.2 Conductance, capacitance and subsequent mobility results

The conductance measurements showed that the open circuit drain current of the Q1 structure (1093SCO3A) increased by a factor of 2.8 from 0.25 to 0.7mA, as the temperature was reduced from 300 to 24K (as shown in Figure 49). A similar increase in drain current was discovered in the Q2 structure (1230SC13A), but to a greater extent (as shown in Figure 50). The open-circuit drain current of the Q2 structure (1230SC13A) dramatically increased by a factor of 4 from 0.36 to 1.60mA. Both devices pinched-off well, with low gate leakage (~10μA). However, this is where the similarities ended. The pinch-off voltage of the Q2 structure was found to vary over the measured temperature range, shifting from approximately -7 to -7.5V. This was in contrast to the Q1 structure which showed a constant pinch-off voltage of -6V. The capacitance measurements similarly indicated that the pinch-off voltage of the Q2 structure was temperature dependent, whilst the Q1 structure's pinch-off voltage was constant with temperature. Gate capacitance of the Q1 and Q2 structures with respect to gate-source voltage are shown in Figure 51 and Figure 52, respectively. Once again 'turn up' occurred in the Q1 structure but not in the Q2 structure. Interestingly though, the effect was reduced at lower temperatures. The 300K curve showed the most 'turn up' whilst the 24K curve showed the least. This result is inconsistent with a defect-related effect, because the defect energy would cross the Fermi level at all temperatures, and the defects would be emptied or filled with changes in bias at any temperature. However, the 'turn up' was soon removed from the Q1 structure as a by-product of attempts by the QinetiQ growers to reduce defect densities within the devices. The mobilities of the Q1 and Q2 structures calculated from the conductance and capacitance measurements are given against number density in Figure 53 and Figure 54, respectively.

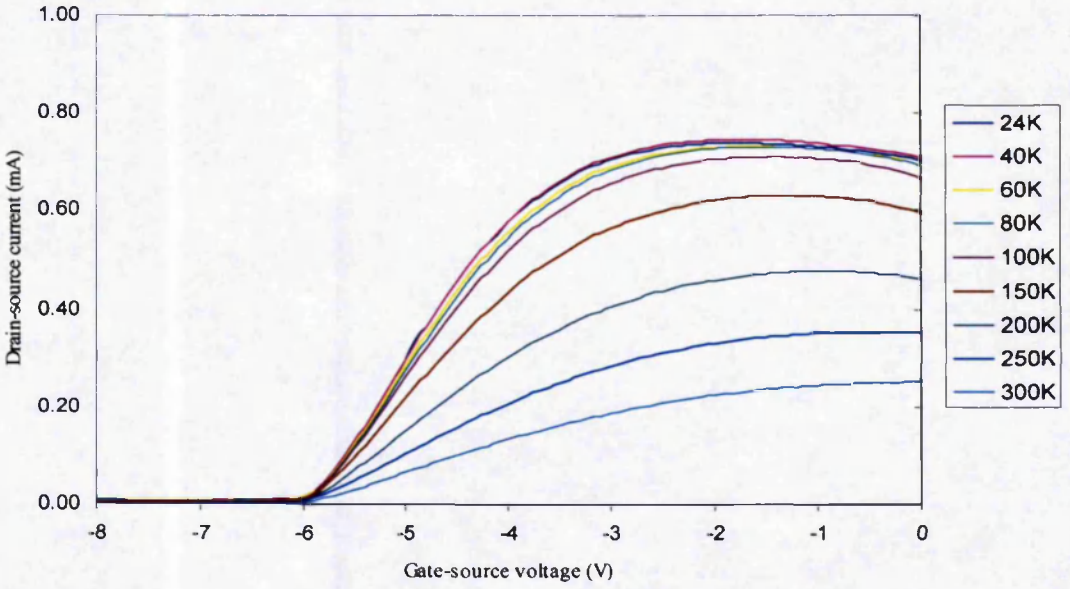

Figure 49: Q1 structure (without AlN) wafer 1093SCO3A corrected drain-source current as a function of gate-source voltage over the temperature range of 24 to 300K.

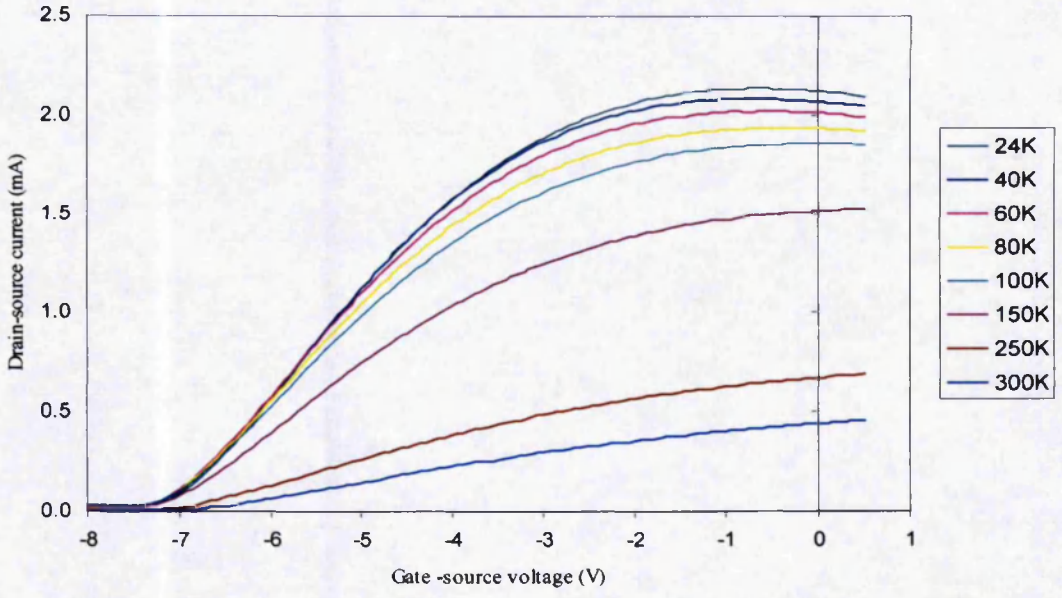

Figure 50: Q2 structure (with AlN) wafer 1230SC13A corrected drain-source current as a function of gate-source voltage over the temperature range of 24 to 300K.

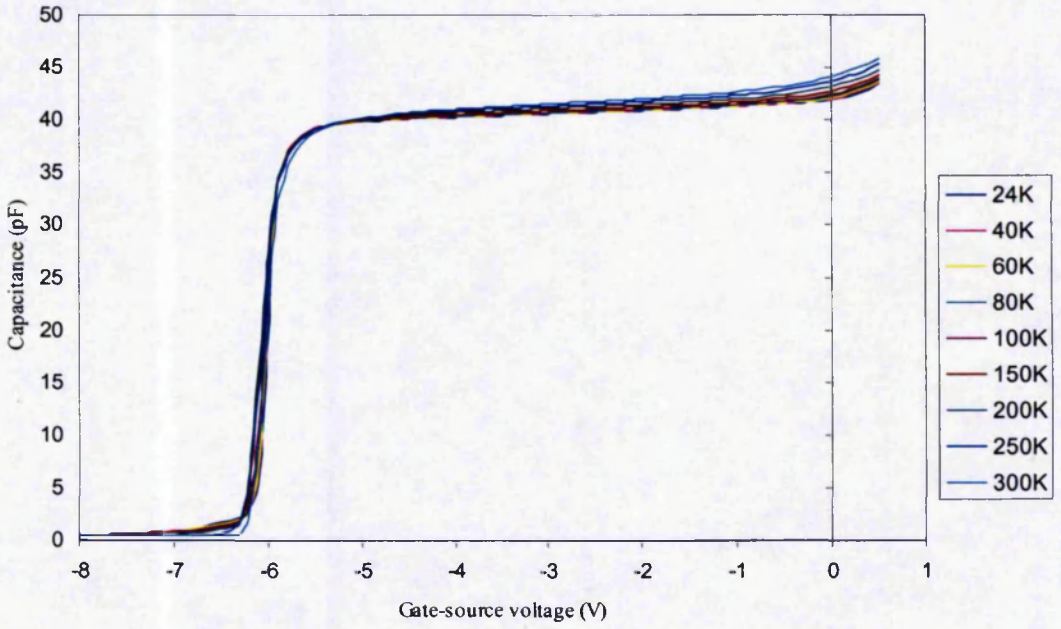

Figure 51: Q1 structure (without AlN) wafer 1093SCO3A capacitance as a function of gate-source voltage over the temperature range of 24 to 300K.

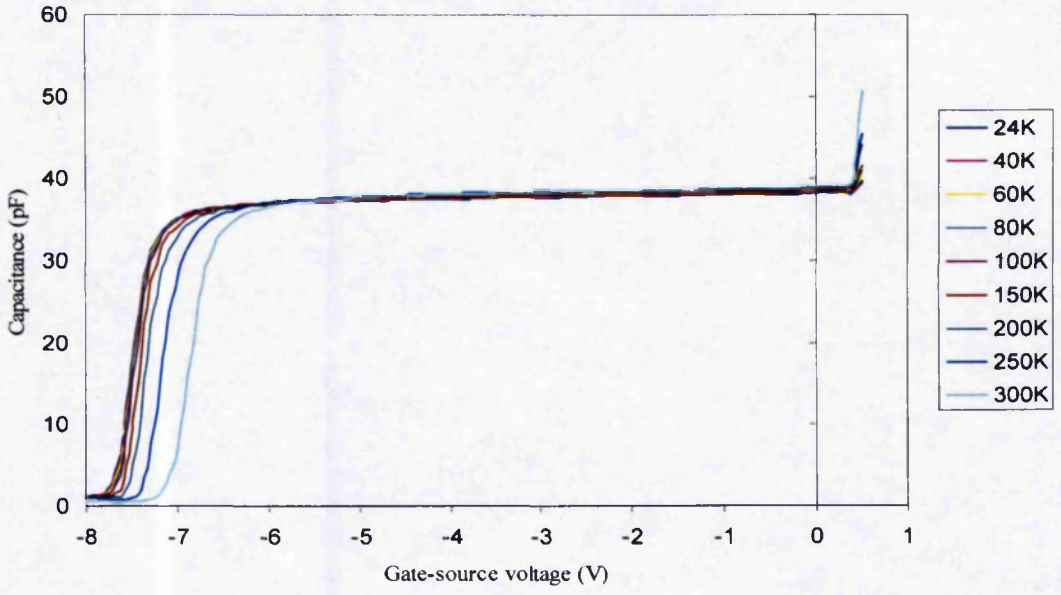

Figure 52: Q2 structure (with AlN) wafer 1230SC13A capacitance as a function of gate-source voltage over the temperature range of 24 to 300K.

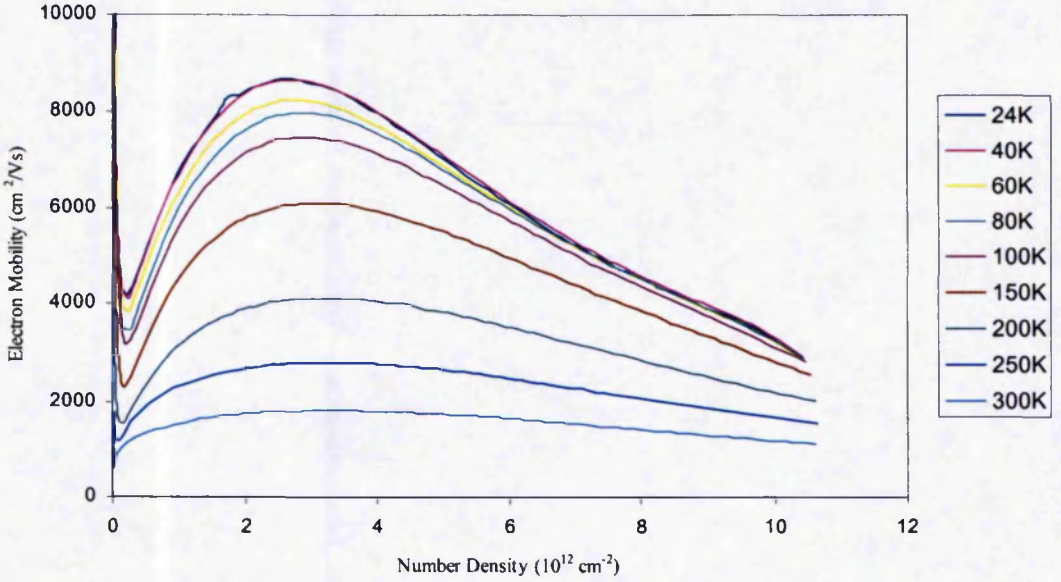

Figure 53: Electron mobility of the Q1 structure (without AlN) wafer 1093SCO3A as a function of number density from 300 to 24K.

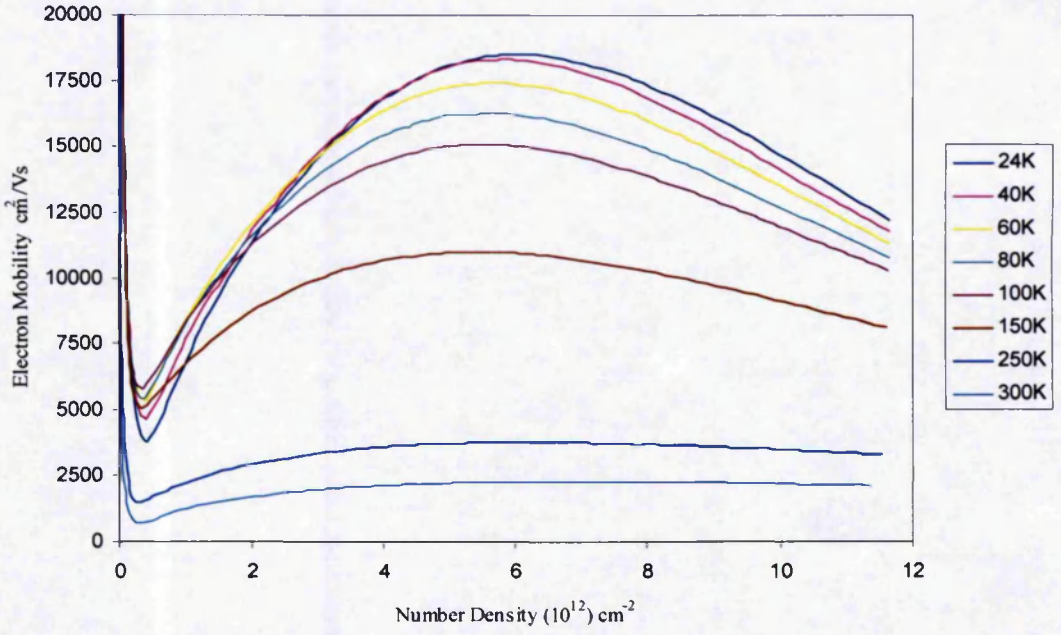

Figure 54: Electron mobility of the Q2 structure (with AlN) wafer 1230SC13A as a function of number density from 300 to 24K.

The Q2 structure (with AlN) wafer 1230SC13A had a peak mobility of ~18000 cm^2/Vs at a number density of $6x10^{12}$ cm^{-2}, while Q1 structure showed a maximum peak mobility of only ~8500 cm^2/Vs at a number density of 3 $x10^{12}$ cm^{-2} at 24K. As previously mentioned, the mobility calculation was less accurate near pinch-off because of differences in the pinch-off voltage of the current and the capacitance measurements. Both structures indicated that mobility increased considerably as the temperature was reduced. The mobility is given by:

$$\mu = \frac{\sigma}{qN} \tag{5.1}$$

The increase in conductance and hence mobility was attributed to a fall in phonon scattering with reducing temperature.

The fact that the Q2 structure (with AlN) wafer 1230SC13A had higher peak mobility than the Q1 structure was attributed to the fact that the Q2 structure had a larger 2DEG confinement barrier, and thus the Q2 structure's 2DEG penetrated less into the AlGaN, and thus was less susceptible to scattering. In order to determine the scattering phenomena responsible, 2DEG electron scattering models were generated.

5.3 Electron scattering models

5.3.1 Empirical model

The 2DEG mobility is limited by numerous scattering mechanisms which are normally assumed to be independent. The initial attempt to model the 2DEG scattering mechanisms split the scattering into two terms based on temperature dependence. The temperature independent scattering was assumed to be constant (A), whilst the temperature dependent scattering was assumed to follow a weighted power law (BT^n).

QinetiQ Schrödinger-Poisson simulations suggested that the 2DEG was only partially degenerate with up to 6% of electrons being located in higher subbands [5]. Nevertheless, Mattheisen's rule which states that the scattering rates can be added together independently was used and inter-subband scattering was ignored. Hence the data was fitted to the equation

$$\frac{1}{\mu} = A + BT^n \tag{5.2}$$

Through plotting $Log(\frac{1}{\mu} - A)$ against $LogT$ for each gate-source voltage and varying A to give straight lines, the value of n was extracted from the gradient, this was performed for both structures. Given below is the log graph for the Q1 structure.

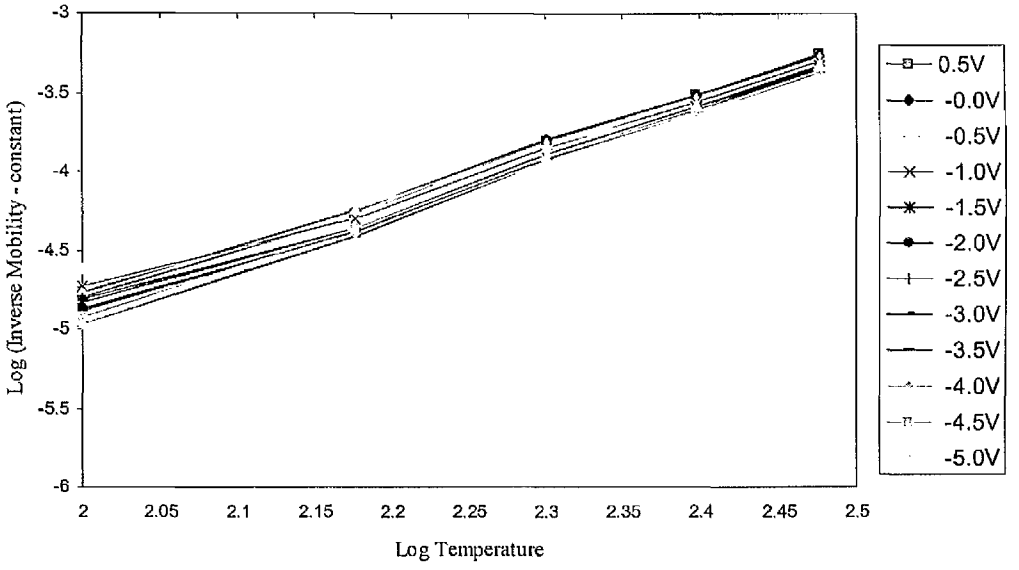

Figure 55: Log (Inverse mobility minus Constant) as a function of Log temperature at V_{GS} = 0.5 to -5V at -0.5V steps for the Q1 structure.

The gradient (n) equalled 3 for both structures (i.e. $\frac{1}{\mu} = A + BT^3$). Therefore, the graph $1/\mu$ against T^3 was plotted, in order to determine the temperature independent

scattering term (A) from the Y-axis intercept and the temperature dependent scattering term (B) from the gradient. Shown in Figure 56 is the graph for the Q1 structure, from which the values A and B were extracted for different gate-source voltages.

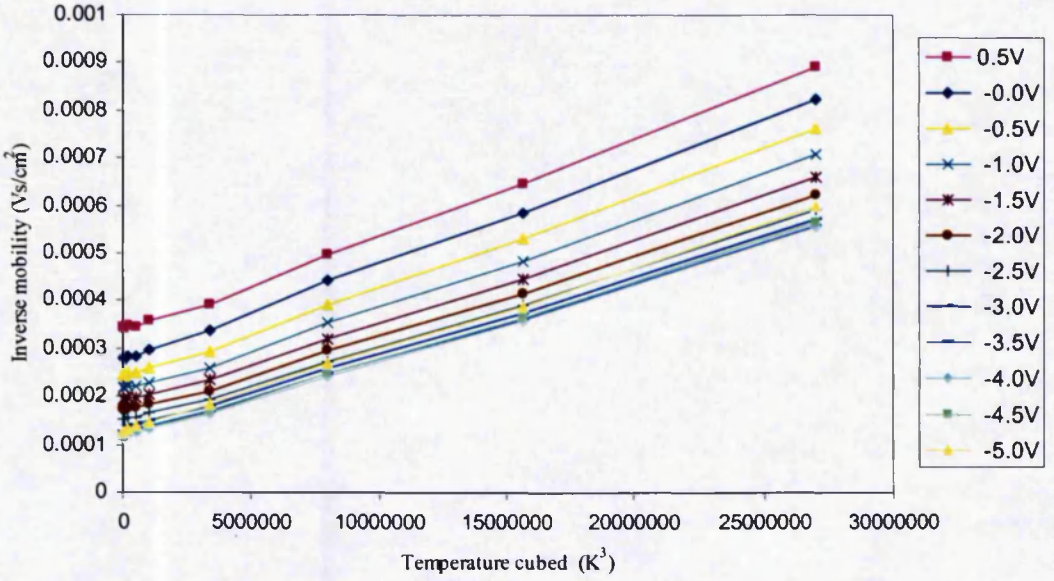

Figure 56: Inverse mobility against Temperature cubed at V_{GS} = 0.5 to -5V at -0.5V steps. Y-axis intercepts = A, gradients = B

Having extracted the scattering terms A and B from both structures they were plotted against gate-source voltage (in Figure 57 and Figure 58), so that comparisons could be made regarding the scattering mechanisms of the two different structures. As hoped, the temperature dependent scattering (phonon scattering) in both structures was found to be similar and fairly constant against gate-source voltage, and hence electron number density, and unaffected by the AlN layer. As suspected, the temperature independent scattering mechanism (mainly alloy scattering) increased dramatically in the Q1 structure as a function of gate-source voltage, whilst remaining relatively constant in the Q2 structure. That suggests that the AlN layer significantly reduces temperature independent scattering at high number densities.

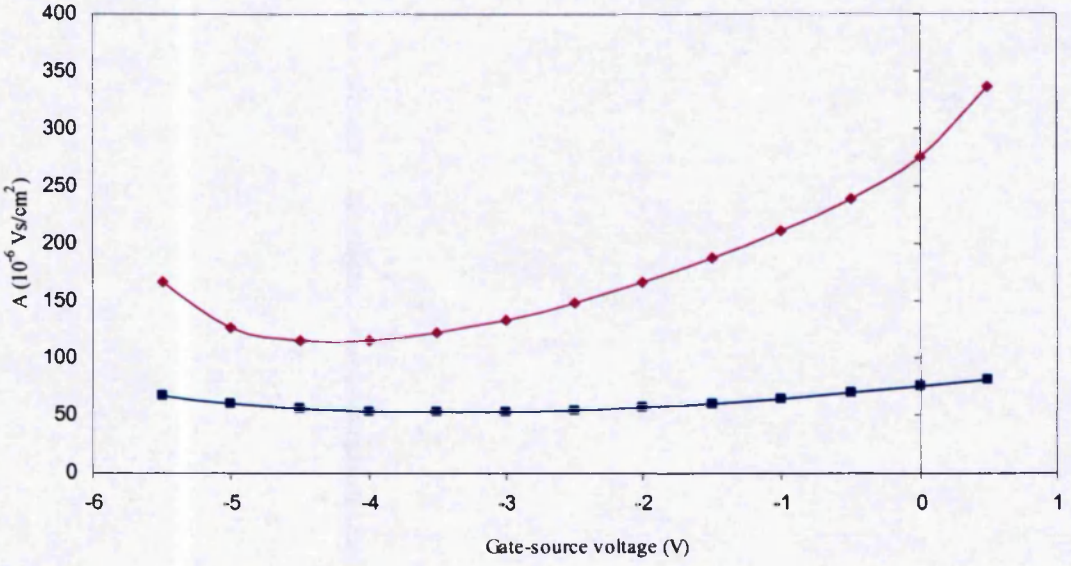

Figure 57: Temperature independent scattering (A) within the Q1 (pink) and Q2 (blue) structures as a function of gate-source voltage.

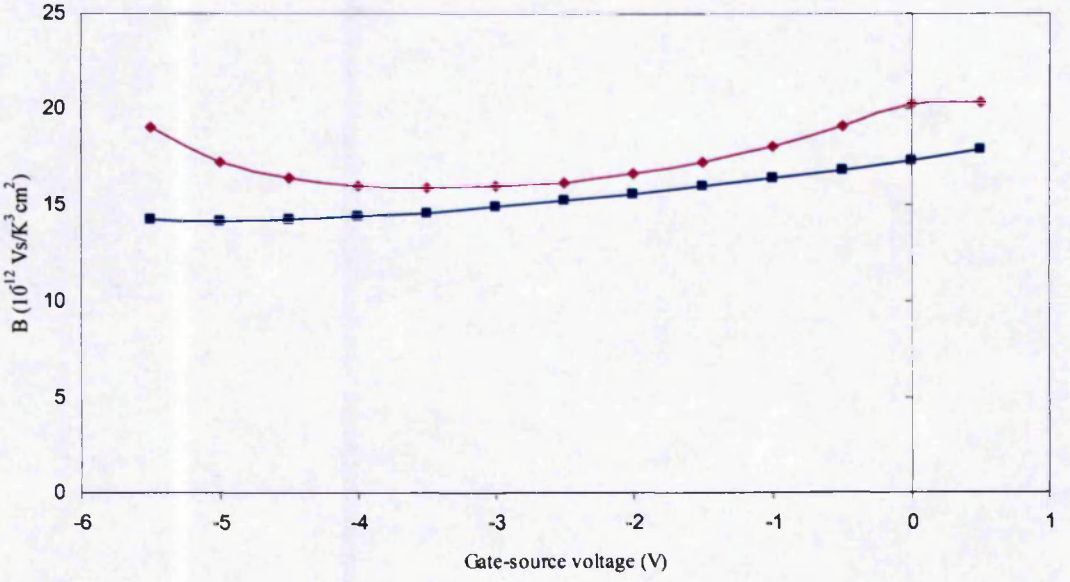

Figure 58: Temperature dependent scattering (B) within the Q1 (pink) and Q2 (blue) structures as a function of gate-source voltage.

5.3.2 Second model

Although the first model aided in the understanding of the different structures, it was purely phenomenological. A second more accurate model was formulated by representing the temperature dependent scattering components individually. In the second model three different groups of scattering mechanisms were differentiated by their temperature dependence: a) temperature independent term mainly alloy scattering. b) Acoustic phonon scattering (deformational and piezoelectric) whose scattering rate increases linearly with temperature. c) Polar optical phonon scattering which increases roughly exponentially with temperature up to around room temperature with an activation energy given by the optical phonon energy E_{POP} of 91meV. Once again Mattheisen's rule was used to add the scattering rates. Thus the data was fitted to a function of the form:

$$\frac{1}{\mu} = r_1 + r_2 + r_3 = A + BT + C\exp(\frac{-E_{POP}}{kT}) \qquad (5.3)$$

Where A, B and C are the scaling factors for each of the scattering terms. The various forms of scattering are evaluated below. The temperature dependence of Coulomb scattering is proportion kT^{-1} near room temperature and will result in an underestimated acoustic phonon scattering term, while at lower temperatures near 77K the dependence becomes complicated by the screening effect [134].

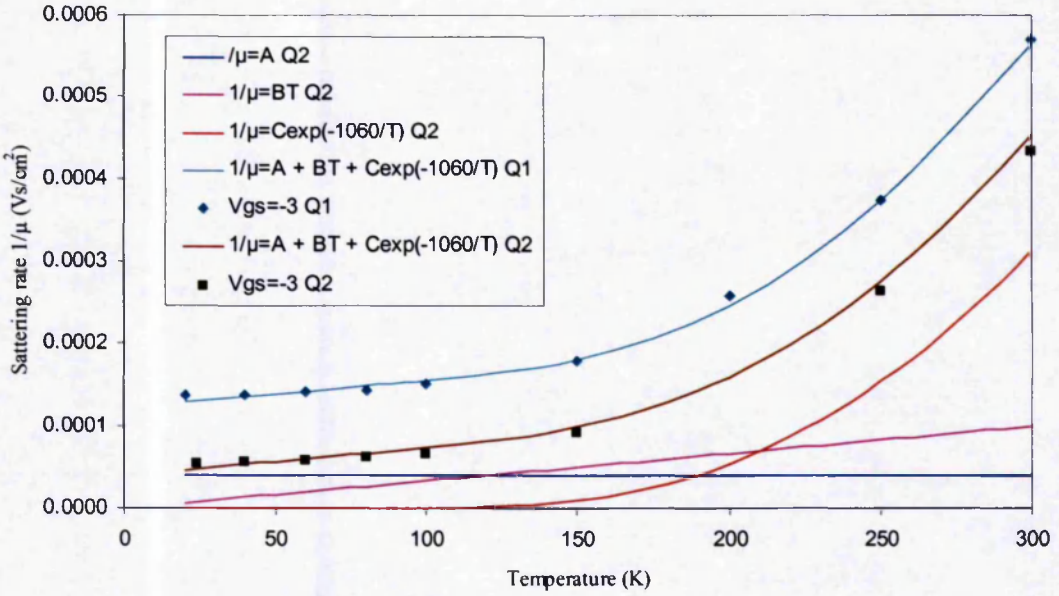

Figure 59: Extracted scattering rate with fits for V_{GS} = -3V.

This simple model fits the temperature dependence of the mobility remarkably well over the full range of number density, except close to pinch-off and for forward bias. Figure 59 shows an example non-linear least squares fit (using the Levenburg-Marquardt algorithm) to inverse mobility data at V_{GS} = -3V (corresponding to a number density of around $5x10^{12}$ cm^{-2}) for both the Q1 (without AlN layer) and Q2 (with AlN layer) structures. The three scattering terms making up the scattering rate in equation (5.3) are plotted in Figure 59 for the device with the AlN layer.

5.3.3 Temperature dependent scattering terms

5.3.3.1 Acoustic phonon scattering

As can be observed in Figure 60, the acoustic phonon scattering factor increased linearly from $0.3x10^{-6}$ to $0.4x10^{-6}$ Vs/ Kcm^2. This result is consistent with Knap et al [108] who

showed experimentally and theoretically that $r_2 = BT$, with B~$3x10^{-7}$ Vs/ Kcm^2, increases with number density before saturating above $5x10^{12}cm^{-2}$ electrons in the 2DEG.

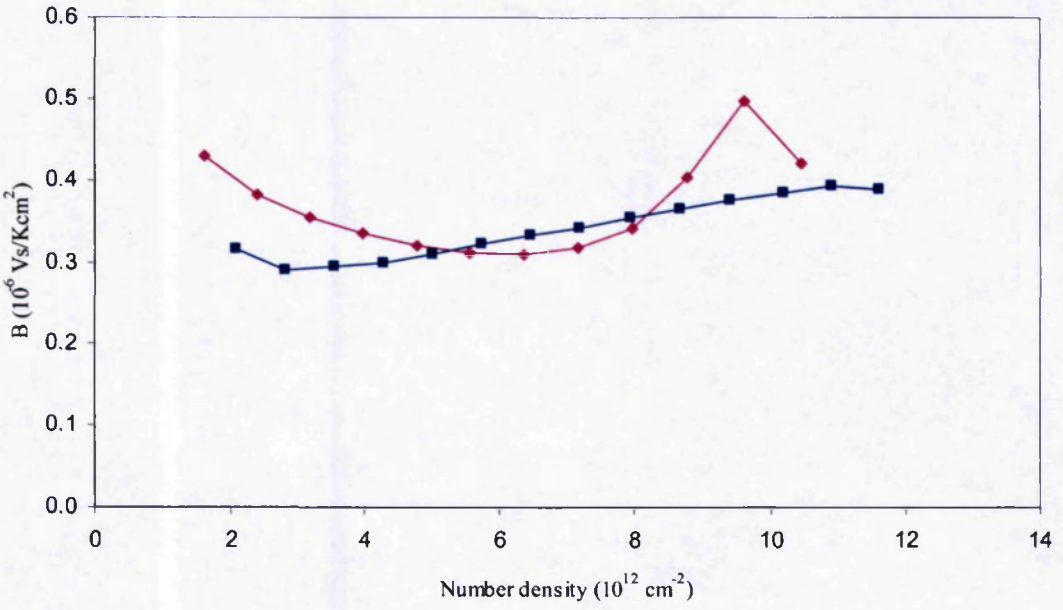

Figure 60: Acoustic phonon scattering co-efficient B against number density for both the Q1 (pink) and Q2 (blue) structures.

The value of B is remarkably close to that found by Knap et al and increases with electron number density. It should be noted that this term in the fit is the smallest and is probably the one which will be most susceptible to error in the extraction. This is particularly true for the Q1 data, so the Q2 fit is more believable.

5.3.3.2 Polar optical phonon scattering

Through studies of AlGaAs/GaAs heterojunctions Hirakawa & Sakaki [135] determined that in a degenerate gas, where only the lowest subband is occupied, the most significant

temperature dependence comes from the phonon occupation number. In addition, there is a clear statement in Katz *et al* [136] that the polar optical phonon scattering results in an exponential dependence on temperature. The result of using $r_3 = C \exp(\frac{-E_{LO}}{kT})$ where $E_{LO} = 91\text{meV}$ can be seen in Figure 61.

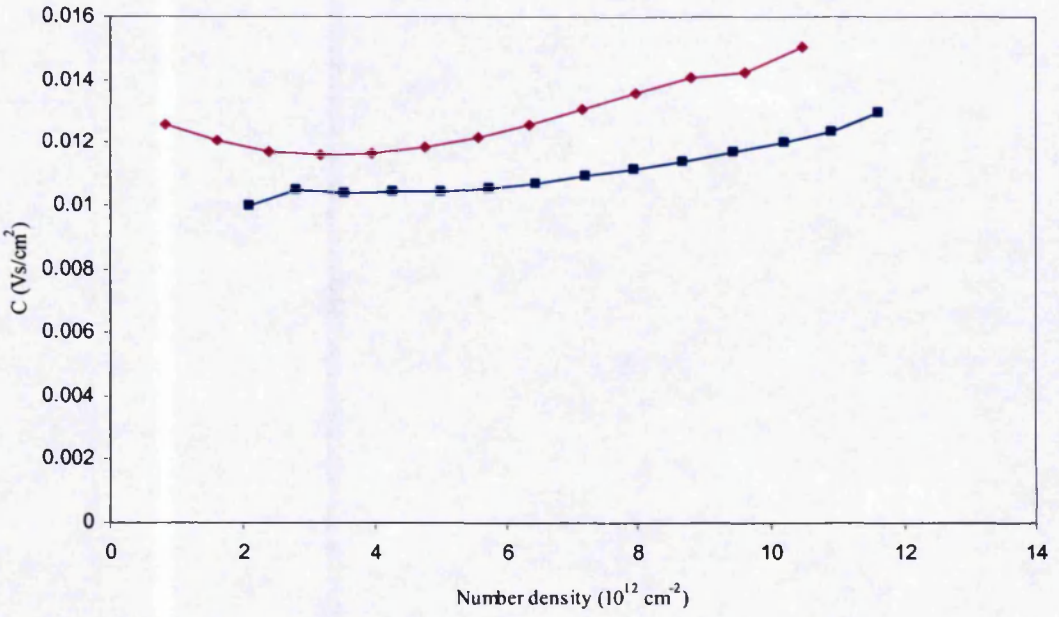

Figure 61: Polar optical scattering in Q1 (pink) and Q2 (blue).

Figure 61 indicates that the magnitude of the polar optical scattering is very similar for both structures. The model shows there is probably a gradual increase in scattering with increasing number density, the cause of which is not fully understood.

5.3.4 Temperature independent scattering terms

The temperature independent term (shown in Figure 62 as a function of number density) includes: Coulomb scattering (from point and line defects), alloy scattering and surface roughness scattering.

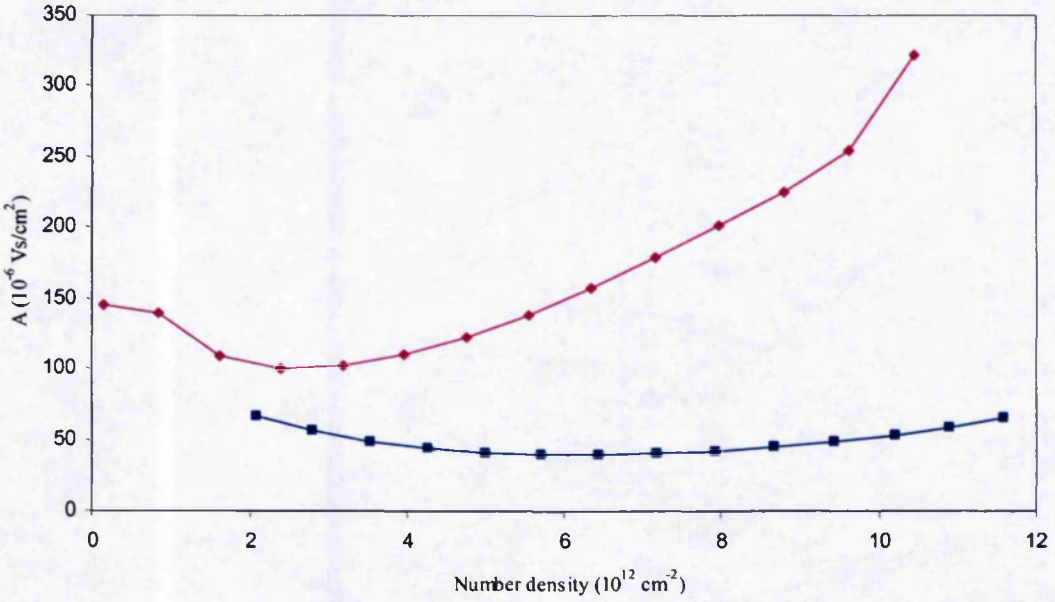

Figure 62: Temperature independent scattering in Q1 (pink) and Q2 (blue).

As expected, there is evidence of much larger temperature independent scattering occurring in the device with no AlN layer, and hence the AlN exclusion layer significantly reduces the temperature independent scattering mechanisms occurring in the 2DEG.

5.3.4.1 Alloy scattering

The alloy scattering contribution of the total scattering rate was calculated with a single unknown scaling factor γ. So the alloy scattering rate r_A was expressed by the following equation:

$$r_A = \gamma R \tag{5.4}$$

where R is the 'relative alloy scattering rate' [99] given by

$$R \propto \int dz \, |\psi(z)|^4 \, 4x(z)(1-x(z)) \tag{5.5}$$

It depends upon the aluminium fraction $x(z)$, and the electron subband wavefunction $\psi(z)$ and is indirectly proportional to length [99]. The relative scattering rate increases with increasing alloy disorder $x(1-x)$ and with increasing wavefunction penetration into the alloy.

Assuming that the difference between the two samples is solely due to alloy scattering, the effect of modelling parameter gamma was tested. The difference between the temperature independent term with and without the AlN layer was extracted using a spline interpolation between the experimental points. Then the difference between the modelled alloy scattering factor with and without AlN was calculated. The scaling factor γ was then adjusted to fit the experimental scattering rate difference curve at a value of $7.5\text{x}10^{12}$ cm^{-2} (i.e. in the middle of the data range where it is most accurate). This gave a scaling factor $\gamma = 1.83\text{x}10^{-9}$ Vs/cm. Using the extracted γ value, the modelled alloy scattering rates with and without the AlN layer were plotted. To calculate the residual scattering the modelled alloy scattering rates were subtracted from the experimental temperature independent term. The modelled alloy scattering rate, the residual scattering rate (Coulomb plus surface roughness scattering) and the experimental temperature independent term for both structures are all shown as a function of electron number density in Figure 63.

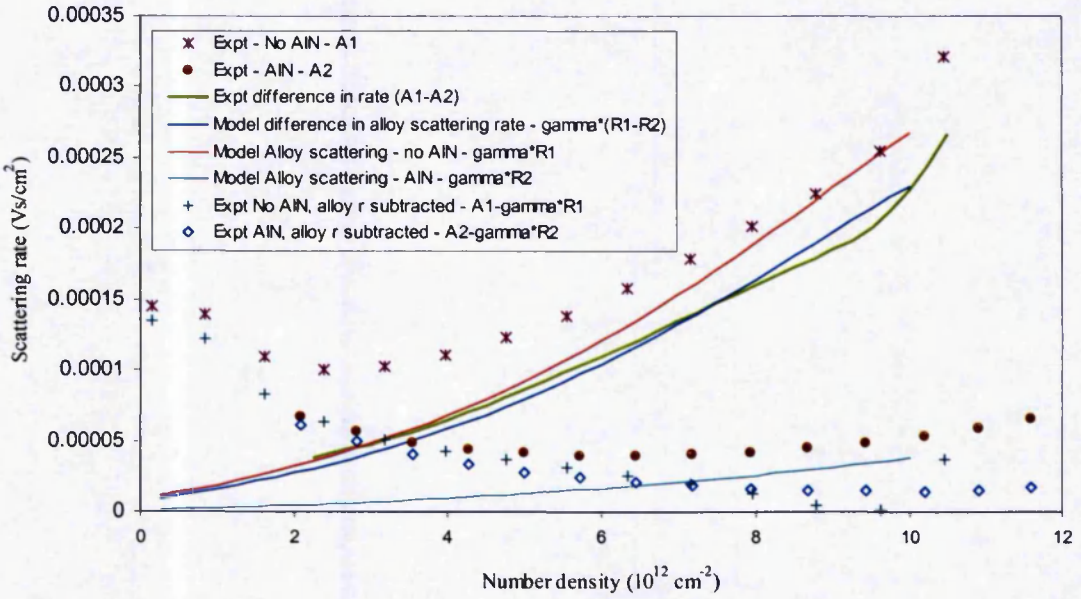

Figure 63: Separation of temperature independent scattering

There is excellent agreement between the calculated scattering factor and the experimental data as a function of the number density. Alloy scattering could be represented by the following for the Q1 structure (without the AlN layer):

$$r_{Q1} = 1\text{x}10^{-5} + 7.2\text{x}10^{-18}N + 1.9\text{x}10^{-30}N^2 \qquad (5.6)$$

and for Q2 structure (with AlN layer)

$$r_{Q2} = 1.6\text{x}10^{-6} + 9\text{x}10^{-19}N + 2.7\text{x}10^{-31}N^2 \qquad (5.7)$$

5.3.4.2 Coulomb scattering

After subtracting the alloy scattering term, the residual scattering term is broadly similar for both structures, shown as pluses and open diamonds in Figure 63, increasing

smoothly with reducing number density. It should be noted that, the errors are much larger for the device without AlN layer, especially at high number density because the calculation involves the subtraction of a larger Q1 alloy scattering (red line) compared to the smaller Q2 alloy scattering (light blue line).

The experiments show that at low electron number densities the scattering rate seems to increase, presumably due to Coulomb scattering. The agreement between the two samples in this regime suggests that the Coulomb scattering is similar in both cases. Fitting the data with a power law gives roughly $r_C = 1.5\text{x}10^7\ N^{-1}$. In the literature, Hsu & Walukiewicz [101] suggests that Coulomb scattering drops with increasing number density (N). In addition, Katz et al [136] state that coulomb scattering drops as N^{-2} or $N^{-2.5}$.

5.3.4.3 Surface roughness

In the AlN sample, the residual scattering showed a gradual increase with respect to electron number density consistent with the expectation for roughness scattering. At high number density ($1\text{x}10^{13}\text{cm}^{-2}$) the residual scattering will be dominated by roughness scattering, hence giving a maximum roughness scattering contribution of about $r_{SR} = 2.5\text{x}10^{-5}$ Vs/cm^2 (mobility of 40,000cm^2/Vs in the absence of all other contributions).

5.4 Comparison of model with the experimental data

In order to thoroughly test the accuracy of the model, high temperature measurements where taken and compared against model predictions. Extrapolating the model to 600K (which is likely to be the real channel temperature in operation) gave an idea of the expected device operating mobility. The mobility of the devices were calculated in the usual way using equation (5.1). The capacitance and conductance of the same Q1

(1093SCO3A) and Q2 (1230SC13A) devices were measured at 50K intervals between 300 and 500K using a HP4191A RF low impedance analyser and a HP4145B semiconductor parameter analyser. The maximum achievable device temperature was limited by the heated chuck to 500K. As can be seen in Figure 64 and Figure 65 the predictions are remarkably accurate for both the Q1 and Q2 structure. The values of sheet resistivity and contact resistance, used in the high temperature mobility calculations were extrapolated from the previous low temperature TLM data given in section 5.2.1.1.

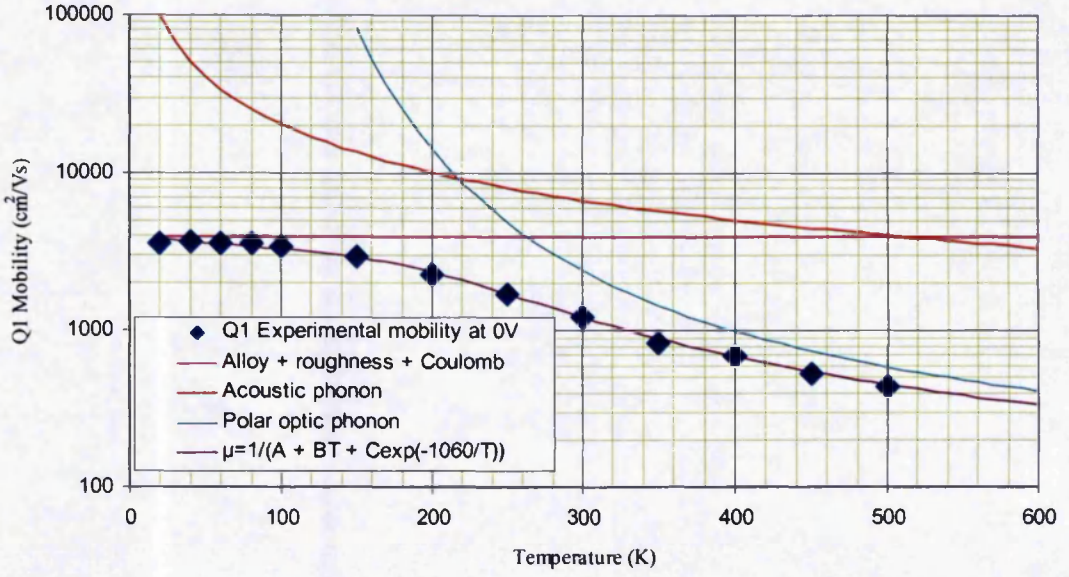

Figure 64: Mobility predictions compared with experimental data for Q1

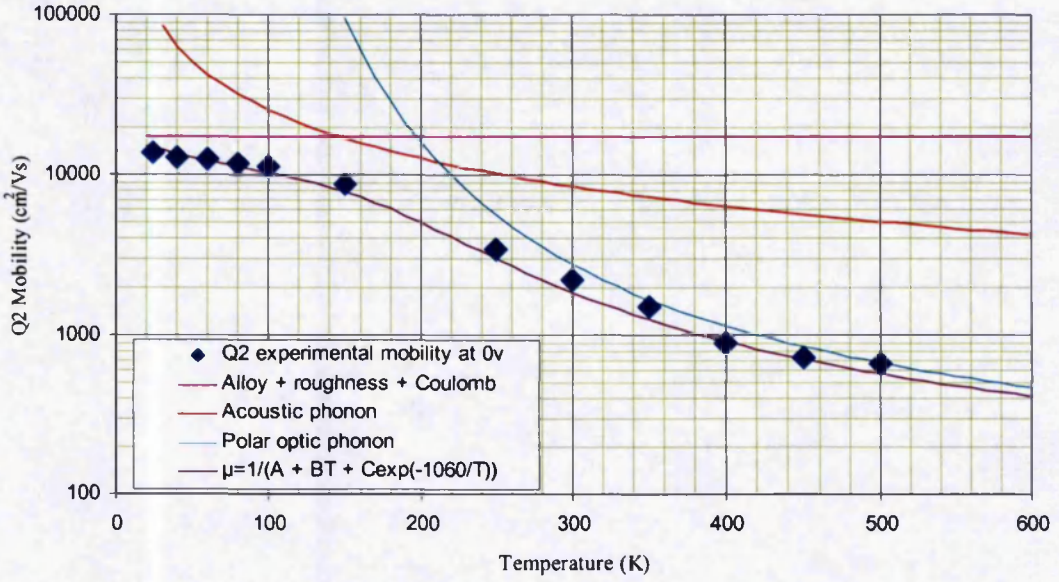

Figure 65: Mobility predictions compared with experimental data for Q2

5.5 Thermal variation of Q2 device characteristics

For more information about the Q2 structure, the barrier height and ideality factor the Schottky contacts were measured as a function of temperature. The change in pinch-off voltage with temperature was also measured with respect to bias conditions. However, all these measurement were performed on a different Q2 wafer (1318SC13B) using FatFET device 0419.

5.5.1 Measurement of barrier height and ideality factor

Both the barrier height and ideality factor were calculated using information gathered from forward current voltage diode characteristics of the NiAu Schottky gate contacts. The diode characteristics were measured using a HP4145B semiconductor parameter analyser. A logarithmic graph of the forward bias diode characteristics is shown in

Figure 66. The y-axis intercepts of the forward bias diode characteristics are equal to the saturation currents at those particular temperatures.

The barrier height was calculated using the following equation.

$$\Phi_b = \frac{kT}{q} In\left(\frac{SA^{**}T^2}{I_{SAT}}\right) \tag{5.8}$$

where k is the Boltzmann constant (1.38 x10^{-23} J.K^{-1}), T is temperature in Kelvin, q is the charge on an electron, I_{SAT} is the saturation current, S is the area of the contact in cm^2 and A^{**} is the effective Richardson constant (3.02 x 10^5 A.m^{-2}.k^{-2} or 30.2 A.cm^{-2}.k^{-2}) calculated from

$$A^{**} = \frac{4\pi q m_e^* k^2}{h^3} \tag{5.9}$$

where h is plank constant (6.626 x10^{-34} Js) and m_e^* is the effective mass of $Al_{25}Ga_{75}N$. The effective mass was calculated using linear interpolation between $m^*_{GaN} = 0.22m_o$ [137, 138] and $m^*_{AlN} = 0.35m_o$ [137] giving $m^*_{Al25Ga75N} = (0.2525 * 9.1x10^{-31} = 2.29x10^{-31}kg)$. It should be noted that values used in literature for m^*_{AlN} vary significantly from $0.35m_o$ [137] to $0.48m_o$ [138].

The ideality factor was calculated using the forward diode characteristics. By taking the slope from the linear part of the graph as shown Figure 66 the ideality factor was calculated using the following equation:

$$n = \frac{q\Delta V}{kT\Delta(\ln I)} \tag{5.10}$$

where $\Delta(\ln I)$ and ΔV are the change in current and voltage.

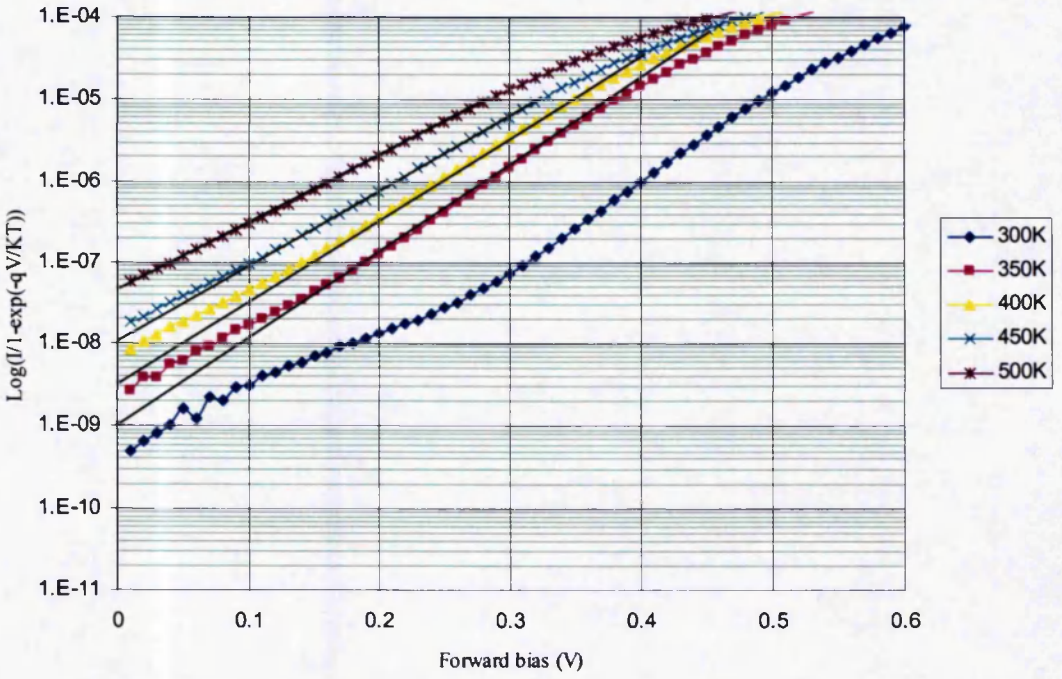

Figure 66: Experimental calculation of ideality factor and barrier height (from extrapolated y-axis intercept I_{SAT})

5.5.2 Barrier height and ideality factor results

The temperature variation of the Schottky barrier height (SBH) and the ideality factor are given in Figure 67 and Figure 68, respectively. The SBH was found to increase with temperature from 0.8eV at 300K to 1.05eV at 500K. The decrease in ideality factor with temperature suggests that the dominant transport mechanism across the barrier changes from mainly tunnelling at room temperature to thermionic emission at high temperatures. Therefore, the 500K SBH value of 1.05eV was thought to be the most accurate value.

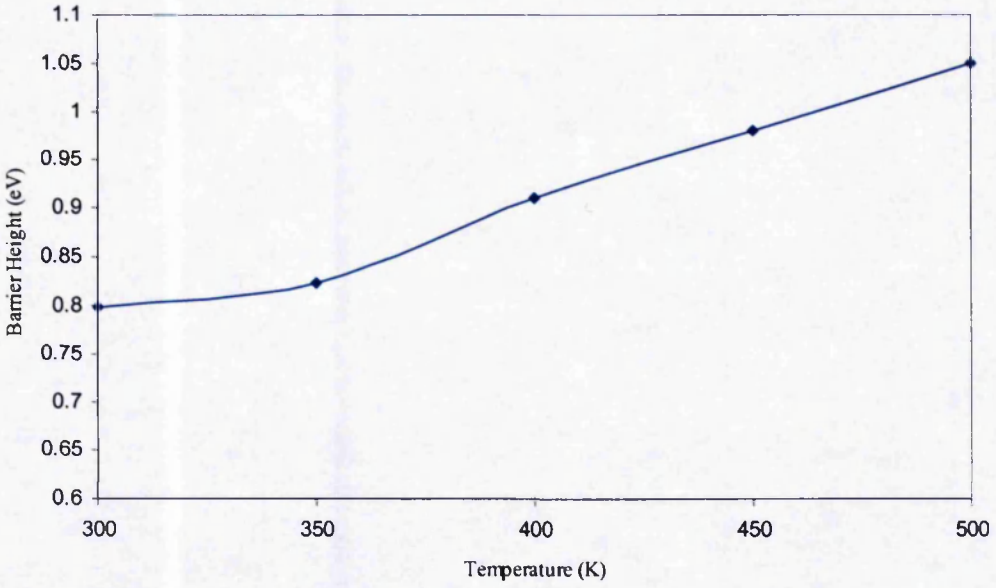

Figure 67: Barrier height against temperature for the Q2 structure

These results are not unusual, T.Sawada et al [139] found that Ni SBHs on n-AlGaN (20%) varied from 0.64eV at 300K to 1.08eV at 500K. They also concluded that the difference between their experiment results and their theoretical SBH of 1.4eV (from A^{**} = 30.2 $A.cm^{-2}.k^{-2}$) were due to large tunnelling leakage currents indicated by large ideality factors greater than 1.2.

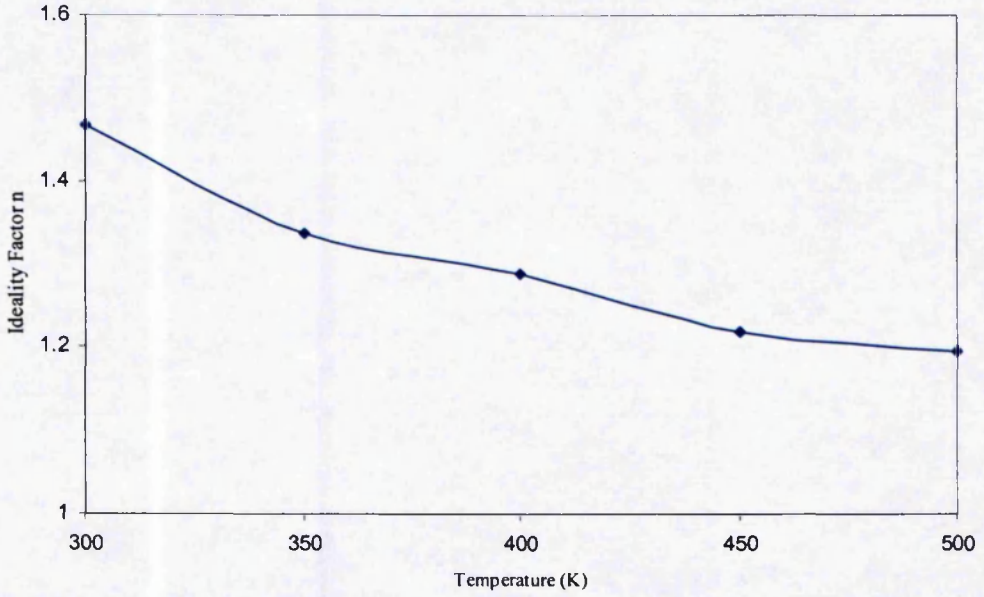

Figure 68: Ideality factor against temperature for the Q2 structure

Although, the measured ideality factor of 1.54 at 300K is poor, it is consistent with the literature. Monroy *et al* [140] found that the ideality factor of Schottkys on AlGaN/SiC varied between 1.2 -1.6 at 300K depending on Al mole fraction and metal used, whilst Qiao *et al* [137] reported an ideality factor of 1.37 for a Au Schottky on AlGaN (23%)/SiC at 300K.

Alternatively defects in the AlGaN layer could produce local barrier lowering, causing the barrier height to be underestimated. This would also explain the poor ideality. The temperature variation of the barrier height could then be attributed to temperature variation of the local defects.

5.5.3 Capacitance experiments

The measurements were performed on the Q2 wafer (1318SC13B) FatFET device using a HP4191A work-station. The gate capacitance was monitored as the gate-source voltage was swept from 0.5 to -9V in 100mV steps. The capacitance was measured at 300K, the gate was then biased and held at 0V whilst it was cooled to 30K using a closed-loop He cryostat. The device capacitance was then measured before being warmed to room temperature under no bias. Once at room temperature the device capacitance was re-measured. The process was then repeated biasing the device at -10V and +10V.

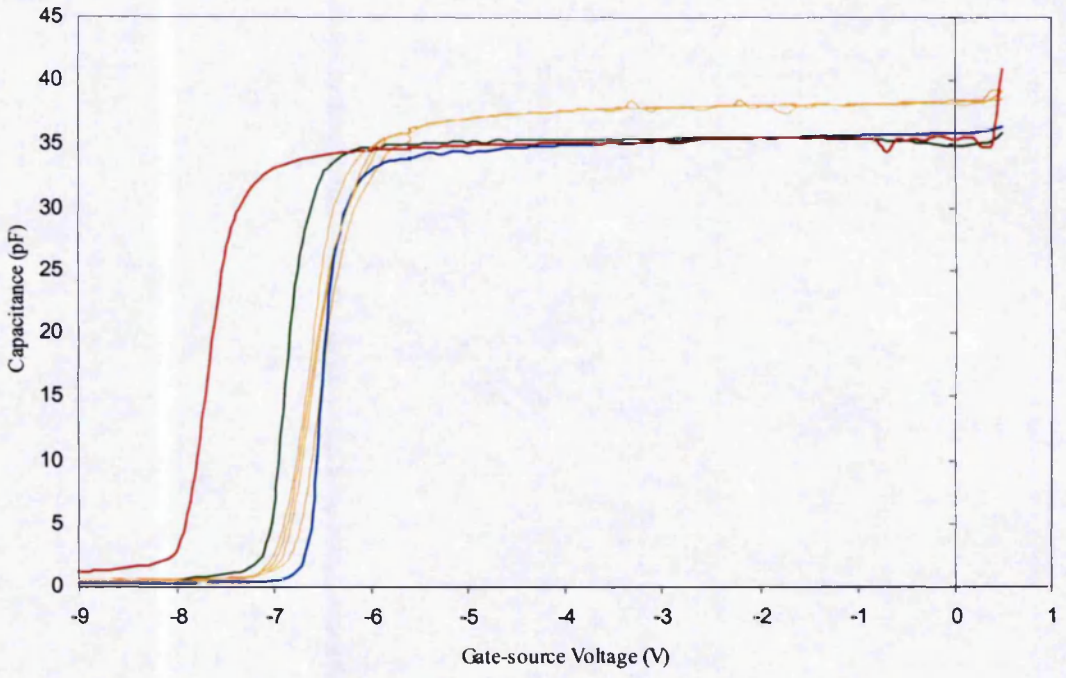

Figure 69: Temperature induced capacitance variation under different biased conditions.

All room temperature sweeps (tan), 30K Plus 10V hold (red), 30K 0V hold (green), 30K minus 10V hold (blue).

As shown above in Figure 69, there are two aspects to the data, there is a change in the

capacitance and there is a shift in the pinch-off voltage. The variation in capacitance could be attributed to either a change in the dielectric constant, or to the sheet charge moving closer to the surface at elevated temperatures. Since this was a Q2 device, any movement of the sheet charge towards the surface would be severely limited by the AlN exclusion layer. Through integration of the capacitance curves, the change in the 2DEG number density with respect to the bias conditions was calculated.

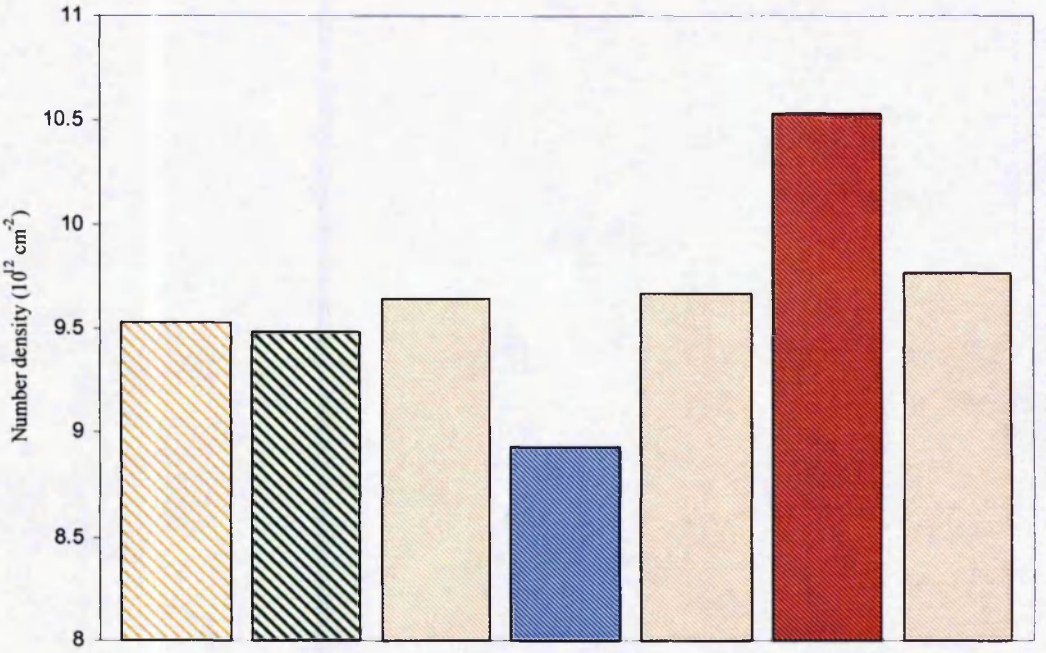

Figure 70: Temperature induced 2DEG number density variation under different biased conditions. All room temperature sweeps (tan), 30K 0V hold (green), 30K minus 10V hold (blue), 30K Plus 10V hold (red).

Despite the fact that, when the device was cooled under 0V bias there was a shift in pinch off and the capacitance fell, the 2DEG number density was relatively constant, only a 0.5% fall was observed. Reductions in carrier concentrations with temperature are not unusual and are often reported [111, 114] without being the focus of the publication. Therefore the fall in capacitance and the pinch-off shift at zero bias may be

due to a 10% change in the dielectric constant. However, this seems a large effect and has not been reported in the literature previously.

Biasing the device at positive 10V during cooling resulted in about $5x10^{11}$ cm^{-2} of effective electron trapping, whilst biasing the device at negative 10V during cooling caused about $1x10^{12}$ cm^{-2} of effective charge being exposed. Therefore, the movement of charge was not balanced under both polarities. However, the phase angle during the positive 10V sweep averaged 60° indicating that substantial leakage was occurring throughout that measurement. It was concluded that the gate biasing during cooling caused a mechanism similar to that of 'the virtual gate mechanism' to occur at the surface, and that the shift in pinch-off voltage seen in the capacitance sweeps was as a result of the trapping and exposure of charge at the surface due to unintentional biasing between measurements.

5.5.4 Arrhenius plot

This method of calculating barrier height is insensitive to the Richardson constant. Plotting Log (J/T^2) against 1000/T gives Log (A**) at the y axis intercept and the gradient gives $\frac{-\Phi_b q}{k}$. As shown in Figure 71 the graph intercept is -11.369 giving A** = $1.16x\ 10^{-5}$ $cm^{-2}k^{-2}$ which is most certainly incorrect. The error is attributed to the fact both the ideality factor and the barrier height vary with temperature. The gradient equals -4.66, giving Φ_b = 400meV.

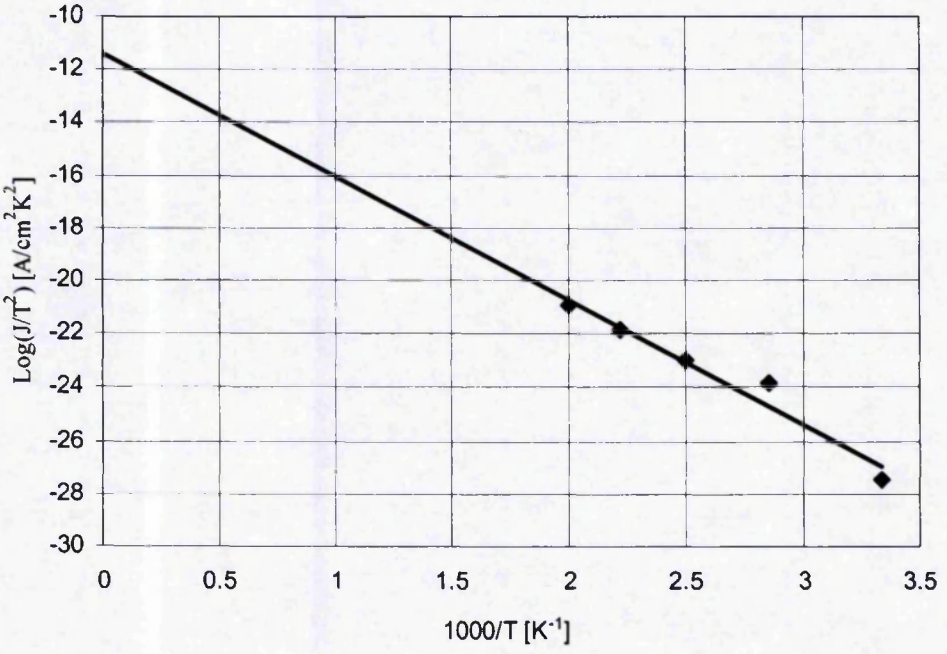

Figure 71: Arrhenius plot for the Q2 structure

5.6 Conclusions

The separation of the scattering mechanisms into independent (A) and dependent (B) terms, has lead to the discovery that phonon scattering is the dominant scattering mechanism at room temperature. In addition, the AlN layer has been found to reduce alloy scattering at high carrier densities and thereby allowing a high mobility to be maintained. High- temperature mobility model predictions were found to be accurate indicating that any variation in the pinch-off voltage within the Q2 had only a negligible effect on the extracted models.

6 CONCLUSIONS AND FUTURE WORK

6.1 Current collapse

As a result of both the passivation and gate lag measurements it has been concluded that current collapse is unquestionably affected by the device surface. The gate lag measurements were able to directly measure a significant increase (from ~5 to 30Ω) in the resistances associated with the ungated surface regions near source and drain during negative gate biasing, whilst the channel resistance remained relatively constant indicating negligible trapping in the AlGaN layer. The measurements supported the virtual gate concept, i.e. that when the gate was stressed with a large negative bias, electrons migrated onto the ungated regions of the device producing an increased parasitic resistance and a decreased drain current.

The passivation measurements showed that under the correct deposition conditions Si_3N_4 passivation can help to reduce current collapse (Type F in

Table 3). However, under the wrong deposition conditions (Type B) passivation can increase current collapse. In addition, there is a possibility of increased gate leakage. The pulsed comparative study of passivation types F and B indicated that the movement of electrons was dependent upon the pulse length and the applied electric field, and that the better passivation (type F) didn't prevent the movement of electron on to the surface of the device, but merely enabled them, by way of shallower surface traps, to move on and off the surface at an increased rate.

6.2 Mobility

All the measurements of mobility as a function of temperature gave evidence that SiC devices have higher mobilities than sapphire based devices. This is attributed to firstly SiC being a better thermal conductor - reducing the self-heating within the device and thus reducing the phonon scattering within the 2DEG at AlGaN/GAN interface. Secondly, that the lattice mismatch between SiC and GaN (~3%) is smaller than between sapphire and GaN (~13%). Consequently growth on sapphire is more difficult and usually results in dislocation densities being typically a factor of 5-10 times higher than those on SiC substrates. This leads to a rougher AlGaN/GAN interface, more electron scattering and lower 2DEG mobility. Thus experimental data confirms the theoretical predictions [100] i.e. that maximum mobility at room temperature is limited by polar optical phonon scattering.

It was found that the fall in room temperature mobility at high number density could be prevented by inserting an AlN interlayer. Improvements in mobility resulting from the AlN layer were immediately apparent. At room temperature with no applied voltage the mobility was 1860 with, and 1210 cm^2/Vs without, the AlN layer. As shown in the energy band diagrams the thin AlN layer significantly increased the GaN /AlGaN effective conduction band offset, thereby reducing the penetration of the 2DEG wavefunction into the AlGaN barrier layer and reducing scattering.

The drain current in of both structures was found to increase as the device temperature was reduced. The increase in current was attributed to a reduction in phonon scattering. As a result of the reduced scattering the current flow increased, and in turn the conductance and the 2DEG mobility of both devices increased.

Separating the scattering mechanisms into temperature independent (A) and dependent (B) terms, led to the generation of an empirical model $\frac{1}{\mu} = A + BT^3$ which indicated that the temperature dependent terms of both structures were very similar (as shown in Figure 58). However, the AlN layer was found to significantly reduce temperature independent scattering (shown in Figure 57) especially at high carrier densities. Although this model helped in understanding the structures, it was solely phenomenological.

Therefore this model was abandoned in favour of a more accurate model, which separated phonon scattering into its individual components (Acoustic (B) and Optical (C)). The new model $\frac{1}{\mu} = r = A + BT + C \exp(\frac{E_{LO}}{kT})$, a simple physically based analytical expression, has been shown to accurately fit the mobility data over the entire temperature range. The acoustic (Figure 60) and the polar optical scattering (Figure 61) were found to be similar in both structures. Polar optical scattering was found to be the dominant scattering mechanism at room temperature. Once again the temperature independent scattering term was ascertained as the significant difference between the structures. As shown in Figure 62, the scattering occurring at high carrier concentrations in the Q1 structure is approximately six times greater than that in the Q2 structure. By separating the temperature independent term into its constituent parts (shown in Figure 63), it was established that alloy scattering was the dominant temperature-independent mechanism, as expected, and that the inclusion of an AlN layer reduced its importance by at least a factor of five. Extraction of the residual scattering terms showed that the coulomb scattering was strongest at low carrier densities and that interface roughness scattering increased with carrier density. However, the residual terms are small in

comparison to the alloy and polar optical phonon scattering and are insignificant at room temperature in the layers measured. Although high-performance transistors have been demonstrated using the AlN layer, the small signal performance has been comparable to conventional designs [105, 129], because maximum f_τ is obtained at a gate voltage near pinch-off at low carrier densities, thus negating the benefits of the AlN exclusion layer. The benefits should be more obvious under realistic operating conditions, where at high fields, the electron waveforms spill into the AlGaN, potentially reducing the mobility and the saturation velocity.

6.3 Pinch-off variation

The variation of pinch-off voltage within the Q2 device was alarming and was investigated further. However, the variation only occurred at low electron number density and therefore since the comparative study focused mainly on the differences in mobility at high electron number density, it didn't affect validity of the results generated from the study. This view is supported by the fact that extrapolations of the model were found to predict accurately the mobility of the devices when operated at elevated temperatures.

6.4 Barrier height and ideality

Defects in the AlGaN layer are thought to produce local barrier lowering, causing the barrier height to be underestimated and this would also explain the poor ideality. The temperature variation of the barrier height is thought to be due to temperature variation of the local defects.

6.5 Summary

The research presented in this thesis has indicated, through direct measurements of parasitic resistances, that current collapse is caused by the formation of a 'virtual gate' on the device surface during negative gate biasing. Passivation has been found to reduce current collapse. The fall in mobility at high electron number densities has been discovered to be as a result of alloy scattering. The alloying scattering can be significantly reduced by the insertion of a thin AlN exclusion layer between the GaN and AlGaN layers.

6.6 Future work

6.6.1 Current collapse

The introduction of a GaN cap layer and the use of double layer passivation have both been reported in the literature to reduce current collapse, and require further investigation. However, the author feels that most progress can be made through the utilisation of new device structures, such as the double heterojunction AlGaN/GaN HEMT. This is because, by re-structuring the device the troublesome surface states are moved inside the device, thus removing any possibility of them interacting with electrons from the gate electrode.

6.6.2 Mobility

The research presented in the thesis has shown that the introduction of a thin AlN exclusion layer permits the 2DEG mobility to be maintained at high carrier concentrations, by reducing alloy scattering. Although, the pinch-off variation of the Q2 device did not affect the 2DEG scattering measurements, further investigation into why it only occurred in the Q2 device is required.

REFERENCES

[1] R. J. Trew and M. W. Shin, "Wide bandgap semiconductor MESFETs for high temperature applications," presented at Proceedings of the 3rd International Workshop on Integrated Nonlinear Microwave and Millimeterwave Circuits, Oct 5-7 1994, Duisburg, Ger, 1994.

[2] M. Kuball, J. M. Hayes, M. J. Uren, I. Martin, J. C. H. Birbeck, R. S. Balmer, and B. T. Hughes, "Measurement of temperature in active high-power AlGaN/GaN HFETs using Raman spectroscopy," *IEEE Electron Device Letters*, vol. 23, pp. 7-9, 2002.

[3] M. Kuball, S. Rajasingam, A. Sarua, M. J. Uren, T. Martin, B. T. Hughes, K. P. Hilton, and R. S. Balmer, "Measurement of temperature distribution in multifinger AlGaN/GaN heterostructure field-effect transistors using micro-Raman spectroscopy," *Applied Physics Letters*, vol. 82, pp. 124-6, 2003.

[4] M. Kuball, M. J. Uren, J. M. Hayes, T. Martin, J. C. H. Birbeck, R. S. Balmer, and B. T. Hughes, "Self-heating effects in high-power AlGaN/GaN HFETs," presented at GaN and Related Alloys - 2001, 26-30 Jan. 2001, Boston, MA, USA, 2002.

[5] "Internal QinetiQ document."

[6] L. F. Eastman, V. Tilak, J. Smart, B. M. Green, E. M. Chumbes, R. Dimitrov, H. Kim, O. S. Ambacher, N. Weimann, T. Prunty, M. Murphy, W. J. Schaff, and J. R. Shealy, "Undoped AlGaN/GaN HEMTs for microwave power amplification," *IEEE Transactions on Electron Devices*, vol. 48, pp. 479-85, 2001.

[7] O. Ambacher, B. Foutz, J. Smart, J. R. Shealy, N. G. Weimann, K. Chu, M. Murphy, A. J. Sierakowski, W. J. Schaff, L. F. Eastman, R. Dimitrov, A. Mitchell, and M. Stutzmann, "Two dimensional electron gases induced by spontaneous and piezoelectric polarization in undoped and doped AlGaN/GaN heterostructures," *Journal of Applied Physics*, vol. 87, pp. 334-44, 2000.

[8] G. D. O'Clock, Jr. and M. T. Duffy, "Acoustic surface wave properties of epitaxially grown aluminum nitride and gallium nitride on sapphire," *Applied Physics Letters*, vol. 23, pp. 55-6, 1973.

[9] O. Ambacher, J. Smart, J. R. Shealy, N. G. Weimann, K. Chu, M. Murphy, W. J. Schaff, L. F. Eastman, R. Dimitrov, L. Wittmer, M. Stutzmann, W. Rieger, and J. Hilsenbeck, "Two-dimensional electron gases induced by spontaneous and piezoelectric polarization charges in N- and Ga-face AlGaN/GaN heterostructures," *Journal of Applied Physics*, vol. 85, pp. 3222-33, 1999.

[10] U. K. Mishra, P. Parikh, and Y.-F. Wu, "AlGaN/GaN HEMTs-an overview of device operation and applications," *Proceedings of the IEEE*, vol. 90, pp. 1022-31, 2002.

[11] P. M. Asbeck, E. T. Yu, S. S. Lau, G. J. Sullivan, J. Van Hove, and J. Redwing, "Piezoelectric charge densities in AlGaN/GaN HFETs," *Electronics Letters*, vol. 33, pp. 1230-1, 1997.

[12] O. Ambacher, J. Majewski, C. Miskys, A. Link, M. Hermann, M. Eickhoff, M. Stutzmann, F. Bernardini, V. Fiorentini, V. Tilak, B. Schaff, and L. F. Eastman, "Pyroelectric properties of Al(In)GaN/GaN hetero- and quantum well

structures," *Journal of Physics: Condensed Matter*, vol. 14, pp. 3399-434, 2002.
[13] B. Jogai, "Three-dimensional strain field calculations in multiple InN/AlN wurtzite quantum dots," *Journal of Applied Physics*, vol. 90, pp. 699-704, 2001.
[14] J. F. Nye, *Ohysical Properties of Crystals: Their Representation by Tensors and Matrices*: Oxford Clarendon, 1985.
[15] Rashmi, A. Kranti, S. Haldar, and R. S. Gupta, "An accurate charge control model for spontaneous and piezoelectric polarization dependent two-dimensional electron gas sheet charge density of lattice-mismatched AlGaN/GaN HEMTs," *Solid-State Electronics*, vol. 46, pp. 621-30, 2002.
[16] E. M. Chumbes, A. T. Schremer, J. A. Smart, D. Hogue, J. Komiak, and J. R. Shealy, "Microwave performance of AlGaN/GaN high electron mobility transistors on Si(111) substrates," presented at International Electron Devices Meeting 1999. Technical Digest, 5-8 Dec. 1999, Washington, DC, USA, 1999.
[17] V. Hoel, N. Vellas, C. Gaquiere, J. C. De Jaeger, Y. Cordier, F. Semond, F. Natali, and J. Massies, "High-power AlGaN/GaN HEMTs on resistive silicon substrate," *Electronics Letters*, vol. 38, pp. 750-2, 2002.
[18] P. Javorka, M. Wolter, A. Alam, A. Fox, M. Marso, M. Heuken, and P. Kordos, "Optimization of AlGaN/GaN HEMT performance," presented at 2001 International Symposium on Electron Devices for Microwave and Optoelectronic Applications. EDMO 2001, 15-16 Nov. 2001, Vienna, Austria, 2001.
[19] P. Javorka, A. Alam, A. Fox, M. Marso, M. Heuken, and P. Kordos, "AlGaN/GaN HEMTs on silicon substrates with f_T of 32/20 GHz and f_{max} of 27/22 GHz for 0.5/0.7 μm gate length," *Electronics Letters*, vol. 38, pp. 288-289, 2002.
[20] P. Javorka, J. Bernat, A. Fox, M. Marso, H. Luth, and P. Kordos, "Influence of SiO/sub 2/ and Si/sub 3/N/sub 4/ passivation on AlGaN/GaN/Si HEMT performance," *Electronics Letters*, vol. 39, pp. 1155-7, 2003.
[21] H. Kalisch, Y. Dikme, G. Gerstenbrandt, A. Alam, A. Szymakowski, H. Klockenhoff, C. Rieckmann, M. Heuken, R. H. Jansen, P. Javorka, M. Marso, A. Fox, P. Kordos, and H. Luth, "Growth and characterisation of AlGaN/GaN HEMT on silicon substrates," *Physica Status Solidi A*, vol. 194, pp. 464-7, 2002.
[22] A. S. Brown, W. A. Doolittle, S. Kang, J.-J. Shen, Z. L. Wang, and Z. Dai, "Growth of GaN on lithium gallate (LiGaO₂) substrates for material integration," *Journal of Electronic Materials*
The 1999 International Conference on Compliant and Alternative Substrate Technology, Sep 19-Sep 23 1999, vol. 29, pp. 894-896, 2000.
[23] R. S. Balmer, C. Pickering, A. M. Kier, J. C. H. Birbeck, M. Saker, and T. Martin, "In situ optical monitoring of AlGaN thickness and composition during MOVPE growth of AlGaN/GaN microwave HFETs," *Journal of Crystal Growth*, vol. 230, pp. 361-367, 2001.
[24] S. Keller, B. P. Keller, Y.-F. Wu, B. Heying, D. Kapolnek, J. S. Speck, U. K. Mishra, and S. P. DenBaars, "Influence of sapphire nitridation on properties of gallium nitride grown by metalorganic chemical vapor deposition," *Applied Physics Letters*, vol. 68, pp. 1525-7, 1996.
[25] I. Akasaki, H. Amano, Y. Koide, K. Hiramatsu, and N. Sawaki, "Effects of ain buffer layer on crystallographic structure and on electrical and optical properties of GaN and Ga_{1-x}Al_xN (0 < x <= 0.4) films grown on sapphire substrate by MOVPE," *Journal of Crystal Growth*

Proceedings of US/Japan Seminar on Alloy Semiconductor Physics and Electronics, Oct 25-27 1988, vol. 98, pp. 209-219, 1989.

[26] J. R. Shealy, V. Kaper, V. Tilak, T. Prunty, J. A. Smart, B. Green, and L. F. Eastman, "An AlGaN/GaN high-electron-mobility transistor with an AlN sub-buffer layer," *Journal of Physics: Condensed Matter*, vol. 14, pp. 3499-509, 2002.

[27] P. Kordos, M. Morvic, J. Betko, J. M. Van Hove, A. M. Wowchak, and P. P. Chow, "Conductivity and Hall effect characterization of highly resistive molecular-beam epitaxial GaN layers," *Journal of Applied Physics*, vol. 88, pp. 5821-5826, 2000.

[28] M. A. Khan, J. N. Kuznia, A. R. Bhattarai, and D. T. Olson, "Metal semiconductor field effect transistor based on single crystal GaN," *Applied Physics Letters*, vol. 62, pp. 1786-7, 1993.

[29] M. A. Khan, A. Bhattarai, J. N. Kuznia, and D. T. Olson, "High electron mobility transistor based on a GaN-Al/sub x/Ga/sub 1-x/N heterojunction," *Applied Physics Letters*, vol. 63, pp. 1214-15, 1993.

[30] M. A. Khan, "Microwave performance of a 0.2 _m gate AlGaN/GaN heterostructure field effect transistor," *Appl. Phys. Lett*, vol. vol. 65, pp. 1121-1123, 1994.

[31] Y.-F. Wu, B. P. Keller, S. Keller, D. Kapolnek, P. Kozodoy, S. P. Denbaars, and U. K. Mishra, "Very high breakdown voltage and large transconductance realized on GaN heterojunction field effect transistors," *Applied Physics Letters*, vol. 69, pp. 1438-40, 2.

[32] Y.-F. Wu, B. P. Keller, S. Keller, D. Kapolnek, S. P. Denbaars, and U. K. Mishra, "Measured microwave power performance of AlGaN/GaN MODFET," *IEEE Electron Device Letters*, vol. 17, pp. 455-7, 1996.

[33] Y.-F. Wu, S. Keller, P. Kozodoy, B. P. Keller, P. Parikh, D. Kapolnek, S. P. Denbaars, and U. K. Mishra, "Bias dependent microwave performance of AlGaN/GaN MODFET's up to 100 V," *IEEE Electron Device Letters*, vol. 18, pp. 290-2, 1997.

[34] Y.-F. Wu, B. P. Keller, S. Keller, N. X. Nguyen, M. Le, C. Nguyen, T. J. Jenkins, L. T. Kehias, S. P. Denbaars, and U. K. Mishra, "Short channel AlGaN/GaN MODFET's with 50-GHz f/sub T/ and 1.7-W/mm output-power at 10 GHz," *IEEE Electron Device Letters*, vol. 18, pp. 438-40, 1997.

[35] Y.-F. Wu, B. P. Keller, P. Fini, S. Keller, T. J. Jenkins, L. T. Kehias, S. P. Denbaars, and U. K. Mishra, "High Al-content AlGaN/GaN MODFETs for ultrahigh performance," *IEEE Electron Device Letters*, vol. 19, pp. 50-3, 1998.

[36] Y.-F. Wu, B. P. Keller, P. Fini, J. Pusl, M. Le, N. X. Nguyen, C. Nguyen, D. Widman, S. Keller, S. P. Denbaars, and U. K. Mishra, "Short-channel Al/sub 0.5/Ga/sub 0.5/N-GaN MODFETs with power density >3 W/mm at 18 GHz," *Electronics Letters*, vol. 33, pp. 1742-3, 25.

[37] S. C. Binari, J. M. Redwing, G. Kelner, and W. Kruppa, "AlGaN/GaN HEMTs grown on SiC substrates," *Electronics Letters*, vol. 33, pp. 242-3, 1997.

[38] G. J. Sullivan, J. A. Higgins, M. Y. Chen, J. W. Yang, Q. Chen, R. L. Pierson, and B. T. McDermott, "High power RF operation of AlGaN/GaN HEMTs grown on insulating silicon carbide substrates," *Electronics Letters*, vol. 34, pp. 922-4, 1998.

[39] S. T. Sheppard, K. Doverspike, W. L. Pribble, S. T. Allen, J. W. Palmour, L. T.

Kehias, and T. J. Jenkins, "High-power microwave GaN/AlGaN HEMTs on semi-insulating silicon carbide substrates," *IEEE Electron Device Letters*, vol. 20, pp. 161-3, 1999.

[40] Y.-F. Wu, D. Kapolnek, J. P. Ibbetson, P. Parikh, B. P. Keller, and U. K. Mishra, "Very-high power density AlGaN/GaN HEMTs," *IEEE Transactions on Electron Devices*, vol. 48, pp. 586-590, 2001.

[41] V. Tilak, B. Green, V. Kaper, H. Kim, T. Prunty, J. Smart, J. Shealy, and L. Eastman, "Influence of barrier thickness on the high-power performance of AlGaN/GaN HEMTs," *IEEE Electron Device Letters*, vol. 22, pp. 504-6, 2001.

[42] Y. Ando, Y. Okamoto, H. Miyamoto, N. Hayama, T. Nakayama, K. Kasahara, and M. Kuzuhara, "A 110-W AlGaN/GaN heterojunction FET on thinned sapphire substrate," presented at International Electron Devices Meeting. Technical Digest, 2-5 Dec. 2001, Washington, DC, USA, 2001.

[43] Y.-F. Wu, P. M. Chavarkar, M. Moore, P. Parikh, B. P. Keller, and U. K. Mishra, "A 50-W AlGaN/GaN HEMT amplifier," presented at 2000 IEEE International Electron Devices Meeting, Dec 10-13 2000, San Francisco, CA, 2000.

[44] K. Kasahara, H. Miyamoto, Y. Ando, Y. Okamoto, T. Nakayama, and M. Kuzuhara, "Ka-band 2.3W power AlGaN/GaN heterojunction FET," presented at IEEE International Electron Devices Meeting, 8-11 Dec. 2002, San Francisco, CA, USA, 2002.

[45] R. Sandhu, M. Wojtowicz, M. Barsky, R. Tsai, I. Smorchkova, C. Namba, P. H. Liu, R. Dia, M. Truong, D. Ko, J. W. Yang, H. Wang, and M. A. Khan, "1.6 w/mm, 26% PAE AlGaN/GaN HEMT operation at 29GHz," presented at International Electron Devices Meeting. Technical Digest, 2-5 Dec. 2001, Washington, DC, USA, 2001.

[46] R. Sandhu, M. Wojtowicz, I. Smorchkova, M. Barsky, R. Tsai, J. W. Yang, H. Wang, and M. A. Khan, "3.2 W/mm, 71% PAE AlGaN/GaN HEMT operation at 20 GHz," presented at Device Research Conference, 24-26 June 2002, Santa Barbara, CA, USA, 2002.

[47] V. Kumar, W. Lu, R. Schwindt, J. Van Hove, P. Chow, and I. Adesida, "0.25 mu m gate-length, MBE-grown AlGaN/GaN HEMTs with high current and high f/sub T/," *Electronics Letters*, vol. 37, pp. 858-9, 2001.

[48] V. Kumar, W. Lu, F. A. Khan, R. Schwindt, A. Kuliev, J. Yang, A. A. Khan, and I. Adesida, "High performance 0.15 mu m recessed gate AlGaN/GaN HEMTs on sapphire," presented at International Electron Devices Meeting. Technical Digest, 2-5 Dec. 2001, Washington, DC, USA, 2001.

[49] V. Kumar, W. Lu, F. A. Khan, R. Schwindt, A. Kuliev, G. Simin, J. Yang, M. Asif Khan, and I. Adesida, "High performance 0.25 mu m gate-length AlGaN/GaN HEMTs on sapphire with transconductance of over 400 mS/mm," *Electronics Letters*, vol. 38, pp. 252-3, 2002.

[50] V. Kumar, A. Kuliev, R. Schwindt, G. Simin, J. Yang, M. Asif Khan, and I. Adesida, "High-performance AlGaN/GaN high electron mobility transistors on SiC," *Physica Status Solidi A*, vol. 194, pp. 456-9, 2002.

[51] V. Kumar, W. Lu, F. A. Khan, R. Schwindt, E. Piner, and I. Adesida, "Recessed 0.25 mu m gate AlGaN/GaN HEMTs on SiC with high gate-drain breakdown voltage using ICP-RIE," *Electronics Letters*, vol. 37, pp. 1483-5, 2001.

[52] V. Kumar, W. Lu, R. Schwindt, A. Kuliev, G. Simin, J. Yang, M. Asif Khan, and I. Adesida, "AlGaN/GaN HEMTs on SiC with f/sub T/ of over 120 GHz," *IEEE*

Electron Device Letters, vol. 23, pp. 455-7, 2002.

[53] K. Asano, Y. Miyoshi, K. Ishikura, Y. Nashimoto, M. Kuzuhara, and M. Mizuta, "Novel high power AlGaAs/GaAs HFET with a field-modulating plate operated at 35 V drain voltage," presented at International Electron Devices Meeting 1998. Technical Digest, 6-9 Dec. 1998, San Francisco, CA, USA, 1998.

[54] N.-Q. Zhang, S. Keller, G. Parish, S. Heikman, S. P. DenBaars, and U. K. Mishra, "High breakdown GaN HEMT with overlapping gate structure," *IEEE Electron Device Letters*, vol. 21, pp. 373-5, 2000.

[55] Y. Ando, Y. Okamoto, H. Miyamoto, T. Nakayama, T. Inoue, and M. Kuzuhara, "10-W/mm AlGaN-GaN HFET with a field modulating plate," *IEEE Electron Device Letters*, vol. 24, pp. 289-91, 2003.

[56] J. Li, S. J. Cai, G. Z. Pan, Y. L. Chen, C. P. Wen, and K. L. Wang, "High breakdown voltage GaN HFET with field plate," *Electronics Letters*, vol. 37, pp. 196-7, 2001.

[57] Y. Ando, Y. Okamoto, K. Hataya, T. Nakayama, H. Miyamoto, T. Inoue, and M. Kuzuhara, "12 W/mm recessed-gate AlGaN/GaN heterojunction field-plate FET," presented at IEEE International Electron Devices Meeting 2003, 8-10 Dec. 2003, Washington, DC, USA, 2003.

[58] Y. Okamoto, Y. Ando, K. Hataya, T. Nakayama, H. Miyamoto, T. Inoue, M. Senda, K. Hirata, M. Kosaki, N. Shibata, and M. Kuzuhara, "179 W recessed-gate AlGaN/GaN heterojunction FET with field-modulating plate," *Electronics Letters*, vol. 40, pp. 629-31, 2004.

[59] Y. Okamoto, Y. Ando, H. Miyamoto, T. Nakayama, T. Inoue, and M. Kuzuhara, "An 80W AlGaN/GaN heterojunction FET with a field-modulating plate," presented at IEEE MTT-S International Microwave Symposium - IMS 2003, 8-13 June 2003, Philadelphia, PA, USA, 2003.

[60] Y. Okamoto, Y. Ando, K. Hataya, H. Miyamoto, T. Nakayama, T. Inoue, and M. Kuzuhara, "96 W AlGaN/GaN heterojunction FET with field-modulating plate," *Electronics Letters*, vol. 39, pp. 1474-5, 2003.

[61] Y. Okamoto, Y. Ando, K. Hataya, T. Nakayama, H. Miyamoto, T. Inoue, M. Senda, K. Hirata, M. Kosaki, N. Shibata, and M. Kuzuhara, "A 149W recessed-gate AlGaN/GaN FP-FET," presented at 2004 IEEE MTT-S International Microwave Symposium Digest, 6-11 June 2004, Fort Worth, TX, USA, 2004.

[62] A. Chini, D. Buttari, R. Coffie, S. Heikman, S. Keller, and U. K. Mishra, "12 W/mm power density AlGaN/GaN HEMTs on sapphire substrate," *Electronics Letters*, vol. 40, pp. 73-4, 2004.

[63] Y.-F. Wu, A. Saxler, M. Moore, R. P. Smith, S. Sheppard, P. M. Chavarkar, T. Wisleder, U. K. Mishra, and P. Parikh, "30-W/mm GaN HEMTs by field plate optimization," *IEEE Electron Device Letters*, vol. 25, pp. 117-19, 2004.

[64] N. G. Weimann, M. J. Manfra, S. Chakraborty, and D. M. Tennant, "Submicron AlGaN/GaN HEMTs with very high drain current density grown by plasma-assisted MBE on 6H-SiC," *IEEE Electron Device Letters*, vol. 23, pp. 691-3, 2002.

[65] A. M. Wells, M. J. Uren, R. Balmer, K. P. Hilton, T. Martin, and M. Missous, "Direct demonstration of the 'virtual gate' mechanism for current collapse in AlGaN/GaN HFETs," *Solid-State Electronics*, vol. 49, pp. 279-282, 2004.

[66] M. A. Khan, M. S. Shur, Q. C. Chen, and J. N. Kuznia, "Current/voltage characteristic collapse in AlGaN/GaN heterostructure insulated gate field effect

transistors at high drain bias," *ELECTRONICS LETTERS*, vol. 30, pp. 2175-6, 1994.

[67] L. F. Eastman, "Results, potential and challenges of high power GaN-based transistors," *Physica Status Solidi A*
3rd International Conference on Nitride Semiconductors, 4-9 July 1999, vol. 176, pp. 175-8, 1999.

[68] C. Nguyen, N. X. Nguyen, and D. E. Grider, "Drain current compression in GaN MODFETs under large-signal modulation at microwave frequencies," *Electronics Letters*, vol. 35, pp. 1380-2, 1999.

[69] E. Kohn, I. Daumiller, P. Schmid, N. X. Nguyen, and C. N. Nguyen, "Large signal frequency dispersion of AlGaN/GaN heterostructure field effect transistors," *Electronics Letters*, vol. 35, pp. 1022-4, 1999.

[70] Y.-F. Wu, B. P. Keller, S. Keller, J. J. Xu, B. J. Thibeault, S. P. Denbaars, and U. K. Mishra, "GaN-based FETs for microwave power amplification," *IEICE Transactions on Electronics*, vol. E82-C, pp. 1895-905, 1999.

[71] R. Vetury, N. Q. Zhang, S. Keller, and U. K. Mishra, "The impact of surface states on the DC and RF characteristics of AlGaN/GaN HFETs," *IEEE Transactions on Electron Devices*, vol. 48, pp. 560-6, 2001.

[72] Y.-F. Wu, P. M. Chavarkar, M. Moore, P. Parikh, and U. K. Mishra, "Bias-dependent performance of high-power AlGaN/GaN HEMTs," presented at International Electron Devices Meeting. Technical Digest, 2-5 Dec. 2001, Washington, DC, USA, 2001.

[73] P. B. Klein, J. A. Freitas, Jr., S. C. Binari, and A. E. Wickenden, "Observation of deep traps responsible for current collapse in GaN metal-semiconductor field-effect transistors," *Applied Physics Letters*, vol. 75, pp. 4016-18, 1999.

[74] P. B. Klein, S. C. Binari, K. Ikossi-Anastasiou, A. E. Wickenden, D. D. Koleske, R. L. Henry, and D. S. Katzer, "Investigation of traps producing current collapse in AlGaN/GaN high electron mobility transistors," *Electronics Letters*, vol. 37, pp. 661-2, 2001.

[75] P. B. Klein, S. C. Binari, K. Ikossi, A. E. Wickenden, D. D. Koleske, and R. L. Henry, "Effect of deep traps on sheet charge in AlGaN/GaN high electron mobility transistors," *Electronics Letters*, vol. 37, pp. 1550-1, 2001.

[76] P. B. Klein, S. C. Binari, K. Ikossi, A. E. Wickenden, D. D. Koleske, and R. L. Henry, "Current collapse and the role of carbon in AlGaN/GaN high electron mobility transistors grown by metalorganic vapor-phase epitaxy," *Applied Physics Letters*, vol. 79, pp. 3527-9, 2001.

[77] S. C. Binari, K. Ikossi-Anastasiou, W. Kruppa, H. B. Dietrich, G. Kelner, R. L. Henry, D. D. Koleske, and A. E. Wickenden, "Correlation of drain current pulsed response with microwave power output in AlGaN/GaN HEMTs," presented at Wide-Bandgap Semiconductors for High-Power, High-Frequency and High-Temperature Applications - 1999. Symposium, 5-8 April 1999, San Francisco, CA, USA, 1999.

[78] S. C. Binari, K. Ikossi, J. A. Roussos, W. Kruppa, D. Park, H. B. Dietrich, D. D. Koleske, A. E. Wickenden, and R. L. Henry, "Trapping effects and microwave power performance in AlGaN/GaN HEMTs," *IEEE Transactions on Electron Devices*, vol. 48, pp. 465-71, 2001.

[79] S. C. Binari, P. B. Klein, and T. E. Kazior, "Trapping effects in GaN and SiC microwave FETs," *Proceedings of the IEEE*, vol. 90, pp. 1048-58, 2002.

[80] S. C. Binari, P. B. Klein, and T. E. Kazior, "Trapping effects in wide-bandgap microwave FETs," presented at Proceedings of 2002 International Microwave Symposium (MTT 2002), 2-7 June 2002, Seattle, WA, USA, 2002.

[81] A. Tarakji, G. Simin, N. Ilinskaya, X. Hu, A. Kumar, A. Koudymov, J. Yang, M. A. Khan, M. S. Shur, and R. Gaska, "Mechanism of radio-frequency current collapse in GaN-AlGaN field-effect transistors," *Applied Physics Letters*, vol. 78, pp. 2169-71, 2001.

[82] A. Tarakji, X. Hu, A. Koudymov, G. Simin, J. Yang, M. A. Khan, M. S. Shur, and R. Gaska, "DC and microwave performance of a GaN/AlGaN MOSHFET under high temperature stress," *Solid-State Electronics*, vol. 46, pp. 1211-14, 2002.

[83] O. Mitrofanov and M. Manfra, "Dynamics of trapped charge in GaN/AlGaN/GaN high electron mobility transistors grown by plasma-assisted molecular beam epitaxy," *Applied Physics Letters*, vol. 84, pp. 422-4, 2004.

[84] G. Koley, V. Tilak, L. F. Eastman, and M. G. Spencer, "Slow transients observed in AlGaN/GaN HFETs: effects of SiN/sub x/ passivation and UV illumination," *IEEE Transactions on Electron Devices*, vol. 50, pp. 886-93, 2003.

[85] G. Verzellesi, R. Pierobon, F. Rampazzo, G. Meneghesso, A. Chini, U. K. Mishra, C. Canali, and E. Zanoni, "Experimental/numerical investigation on current collapse in AlGaN/GaN HEMT's," presented at IEEE International Electron Devices Meeting, 8-11 Dec. 2002, San Francisco, CA, USA, 2002.

[86] Y. Ohno, M. Akita, S. Kishimoto, K. Maezawa, and T. Mizutani, "Temperature distribution measurement in AlGaN/GaN high-electron-mobility transistors by micro-Raman scattering spectroscopy," *Japanese Journal of Applied Physics, Part 2 (Letters)*, vol. 41, pp. 452-4, 2002.

[87] Y. Ohno, T. Nakao, M. Akita, S. Kishimoto, K. Maezawa, and T. Mizutani, "Electroluminescence in AlGaN/GaN HEMTs," presented at Compound Semiconductors 2001. Proceedings of the Twenty-Eighth International Symposium on Compound Semiconductors, 1-4 Oct. 2001, Tokyo, Japan, 2002.

[88] T. Nakao, Y. Ohno, M. Akita, S. Kishimoto, K. Maezawa, and T. Mizutani, "Electroluminescence in AlGaN/GaN high electron mobility transistors under high bias voltage," *Japanese Journal of Applied Physics, Part 1 (Regular Papers, Short Notes & Review Papers)*, vol. 41, pp. 1990-1, 2002.

[89] T. Mizutani, Y. Ohno, M. Akita, S. Kishimoto, and K. Maezawa, "Current collapse in AlGaN/GaN HEMTs investigated by electrical and optical characterizations," *Physica Status Solidi A*, vol. 194, pp. 447-51, 2002.

[90] A. Vertiatchikh, L. F. Eastman, W. J. Schaff, and I. Prunty, "Effect of surface passivation of AlGaN/GaN heterostructure field-effect transistor," *Electronics Letters*, vol. 38, pp. 388-9, 2002.

[91] B. M. Green, K. K. Chu, E. M. Chumbes, J. A. Smart, J. R. Shealy, and L. F. Eastman, "The effect of surface passivation on the microwave characteristics of undoped AlGaN/GaN HEMTs," *IEEE Electron Device Letters*, vol. 21, pp. 268-70, 2000.

[92] W. S. Tan, P. A. Houston, P. J. Parbrook, G. Hill, and R. J. Airey, "Comparison of different surface passivation dielectrics in AlGaN/GaN heterostructure field-effect transistors," *Journal of Physics D (Applied Physics)*, vol. 35, pp. 595-8, 2002.

[93] N.-Q. Zhang, B. Moran, S. P. DenBaars, U. K. Mishra, X. W. Wang, and T. P.

Ma, "Effects of surface traps on breakdown voltage and switching speed of GaN power switching HEMTs," presented at International Electron Devices Meeting. Technical Digest, 2-5 Dec. 2001, Washington, DC, USA, 2001.

[94] J.-S. Lee, A. Vescan, A. Wieszt, R. Dietrich, H. Leier, and Y.-S. Kwon, "Characteristics of AlGaN/GaN HEMT devices with SiN passivation," presented at International Electron Devices Meeting. Technical Digest. IEDM, 10-13 Dec. 2000, San Francisco, CA, USA, 2000.

[95] T. Kikkawa, M. Nagahara, N. Okamoto, Y. Tateno, Y. Yamaguchi, N. Hara, K. Joshin, and P. M. Asbeck, "Surface-charge controlled AlGaN/GaN-power HFET without current collapse and gm dispersion," presented at International Electron Devices Meeting. Technical Digest, 2-5 Dec. 2001, Washington, DC, USA, 2001.

[96] J. P. Ibbetson, P. T. Fini, K. D. Ness, S. P. DenBars, J. S. Speck, and U. K. Mishra, "Polarization effects, surface states, and the source of electrons in AlGaN/GaN heterostructure field effect transistors," *Applied Physics Letters*, vol. 77, pp. 250-2, 2000.

[97] R. Coffie, D. Buttari, S. Heikman, S. Keller, A. Chini, L. Shen, and U. K. Mishra, "p-capped GaN-AlGaN-GaN high-electron mobility transistors (HEMTs)," *IEEE Electron Device Letters*, vol. 23, pp. 588-590, 2002.

[98] M. Neuburger , I. Daumiller, M. Kunze, M. Seyboth, T. Jenkins, J. Van Norstand, and E. Kohn, "Influence of polarization on the properties of GaN based FET structures," *Physica Status Solidi C*, vol. 0, pp. 1919-1939, 2003.

[99] R. S. Balmer, K. P. Hilton, K. J. Nash, M. J. Uren, D. J. Wallis, D. Lee, A. Wells, M. Missous, and T. Martin, "Analysis of thin AlN carrier exclusion layers in AlGaN/GaN microwave heterojunction field-effect transistors," *Semiconductor Science and Technology*, vol. 19, pp. 65-7, 2004.

[100] B. K. Ridley, B. E. Foutz, and L. F. Eastman, "Mobility of electrons in bulk GaN and Al/sub x/Ga/sub 1-x/N/GaN heterostructures," *Physical Review B (Condensed Matter)*, vol. 61, pp. 16862-9, 2000.

[101] L. Hsu and W. Walukiewicz, "Electron mobility in Al/sub x/Ga/sub 1-x/N/GaN heterostructures," *Physical Review B (Condensed Matter)*, vol. 56, pp. 1520-8, 1997.

[102] L. Hsu and W. Walukiewicz, "Effect of polarization fields on transport properties in AlGaN/GaN heterostructures," *Journal of Applied Physics*, vol. 89, pp. 1783-9, 2001.

[103] I. P. Smorchkova, C. R. Elsass, J. P. Ibbetson, R. Vetury, B. Heying, P. Fini, E. Haus, S. P. DenBaars, J. S. Speck, and U. K. Mishra, "Polarization-induced charge and electron mobility in AlGaN/GaN heterostructures grown by plasma-assisted molecular-beam epitaxy," *Journal of Applied Physics*, vol. 86, pp. 4520-6, 1999.

[104] I. P. Smorchkova, L. Chen, T. Mates, L. Shen, S. Heikman, B. Moran, S. Keller, S. P. DenBaars, J. S. Speck, and U. K. Mishra, "AlN/GaN and (Al,Ga)N/AlN/GaN two-dimensional electron gas structures grown by plasma-assisted molecular-beam epitaxy," *Journal of Applied Physics*, vol. 90, pp. 5196-201, 2001.

[105] L. Shen, S. Heikman, B. Moran, R. Coffie, N.-Q. Zhang, D. Buttari, I. P. Smorchkova, S. Keller, S. P. DenBaars, and U. K. Mishra, "AlGaN/AlN/GaN high-power microwave HEMT," *IEEE Electron Device Letters*, vol. 22, pp. 457-

9, 2001.
[106] M. Hiroki, N. Maeda, and N. Kobayashi, "Metalorganic vapor phase epitaxy growth of AlGaN/GaN heterostructures on sapphire substrates," *Journal of Crystal Growth*, vol. 237-239, pp. 956-60, 2002.
[107] Z. Zhong, O. Ambacher, A. Link, V. Holy, J. Stangl, R. T. Lechner, T. Roch, and G. Bauer, "Influence of GaN domain size on the electron mobility of two-dimensional electron gases in AlGaN/GaN heterostructures determined by X-ray reflectivity and diffraction," *Applied Physics Letters*, vol. 80, pp. 3521-3, 2002.
[108] W. Knap, E. Borovitskaya, M. S. Shur, L. Hsu, W. Walukiewicz, E. Frayssinet, P. Lorenzini, N. Grandjean, C. Skierbiszewski, P. Prystawko, M. Leszczynski, and I. Grzegory, "Acoustic phonon scattering of two-dimensional electrons in GaN/AlGaN heterostructures," *Applied Physics Letters*, vol. 80, pp. 1228-30, 2002.
[109] A. Saxler, P. Debray, R. Perrin, S. Elhamri, W. C. Mitchel, C. R. Elsass, I. P. Smorchkova, B. Heying, E. Haus, P. Fini, J. P. Ibbetson, S. Keller, P. M. Petroff, S. P. DenBaars, U. K. Mishra, and J. S. Speck, "Characterization of an AlGaN/GaN two-dimensional electron gas structure," *Journal of Applied Physics*, vol. 87, pp. 369-74, 2000.
[110] Y. Zhang, I. P. Smorchkova, C. R. Elsass, S. Keller, J. P. Ibbetson, S. Denbaars, U. K. Mishra, and J. Singh, "Charge control and mobility in AlGaN/GaN transistors: Experimental and theoretical studies," *Journal of Applied Physics*, vol. 87, pp. 7981-7, 2000.
[111] C. F. Lin, H. C. Cheng, J. A. Huang, M. S. Feng, J. D. Guo, and G. C. Chi, "Mobility enhancements in AlGaN/GaN/SiC with stair-step and graded heterostructures," *Applied Physics Letters*, vol. 70, pp. 2583-5, 1997.
[112] X. Z. Dang, P. M. Asbeck, E. T. Yu, G. J. Sullivan, M. Y. Chen, B. T. McDermott, K. S. Boutros, and J. M. Redwing, "Measurement of drift mobility in AlGaN/GaN heterostructure field-effect transistor," *Applied Physics Letters*, vol. 74, pp. 3890-2, 1999.
[113] R. Gaska, J. W. Yang, A. Osinsky, Q. Chen, M. Asif Khan, A. O. Orlov, G. L. Snider, and M. S. Shur, "Electron transport in AlGaN-GaN heterostructures grown on 6H-SiC substrates," *Applied Physics Letters*, vol. 72, pp. 707-9, 1998.
[114] R. Gaska, M. S. Shur, A. D. Bykhovski, A. O. Orlov, and G. L. Snider, "Electron mobility in modulation-doped AlGaN-GaN heterostructures," *Applied Physics Letters*, vol. 74, pp. 287-9, 1999.
[115] J. W. Johnson, J. Han, A. G. Baca, R. D. Briggs, R. J. Shul, J. R. Wendt, C. Monier, F. Ren, B. Luo, S. N. G. Chu, D. Tsvetkov, V. Dmitriev, and S. J. Pearton, "Comparison of AlGaN/GaN high electron mobility transistors grown on AlN/SiC templates or sapphire," *Solid-State Electronics*, vol. 46, pp. 513-523, 2002.
[116] M. J. Uren, D. Lee, B. T. Hughes, P. J. M. Parmiter, J. C. Birbeck, R. Balmer, T. Martin, R. H. Wallis, and S. K. Jones, "Electrical characterisation of AlGaN/GaN heterostructure wafers for high-power HFETs," *Journal of Crystal Growth*, vol. 230, pp. 579-583, 2001.
[117] M. J. Uren, D. Herbert, T. Martin, B. T. Hughes, J. Birbeck, R. Balmer, A. J. Pidduck, and S. K. Jones, "Back bias effects in AlGaN/GaN HFETs," *Physica Status Solidi A*
Fourth International Conference on Nitride Semiconductors, 16-20 July 2001,

vol. 188, pp. 195-8, 2001.
[118] M. J. Uren, T. Martin, B. T. Hughes, K. P. Hilton, A. Wells, R. S. Balmer, D. C. Herbert, A. M. Keir, D. J. Wallis, A. J. Pidduck, and M. Missous, "Channel mobility in AlGaN/GaN HFETs on SiC and sapphire substrates," *Physica Status Solidi C*, pp. 468-71, 2002.
[119] M. Marso, J. Bernat, P. Javorka, and P. Kordos, "Influence of a carrier supply layer on carrier density and drift mobility of AlGaN/GaN/SiC high-electron-mobility transistors," *Applied Physics Letters*, vol. 84, pp. 2928-2930, 2004.
[120] H. Amano, N. Sawaki, I. Akasaki, and Y. Toyoda, "Metalorganic vapor phase epitaxial growth of a high quality GaN film using an AlN buffer layer," *Applied Physics Letters*, vol. 48, pp. 353-5, 1986.
[121] H. Amano, M. Iwaya, T. Kashima, M. Katsuragawa, I. Akasaki, J. Han, S. Hearne, J. A. Floro, E. Cheson, and J. Figiel, "Stress and defect control in GaN using low temperature interlayers," *Japanese Journal of Applied Physics, Part 2 (Letters)*, vol. 37, pp. 1540-2, 1998.
[122] H. Amano, M. Iwaya, N. Hayashi, T. Kashima, S. Nitta, C. Wetzel, and I. Akasaki, "Control of dislocations and stress in AlGaN on sapphire using a low temperature interlayer," *Physica Status Solidi B*
3rd International Conference on Nitride Semiconductors, 4-9 July 1999, vol. 216, pp. 683-9, 1999.
[123] Z. Bougrioua, I. Moerman, L. Nistor, B. Van Daele, E. Monroy, T. Palacios, F. Calle, and M. Leroux, "Engineering of an insulating buffer and use of AlN interlayers: two optimisations for AlGaN-GaN HEMT-like structures," *Physica Status Solidi C*, pp. 93-100, 2003.
[124] M. Germain, M. Leys, S. Boeykens, S. Degroote, W. Wang, D. Schreurs, W. Ruythooren, K.-H. Choi, B. Van Daele, G. Van Tendeloo, and G. Borghs, "High electron mobility in AlGaN/GaN HEMT grown on sapphire: strain modification by means of AlN interlayers," presented at GaN and Related Alloys - 2003 Symposium, 1-5 Dec. 2003, Boston, MA, USA, 2004.
[125] I.-H. Lee, T. G. Kim, and Y. Park, "Growth of crack-free AlGaN film on high-temperature thin AlN interlayer," *Journal of Crystal Growth*, vol. 234, pp. 305-10, 2002.
[126] A. P. Zhang, L. B. Rowland, E. B. Kaminsky, J. B. Tucker, J. W. Kretchmer, A. F. Allen, J. Cook, and B. J. Edward, "9.2 W/mm (13.8 W) AlGaN/GaN HEMTs at 10 GHz and 55 V drain bias," *Electronics Letters*, vol. 39, pp. 245-7, 2003.
[127] J. P. Zhang, H. M. Wang, M. E. Gaevski, C. Q. Chen, Q. Fareed, J. W. Yang, G. Simin, and M. A. Khan, "Crack-free thick AlGaN grown on sapphire using AlN/AlGaN superlattices for strain management," *Applied Physics Letters*, vol. 80, pp. 3542-4, 2002.
[128] C. Q. Chen, J. P. Zhang, M. E. Gaevski, H. M. Wang, W. H. Sun, R. S. Q. Fareed, J. W. Yang, and M. A. Khan, "AlGaN layers grown on GaN using strain-relief interlayers," *Applied Physics Letters*, vol. 81, pp. 4961-3, 2002.
[129] M. M. Wong, U. Chowdhury, D. Sicault, D. T. Becher, J. C. Denyszyn, T. G. Zhu, M. Feng, and R. D. Dupuis, "Delta-doped AlGaN/AlN/GaN microwave HFETs grown by metalorganic chemical vapour deposition," *Electronics Letters*, vol. 38, pp. 428-9, 2002.
[130] R. S. Balmer, K. P. Hilton, K. J. Nash, M. J. Uren, D. J. Wallis, A. Wells, M. Missous, and T. Martin, "AlGaN/GaN microwave HFET including a thin AlN

carrier exclusion layer," *Physica Status Solidi C*, pp. 2331-2334, 2003.
[131] R. S. Balmer, D. E. J. Soley, K. P. Hilton, K. J. Nash, M. J. Uren, D. J. Wallis, A. Wells, M. Missous, and T. Martin, "AlGaN/GaN microwave HFET including a thin AlN carrier exclusion layer," presented at 10th European Workshop on MOVPE,, Lecce (Italy), 2003.
[132] Y.-F. Wu, B. P. Keller, P. Fini, J. Pusl, M. Le, N. X. Nguyen, C. Nguyen, D. Widman, S. Keller, S. P. Denbaars, and U. K. Mishra, "Short-channel Al/sub 0.5/Ga/sub 0.5/N-GaN MODFETs with power density >3 W/mm at 18 GHz," *Electronics Letters*, vol. 33, pp. 1742-3, 1997.
[133] V. Desmaris, J. Eriksson, N. Rorsman, and H. Zirath, "Low-Resistance Si/Ti/Al/Ni/Au Multilayer Ohmic Contact to Undoped AlGaN/ GaN Heterostructures," *Electrochemical and Solid-State Letters*, vol. 7, pp. 72-74, 2004.
[134] T. Ando, A. B. Fowler, and F. Stern, "Electronic properties of two-dimensional systems.," *Rev. Mod. Phys.*, vol. 54, pp. 437-672, 1982.
[135] K. Hirakawa and H. Sakaki, "Mobility of the two-dimensional electron gas at selectively doped n-type Al/sub x/Ga/sub 1-x/As/GaAs heterojunctions with controlled electron concentrations," *Physical Review B (Condensed Matter)*, vol. 33, pp. 8291-303, 1986.
[136] O. Katz, A. Horn, G. Bahir, and J. Salzman, "Electron mobility in an AlGaN/GaN two-dimensional electron gas. I. Carrier concentration dependent mobility," *IEEE Transactions on Electron Devices*, vol. 50, pp. 2002-8, 2003.
[137] D. Qiao, L. S. Yu, S. S. Lau, J. M. Redwing, J. Y. Lin, and H. X. Jiang, "Dependence of Ni/AlGaN Schottky barrier height on Al mole fraction," *Journal of Applied Physics*, vol. 87, pp. 801-4, 2000.
[138] L. S. Yu, D. J. Qiao, Q. J. Xing, S. S. Lau, K. S. Boutros, and J. M. Redwing, "Ni and Ti Schottky barriers on n-AlGaN grown on SiC substrates," *Applied Physics Letters*, vol. 73, pp. 238-40, 1998.
[139] T. Sawada, Y. Izumi, N. Kimura, K. Suzuki, K. Imai, S. W. Kim, and T. Suzuki, "Properties of GaN and AlGaN Schottky contacts revealed from I-V-T and C-V-T measurements," *Applied Surface Science*
Fourth International Symposium on the Control of Semiconductor Interfaces, 21-25 Oct. 2002, vol. 216, pp. 192-7, 2003.
[140] E. Monroy, F. Calle, T. Palacios, J. Sanchez-Osorio, M. Verdu, F. J. Sanchez, M. T. Montojo, F. Omnes, Z. Bougrioua, I. Moerman, and P. Ruterana, "Reliability of Schottky contacts on AlGaN," *Physica Status Solidi A*
Fourth International Conference on Nitride Semiconductors, 16-20 July 2001, vol. 188, pp. 367-70, 2001.